CRANFIELD UNIVERSITY

John Rickman

Internally bevelled conoidal entry wounds in sandwich bones; their genesis, impact dynamics and macroscopic and microscopic morphology

Cranfield Forensic Institute

PhD

Academic year 2015-2021

Supervisor Dr Jon Painter

Secondary supervisor Dr Rachael Hazael

January 2021

CRANFIELD UNIVERSITY

Cranfield Forensic Institute

PhD

Academic year 2015-2021

JOHN RICKMAN

Internally bevelled conoidal entry wounds in sandwich bones; genesis, impact dynamics and their macroscopic and microscopic morphology

Supervisor Dr Jon Painter

Secondary supervisor Dr Rachael Hazael

January 2021

ABSRACT

Projectile trauma to the sandwich bones of the neurocranium is of considerable forensic anthropological importance due to the high lethality associated with gunshot wounds to this anatomical region. The internally bevelled conoidal wound that typically results from perpendicular projectile impact has long been considered diagnostic of bullet involvement and is utilised in both differential diagnosis of gunshot trauma and in making trajectory determinations using the direction of bevel asymmetry as an indicator. However, despite the importance of these activities in forensic anthropological casework the fracture mechanisms underlying bevel formation have remained elusive, with multiple hypotheses presented but few empirical investigations carried out to test them. Further diagnostic complexity has been introduced by the recognition that bevelling also results from low-velocity impacts and that taphonomic agencies can both modify and create internally bevelled fractures. Despite the fact that bone is a complex hierarchical material the majority of analyses of projectile entry wounds in sandwich bones have been conducted at the macroscopic scale, leaving important questions as to whether lower scales of organisation may yield signatures of diagnostic importance.

This thesis presents the findings of an experimental investigation into the fracture mechanisms that underlie internal bevelling and presents an analysis of the relationships between the dynamics of impact and quantitative wound morphology. A refined nomenclature for the components of internally bevelled fractures is presented and the layers composing the bevel formally defined. This thesis also presents a Scanning Electron Microscope (SEM) analysis of the effects of projectile impact on compact bone at lower hierarchical scales of bone organisation. Examination of fracture morphology with micro-computerised tomography (μ-CT) coupled with high-speed videography of the impact events revealed a novel cone cracking mechanism that fundamentally changes our understanding of bevel morphology. This mechanism explains how internal bevelling results from both low- and high-velocity impact events and suggests caution should be applied to trajectory determinations made using bevel asymmetry alone. Quantitative analysis of the perforation event revealed, for the first time in sandwich bones, a power relationship between incident velocity and absorbed kinetic energy. SEM analysis of cortical bone around the entry captured the early genesis of conoidal wounds through ring crack formation. Analysis of the periphery of the entry revealed two types of plastic deformation that are suggestive of changes to hydroxyapatite (HA) crystal structure that may be of diagnostic utility. Collectively, the findings presented in this thesis will enhance the diagnosis and interpretation of conoidal wounds in both forensic and archaeological contexts.

Keywords

Projectile trauma; sandwich bone; internal bevel; cone cracking; impact dynamics; bevel morphology; SEM; hydroxyapatite; plastic deformation

ACKNOWLEDGEMENTS

I am indebted to Dr James Shackel for providing me with the opportunity to carry on my research into projectile trauma, a journey that I started a decade ago, and to Dr Nicholas Marques-Grant for taking the time to forward my first email to James. I would also like to thank James for his guidance and support whilst he was my supervisor for the first two thirds of the research.

I would like to thank Dr Jon Painter for agreeing to become my new supervisor and for his invaluable advice and guidance upon doing so. I also extend my thanks to my secondary supervisor Dr Rachael Hazael, who like Jon has always been available and whose advice has been extremely useful. My thanks also go to Dr David Lane for his advice over the course of the research.

The experimental work carried out in this thesis could not have happened without the input and expertise of multiple people. I offer my thanks to Alan Peare, Andrew Roberts, and Dr David Wood for setting up and running the shooting apparatus. I am grateful to Dr Jon Rock for our many conversations over the course of my research which provided both encouragement and support. I am extremely grateful to Adrian Mustey for his assistance with many aspects of my practical work, from finding new bandsaw blades at a moment's notice to lending me his set of pristine casting pots for the SEM work.

I would not have been able to pursue this PhD without the incredible support of my partner Nicky, who not only provided the funds to pay for it but has also listened to countless hundreds of hours of me talking about bevelled entry wounds and how best to approach writing about them. I would like to thank my parents for their encouragement and support. My Mum, like Nicky, had to endure many hours of ramblings about sandwich bones and bevels and kindly assisted with the cost of driving the weekly two-hundred-mile round trip to campus and back. Walking in the Surrey Hills with my dogs and family has provided important time to get away from a computer screen in the fresh air, and I am grateful to my four-legged family members for their antics which have provided happy distractions during long hours of typing and reading.

TABLE OF CONTENTS

LIST OF FIGURES

LIST OF TABLES

LIST OF ABBREVIATIONS

B	Bending without fracture
C	Ring crack
CH	Channel
CEn	Cortical entry
CEx	Cortical exit
CP	Cortical pore
CR	Cortical roof
CRF	Cortical roof fragment
CS	Cortical surface
D	Densification of trabecular cells
Df	Distal fracture edge of cortical roof fragment
DL	Delamination
E_i	Incident kinetic energy
E_r	Residual kinetic energy
ΔE	Absorbed kinetic energy
EnCF	Entry cortical fracture edge
ExCF	Exit cortical fracture edge
F	Nutrient foramen
HA	Hydroxyapatite
IB	Internal bevel
ICP	Inner cortical plate
J	Joules
m	Projectile mass
Mf	Medial edge of cortical roof fragment
m/s	Metres per second
P	Putty used to seal the floor of the cortical entry
PDz	Plastically deformed zone
PPD	Peripheral plastic deformation
S	Stellate fracture
SPD	Surface-modified plastic deformation
ST	Soft tissue

Tr	Trabecular connection
VC	Vascular canal
v	Velocity
v_1	Incident velocity
v_2	Residual velocity

CHAPTER 1, INTRODUCTION

1.1. The significance of projectile trauma

Although there are multiple mechanisms that can potentially be used to inflict harm in interpersonal violence [1], data from numerous sources suggests that projectile trauma is a leading cause of human mortality in both civilian and military contexts. Small arms, which includes such weapons as handguns, rifles, and sub-machine guns [2], possess a number of traits that contribute to their lethality including ease of use, durability, portability, and use across military, law enforcement and civilian contexts [3]. Globally, estimates suggest that small arms are responsible for 40% of homicide, between 60- 90% of conflict and 6% of suicide deaths [4]. Furthermore, the actual death toll attributed to small arms in conflict situations is likely to be larger since it extends into the post- warfare environment, with populations subsequently more vulnerable to firearm induced homicide [3]. In the United States, firearm injuries are the commonest type of trauma encountered in forensic situations [5]. Estimates of global death tolls produced by small arms suggest more than 500,000 people are killed by them annually [3], with approximately 200,000 being represented by non-conflict firearm deaths [6]. This mechanism of trauma is thus of extreme importance to those involved in medicolegal investigations, including forensic anthropologists working with decomposed, fragmented, and otherwise degraded remains where modification of trauma and loss of information is to be expected [7].

1.2. The significance of entry wounds in sandwich bones

The typical adult human skeleton contains 206 bones that are commonly categorised by anatomists according to their shape as *long bones*, *short bones*, *irregular bones*, and *sandwich* (or *flat*) *bones* [8]. Outside of this shape classification, additional bones are termed *sesamoid* (formed in tendon) and *sutural ossicles*, which form along suture lines in the skull [8]. Whilst any of these bones may be involved in projectile trauma, with one estimate reporting bone involvement in nearly 93% of homicide victims [9], perforation of the sandwich bones of the neurocranium is of particular significance due to the high lethality of gunshots to the head, which can be as high as 90% in civilian settings [10]. Entry wounds in these bones are of critical importance as they are the first point of contact of the projectile with osseous tissue and may therefore retain critical information about the impact event that might be of use in trauma diagnosis and interpretation.

1.3. Internal bevelling and the challenges of differential diagnosis and interpretation

The process of skeletal trauma analysis may be conveniently divided into *differential diagnosis* and *interpretation*. Differential diagnosis includes the process of distinguishing anti- from peri-mortem trauma [11] and the latter from post-mortem fractures [12], differentiating genuine traumatic features from pathological changes, normal skeletal variation and defects induced by taphonomic agencies [13] and, finally, providing an assessment as to the *mechanism* of trauma (i.e. blunt, sharp, projectile or

thermal) [14]. For projectile trauma, *interpretation* includes such aspects as trajectory determination [14], wound sequencing [15, 16], and estimations of range, velocity, calibre and projectile design ([17]. The multitude of factors that can be involved in the processes of differential diagnosis and interpretation make the analysis of skeletal trauma extremely challenging [13]. This section will highlight that this is no less true for projectile trauma and introduce the key gaps in knowledge that led to the overall aim and research objectives of the thesis.

In cross-section sandwich bones are composed of an outer cortical plate and an internal cortical plate separated by a layer of trabecular bone [8]. Perpendicular perforation of sandwich bones that are of sufficient thickness results in an approximately circular hole in the outer cortical table and a characteristic *bevel* or cratered fracture which widens in the direction of projectile travel [18, 19]. Variations on this morphology include an absence of bevelling in thin bones [19, 20] and, although rarely reported, an additional *reverse* or *external* bevel flaring in the ectocranial direction in the outer cortical plate (see Chapter 2 for references relating to this phenomenon). The bevelled entry wound is of extreme importance in medicolegal contexts because it has, for some time, been considered diagnostic of gunshot trauma [18]. Additional importance has been placed on bevel asymmetry in trajectory determinations, with symmetrical bevels purported to result from perpendicular impact and asymmetrical bevels from tangential ones [16, 21].

Despite the importance of projectile trauma in forensic contexts and the emphasis placed on bevelling in both trauma diagnosis and interpretation, Chapter 2 will highlight that there is currently no agreement in the literature as to how the bevel is formed and a very limited amount of empirical work investigating the fracture mechanisms involved. Research with human material has also found a poor correlation between trajectory and bevel asymmetry in entry wounds [20], and it is therefore critical that the mechanisms underlying bevel shape are investigated further. Internal bevelling identical in form to that produced by bullets can also result from low-velocity (i.e., non-ballistic) impacts [22-24], a finding that poses a significant diagnostic challenge when working with fragmented and dispersed remains in the absence of a recovered projectile or exit wound. This overlap across different velocity impacts is accentuated by the fact that there is currently no established method to determine projectile velocity from macroscopic fracture patterns [17], and little understanding as to how incident velocity or absorbed kinetic energy influences entry wound morphology. The discovery of potential signatures that might refine velocity estimations during fracture interpretation would be of considerable value.

In addition to the above gaps in knowledge, further diagnostic challenges are raised by the fact that entry wounds must be differentially diagnosed from multiple other agencies that can result in perforation; they may be modified by taphonomic processes such as rodent gnawing [25] and exposure to fire [26]. These challenges necessitated a search for novel signatures that, in addition to revealing information about incident velocity, may also assist with differential diagnosis of projectile trauma. Chapter 2 demonstrates that a critical gap in knowledge in our search for such diagnostic signatures is the current emphasis on trauma analysis at the macroscopic scale, despite the fact that bone is a complex

hierarchical material [27] and as such may retain information at lower levels of structural organisation. The gaps in knowledge described above led to the formulation of the overall aim and research objectives set out below.

1.4 Overall aim and objectives of the research

The aim of this research was to facilitate the forensic interpretation of bevelled entry wounds in sandwich bones by empirically investigating the fracture processes underlying their genesis, and by carrying out a detailed examination of their morphology at different hierarchical scales.

To achieve this aim, the research objectives were to:

1. Enhance the description, analysis, and classification of conoidal wounds by developing a detailed nomenclature for their morphological components (**Chapter 3**).

2. Determine the fracture mechanisms underlying the genesis of conoidal wounds using a combination of high-speed videography and morphological analysis with micro-computerised tomography (μ-CT) (**Chapters 3 and 4**).

3.a. Generate and interpret impact dynamics data to establish how sandwich bones behave during perforation and to determine how that behaviour is influenced by the fracture mechanisms identified in objective 2 (**Chapter 5**).

3.b. Carry out a quantitative morphological analysis of conoidal wounds to detect any relationships between morphology, incident velocity and absorbed kinetic energy (**Chapter 5**).

4. Employ Scanning Electron Microscopy (SEM) to identify features associated with the genesis of conoidal wounds and to determine if projectile impact results in morphological changes at lower hierarchical scales that might be of diagnostic utility (**Chapter 6**).

The diagnostic and interpretive challenges and the relationships between these research objectives are shown in **Fig.1.1**.

1.5 Impact

Publication of the papers presented in Chapters 2 and 3 led to a collaborative paper with Dr Angi Christensen and Dr Hugh Berryman that further developed the fractography and failure analysis of bevelling in bone after impacts. The paper title and the present author's contributions are presented in Appendix 3.

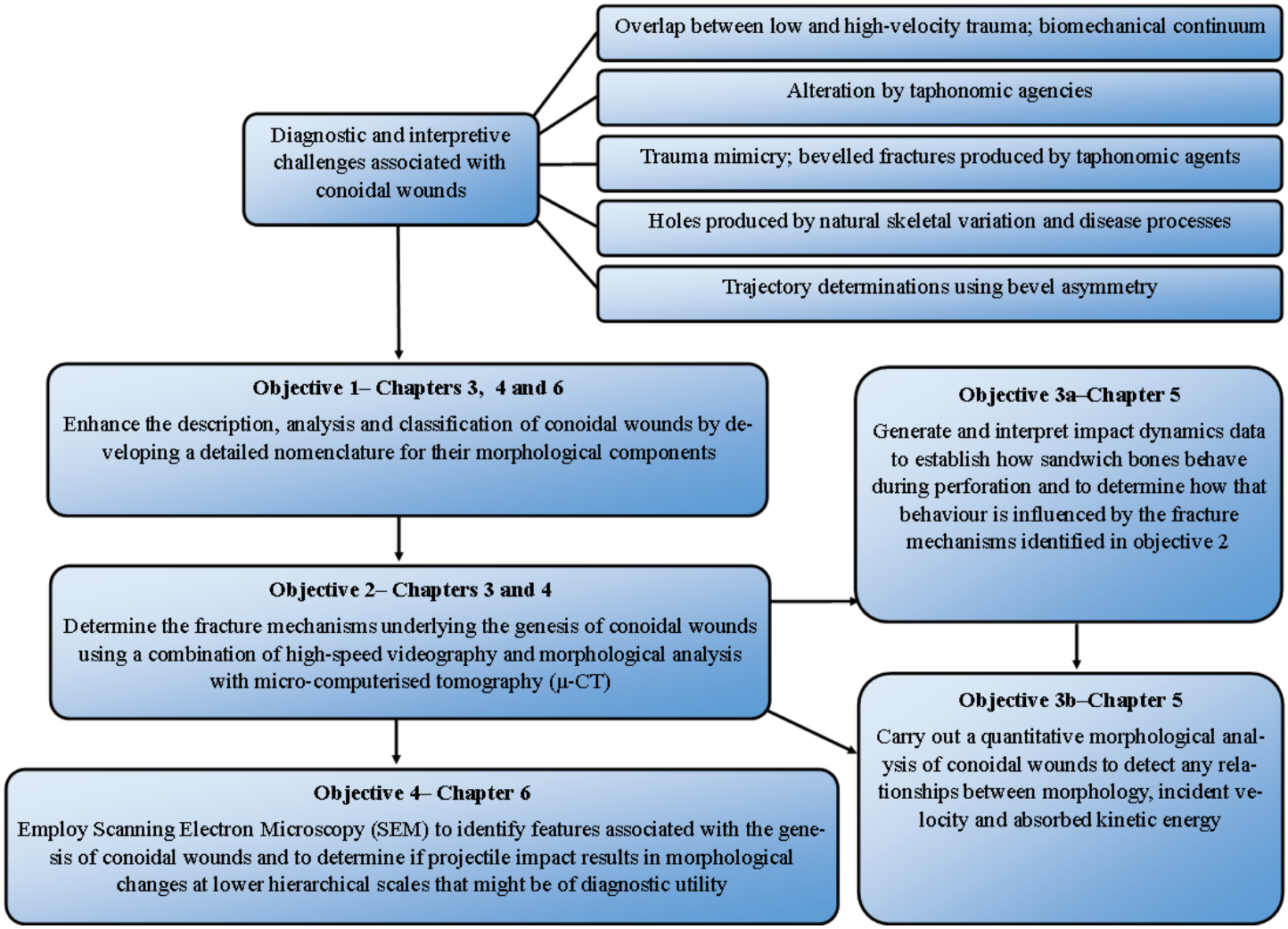

Fig.1.1 Key diagnostic and interpretive challenges and the relationships between research objectives

1.6. References

[1] Matoso IM, Freire AR, Santos LSdM, Deruge Junior E, Rossi AC, Prado FB (2014). Comparison of gunshot entrance morphologies caused by .40 caliber Smith & Wesson, .380-caliber, and 9 mm Luger bullets: a finite element analysis study. PLOS ONE 9 (10): e111192.https://doi.org/10.1371/journal.pone.0111192 [Online] Available at https://journals.plos.org/plosone/article?id=10.1371/journal.pone.0111192 (accessed 29/5/2015)

[2] Beauchamp C (2008). Micro-disarmament: controlling small arms and light weapons and the international agenda. In Pomery C (Ed) APSA 2008 1-18 [Online] Available at https://researchoutput.csu.edu.au/en/publications/micro-disarmament-controlling-small-arms-and-light-weapons-and-th (Accessed 15/5/2015)

[3] Muggah R, Berman E (2001). Humanitarianism under threat: the humanitarian impact of small arms and light weapons. Small Arms Survey, Centre for humanitarian dialogue 3 [Online] Available at https://reliefweb.int/report/world/humanitarianism-under-threat-humanitarian-impacts-small-arms-and-light-weapons (Accessed 15/5/15)

[4] Florquin N (2006). The instrument matters; assessing the cost of small arms violence. In Small Arms Survey 2006: Unfinished business [Online] Available at http://www.smallarmssurvey.org/fileadmin/docs/A-Yearbook/2006/en/Small-Arms-Survey-2006-Chapter-08-EN.pdf (accessed 9/7//2015)

[5] Berryman HE, Shirley NR, Lanfear AK (2012). Basic gunshot trauma interpretation in forensic anthropology. In Tersigni-Tarrant MA, Shirley NR (eds) Forensic Anthropology: An introduction, CRC Press, Taylor and Francis group, Florida pp 291-306

[6] Florquin N, Wille C (2004). A common tool: firearms, violence and crime. In Small Arms Survey 2004: Rights at risk pp 173-211 [Online] Available at http://www.smallarmssurvey.org/fileadmin/docs/A-Yearbook/2004/en/Small-Arms-Survey-2004-Chapter-06a-EN.pdf (accessed 9/7/2015)

[7] Quatrehomme G, İşcan MY (1999). Characteristics of gunshot wounds in the skull. J. Forensic Sci. 44 (3): 568–76.

[8] Tortora G J and Derrickson B (2006). Principles of anatomy and physiology. John Wiley and Sons, Inc., USA

[9] Fleiger A, Kölzer SC, Plenzig S, Heinbuch S, Kettner M, Ramsthaler F, Verhoff MA (2016). Bony injuries in homicide cases (1994-2014). A retrospective study. Int J Legal Med 130: 1401-1408

[10] Mota A, Klug WS, Otriz M, Pandolfi A (2003). Finite-element simulation of firearm injury to the human cranium. Comput. Mech 31: 115-121

[11] Cunha E, Pinheiro J (2009). In Blau S, Ubelaker DH (eds) Handbook of Forensic Anthropology and Archaeology, Left Coast Press, California, pp 246-262

[12] Symes SA, L'Abbé EN, Stull KE, Lacroix M, Pokines JT (2014) Taphonomy and the timing of bone fractures. In Pokines JT, Symes SA (eds) Manual of forensic taphonomy. CRC Press, Taylor and Francis group, Florida pp 341- 362

[13] Loe L (2009) Perimortem trauma. In Blau S, Ubelaker DH (eds) Handbook of Forensic Anthropology and Archaeology, Left Coast Press, California, pp 263-283.

[14] Scientific Working Group for Forensic Anthropology (SWGANTH) (2011). Trauma Analysis. 27/5/2011 [Online] Available at https://www.nist.gov/system/files/documents/2018/03/13/swganth_trauma.pdf

(Accessed 24/6/2015)

[15] Madea B, Staak M (1988) Determination of the sequence of gunshot wounds of the skull. J. Forensic Sci. Soc 28: 321-328

[16] Rhine S, Curran BK (1990) Multiple gunshot wounds to the head: An anthropological review. J. Forensic Sci. 35 (3): 1236-1245

[17] Berryman HE (2019) A systematic approach to the interpretation of gunshot trauma. Forensic Sci. Int. 301: 306-317

[18] Berryman HE, Symes SA (1998) Recognising gunshot and cranial trauma through fracture interpretation. In Reichs, K J (ed) Forensic Osteology: advances in the identification of human remains. Charles C Thomas Publishers, Springfield, pp 333-352

[19] Di Maio VJM (1999). Gunshot wounds: practical aspects of firearms, ballistics and forensic techniques. CRC Press, Boca Raton, Florida

[20] Quatrehomme G, İşcan MY (1998) Analysis of bevelling in gunshot entrance wounds. Forensic Sci. Int. 93: 45-60

[21] Spitz WU (2006) Injuries by gunfire. In Spitz WU, Spitz DJ, Clark R (eds) Spitz and Fisher's medicolegal investigation of death: guidelines for the application of pathology to crime investigation, Charles C Thomas Publishers, Springfield. [Online] Available from: Proquest Ebook Central (accessed 9.11.17)

[22] Vermeij EJ, Zoon PD, Chang SBCG et al (2012). Analysis of microtraces in invasive traumas using SEM/EDS. Forensic Sci. Int. 214 (1): 96-104

[23] Spatola BF (2015). Atypical gunshot and blunt force injuries: wounds along the biomechanical continuum. In Passalacqua NV, Rainwater CW (eds) Skeletal trauma analysis: case studies in context. John Wiley & Sons, West Sussex, pp 7-26

[24] Quatrehomme G, Piercecchi-Marti M, Buchet L, Alunni V (2016) Bone bevelling caused by blunt trauma: a case report. Int J Legal Med 130 (3): 771-775 https:// doi.org/10.1007/s00414-015-1293-0

[25] Nawrocki SP (2009) Forensic taphonomy. In Blau S, Ubelaker DH (eds) Handbook of Forensic Anthropology and Archaeology, Left Coast Press, California, pp 284-294

[26] Collini F, Amadasi A, Mazzucchi A, Porta D, Regazolla VL, Garofalo P, Di Blasio A, Cattaneo C (2015) The erratic behaviour of lesions in burnt bone. J. Forensic Sci. 60 (5): 1290-1294

[27] Weiner S, Wagner HD (1998) The material bone: structure-mechanical function relations. Annu Rev Mat Sci 28: 271-298

CHAPTER 2, PAPER 1

A review of the literature on bevelled entry wounds in sandwich bones; nomenclature, formation, impact dynamics, and morphology across different hierarchical scales

John M Rickman*, Dr Jonathan Painter**, Dr Rachael Hazael***

2.1. Abstract

The bevelled fracture that results from projectile perforation of sandwich bones is a traumatic feature utilised for critical diagnostic and trajectory determinations. Recent discoveries indicating that bevelled fractures can result from low velocity impacts have raised important questions about how high velocity trauma projectile trauma may be diagnosed. In forensic anthropological contexts bevelled fractures must also be analysed when they have endured exposure to numerous taphonomic agencies, some of which can also produce bevelled fractures resembling projectile injuries. This paper considers the existing nomenclature for bevelled fractures in sandwich bones and critically reviews the literature relating to their formation, impact dynamics, and morphology at different hierarchical scales. It is demonstrated that there is a need for a refined nomenclature and that there is currently no consensus as to how the bevel is formed. It is also shown that there is only limited impact dynamics data for sandwich bone perforation and that further quantitative analyses of their morphology are needed. Finally, it is highlighted that microscopic analyses have identified research areas with potential diagnostic utility.

Cranfield Forensic Institute, Cranfield University, Defence Academy of the United Kingdom, Shrivenham SN6 8LA

****Centre for Defence Engineering, Cranfield University, Defence Academy of the United Kingdom, Shrivenham, SN6 8LA*

*Corresponding author email address: j.m.rickman@cranfield.ac.uk

*Phone: +44 (0) 1793 785531

*ORCID: 0000-002-1188-8805

**Email address j.d.painter@cranfield.ac.uk

**Phone: +44 (0) 1793 785392

***Email address rachael.hazael@cranfield,ac,uk

***Phone +44 (0) 1793 785414

Keywords

Projectile trauma; bevelling; sandwich bones; impact dynamics; bevel morphology; microscopic analysis

2.2. Introduction

Projectile perforation of tri-layered sandwich bones typically results in a circular entry hole in the outer cortical plate and a larger bevel flaring outward in the shape of a cone on the exiting side [1] (**Fig.2.1.**). Although this fracture type has traditionally been considered diagnostic of bullet involvement [2], case experience has revealed that identical bevelled fractures can also result from low velocity impacts [2, 3, 4], thus raising the question as to how this fracture type is formed and if the mechanism is the same across impact velocities. In addition to difficulties associated with determination of the ballistic origin of a bevelled fracture, holes in the cranium must be distinguished from features such as the sternal aperture [5-7], Foramen of Huschke [8, 343], missing sutural ossicles [8, 337; 9], and surgical or pathological modifications [10]. Although a good working knowledge of human skeletal biology will assist in identifying such features, degradation and fragmentation in skeletonised cases may complicate the process [9]. Sites of potential projectile trauma must also be differentially diagnosed if the material has undergone such taphonomic modifications as canid scavenging [11, 12], rodent gnawing of fracture margins [13, 290], and weathering, which can itself result in perforations [14]. Traumatic fractures may also be altered by fire [e.g. 15-17], a process which not only destroys traumatic information [15] but can also create bevelled fractures identical in form to those caused by projectiles [18, 19].

Despite the importance of ballistic trauma to the sandwich bones of the cranium and the difficulties that can arise during differential diagnosis, this review will demonstrate that there is currently no established nomenclature for the morphological components of bevelled fractures and no consensus as to how they are formed. Furthermore, although impact dynamics data can reveal much about how a material fails during perforation [20], it will be shown that little is known about the dynamic behaviour of sandwich bones during ballistic impact or about how that behaviour might relate to fracture morphology. At present, a significant deficit in the diagnostic toolkit is a lack of accurate methods to determine projectile velocity from macroscopic analysis of fracture morphology [21]. With this deficit in mind, it is important to consider that bone is a complex hierarchical material [22, 23] and that examination at lower scales of organisation may yield useful diagnostic signatures. Accordingly, this review will consider the findings of microscopic analyses and highlight that the potential diagnostic utility of examination of bevelled fractures at lower hierarchical scales is only starting to be explored.

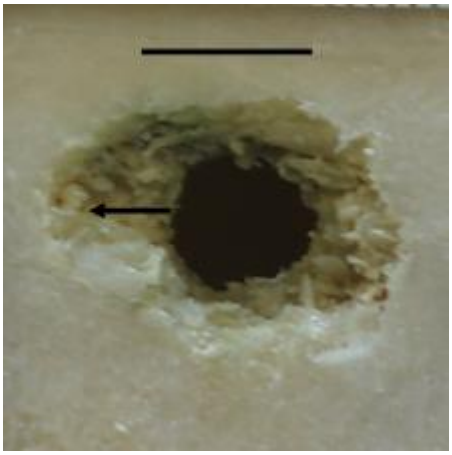

Fig.2.1 View of internal bevel in a bovine (*Bos taurus*) scapula, experimentally induced with a 7.62 x 51 mm NATO full metal jacket (FMJ) projectile; scale bar 10 mm; although the bevel is readily identified in the image, the laminae composing it remain undefined and the morphological components of the entire fracture have yet to be identified and formally named; note that this bevel is asymmetrical, a feature considered to reveal projectile trajectory (identified by the black arrow)

2.3. Nomenclature of bevelled perforating fractures

A refined nomenclature for the morphological components of trauma types, including bevelled fractures, is a necessary pre-requisite for accurate trauma categorisation, description, and differential diagnosis. However, whilst the bevelled perforating fracture type has been documented for many years [24], and is included across the secondary literature on projectile trauma [e.g. see 7, 25-29], a full and detailed nomenclature for the structural components of this unique fracture morphology in sandwich bones has yet to be developed. This deficit means that the specific laminae composing the bevel have never been formally defined, a taxonomic gap which is particularly significant when it is considered that bevelling is not only used for trauma classification but also for trajectory determinations using bevel asymmetry [30, 31]. To date, the only existing nomenclature for fractures resulting from the transit of a projectile through the cranium classifies them according to the sequence in which they form rather than their structural components, with the bevelled entry termed the *primary fracture* to distinguish it from the *secondary* (radial) and *tertiary* (concentric) fractures which may form subsequently [32]. However, while this classification is temporally informative, it does not allow more detailed morphological analyses of the bevelled fracture itself. Work using micro-computerised tomography (μCT) to analyse bevelled fractures in pig ribs has discussed bevel formation but did not develop a detailed nomenclature or define the laminae composing the bevel [33]. For the purposes of this review, the bevelled fracture resulting from perforation is henceforth termed a *conoidal wound* due to its distinct morphology.

2.4. Hypotheses proposed for the formation of conoidal wounds

To date, a lack of experimental analyses examining the genesis of conoidal wounds has resulted in a multitude of explanations for their formation (summarised in **Table 2.1**). In an early hypothesis, Shattock [24] asserted that the conoidal wound is formed due to lack of support of the inner cortical plate during projectile exit. Rhine and Curran [34] proposed that during impact the projectile compresses the internal table inwards, eventually exceeding its elastic limits and creating a larger hole on the endocranial aspect when it fails under tension. Klepinger [35] proposed essentially the same compressive/ tensile failure mechanism for the formation of the exit wound, but elicited plug formation for the creation of the entry wound. A key problem with the compressive/ tensile hypothesis is that the viscoelastic behaviour of bone dictates that it behaves as a brittle material at high loading rates [36, 37] and it is therefore unlikely to undergo significant bending during high velocity projectile impact. Byers [8] did not consider intrinsic fracture mechanisms in the bone to be responsible for bevelling, and instead suggested that it resulted from an enlargement in calibre due to projectile deformation. However, although projectile deformation may play a role in fracture processes during penetration, it cannot by itself account for bevel production as bevelling is also produced by non-deforming projectiles. A further flaw that applies to all the previously described mechanisms is that they do not readily account for the observed conoidal morphology.

Berryman [21] accounted for the conoidal bevel by analogising sandwich bone perforation to a loaded cantilevered beam. According to this mechanism the loaded beam initially fails under tension, with additional shear stresses then angulating the crack towards the fixed ends. While this model suggests how the crack might angulate with respect to the surface normal, it does not indicate how the crack would propagate across the two cortical-trabecular interfaces or how it would propagate through the trabecular cells. In an entirely different mechanism involving shock waves, Thornton *et al* [38] proposed that bevelling was produced by a process of "scabbing" due to interference between outgoing compressive waves and incoming reflected tensile waves, with bevelling caused by a decrease in scab size with depth on the exiting side. When considering this hypothesis it is important to note that these authors described the process in detail for a homogeneous plate of glass rather than bone, and it is not obvious how scabbing would occur in the trabecular lamina of a sandwich bone. In addition, scabbing seems unlikely to account for bevelling due to low velocity impacts with such objects as a bike lock [3], umbrella tip [4] and wind-borne beach umbrella vane [2], where the magnitude of shock waves would be much lower than those elicited by ballistic impact.

Hypothesis	References	Explanation
Lack of support of the inner cortical plate	[24]	Material on the inner side has nothing to support it, resulting in greater damage there. Shattock [24] analogised the process to the greater damage seen at the exit hole if a nail is driven through wood
Compressive/ tensile failure	[34, 35]	Bevel forms under tension when elastic limits of the inner cortical table are exceeded during bending
Projectile deformation	[8]	Increase in projectile calibre due to deformation occurs prior to exit, resulting in a larger exit hole and bevelling
Scabbing	[38]	Impact creates expanding compressive shock waves that reflect as tensile waves at the free boundary of the inner cortical plate. Interference between outgoing and incoming waves results in fragments of bone (scabs) coming away from the inner cortical plate. A decrease in scab size with depth results in a conoidal morphology
Crack angulation towards fixed bone	[21]	After crack initiation under tension, shear stresses angle the crack outwards towards the "fixed" areas of bone around the impact site
Temporary cavitation	[39, 40, 44]	Originally proposed for the femoral epiphysis; temporary cavitation theorised to occur in the marrow within the trabeculae, with fluid expansion fracturing the bone. In soft tissues the temporary cavity collapses leaving a permanent cavity; in bone the two cavities would be synonymous
Plug and spall	[26, 179; 27, 28, 374; 29, 357; 33, 47]	Projectile impact shears a plug of bone from the outer cortical plate which then creates the bevel by causing fragmentation (spall) at exit. Kimmerle and Baraybar [27] suggested bevelling was caused by plug shear through the trabeculae; Kieser *et al* [33] indicated a role for material accumulation ahead of the plug and compressive waves in bevel formation

TABLE 2.1 Hypotheses for the formation of conoidal wounds with a brief account of the mechanisms proposed

Experimental work with nearly fully defleshed distal human femora has demonstrated that in this trabecular-rich area, a change in perforation morphology was observed with an increase in impact velocity from a simple tunnel through the bone at low velocities to a large conoidal bevel at higher velocities [39, 40]. Noting that this process did not occur in dried femora, these authors attributed the conoidal morphology to temporary cavitation in the red marrow located within the abundant trabeculae, with the bevel so formed thus representing the permanent cavity [39]. Whilst this difference between hydrated and dry bone is compelling, the potential role of temporary cavitation in bone fracture during projectile impact is still uncertain. Subsequent work with long human bone diaphyses showed no difference between dried and hydrated specimens, leading the authors to conclude that temporary cavitation was not involved in long bone shaft perforation [41]. This latter finding is in direct contrast to later work which has reported temporary cavitation in calf (*Bos taurus*) femoral shafts embedded in 20% gelatine [42, 43], although it must be borne in mind that the shafts of *Bos* long bones have a greater diameter than that seen in human femora and differences in medullary and marrow volume were not quantified.

Although there is no experimental evidence in support of the bevel being produced by temporary cavitation in sandwich bones, this mechanism has been utilised to explain bevel formation in the cranium [44]. The assumption that this process is operative in sandwich bones is, however, difficult to reconcile with the fact that bevelling is consistently seen in this bone type despite the fact the trabecular layer varies considerably in porosity and thickness between individuals [45]. The trabecular layer is also much thinner in sandwich bones than in the femoral epiphysis and it is not clear if such a thin layer would allow temporary cavitation to occur. Temporary cavitation increases in magnitude with projectile velocity, with cavities up to 12.5 times larger than projectile calibre being generated with high velocity rifle bullets [25]. Accordingly, if temporary cavitation is operative in sandwich bones, it can be predicted that bevel size would increase significantly with an increase in velocity. A qualitative increase in the amount of damage with an increase in velocity has been reported in a Finite Element Analysis (FE) of projectile impact to the human mandible [46], although this FE model was not verified experimentally and images of damage morphology were not provided. Additional quantitative analyses of the effects of an increase in impact velocity on bevel size will provide valuable data on the question of what role, if any, temporary cavitation might play in bevel formation in sandwich bones.

The most widely cited mechanism for the production of conoidal fractures is plug and spall, which is described (although not always explicitly named) in much of the secondary literature [26-29]. According to most interpretations of this mechanism, bevel production is a two-phase process involving the projectile shearing a disc of bone from the outer cortical plate (the plugging phase) followed by bevel production due to fracture as the projectile-plug combination exits at the inner cortical plate (the spall phase) (**Fig.2.2**.) [26, 28, 29, 47]. In a slightly different interpretation of plug and spall, Kimmerle and Baraybar [27] suggested that the bevel is formed by the plug shearing through the trabeculae, with

the bevel thus forming before projectile exit at the inner cortical plate. Despite wide usage in the literature, none of the descriptions offered for plug and spall specifically identify the fracture mechanisms underlying the conoidal morphology, and strong experimental evidence in support of it is lacking. Analysis of conoidal fractures in porcine ribs with micro-computerised tomography (μCT) led to an interpretation that material accumulation ahead of a sheared plug was partly responsible for bevel formation, but this study did not observe plug formation [33]. Indeed, thorough searching of the primary literature revealed no experimental work capturing the process of plug and spall in operation.

A key mechanistic problem with plug and spall is that it is difficult to reconcile how a sheared cortical plug would not itself be fragmented by the high contact stresses generated during ballistic impact, estimated to be 100 tons/inch^2 (6.45 cm^2) for a 5.6 mm projectile travelling at 366 metres per second (m/s) [33, citing Davies 1956]. An additional and even more significant issue is that recovered plugs, all generated by lower velocity impacts, consist of all three layers of the sandwich bone [48-50]. Whilst it has been speculated that these tri-layered plugs are an alternative expression of plug and spall associated with low velocity blunt force impacts [50], it is entirely possible that they may also be formed during high velocity ballistic impacts but undergo extensive or complete comminution. Previous μCT analysis of red deer (*Cervus elephas*) femora subjected to low velocity impacts with spherical projectiles has successfully captured the formation of cone-type cracks in compact bone and, at higher velocities, the formation of butterfly fractures [51]. Formation of cone cracks in the cortex of long bones thus raises the question as to whether they are involved in conoidal wound formation in sandwich bones. High speed videography of projectile entry and exit at different impact velocities coupled with μCT examination of the resultant cross-sectional structure is required to capture the fracture processes that are operative during conoidal wound formation in sandwich bones.

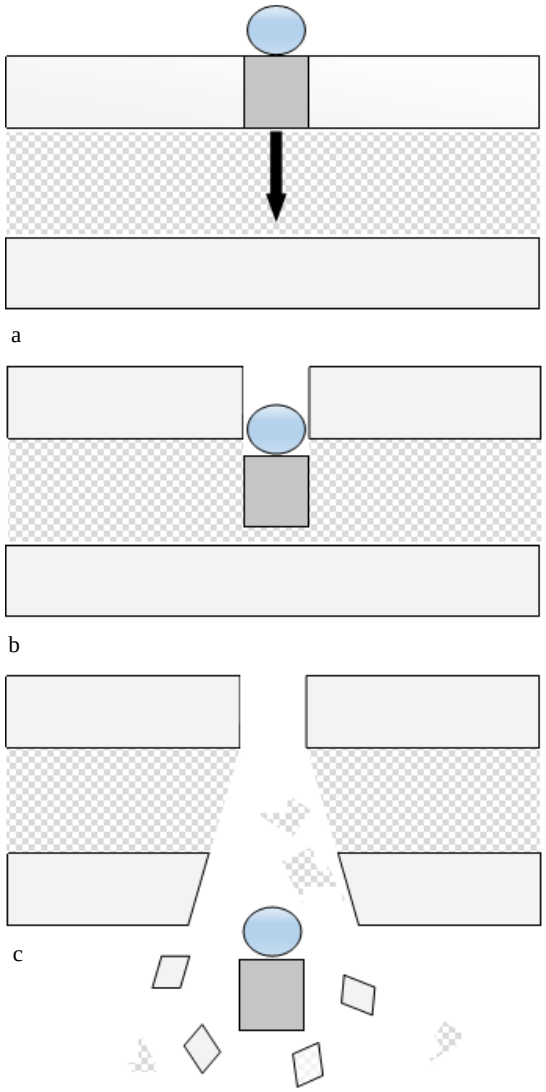

Fig.2.2

Simplified diagram of the plug and spall hypothesis, illustrated with a spherical projectile; **a**, projectile impact shears a plug in the outer cortical layer (the plugging phase); **b**, the projectile and cortical shear plug move through the trabecular layer; **c**, the projectile and shear plug fracture and exit the inner cortical pate, creating the bevel (the spall phase); note that Kimmerle and Baraybar [27] suggested the bevel is created by the plug shearing through the trabeculae, and according to this interpretation the bevel would be created during perforation rather than exit

2.5. Impact dynamics

Analysis of the dynamics of impact reveals important information about the failure mechanisms a given material undergoes during perforation [20] and will thus assist in examining how conoidal wounds form. In biological structures, where these failure mechanisms manifest as tissue destruction and wounding, an understanding of the energetics of impact is also fundamental to the development of a satisfactory quantitative understanding of tissue wounding processes during ballistic impact. In addition, recent decades have seen a growing literature on the suitability of biomimetic analogues for experimental use, and although some have found the behaviour of these synthetic systems to be similar to bone [52-56] others have highlighted their limitations [57-60]. Base-line data on the dynamics of impact to bone will provide additional avenues with which to test and enhance the biomimetic value of synthetic systems.

The literature on bone impact dynamics in general is scarce, and that for sandwich bones even more so. Currently, in-depth analyses of the energetics of penetration in human bone are limited to that of a linked experimental series utilising 6.35 mm (0.250 inch) and 10.31 mm (0.406 inch) calibre stainless steel spheres impacting de-fleshed and embalmed human femora at a series of increasing impact velocities [39-41, 61]. This series is notable for the inclusion of what might reasonably be termed energy absorption profiles, which express the amount of energy absorbed as a function of impact velocity. Initial work with 10.31 mm spheres impacting the popliteal surface of the distal femur indicated that the relationship between incident velocity and energy absorption was linear [39], while subsequent work with a larger sample size impacting the same femoral region with 6.35 mm and 10.31 mm spheres resulted in quadratic relationships for both [40]. Impact of the femoral shaft with the same projectile calibres resulted in a quadratic relationship for the 6.35 mm spheres and a linear relationship for the 10.31 mm spheres, although the latter resulted in a quadratic relationship when osteoporotic femora were utilised [41]. Huelke *et al* [39-41] considered these quadratic and linear increases in absorbed energy to indicate greater work of fracture, but kinetic energy is also utilised for additional processes including frictional heating and fragment ejection. Although there has been shown to be a relationship between absorbed energy and new fracture surface area in compact bone [62], work with ceramics has indicated that fragment ejection utilises far more kinetic energy than fragment creation [63]. Accordingly, since the relative importance of fragmentation and fragment ejection in kinetic energy absorption has yet to be clarified in bone, linear and quadratic increases in absorbed energy cannot be fully attributed to greater work of fracture.

Whilst the absolute amount of kinetic energy absorbed was shown to increase with increasing velocity according to power or linear functions, when absorbed kinetic energy was expressed as a *proportion* of available kinetic energy, Huelke *et al* [39, 40] found an inverse relationship with velocity in the femoral epiphysis. This phenomenon is likely a manifestation of the smaller projectile-bone contact time at higher velocity and indicates that, in energetic terms, bone tissue does not represent a large factor in the total amount of energy lost by the projectile during the initial phase of perforation.

In addition to energy absorption profiles, Huelke *et al* [40, 41] also provided data on the effect of both projectile calibre and mass on energy absorption and qualitative extent of fracture. In both femoral regions the larger spheres were found to expend more energy and cause more damage during perforation than the smaller spheres [40, 41]. Although data was not provided for the diaphysis, in the epiphysis the proportion of available kinetic energy absorbed was found to be inversely related to velocity for both projectile types, with the larger calibre losing proportionally less energy at the same impact velocity [40]. Later work in the series utilising projectiles of identical calibre but different mass found that mass had little to no effect on the amount of energy absorbed and damage created [61]. Comparison of the two 6.35 mm spheres with 10.31 mm spheres revealed that the latter lost more energy and caused more damage than the former at identical impact velocities, highlighting the importance of calibre in the extent of bone fracture [61].

At present, the only published literature on the dynamics of sandwich bone perforation is the FE model of Tang *et al* [46], which provided data on 6.3 mm spheres and 7.62 spitzer tipped bullets, both made of carbon steel, perforating the human mandibular angle at three velocities (400 m/s, 734 m/s, and 1109,185 m/s) and three impact angles (45^{o}, 67.5^{o} and 90^{o}). For both projectile types and at each impact velocity, total energy absorption and the proportion of energy absorbed were highest at 45^{o} and lowest at 90^{o}. In common with data for human long bones [39, 40], higher velocity impact was associated with an increase in absolute energy absorption but a decrease in the percentage of available kinetic energy absorbed. Though this preliminary study is valuable and forms an important baseline for future analyses, lack of experimental verification means it is not precisely clear how this simulated data compares to the behaviour of real bone. Previous FE analysis of ballistic perforation of the pig mandibular angle has indicated that such modelling can provide biologically accurate simulations, with no significant difference detected between experimental and simulated residual velocities, transferred energy, and entry surface areas [64]. Observation of the results of Chen *et al* [64] also highlights the effect of biological variation on dynamic behaviour compared to FE model output; for example, whilst their experimental data yielded a mean energy transfer of 141 Joules (J) ± 58.4, the simulation provided a mean value of 170.8 J ± 5.6. Controlling for biological variation is advantageous in the sense it allows the effects of extrinsic factors such as projectile design and velocity to be examined, although inclusion of variations in biological factors such as mineralisation, absolute thickness and the relative thickness of each bony lamina in future FE analyses would inform our understanding of the intrinsic factors underlying the dynamic behaviour of sandwich bones.

2.6. Morphometric analyses of conoidal wounds

To date, the vast majority of the primary forensic literature on gunshot trauma to bone has provided qualitative descriptions of fracture morphology and how it relates to trauma analysis including such tasks as wound sequencing [34, 65] and trajectory determination [32], as well as general gunshot trauma interpretation in the cranium [21], chest [66] and single skeletons [e.g. 67]. Qualitative descriptions

have also considered atypical morphologies including reverse bevelling [47, 68-73], keyhole defects [74-77] and plastically deformed fractures [36]. FE analyses have generally provided qualitative assessments of fracture morphology [41, 78], and when quantitative data has been provided it has been to compare fractures produced by different projectile types using either surface areas [79] or simple linear dimensions [80]. Qualitative descriptions of the typical morphology of conoidal wounds in bone also prevail in the secondary literature [e.g. 1, 7, 8, 25-28].

Quantitative analysis of bevel size in non-human bone has to date been utilised for comparative purposes, either to experimentally verify the output of an FE model [64] or to compare the morphology of conoidal wounds in bovine scapulae to those in a polyurethane bone substitute (PBS) [59]. Quantitative analyses of the morphology of large contemporary samples of conoidal entry wounds in human material are limited to the series provided by Quatrehomme and İşcan [31, 81, 82], although only the earliest in that series focuses entirely on the morphology of the entry wound. Work analysing the relationship between calibre and the size of the entry hole by Berryman *et al* [83] (1995), Ross [84], and Paschall and Ross [44] has provided some additional data on the extrinsic and intrinsic factors influencing the size of the entry hole.

Quatrehomme and İşcan [31] utilised a forensic sample of 39 gunshot entry wounds, all but 6 in cranial material, to examine and quantify bevelling. To test the contention that the direction of asymmetry reveals projectile trajectory [25, 30], the correlation between bevel asymmetry and trajectory was also analysed. Bevelling, quantified as the ratio of exit/ entry surface for a single perforation, was found in 36 cases but was absent in areas of thin bone. The ratios of exit/entry ranged from 1.04 to 7.70, and a significant correlation was found between the surface area of the entry and associated exit. These authors noted that, although most entry wounds were circular or oval, they exhibited asymmetrical bevelling. Circular and oval entry shapes were also found to be the commonest morphology in two subsequent analyses [81, 82] with irregular shapes being more common in exit wounds due to projectile yaw or deformation [81]. Interestingly, despite the perceived correlation between bevel asymmetry and trajectory in entry wounds, only 5 cases demonstrated a strong relationship between these variables [31]. In total, symmetrical bevelling was present in only six cases and was found to be independent of irregular entry shape. This phenomenon, which remains unexplained, has also been vividly demonstrated in two cranial shrapnel impacts by Kimmerle and Baraybar [27, 108], where irregular entry shape was associated with nearly symmetrical circumferential exposure of the trabeculae.

The factors underlying the morphology (including shape and size) of a given conoidal fracture are likely to be numerous and can be divided into intrinsic (tissue related) and extrinsic (projectile related) factors. In their analysis, Quatrehomme and İşcan [31] conjectured that bevel shape was determined by such intrinsic features as cortical thickness, proximity to sutures, and the presence of granular foveae and emissary veins. In their analysis of the relationship between entry size and bullet calibre, Berryman *et al* [83] indicated that entry hole morphology was determined by the angle of

impact, bullet construction, bullet impact with intermediate targets and the presence of pre-existing fractures, which resulted in smaller holes. Additional data on the effects of the composition and anatomy of the impacted bone on fracture morphology was later provided by Ross [84], who examined 73 autopsy- derived specimens. As part of this investigation, Ross [84] examined the influence of cranial thickness and noted that larger entry holes were associated with thicker impacted bone. Subsequent work by Paschall and Ross [44] has demonstrated that, in addition to the effects of absolute bone thickness and calibre on hole size, higher bone mineral density was also associated with larger entry holes.

Whilst the previously described literature currently represents the largest body of quantitative analyses of conoidal wounds undertaken to date, all samples were derived from forensic cases where key variables such as absorbed energy were not known. Further controlled experimentation is therefore necessary to elucidate how such factors as projectile velocity and energy absorption influence fracture morphology. The emphasis placed on bevel shape for trajectory determinations also necessitates additional analyses of the frequency of bevel symmetry and asymmetry and the factors that underlie it. The importance of the latter process is emphasised by the qualitative finding of Langley [66] that bevels in ribs tended to be more oval than those seen in cranial material. Although the frequency of bevel elongation was not provided, if this is a morphological signature of conoidal wounds in ribs it will be of considerable significance to trajectory determinations. For example, Komar and Buikstra [26] described an impacted rib with oval internal bevelling running parallel to the long axis of the shaft and concluded that a left to right bullet trajectory was responsible. However, if oval bevelling is characteristic of rib impacts *irrespective of trajectory*, such a determination might not necessarily be correct.

2.7. The potential diagnostic utility of examination of fracture and surface morphology at lower hierarchical scales of bone organisation

Recent years have seen calls for a move away from the traditional weapons-based trauma taxonomy which includes sharp, blunt, ballistic (projectile) and thermal trauma to a scheme that views skeletal trauma as being the result not of a specific weapon type but of biomechanical factors such as loading rate, the surface area of the impacting body and the rate of deceleration [85, 86]. However, although this concept is based upon sound biomechanical and physical laws, identification of the weapon type involved remains critical to medicolegal investigations [87]. Accordingly, while traumatic features induced by projectiles may not always be readily identified and diagnosed, it is critical that attempts are made to identify novel diagnostic signatures that may assist in trauma diagnosis and interpretation. To date, skeletal trauma morphology has been almost entirely considered at the macroscopic scale despite the fact that bone is an extremely complex hierarchical material ranging from the level of collagen fibrils and hydroxyapatite crystals at the nanoscale to the whole bone at the macroscale [22].

Accordingly, in common with gaps in our understanding of conoidal wounds in general, much remains to be learned about the effects of projectile impact at lower hierarchical scales of bone organisation.

Scanning Electron Microscopy (SEM) is a particularly useful technique in the analysis of fracture surfaces and bone topography due to its high depth of field and exceptional magnification powers. This technique has been successfully employed in fractographic studies of bone for many years, yielding data on such areas as fracture surface morphology in relation to strain rate [88-90], general fracture surface morphology [91, 92], and the microstructural features pre-disposing bone to fracture [93]. It has also been successfully employed to examine taphonomic marks in palaeoanthropological [e.g. 94-98] and archaeological contexts [99]. Despite its capabilities, in the forensic literature SEM has predominantly been employed to examine sharp [100-102] and blunt force trauma [103], with an extremely limited number of studies examining projectile trauma.

Early fractographic work examining compact bone fracture surfaces with SEM has yielded information that may be of use in the examination of conoidal wounds, although such analyses have yet to filter widely into the forensic literature. While not conducted on fractures induced by ballistic impact, examination of fracture surface topography revealed that cracks propagating at low loading rates followed tortuous routes along lines of least resistance through the inter-lamellar microstructure; in contrast, at higher loading rates the cracks showed no such preference and the resultant surface was therefore smoother [88-90]. This difference in crack path has subsequently been shown to be of some use in differentiating blast trauma from lower velocity events using histological examination of osteons in relation to the crack path [104]. Replication of this technique across sections of projectile entry fractures is necessary to see if this method is also of use in velocity determinations with conoidal wounds. Additional quantitative analysis of surface roughness using such techniques as Atomic Force Microscopy or Optical Profiling of the fracture edge may also prove useful.

Forensic analysis of actual ballistic entry fractures with the SEM began with the work of Speeter and Ohnsorge [105], who examined them in 49 human femurs. Fracture surface analysis indicated that projectile trajectory was revealed in displaced microscopic fragments of both cortical and trabecular bone and, at a lower scale, in deflected sections of individual lamellae. Small, scraped areas of cortical bone exhibiting linear striations resembling bullet rifling marks were also reported along the shot channel. Although this feature was considered a trajectory indicator, it is not yet clear how accurate or repeatable such determinations would be if shot direction was not produced in controlled experimental conditions. Further work is also needed to establish how frequently this feature is present and if it is influenced by projectile construction. Whilst the retention of rifling marks has diagnostic implications, in skeletal material exposed to taphonomic inputs such striations would have to be distinguished from striations produced by other mechanisms such as those resulting from rodent gnawing.

In a subsequent analysis, Gaîdash *et al* [106] employed a combination of various techniques including SEM, Atomic Force Microscopy (AFM), nanohardness, and X-ray diffraction (XRD) to analyse projectile-induced changes in the bone matrix and reported an increase in porosity and a

decrease in hardness of the cortical bone as the edge of the entry hole was approached. These authors attributed this softening to shock wave amorphization of the hydroxyapatite (HA) crystal structure and a resultant disruption of the relationship between crystals. At present, it is not clear what impact velocities might be sufficient to result in such an effect and nor is it known if it occurs around the entire perimeter of the fracture edge. Additional changes to the mineral phase in the form of smoothed cortical bone have also been detected using SEM at the projectile-bone interface in pig ribs perforated with .22 calibre projectiles, although in this case the change was attributed to melting of HA crystals due to frictional heating [33]. Whilst some of the kinetic energy is indeed converted to heat during the impact event, analyses of heated bone have indicated that melting of HA crystals only occurs above 800^{o}C [107], and it is currently not known if ballistic impact is of sufficient magnitude or duration to generate such high temperatures.

The most recent SEM analysis of the microstructure of conoidal wounds is that of Rickman and Smith [108], who examined cortical entry holes in bovine scapulae induced by Full Metal Jacket (FMJ) and Soft Point (SP) projectiles as well as a captive bolt gun. In this analysis, entry-exit trajectory was recorded in deflections of large segments of lamellar plates and in smaller lamellar fragments. Side-to side directionality was suggested by lateral displacement of fragments around the edge of the entry, although such displacements may also have been induced by projectile spin. Soft point projectiles appeared to cause greater lamellar fragmentation and disruption than FMJ projectiles, a feature attributed to the greater energy losses associated with deforming projectiles. Large microcracks were observed emanating from the entry holes induced by both FMJ and SP projectiles, though they were more common and larger with the SP projectiles. In light of the fact that bone should behave as a brittle material at high loading rates due to its viscoelastic behaviour ([36, 37], a striking morphological feature associated with the FMJ projectiles and captive bolt was plastic deformation of the cortical bone in the direction of projectile travel. The mechanisms underlying this paradoxical plastic deformation remain unknown, and further work is therefore required to examine its morphology and distribution around the entry hole. Whilst utilisation of two projectile types by Rickman and Smith [108] enabled comparison of fracture morphology between deforming and non-deforming projectile designs, it also introduced additional variables such as differing impact velocities, projectile yaw, and gyroscopic spin. Future work should therefore seek to eliminate such variables by using spherical, non-deforming projectiles at controlled and varied impact velocities.

2.8. Conclusions

Conoidal wounds represent an enigmatic fracture type upon which critical differential diagnoses and trauma interpretations are based. A comprehensive understanding of conoidal wounds must include a refined nomenclature for their structural components, an elucidation of the fracture mechanisms underlying their formation, and a detailed understanding of both their macroscopic and microscopic structure. Cross-sectional fracture analysis and high-speed videography coupled with an analysis of quantitative impact dynamics data will be critical in understanding underlying fracture processes and will also yield data that will enhance the biofidelity of synthetic systems. Future quantitative morphometric analysis coupled with impact dynamics data will allow investigations of the roles impact velocity and absorbed kinetic energy might play in wound morphology. Finally, SEM analysis of the microarchitecture of conoidal wounds is necessary to identify and examine potential diagnostic indicators at lower hierarchical scales of bone organisation.

2.9. References

[1] Berryman HE, Symes SA (1998) Recognising gunshot and cranial trauma through fracture interpretation. In Reichs, K J (ed) Forensic Osteology: advances in the identification of human remains. Charles C Thomas Publishers, Springfield, pp 333-352

[2] Quatrehomme G, Piercecchi-Marti M, Buchet L, Alunni V (2016) Bone bevelling caused by blunt trauma: a case report. Int J Legal Med 130 (3): 771-775

[3] Vermeij EJ, Zoon PD, Chang SBCG, Keereweer I, Pieterman R, Gerretsen RRR (2012). Analysis of microtraces in invasive traumas using SEM/EDS. Forensic Sci. Int. 214 (1): 96-104

[4] Spatola BF (2015). Atypical gunshot and blunt force injuries: wounds along the biomechanical continuum. In Passalacqua NV, Rainwater CW (eds) Skeletal trauma analysis: case studies in context. John Wiley & Sons, West Sussex, pp 7-26

[5] Taylor HL (1974) The sternal foramen: the possible forensic misinterpretation of an anatomic abnormality. J. Forensic Sci. 19 (4): 730-734

[6] de la Grandmaison GL, Brion F, Durigon M (2001) Frequency of bone lesions: an inadequate criterion for gunshot wound diagnosis in skeletal remains. J. Forensic Sci. 46 (3): 593–595

[7] Loe L (2009) Perimortem trauma. In: Blau S, Ubelaker DH (eds) Handbook of forensic anthropology and archaeology. Walnut Creek, CA: Left Coast Press Inc, 263–283

[8] Byers SN (2002) Introduction to forensic anthropology. Boston, MA: Allyn and Bacon

[9] Machado MPS, Simões MP, Gamba TO, Flores IL et al (2016) A Wormian bone, mimicking a gunshot entrance wound of the skull, in an anthropological specimen. J. Forensic Sci. 61 (3): 855-857

[10] Kaufman MH, Whitaker D, McTavish J (1997) Differential diagnosis of holes in the calvarium: application of modern clinical data to palaeopathology. J. Archaeol. Sci. 24: 193-218

[11] Moraitis K, Spiliopoulou C (2010) Forensic implications of carnivore scavenging on human remains recovered from outdoor locations in Greece. J Forensic Leg Med 7: 298–303.

[12] Willey P, Snyder L (1989) Canid modification of human remains: implications for the time-since-death estimations. J. Forensic Sci. 34 (4): 894-901

[13] Nawrocki SP (2009) Forensic taphonomy. In Blau S, Ubelaker DH (eds) Handbook of Forensic Anthropology and Archaeology, Left Coast Press, California, pp 284-294

[14] Quatrehomme G, İşcan MY (1997) Postmortem skeletal lesions. Forensic Sci. Int. 89:155–65.

[15] Pope EJ, Smith O'BC (2004) Identification of traumatic injury in burned cranial bone: an experimental approach. J. Forensic Sci. 49 (3): 1-10

[16] Tümer AR, Karacaoğlu E, Keten A, Ünal M (2012) Postmortem burning of the corpses following homicide. J Forensic Leg Med 19: 223-228

[17] Amadasi A, Merli D, Brandone A, Cattaneo C (2014) Chromatic variation in soot soiling: a possible marker for gunshot wounds in burnt bone. J. Forensic Sci. 59 (1): 195-198

[18] Hausmann R, Betz P (2002) Thermally induced entrance wound-like defect of the skull. Forensic Sci. Int. 128: 159-161

[19] Tsokos M (2011) Heat-induced post-mortem defect of the skull simulating an exit gunshot wound of the calvarium Forensic Sci Med Pathol 7: 227-228

[20] Abrate S (1998) Impact on composite structures. Cambridge University Press, Cambridge

[21] Berryman HA (2019) A systematic approach to the interpretation of gunshot wound trauma to the cranium. Forensic Sci. Int. 301: 306-317

[22] Weiner S, Wagner HD (1998) The material bone: structure-mechanical function relations. Annu Rev Mat Sci 28: 271-298

[23] Currey J D (2002) Bones: structure and mechanics. Princeton University Press, New Jersey

[24] Shattock SG (1923) The disruptive phenomena in gunshot injuries; their physics. *Proceedings of the Royal Society of Medicine* 16 (Pathology section):17-34

[25] Di Maio VJM (1999) Gunshot wounds: practical aspects of firearms, ballistics and forensic techniques. CRC Press, Florida

[26] Komar DA, Buikstra JE (2008) Forensic anthropology: contemporary theory and practice. Oxford University Press Inc., New York.

[27] Kimmerle EH, Baraybar JP (2008). Skeletal trauma: identification of injuries resulting from human rights abuses and armed conflict. CRC Press, Florida.

[28] Symes SA, L'Abbé EN, Chapman EN, Wolff I, Dirkmaat DC (2012) Interpreting traumatic injuries to bone in medicolegal investigations. In Dirkmaat DC (ed) A companion to forensic anthropology, Wiley- Blackwell Publishing, West Sussex

[29] Christensen AM, Passalacqua NV, Bartelink EJ (2014) Forensic anthropology: current methods and practice. Academic Press, Oxford

[30] Spitz WU (2006) Injuries by gunfire. In Spitz WU, Spitz DJ, Clark R (eds) Spitz and Fisher's medicolegal investigation of death: guidelines for the application of pathology to crime investigation, Charles C Thomas Publishers, Springfield. Available from: Proquest Ebook Central (accessed 9.11.17)

[31] Quatrehomme G, İşcan MY (1998) Analysis of bevelling in gunshot entrance wounds. Forensic Sci. Int. 93: 45-60

[32] Smith O, Berryman HE, Lahren CH (1987) Cranial fracture patterns and estimate of direction from low velocity gunshot wounds. J. Forensic Sci. 32 (5): 1416-1421

[33] Kieser JA, Tahere J, Agnew C, Kieser DC, Duncan W, Swain MV, Reeves MT (2011) Morphoscopic analysis of experimentally produced bony wounds from low velocity ballistic impact. Forensic Sci Med Pathol 7:322-332

[34] Rhine S, Curran BK (1990) Multiple gunshot wounds to the head: An anthropological review. J. Forensic Sci. 35 (3): 1236-1245

[35] Klepinger LL (2006) Fundamentals of forensic anthropology. John Wiley & Sons, New Jersey

[36] Smith OC, Berryman HE, Symes SA, Francisco JT, Hnilica V (1993) Atypical gunshot exit defects to the cranial vault. J. Forensic Sci. 38 (2): 339-343

[37] Symes SA, L'Abbé EN, Stull KE, Lacroix M, Pokines JT (2014) Taphonomy and the timing of bone fractures. In Pokines JT, Symes SA (eds) Manual of forensic taphonomy. CRC Press, Taylor and Francis group, Florida pp 341- 362

[38] Thornton J, Crim, D, Cashman P (1986). Glass fracture mechanisms: a re-thinking. J. Forensic Sci. 31 (3): 818-824

[39] Huelke Df, Buege LJ, Harger JH (1967). Bone fractures produced by high velocity impacts. Am.J. Anat 20:123-132

[40] Huelke DF, Harger JH, Buege LG, Dingman HG, Harger DR (1968). An experimental study in bio-ballistics: femoral fractures produced by projectiles. J. Biomech. 1:97-105

[41] Huelke DF, Harger JH, Buege LG, Dingman HG (1968). An experimental study in bio-ballistics: femoral fractures produced by projectiles- II, shaft impacts. J. Biomech.1:313-321

[42] Amato JJ, Billy LJ, Lawson NS, Rich NM (1974). High-velocity missile injury: an experimental study of the retentive forces of tissue. Am J Surg 127: 454-459

[43] Amato JJ, Syracuse D, Seaver PR, Rich (1989). Bone as a secondary missile: an experimental study in the fragmenting of bone by high-velocity missiles. J Trauma 29 (3): 609-612

[44] Paschall A, Ross AH (2016). Bone mineral density and wounding capacity of handguns: implications for estimation of caliber. Int J Legal Med 131: 161-166

[45] Motherway JA, Verschueren P, Van Der Perre G, Vander Sloten J, Gilchrist MD (2009). The mechanical properties of cranial bone: the effect of loading rate and cranial sampling position. J. Biomech. 42: 2129-2135

[46] Tang Z, Tu W, Zhang G, Chen Y, Lei T, Tan Y (2012). Dynamic simulation and preliminary Finite Element Analysis of gunshot wounds to the human mandible. Injury, Int. J. Care Injured 43: 660-665

[47] Peterson BL (1991) External beveling of cranial gunshot entrance wounds. J. Forensic Sci. 36 (5): 1592-1595

[48] Murphy MS, Gaither C, Goycochea E, Verano JW, Cock G (2010) Violence and weapon-related trauma at Puruchuko-Huaquerones, Peru. Am J Phys Anthropol 142:636-649

[49] Murphy MS, Spatola B, Weathermon R (2014) Allies today, enemies tomorrow: a comparative analysis of perimortem injuries along the biomechanical continuum. In Martin DL, Anderson CP (eds) Bioarchaeological and forensic perspectives on violence: how violent death is interpreted from skeletal remains, Cambridge University Press, Cambridge, pp 261-288

[50] Bird CE, Fleischman JM (2015) A rare case of an intact bone plug associated with a gunshot exit wound. J. Forensic Sci. 60 (4): 1074-1077

[51] Kieser DC, Riddell R, Kieser JA, Theis J, Swain MV (2013) Bone micro-fracture observations from direct impact of slow velocity projectiles. J Arch Mil Med 2(1): e15614 https:// doi.org 10.5812/jamm.15614 [Online] available at https://sites.kowsarpub.com/jamm/articles/20772.html (Accessed 9/3/2015)

[52] Thali MJ, Kneubuehl BP, Zollinger U, Dirnhoffer R. (2002) The “skin-skull brain model”: a new instrument for the study of gunshot effects. Forensic Sci. Int 125:178-189

[53] Thali MJ, Kneubuehl BP, Zollinger U, Dirnhoffer R. (2002). A study of the morphology of gunshot entrance wounds, in connection with their dynamic creation, utilising the “skin-skull-brain model”. Forensic Sci. Int 125:190-194

[54] Thali MJ, Kneubuehl BP, Zollinger U, Dirnhoffer R (2003). A high-speed study of the dynamic bullet-body interactions produced by grazing gunshots with full metal jacketed and lead projectiles. Forensic Sci. Int 132: 93-98

[55] Kneubuehl BP, Thali MJ (2003). The evaluation of a synthetic long bone structure as a substitute for human tissue in gunshot experiments. Forensic Sci. Int 138:44-49

[56] Taylor SC, Kranioti EF (2018). Cranial trauma in handgun executions: experimental data using polyurethane proxies. Forensic Sci. Int 282:157-167

[57] Muccino E, Porta D, Magli F, Cigada A, Sala R, Gibelli D, Cattaneo C (2013). Applicability of cranial models in urethane resin and foam as a substitute for bone: are synthetic materials reliable? J. Forensic Sci. 58 (5): 1257-63

[58] Raymond DE, Bir CA (2015). A biomechanical evaluation of skull-brain surrogates to blunt high-rate impacts to postmortem subjects. J. Forensic Sci. 60 (2): 370-373

[59] Smith MJ, James S, Pover T, Ball N, Barnetson V, Foster B, Guy C, Rickman J, Walton V (2015). Fantastic plastic? Experimental evaluation of polyurethane bone substitutes as proxies for human bone in trauma simulations. Leg Med (Tokyo) 17: 427-435

[60] Henwood BJ, Appleby-Thomas G (2020). The suitability of synbone ® as a tissue analogue in ballistic impacts. J. Mater. Sci 55: 3022-3033

[61] Harger JH, Huelke DF (1970). Femoral fractures produced by projectiles-the effects of mass and diameter on target damage. J. Biomech.1:487-493

[62] Beardsley CL, Anderson DD, Marsh J.L, Brown TD (2005). Interfragmentary surface area as an index of comminution severity in cortical bone impact. J. Orthop. Res 23:686-690

[63] Woodward RL, Gooch Jr WA, O'Donnell G, Perciballi WJ, Baxter BJ, Pattie SD (1994). A study of fragmentation in the ballistic impact of ceramics. Int. J. Impact Engng 15 (5): 605-618

[64] Chen Y, Miao Y, Xu C, Zhang G, Lei T, Tan Y (2010) Wound ballistics of the mandibular angle: a preliminary Finite Element Analysis and experimental study. J. Biomech 43: 1131-1137

[65] Madea B, Staak M (1988) Determination of the sequence of gunshot wounds of the skull. J. Forensic Sci. Soc 28: 321-328

[66] Langley NR (2007) An anthropological analysis of gunshot wounds to the chest. J. Forensic Sci. 53 (3): 532-537

[67] Ubelaker DH (1996) The remains of Dr Carl Austin Weiss; anthropological analysis. J. Forensic Sci. 41 (1): 60-79

[68] Coe JI (1982) External bevelling of entrance wounds by handguns. Am. J. Forensic Med. 3 (1): 215-219

[69] Baik S-O, Uku JM, Sikirica M (1991) A case of external beveling with an entrance gunshot wound to the skull made by a small calibre rifle bullet. Am. J. Forensic Med. 12 (4): 334-336

[70] Davis GJ (1993) An atypical shotgun entrance wound caused by a sabot slug: all is not as it seems. Am. J. Forensic Med. 14 (2): 162-164

[71] Lantz PE (1994) An atypical, indeterminate-range, cranial gunshot wound of entrance resembling an exit wound. Am. J. Forensic Med. 15 (1): 5-9

[72] Bhoopat T (1995) A case of internal beveling with an exit gunshot wound to the skull. Forensic Sci. Int. 71: 97-101

[73] Radnic B, Curovic I, Damjanjuk I, Radojevic N, Mihailovic (2018) Unusual head gunshot entrance wound- an exception of rules. Rom J Leg Med 26: 138-140

[74] Dixon DS (1982) Keyhole lesions in gunshot wounds of the skull and direction of fire. J. Forensic Sci. 27 (3): 555-566

[75] Dixon Ds (1984) Exit keyhole lesion and direction of fire in a gunshot wound of the skull. J. Forensic Sci. 29 (1): 336-339

[76] Berryman HE, Gunther WM (2000) Keyhole defect production in tubular bone. 45 (2): 483-487

[77] Delannoy Y, Colard T, Le Garff E, Humez S, Gosset D, Hedouin V (2016) The mechanism of the keyhole lesion reassessed: an experimental approach. J. Forensic Leg. Med. 37: 1-7

[78] Matoso IM, Freire AR, Santos LSdM, Deruge Junior E, Rossi AC, Prado FB (2014). Comparison of gunshot entrance morphologies caused by .40 caliber Smith & Wesson, .380-caliber, and 9 mm Luger bullets: a finite element analysis study. PLOS ONE 9 (10): e111192.https://doi.org/10.1371/journal.pone.0111192 [Online] Available at https://journals.plos.org/plosone/article?id=10.1371/journal.pone.0111192 (accessed 29/5/2015)

[79] Rodrigues LL, Costa ST, Rossi AC, Deruge Junior E, Prado FB, Freire AR (2018). Computational simulation of projectile injuries to human parietal bone using finite element analysis. Aust. J. Forensic Sci 51 (4): 446-454

[80] Costa ST, Freire AR, Matoso RI, Daruge Júnior E, Rossi AC, Prado FB. Computational approach to identify different injuries by firearms. J Forensic Sci 62 (2): 361-368

[81] Quatrehomme G, İşcan MY (1998) Gunshot wounds to the skull: comparison of entries and exits. Forensic Sci. Int. 94: 141-146

[82] Quatrehomme G, İşcan MY (1998) Characteristics of gunshot wounds in the skull. J. Forensic Sci. 44 (3): 568-576

[83] Berryman HE, Smith OC, Symes SA (1995). Diameter of cranial gunshot wounds as a function of bullet caliber. J. Forensic Sci. 40 (5): 751-754

[84] Ross AH (1996) Caliber estimation from cranial entrance defect measurements. J. Forensic Sci. 41 (4): 629-633

[85] Kroman A (2010) Rethinking bone trauma: a new biomechanical continuum based approach. 62nd Annual Meeting of the American Academy of Forensic Sciences, Chicago, Illinois

[86] Kroman A, Symes SA (2013) Investigation of skeletal trauma. In DiGangi EA, Moore MK (eds) Research Methods in Human Skeletal Biology, Academic Press, Waltham, Massachusetts pp 219-239

[87] Berryman HE, Shirley NR, Lanfear AK (2012) Low-velocity trauma. In Tersigni-Tarrant MA, Shirley NR (eds) Forensic Anthropology: An introduction, CRC Press, Taylor and Francis group, Florida pp 271-290

[88] Piekarski K (1970) Fracture of bone. J. Appl. Phys. 41:215–223

[89] Pope MH, Outwater JO (1972) The fracture characteristics of bone substance. J. Biomech. 5: 457-465

[90] Melnis W (1983) Effect of the deformation rate on the nature of compound bone tissue fracture. J Compos Mater 19: 100-106

[91] Kimura T, Ogawa K, Kamiya M (1977) Fractography of human intact long bone by bending. Zeitschrift für Rechtsmedizin 79: 301-310

[92] Braidotti P, Branca FP, Stagni L (1997) Scanning Electron Microscopy of human cortical bone failure surfaces. J. Biomech. 30 (2): 155-162

[93] Corondon G, Haworth WL (1986) A fractographic study of human long bone. J. Biomech.19 (3): 207-218

[94] Shipman P (1981) Application of Scanning Electron Microscopy to taphonomic problems. Ann. N. Y. Acad. Sci. 376 (1): 357-385

[95] Shipman P, Rose J (1983) Early hominid hunting, butchering and carcass processing behaviours: approaches to the fossil record. J. Anthropol. Archaeol 2: 57-98

[96] Shipman P, Rose J (1983) Evidence of butchery and hominid activities at Torralba and Ambrona; an evaluation using microscopic techniques. J. Archaeol. Sci. 10: 465-474

[97] Bromage TG, Boyde A (1984) Microscopic criteria for the determination pf directionality of cutmarks on bone. Am. J. Phys. Anthropol 359-366

[98] Olsen SL, Shipman P (1988) Surface modification of bone: trampling versus butchery. J. Archaeol. Sci. 15: 535-553

[99] Smith MJ, Brickley MB, Leach SL (2007) Experimental evidence for lithic projectile injuries: improving identification of an under-recognised phenomenon. J. Archaeol. Sci. 34: 540-553

[100] Bartelink EJ, Wiersema JM, Demaree RS. Quantitative analysis of sharp force trauma: an application of scanning electron microscopy in forensic anthropology. J.Forensic Sci. 46 (6): 1288-1293

[101] Tucker BK, Hutchinson DL, Gilliland MFG, Charles TM, Daniel HJ, Wolfe LD (2001). Microscopic characteristics of hacking trauma. J.Forensic Sci. 46 (2): 234-240

[102] Alunni-Perret V, Muller-Bolla M, Laugier JP, Lupi-Pégurier L, Bertrand MF, Staccini P, Bolla M, Quatrehomme G (2005). Scanning electron microscopy analysis of experimental bone hacking trauma. J.Forensic Sci. 50 (4): 796-801

[103] Zhi-Jin Z, Jia-Zhen Z (1991) Study on the microstructures of skull fracture. Forensic Sci. Int. 50:1–14

[104] Pechníková, M, Mazzarelli D, Poppa P, Gibelli D, Scossa Baggi E, Cattaneo C (2015) Microscopic pattern of bone fractures as an indicator of blast trauma: a pilot study. J.Forensic Sci. 60(5):1140-1145

[105] Speeter D, Ohnsorge J 1973 Investigations for determination of shot direction in bones with Scanning Electron Microscopy. Z Rechtsmedizin 73:137–43

[106] Gaîdash AA, Bashirov RS, Kolkutin VV, Tolmachev IA, Tyurin MV, Bozhchenko AP, Denisov AV (2010) New data on the morphogenesis of gunshot injuries to bone. СУДЕБНО-МЕДИЦИНСКАЯ ЭКСПЕРТИЗА ((Forensic Medical Examination) 4, 2010. Translated in Google translate.

[107] Shipman P, Foster G, Schoeninger M (1984) Burnt bones and teeth: an experimental study of colour, morphology, crystal structure, and shrinkage. J. Archaeol. Sci. 11: 307-325

[108] Rickman JM, Smith MJ (2014) Scanning Electron Microscope analysis of gunshot defects to bone: an underutilised source of information on ballistic trauma. J Forensic Sci 59 (6): 1473-1486

CHAPTER 3, PAPER 2

(Published in *The International Journal of Legal Medicine* 133 (2018): 501-519)

A novel hypothesis for the formation of conoidal projectile wounds in sandwich bones

John M Rickman* (MSc) and Dr James Shackel

3.1. Abstract

When perforated by a projectile sandwich bones typically exhibit wounds with a distinct conoidal morphology that is widely utilised both in wound diagnosis and trajectory determinations. However, the dynamic fracture mechanisms underlying this intriguing wound type have yet to be experimentally verified. The most frequently quoted hypothesis for their formation, plug and spall, is difficult to reconcile with the conoidal morphology exhibited by such wounds. The present article carries out a high-speed videographic and micro-computerised tomographic (µ-CT) analysis of perpendicularly produced projectile wounds induced from 139.15 to 896.84 metres per second (m/s) in pig scapulae. Fundamental data on energy absorption, wound shape and bevel symmetry are presented. Cross-sectional fracture morphology revealed by µ-CT raises the novel hypothesis that tensile stresses induced by the projectile in the outer cortex elicit cone crack formation, and that this cone crack then propagates catastrophically through the entire sandwich structure. This process results in the momentary formation of a bioceramic conoid; a conoidal volume of bone consisting of all three sandwich bone layers separated from the parent bone by the internal bevel. Fragmentation of the separated volume leaves the conoidal wound behind as its counterpart. The significance of this hypothesis in terms of differential diagnosis and interpretation of bevel shape is discussed.

Cranfield Forensic Institute

Cranfield University, Defence Academy of the United Kingdom

Shrivenham

SN6 8LA

*Corresponding author email address: j.m.rickman@cranfield.ac.uk

*Phone: 01793785531

*ORCID: 0000-002-1188-8805

**Email address j.shackel@cranfield.ac.uk

**Phone: 01793785747

Keywords

Skeletal trauma; projectile injuries; forensic anthropology; forensic pathology; fracture; sandwich bones

3.2. Introduction

The potential of a bullet to incapacitate is determined by impact location and thus the anatomical structures damaged along the bullet tract [1], in addition to the amount of energy absorbed by those impacted tissues. In this regard, gunshot wounds to the cranial vault are exceptionally lethal. Mortality data summarised by Aarabi *et al* [2] suggest that up to 71% of victims die at the scene of the shooting, whilst in the United States a 90% mortality rate has been reported in civilian settings [3]. From a forensic perspective, gunshot wounds to the sandwich bones of the skull are thus of considerable interest. In cross- section, sandwich bones are tri-layered structures consisting of two layers, or *laminae*, of cortical bone enclosing a lamina of trabecular bone [4]. Perpendicular entry wounds to such bones typically consist of a circular fracture in the outer cortical layer and a larger cone- shaped area of damage involving the trabeculae and inner cortical layer termed the *bevel* [5], resulting in what may be described as a *conoidal wound*. Such conoidal wounds characteristically flare in the direction of projectile travel, resulting in an *internal bevel* in entry wounds and an *external bevel* in exit wounds [5]. Further trajectory determinations are based on areas of bevel elongation, which are thought to correspond to the specific direction of projectile passage [6, 7]. However, despite the clear importance of such determinations, the fracture mechanisms underlying formation of conoidal wounds remain unclear. In addition, the layers forming the bevel and other cross-sectional features of their microanatomy have to date received no formal definitions.

A significant step in establishing how conoidal wounds form in sandwich bones is identification of the bony layers through which critical fractures propagate to produce the final morphology. The cortical layer of the sandwich bone first impacted by the projectile is here defined as the *outer cortical layer*, and its counterpart the *inner cortical layer*. The region where the trabecular bone meets a cortical layer is here defined as the *cortical- trabecular transition*, with one such region under the outer cortical layer and another above the inner cortical layer. In this paper a crack propagating through a sandwich bone is defined as *inter-laminar* if it passes between layers and separates them (the process of *delamination*), *intra-laminar* if it occurs within a layer and *trans-laminar* if it crosses a layer (**Fig. 3.1**). Cracks are further classified as *mode 1* if produced by tensile stress (crack opening), and *mode 2* if produced by in plane shear, i.e. by one part sliding past another with no crack opening (8). At present, the most widely accepted theory for conoidal wound formation is plug and spall [e.g. 9-11], which proposes that high tensile stresses initiated under the impacting projectile cause the shearing of a plug of bone from the outer cortical layer of the sandwich bone, which then moves ahead of the projectile through the other bone layers. According to this hypothesis, conoidal wound formation is a shear plugging process consisting of two phases:

1. *Projectile entry through the outer cortical layer with associated shear plug formation*
2. *Bevel production during the process of projectile exit*

Critically, this hypothesis proposes that bevel production occurs secondarily to plug formation; however, the specific biomechanical processes underlying bevel production by this cortical plug differ across the literature. Peterson [12] suggested that the cortical disc of bone is pushed through the trabecular layer and then blows out the bevel on the inner layer. Komar and Buikstra [9], Symes *et al* [10], and Christensen *et al* [11] suggested that spall, or fracture, produces the internal bevel without speculating on the stresses involved, while Kimmerle and Baraybar [13] suggested that bevelling is created by the plug shearing through the trabeculae. Kieser *et al* [14] used micro-computerised tomography to analyse cross-sections of pig ribs perforated by .22 handgun projectiles and reported a clear transition between a vertically walled channel through the outer cortical layer and the conoidal bevel beneath. Utilising this interpretation of the wound cross-section, these authors suggested that the sheared cortical plug, together with accumulated fractured material ahead of it, causes internal bevel production through a process of brittle fracture. These theories notwithstanding, it remains unclear as to why, specifically, a conoidal morphology is formed by the plug and spall mechanism, and nor is it clear how a cortical plug could withstand the massive stresses of the impact event without itself fragmenting during the perforation process.

An implicit assumption of the plug and spall hypothesis is that trans-laminar fracture is limited to the outer cortical layer, resulting in production of a plug consisting solely of cortical bone. However, recent descriptions of conoidal wounds associated with intact tri-layered bone plugs in both archaeological and recent material raise the intriguing hypothesis that all three layers of the sandwich bone might fracture as a unit during projectile impact due to trans-laminar fracture propagation through the entire structure. The first description of such plugs was provided by Murphy *et al* [15] who described frontal and parietal plugs associated with perforating wounds of unknown aetiology in archaeological material. Murphy *et al* [16] later described two more entry wound plugs in a parietal (produced by impact with a train) and occipital (produced by a cross-bow bolt), and Bird and Fleischman [17] later provided additional information on a frontal bone exit wound plug produced by low velocity bullet impact. Significantly, these tri-layered bone plugs are conoidal and the hole they fit into in their parent bone is bevelled accordingly; internally for an entry [15, 16], and externally for an exit [17]. The compressive side of the plug in the outer cortical layer may exhibit compressive damage, whilst the tensile side of the plug in the inner cortical layer is often characterised by radial fractures emanating from a central point, a process resulting in a distinct *stellate fracture* pattern. Although this limited number of reports testifies to tri-layered plug formation during at least some low energy impacts, it is currently unknown if their production is fundamental to conoidal wound formation or if these rare examples are atypical in nature.

A number of questions may be posed in relation to the mechanisms underlying conoidal wound formation. Firstly, what plugging mechanisms are operative during projectile perforation of sandwich bones; i.e. is trans-laminar fracture isolated to the outer cortical plate or does it involve all three layers? Secondly, is the same plugging mechanism operative at different velocities? Thirdly, if a role for tri-

layered plugs is suggested by conoidal wound morphology, by what mechanisms are they formed? Fourth, how might these mechanisms influence wound morphology? Fifth, does projectile impact initiate internal damage peripheral to the conoidal wound? In order to begin to address these questions, the present paper presents the findings of a high-speed video and micro-computerised tomographic (µ-CT) analysis of a series of experimentally induced projectile wounds inflicted at a series of increasing velocities to porcine scapulae. Gross wound morphology is described and basic data on energy absorption by sandwich bones during perforation is established. Based on this investigation, a nomenclature for the cross-sectional microanatomy of projectile wounds is developed and a novel theory for the formation of conoidal wounds is presented.

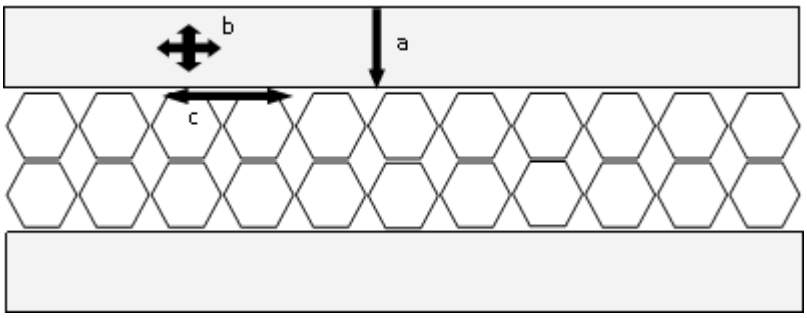

Fig.3.1 Fracture classification scheme utilised for cracks in sandwich bones; outer cortical layer (top rectangle); inner cortical layer (bottom rectangle); trabecular layer represented by hexagons; **a**, *trans-laminar fracture* crosses a lamina; **b**, *intra-laminar fracture* occurs within a lamina and may occur in any direction; **c**, *inter-laminar fracture* or *delamination* occurs between laminae.

3.3. Methods

3.3.1. Projectile type and characteristics

Projectile yaw (deviation from horizontal flight) and deformation significantly affect the amount of energy absorbed during tissue penetration. In order to eliminate the effects of these variables on fracture processes, surface hardened carbon steel spheres (Atlas Ball and Bearings Co. Ltd, United Kingdom) were utilised. Sphere weight and calibre were calculated from 24 spheres. Projectile calibre was measured using digital sliding callipers measuring to one hundredth of a millimetre. To determine projectile hardness, four spheres were ground and polished, mounted in polyester resin and then tested in a HWDM Indentec Micro indenter (Indentec Ltd, United Kingdom); ten readings were taken for the surface hardened exterior and ten for the core of each projectile. Mean hardness for each region was calculated from all four projectiles. Mean Vickers hardness values and projectile specifications are presented in **Table 3.1**. High Vicker's hardness and observation of high-speed footage indicated that projectile deformation could be eliminated from consideration in wounding processes.

Material	Mean surface hardness (Vickers) (n=10)	Mean core hardness (Vickers) (n=10)	Mean diameter (mm) (n=24)	Mean weight (g) (n =24)
Surface hardened carbon steel	717 (33.75)	455 (28.13)	5.98	0.885

TABLE 3.1 Projectile characteristics; standard deviations in parentheses.

3.3.2. Sample selection

Given both the rarity and ethical implications of utilising human bone, this material was considered unsuitable for preliminary investigation. The scapulae of large domesticated artiodactyls, including the cow (*Bos taurus*) and pig (*Sus scrofa*), are sandwich bones that exhibit internally bevelled wounds when subjected to ballistic impact. As such, their suitability as surrogates for the human cranium in experimental ballistic work has been discussed previously [18, 19]. Pig scapulae are smaller and therefore easier to machine, store and secure during testing than cow scapulae and were therefore selected for this experiment.

3.3.3. Sample preparation and velocity groups

Frozen pig scapulae were obtained from animals killed humanely as part of the food chain; samples were only taken from animals 12-14 months of age to ensure ossification of the target region. Specimens were stored frozen in sealed plastic bags at all times apart from when being prepared and impacted. The infraspinous fossa was selected as the impact region due to its larger size; only specimens with soft tissue in this region were utilised. Selected shot direction was lateral to medial, allowing the bevel to form in the flatter subscapular plate. In order to create specimens with a relatively uniform plate configuration, frozen specimens were machined on a bandsaw to approximately 120 mm height; as much of the scapular spine as possible was also removed (**Fig. 3.2**).

Target location in the scapulae was chosen to be 40-50 mm from the nearest edge; once selected, the location was marked with an ink dot. In order to examine wounds inflicted across a series of velocities and to allow comparison of impact data, fleshed specimens were allocated into one of five velocity groups. Each velocity group was allocated a target impact velocity; V_1 (150 m/s); V_2 (350 m/s); V_3 (450 m/s); V_4 (650 m/s); and V_5 (850 m/s), with groups V_2 and V_5 encompassing muzzle velocities of common handgun and rifle ammunition, respectively. To capture examples of soft and hard tissue behaviour during projectile exit, the camera was moved to face the rear of selected specimens. Using this mechanism, exit was filmed in one fleshed V_1 specimen and one fleshed V_2 specimen. To fully visualise bone fracture behaviour during exit, five additional specimens were defrosted and soft tissue dissected away from the inner cortical plate (group D*)*; these specimens were impacted between 139 m/s- 146 m/s. All specimens were defrosted slowly at room temperature in their sealed bags before the ballistic tests.

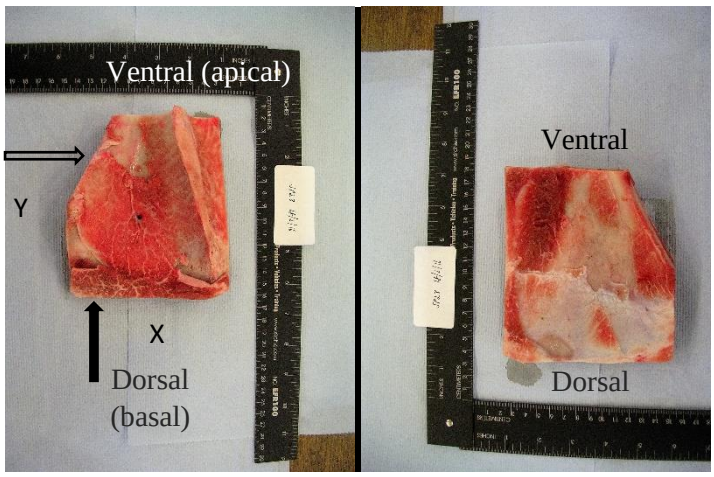

a. Lateral aspect b. Medial aspect

Fig. 3.2 Machined plate of sandwich bone with soft tissue covering orientated in shooting position. Anatomically ventral portion of scapula formed the apex of the plate during shooting. Letters x and y in **3.2a** denote the axes utilised in µ-CT analysis; z-axis (not shown) refers to the depth of the specimen. Longitudinal (y-z) section indicated by open arrow; transverse (x-z) section indicated by closed arrow; x-y section descends through the depth of the plate.

3.3.4. Shooting equipment and high-speed filming

The response of bone to loading is strongly influenced by the direction in which it is loaded; that is, bone is anisotropic [20]. In order to reduce the influence of loading direction on wounding patterns, all specimens were mounted with the broad, anatomically dorsal region acting as the base and the narrower ventral region acting as the apex. Specimens in groups V_1-V_3 were impacted using a compressed air powered 21.3 mm calibre gas gun with a 12 centimetre muzzle-target distance; projectiles were held in a plastic holder (sabot) during firing which fragmented on a metal sabot stripper after exiting the barrel. To approach the desired velocities in the last two velocity groups, an initial round of 12 impacts across groups V_4 and V_5 utilised a 30 mm helium powered gas gun; however, in all but two impacts high-velocity plastic sabot fragments were found to have damaged the impact area. Accordingly, a further thirteen specimens in groups $V_{4\text{-}5}$ were prepared and impacted using an Enfield number three proof housing with a 7.62 mm barrel; projectiles were sabot mounted and fired from a cartridge using a muzzle-target distance of 3.80 m to prevent sabots from impacting the specimens. Projectile perforation in defleshed V_6 specimens was achieved using a compressed air- powered gas gun, capable of velocities approaching 150 m/s.

Phantom high-speed cameras were utilised to obtain high-speed footage of all impacts (Vision research, New Jersey). A Phantom v12 camera operating at 55009 frames per second was utilised for

both side and exit footage in the gas gun experiment. Specimen location during exit filming in the gas gun chamber prevented lateral placement of a second camera for velocity determination; accordingly, velocity was determined using the gas gun's time gate. High-speed footage for V_4 and V_5 was obtained using a Phantom v1212 camera at 37000 frames per second. V_6 exit footage was obtained using a Phantom v1212 camera at 40,000 frames/ sec, whilst lateral footage was obtained using a Phantom v7 camera operating at 5500 frames/sec. Differences in cameras utilised were based solely on equipment availability and the maximum frame rate possible was utilised for each experimental set up. A millimetre scale was placed in view of the camera during filming to allow subsequent velocity determinations. To calculate incident (pre-impact) and residual (post-impact) projectile velocities, the camera was placed to the side of the impacted specimens. Velocities were then determined using Phantom Cine Viewer on a laptop. To allow for variation in the estimation of velocity caused by blurring of the projectile edges, the frame offering the best view of the projectile was selected and a clear location on the projectile noted. Velocity determinations were made using the same frame and location on the projectile on three separate occasions; projectile velocity was taken to be the mean of these three determinations.

3.3.5. Kinetic energy and energy absorption calculations

The kinetic energy, *E*, in joules, of a projectile of mass *m* (in kilograms) and velocity *v* (in metres per second, m/s) is given by:

Eq.1

$$\frac{mv^2}{2}$$

During penetration the kinetic energy of the projectile is transferred to the tissues and utilised to do mechanical work, manifested as tissue wounding. If the projectile retains kinetic energy and exits the impacted body, and if there is no change in mass of the projectile, the kinetic energy absorbed (ΔE) is equal to the difference between the incident kinetic energy (E_i) and residual kinetic energy (E_r) and is given by:

Eq.2

$$\frac{m\left(v_1^2\text{-}v_2^2\right)}{2}$$

Where V_1 is the incident velocity and V_2 the residual velocity. E_i, E_r and ΔE were calculated for each perforation event and the mean of these values determined for each velocity group. The amount of

energy utilised to perforate the bone in relation to available incident kinetic energy was expressed as a percentage using the formula $\Delta E / E_i$ x100. In order to determine the error associated with ΔE values for each individual perforation event, which was calculated from the mean of three velocity determinations, an error propagation formula was generated. The error propagation formula propagates the standard deviations of the projectile velocity and mass measurements in order to provide a standard deviation for the energy absorbed, $[\sigma_{\Delta E}]^2$:

Eq.3

$$[\sigma_{\Delta E}]^2 = \left[\frac{{v_1}^2 - {v_2}^2}{2}\right]^2 [\sigma_m]^2 + \left[\frac{v_1}{2}\right]^2 \left[\sigma_{v_1}\right]^2 + \left[\frac{v_2}{2}\right]^2 \left[\sigma_{v_2}\right]^2$$

Where σ is the standard deviation and *m* is the mass of the projectile in kilograms, v_1 is the impact velocity and v_2 the residual projectile velocity. The standard deviation associated with the kinetic energy absorbed for each individual impact is calculated by taking the square root of $[\sigma_{\Delta E}]^2$.

3.3.6. Impacted specimen analysis and micro-computerised tomography

In order to retain structural features critical to morphological analysis such as displaced bone fragments, soft tissue was left *in-situ* for scanning. Long scan times and large sample size necessitated re-freezing impacted bones to prevent soft tissue decomposition prior to scanning. After impact, the bones were placed into a sealable bag, wrapped in protective tissue and frozen.

For µ-CT analysis, specimens were scanned in an X-Tec XT H 225 µ-CT (Nikon, Japan). In order to maximise resolution, the wound region was selected and observed at 75 kV, 90 µA and 2.25 magnification, giving a voxel size of 89 microns. The scanned volumes were manually reconstructed using Nikon's CT Pro 3D software; to eliminate edge artefacts, the radius of reconstruction was reduced from 100% to 90-95% depending on specimen size and the location of the wound. Volumes were analysed in VGStudeo MAX version 2.2 (Volume graphics, Germany). In order to allow comparison of x-z (transverse) and x-y (longitudinal) planes in VGStudeo MAX, a simple registration was carried out; each sectional plane was orientated so that the specimen occupied the centre of the screen with the cortical entry wound uppermost. In order to use the software's measuring tools, the bone surfaces were identified and highlighted using the surface determination function, which allows the user to specify the background and the material of interest.

3.3.7. Controls

To determine if re-freezing impacted bones resulted in damage alteration, a shot control was µ-CT scanned pre-and post –freezing to allow comparison of damage areas. Surface determination and simple registration were performed on pre- and post- freeze scans. Three damaged and displaced cortical bone regions in the pre-freeze scan were selected and the software's measuring tool utilised to measure the

straight line distance in millimetres between two readily identifiable points in each of these damaged areas. To aid identification of the same landmarks in the post-freeze scan, an image of each location in the pre-freeze scan was saved as a JPEG file. The post-freeze scan was then opened and landmarks identified using the appropriate JPEG image; straight line distances between the same points were then measured and compared to pre-freeze measurements.

3.3.8. Gross wound morphology

Cortical entry wounds were classified as circular, oval, irregular or a combination of these; circular-irregular or oval-irregular wounds were classified as wounds with irregularity occurring in part of the otherwise symmetrical wound margin. Based on cross-sectional views obtained using µ-CT, the internal bevel was defined as a fracture surface encompassing the trabeculae and the fracture edge of the inner cortical layer. Following Quatrehomme and İşcan [21], internal bevels were defined as symmetrical if the bevel formed an evenly distributed wound margin and asymmetrical if any part of the perimeter was noticeably more pronounced. Preliminary µ-CT analysis indicated that the internal bevel is present beneath retained inner cortical plate fragments and these were thus considered part of the bevelled area when determining bevel symmetry. The relationship between the shape of the cortical entry wound and the shape of the internal bevel was assessed utilising µ-CT in both sectional and three-dimensional views.

3.4. Results

A total of 47 specimens were perforated; 13 specimens from groups $V_{4\text{-}5}$ were excluded from analysis due to plastic sabot damage in the 30 mm gas gun chamber or off target impacts when using the projectile housing apparatus. Of the remaining 34 sandwich bones, only the fully fleshed specimens (n= 29) were scanned in the µ-CT and utilised for subsequent computerised analysis. A total of seven inner plate cortical exits were filmed, five with soft tissue removed and two with soft-tissue *in-situ*.

3.4.1. Controls

Comparison of pre-and post-freeze wounds suggested that freezing did not alter gross wound structure. Differences in measurements between pre-freeze and post-freeze scans were 30 µm, 10 µm and 10 µm, respectively. Such sub-millimetre differences between pre-and post-freeze measurements are likely attributable to small variation in surface determinations between scans, to fine differences in placement of each end of the measurement tool, and to the possibility that the selected post-freeze measurement location did not fully correspond exactly to the pre-freeze measurement location.

3.4.2. Kinetic energy absorption and gross wound morphology

The total range of impact velocities was 139.15 m/s to 896.84 m/s; all specimens were fully perforated. Mean incident kinetic energies and mean absorbed kinetic energies are provided for each velocity group in **Table 3.2**. Mean absorbed kinetic energy in group V_5 was 10.73 times greater than in group V_1. An increase in incident kinetic energy resulted in an increase in the amount of energy absorbed. The percentage of available incident kinetic energy absorbed during perforation was inversely related to velocity; whilst just under half of incident kinetic energy was absorbed during perforation in V_1, less than a quarter was absorbed in V_5.

Observation of soft tissue post- impact revealed a dusting of sabot fragments in the soft tissue around the perforation site. While some wound irregularity due to sabot impact cannot be fully ruled out, their presence around both circular and irregular wounds suggested any such effects were absent or minimal. **Table 3.3** provides sample data on gross wound morphology across the five velocity groups. Only group V_1 exhibited the same entry wound shape in all perforated specimens, with all being circular. Increased incident velocity resulted in greater variation in cortical entry wound shape between specimens and an increase in occurrence of irregular wounds. Despite this general trend, there was overlap in entry wound morphology across groups V_2-V_5. In total, the majority of wounds (48.26%) were circular, followed by irregular (27.59%), circular-irregular (13.79%), oval-irregular (6.90%) and oval (3.45%). The majority of wounds exhibited asymmetrical bevelling (82.76%), while symmetrical bevelling was present in only 17.24% of wounds. The high frequency of bevel asymmetry meant that, of the fourteen circular entry wounds, only two (in group V_1) exhibited a symmetrical bevel. Excluding four specimens across V_4 and V_5 where extensive cortical plate damage prevented accurate analysis, irregular cortical entry shape was lost by the internal bevel in 8/10 of the remaining irregular or partially irregular wounds.

There was variation in the extent of damage within groups at higher velocity; for example, whilst one specimen in V_4 and three specimens in V_5 exhibited considerable internal and external cortical plate damage at the impact location, other specimens in these groups showed far less damage despite similar energy absorption values. For example, in V_5 one specimen was perforated at 851.92 m/s, absorbed 60.39 J of energy and exhibited extensive damage to both external and internal plates; another, impacted at 871.02 m/s and absorbing 56.32 J, presented with a neat circular entry with a slightly depressed top margin.

Velocity group	E_i (J)	E_r (J)	ΔE (J)	%	Range ΔE (J)
D (n=5)*	8.93	3.72	5.21	58.37	3.32-6.40
	(0.27)	(1.06)	(1.07)	(12.11)	
V_1 (n=6)**	11.58	5.80	5.78	49.98	5.18-7.13
	(0.95)	(0.88)	(0.72)	(5.32)	
V_2 (n=4)**	55.45	40.27	15.18	27.68	13.46-16.63
	(4.77)	(6.06)	(1.31)	(4.68)	
V_3 (n=3)	93.20	70.33	22.87	24.48	18.72-29.24
	(1.17)	(3.43)	(4.58)	(4.57)	
V_4 (n=5)	191.06	148.37	42.69	22.04	32.18-63.65
	(31.93)	(21.12)	(13.78)	(4.02)	
V_5 (n=7)	318.24	256.19	62.05	19.43	42.38-86.72
	(37.38)	(29.80)	(13.14)	(2.86)	

Table 3.2 Mean incident kinetic energy (E_i), mean residual kinetic energy (E_r), mean absorbed kinetic energy (ΔE) and mean percentage kinetic energy absorbed; all energy data in joules with standard deviations in parentheses. *group D specimens had soft tissue dissected from the inner cortical plate prior to perforation, resulting in an unquantified reduction in energy absorption. **Two specimens from n=8 in V_1 and two of n=6 specimens in V_2 were utilised for perforation filming in a confined gas gun chamber that would not fit two high-speed cameras; velocities could thus not be determined from lateral high-speed footage.

Velocity group	Circular	Oval	Irregular	Circular-irregular	Oval-irregular	Bevel symmetry	
						S	A
V_1	8					2	6
V_2	1		2	2	1	2	4
V_3			2	1		0	3
V_4	3	1	1			0	5
V_5	2		3	1	1	1	6
Total	14	1	8	4	2	5	24
Percentage	48.26	3.45	27.59	13.79	6.90	17.24	82.76

Table 3.3 Entry wound shape and bevel symmetry for n=29 sandwich bone perforation events; S, symmetrical; A, asymmetrical. Morphology determined in fleshed specimens using µ-CT in order to preserve fragile fractured elements on the inner cortical plate.

3.4.3. High-speed footage of inner plate perforation and µ-CT imaging of exit damage

Observation of the inner cortical plate during projectile exit at x4 magnification failed to detect the ejection of a disc of bone corresponding to a sheared plug from the outer cortical layer, although fragmentation of such a structure once formed cannot be ruled out. High-speed footage revealed that tensile stellate fracture of the inner cortical plate was a significant component of the exit process. This fracture type, consisting of numerous radial cracks emanating from a central region of the exit, was clearly observed in three out of the five defleshed specimens and in both fleshed specimens; projectile exit was out of frame in two defleshed perforation events but an apparent stellate fracture was visible in a detached circular fragment in one of these (see below). **Fig.3.3** shows a typical example of projectile exit in a de-fleshed inner plate at 142.51 m/s, with **Fig.3.3a** showing the plate just before exit is initiated (designated time 0). The first indication of the perforation event was a small circular elevation of the cortex in the region that will form the location of the bevelled exit (**Fig.3.3b**); although small, this elevation was detectable when compared to the non-perforated inner plate (**Fig.3.3a**). Within 25 µs the elevation had increased in height and exhibited three radial fractures emanating from its apex (**Fig.3.3c**), forming a distinct stellate fracture that demarcated at least three triangular bone fragments (highlighted in **Fig.3.3d**). As projectile exit proceeded, the cortical fragments elevated (**Fig.3.3e**) and then everted, resulting in their internal faces being uppermost (**Fig.3.3f**). Cortical fragments were then either detached from the inner plate to form larger components of the ejecta plume or remained *in- situ*. Measured from time zero to when the projectile was fully visible, the exit process took a total of 0.225 s at 142.51 m/s.

The crack forming the perimeter of the region of stellate fracture, here designated the *exit cortical fracture edge*, formed the cortical margin of the internal bevel. The radial tensile cracks composing the stellate fracture always arrested at this edge, a phenomenon also clearly visible in µ-CT images of perforated inner cortical plates (see **Fig.3.4.**). This crack arrest process indicates that the internal bevel must form very early during perforation and before radial crack production, and dictates that bevel shape and symmetry is largely determined before the projectile has exited the bone. In one 142.52 m/s perforation, an approximately circular structure consisting of a fractured inner plate of cortical bone was captured moving ahead of the projectile (**Fig.3.4a**). This removed circular section corresponded in part-counterpart fashion to the bevelled exit beneath it, and it thus represented the cortical floor of the conoidal wound volume (**Fig. 3.4.a**, thick arrow). The central portion of this circular plate presented a faint rhomboidal pattern with a centrally located apex, indicating stellate fracture had initiated but not completed there (**Fig.3.4a** thin arrow). In this specimen, fracture of the inner cortical plate during bevel formation allowed displacement of a complete disc of cortical bone. Due to the angle of observation, it was not clear if this circular structure was composed of all three sandwich bone layers. Observation of exit in fleshed specimens at both low (168 m/s) and moderate (333 m/s) velocity revealed the same sequence as observed in de-fleshed specimens. A small elevation appeared, which then grew in height; the walls of this elevation, although covered in soft tissue, were clearly triangular

in shape and formed by stellate fracture (**Fig.3.4b**). The fragments then proceeded through the processes of elevation and eversion before being ejected.

A series of µ-CT images of inner cortical plate damage morphology is provided in **Fig.3.4 c-f**. Triangular fragments on the inner plate of specimens in V_1 and V_2 were often left in an elevated position forming *fragment cones* (**Fig.3.4, c-d**), and when present the region of convergence of the elevated fragments represented the point of projectile exit (**Fig.3.4, d-e).** Subsequent to higher velocity impacts in groups V_2-V_5, inner plate fragments remained confined within the margin of the exit cortical fracture edge but often presented with semi-lunar or rectangular form (**Fig.3.4f**, arrow), with a fractured distal border indicating loss of material in the ejecta plume ((**Fig.3.4f**, white triangle).

3.4.4. µCT fracture analysis of projectile wounds

µ-CT analysis revealed a number of internal morphological features of perforating wounds to sandwich bones and the following nomenclature was developed for analysis. An annotated cross- section typical of perforations across the series is shown in the y-z (longitudinal) plane in **Fig.3.5**. In cross- section, the conoidal morphology of such perforating wounds is readily apparent. The *cortical entry wound* (*1*) is delineated by an *entry cortical fracture edge (2)*. The fractured edges of the trabeculae are discernible and form a *trabecular fracture margin (3)*. The *peripheral trabeculae (4)* may be classified as trabeculae up to 3 mm peripheral to the trabecular fracture margin. The *cortical exit wound (5)* is delineated by an *exit cortical fracture edge (6).* In current terminology the *trabecular fracture margin* and *exit cortical fracture edge* would together constitute the *internal bevel (7)*; however, in-line fracture between the entry cortical fracture edge and the trabecular fracture margin immediately beneath it makes the definition of what layers constitute the internal bevel somewhat arbitrary. The *cortical entry wound* and *internal bevel* together constitute the *wound volume (8)*. Although *trabecular intrusion* into the wound volume was observed in some sections (see **Fig.3.6b**), a distinct feature of the wound volume in the trabecular region is an abrupt border formed by the free edges of fractured trabecular cells.

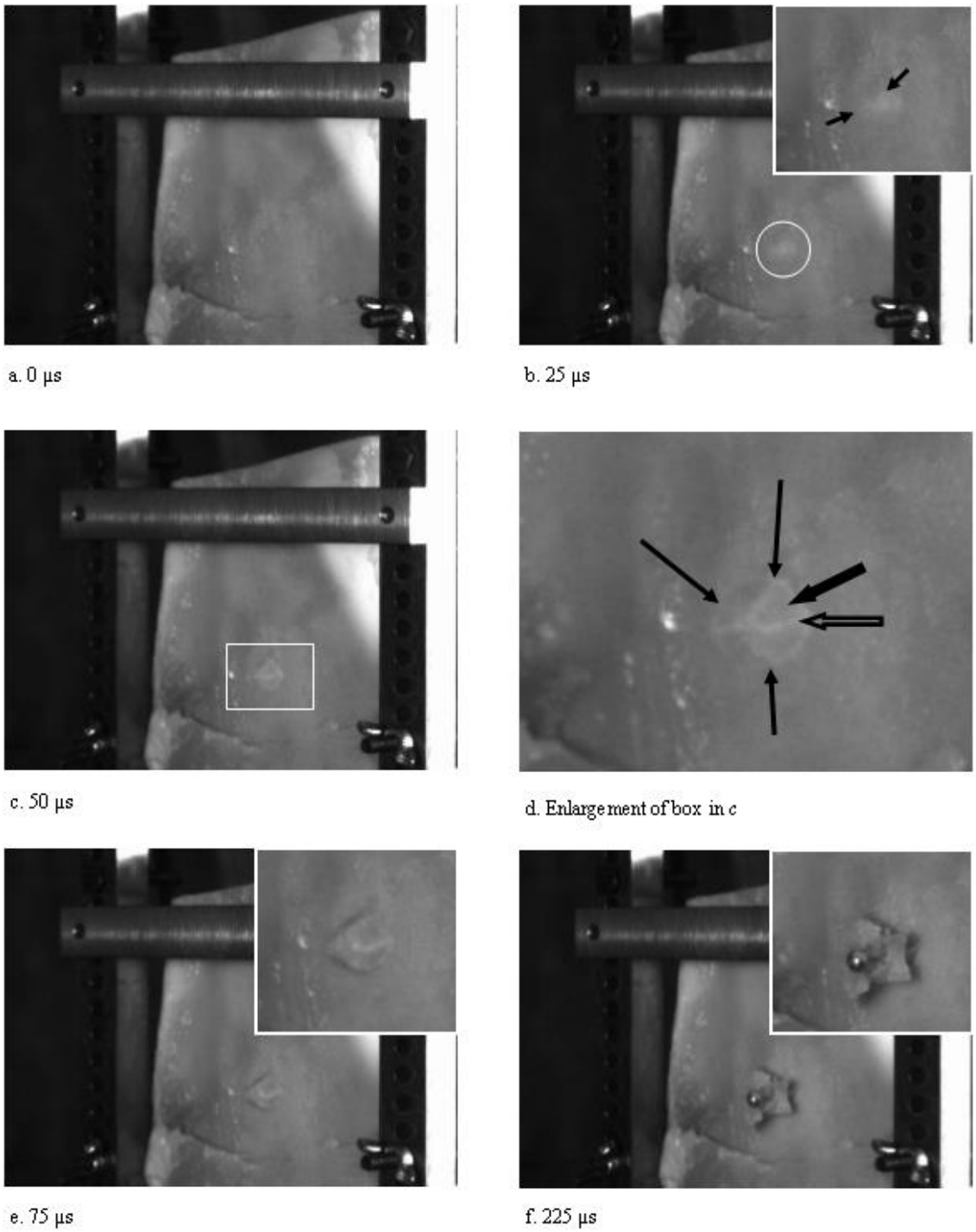

Fig.3.3 Projectile exit, soft tissue removed, incident velocity 142.51 m/s (σ 0.61); **a**. pre-impact. **b**. initial cortical elevation visible as whiter region; enlargement inset shows faint indications of stellate fracture (arrows); **c**. fracture cone (highlighted); **d**. enlargement of fracture cone. Note example of radial fracture (large open arrow) and inner cortical plate fragment (large closed arrow). Small white arrows denote margin of external bevel, the *exit cortical fracture edge*; note that radial fractures arrest at this feature **e**. plate elevation; **f**, plate eversion.

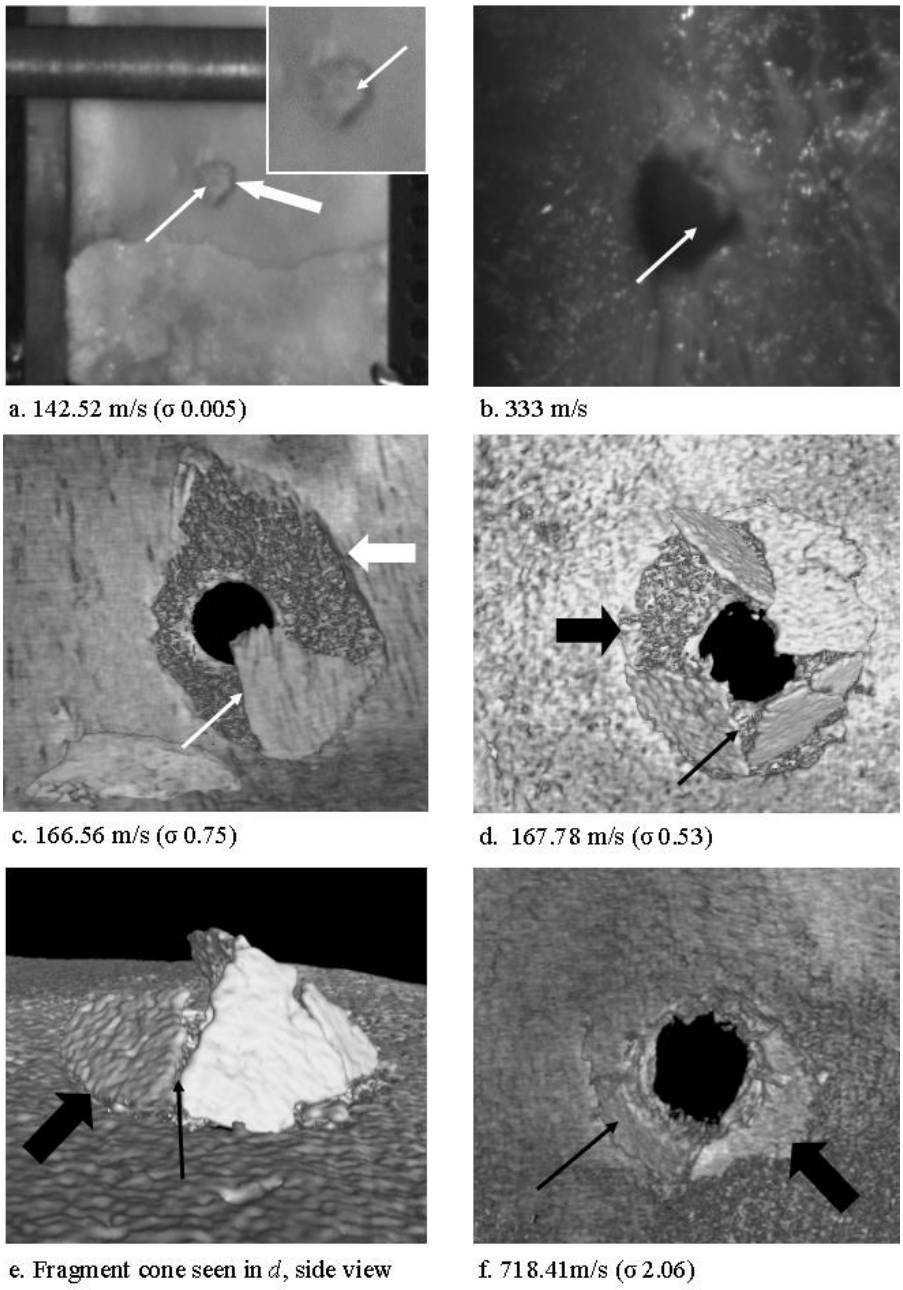

Fig.3.4 High-speed footage of projectile exit and selected µ-CT views of inner cortical plate damage; in all images, thick arrows denote the exit cortical fracture edge of the internal bevel; **a**, circular fragment of inner cortical plate dislodged from exit cortical fracture edge (thick arrow) bearing stellate fracture (thin arrow) and moving ahead of projectile, enlarged image inset; **b**, filmed projectile exit at 333 m/s, just prior to emergence of projectile; triangular plate (arrow) indicates stellate fracture has occurred (velocity determined with time gate); **c-e**, 3D images of inner cortical plate damage morphology revealed by µ-CT of two V_1 specimens; radial cracks of stellate fracture (thin arrows) arrest at the exit cortical fracture edge (thick arrows); **e,** 3D side view of the fragment cone seen in **d**, with radial fracture indicated by small arrow; **f**, rectangular, elevated cortical fragment (thin arrow) resulting from high-velocity impact; note that in all images elevated fragments are circumscribed by the exit cortical fracture edge.

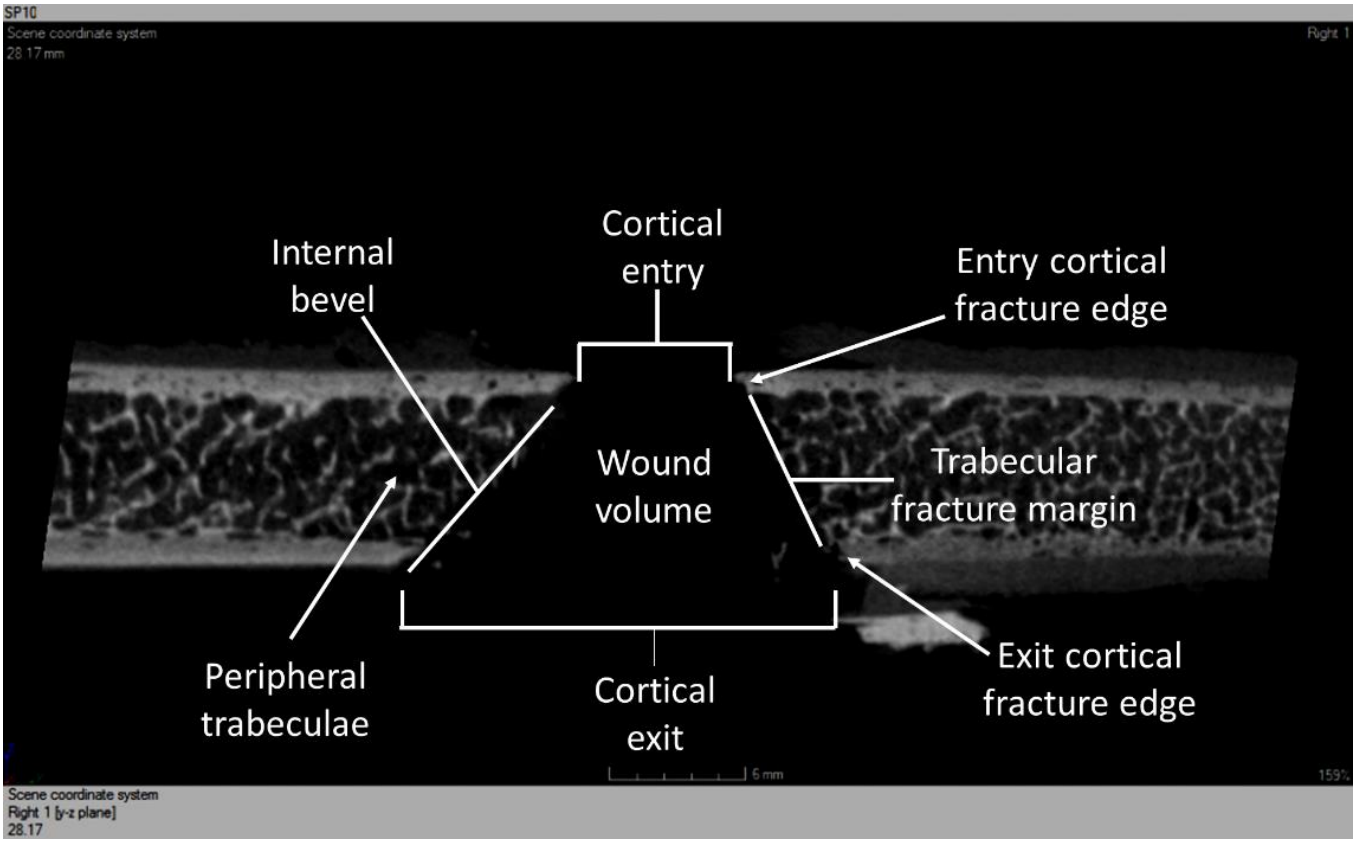

Fig.3.5 µ-CT image, y-z section showing cross-sectional anatomy of a perforating gunshot wound through a sandwich bone, incident velocity 335.55 m/s (σ 1.05); see text for explanation. Projectile passed from above downwards.

In section, a characteristic feature of the entry cortical fracture edges is their angulation with respect to the cortical surface, a structure conforming to the typical cone crack morphology observed in impacted non-biogenic brittle materials such as ceramics (**Fig.3.6, a-c**). This cone crack type morphology was observed in twenty five specimens across the five velocity groups; only four specimens with extensive damage to both cortical layers did not exhibit bilateral angulation at some point in the cross-section. Mean cortical angles of the entry cortical fracture edge were obtained using the angle measuring tool in VGStudeo MAX; the y-z plane (longitudinal) was utilised to avoid any effects induced by curvature of the scapular fossae in the transverse direction. Results for the apical and basal sides of the wounds are presented in **Table 3.4**. Mean cortical angles differed on each side of the wound, with mean basal angles showing less variation than mean apical angles. Individual cortical angles showed considerable overlap across the velocity groups with no apparent association with velocity.

Velocity group	Mean group cortical fracture edge angle, apical half	Mean group cortical fracture edge angle, basal half	Range, apical	Range, basal
1 (n=8)	55.25 (12.19)	49.15 (7.43)	33.02-74.80	38.33-59.42
2 (n=5)*	35.95 (3.30)	43.76 (6.48)	31.15-40.65	31.01-48.34
3 (n=3)	54.97 (9.28)	48.99 (13.27)	41.85-61.89	39.61-58.37
4 (n=3)**	48.13 (5.41)	42.97 (14.81)	41.35-54.60	30.65-63.79
5 (n=5)**	47.06 (6.33)	45.51 (6.66)	36.55-53.40	39.08-54.61

Table 3.4 Mean entry cortical fracture edge angles for wounds exhibiting bilateral angulation of the cortices. All angles obtained from transverse (y-z) plane to eliminate any effects of bone curvature on cortical angles. Standard deviations in parentheses. Fracture and displacement of cortices meant accurate measurement was not possible in one* and two** specimens in groups 2, 4 and 5.

Analysis of fracture propagation at the upper cortical-trabecular interface revealed that, rather than adopting an inter-laminar course, the crack initiated in the outer cortex entered the trabeculae and extended through to the exit cortical fracture edge on the same side, producing a continuous trans-laminar fracture margin through the wound channel and resulting in an internal conoidal symmetry (**Fig.3.6, a-c**; **Fig. 3.6e**). This conoidal symmetry and common fracture edge through the three layers was found in all velocity groups and was thus independent of the absorbed kinetic energy. Lack of inter-laminar fracture at the cortical-trabecular interfaces meant that no specimens showed any evidence of delamination of the sandwich structure around the circumference of the wound channel. Pronounced intra-laminar fracture between cortical layers, produced by lateral deviation of the crack tip *within* the trabecular region, was observed in two thin specimens in groups V_1 and V_5 and one thicker specimen in V_1. The latter specimen, perforated at 166.56 m/s, deviated markedly from the typical wounding pattern (**Fig.3.6d**). In longitudinal (y-z) section, this wound presented with a cylindrical wound channel to approximate mid-trabecular depth; at this point, the trabecular fracture margins deviated laterally in conoidal fashion to create a shallow internal bevel. Cylindrical morphology in the proximal part of the wound is indicative of shear in this region, whilst the conoidal portion is suggestive of a tensile cone cracking failure mode.

Although some deviations in trans-laminar crack path through the sandwich structures were visible, a characteristic feature of the wound cross-sections was a remarkably straight fracture edge (**Fig.3.6, a-c**). Deviations in the crack path from linearity may be attributed to inhomogeneities in bone microstructure and in particular to the orientation of trabecular struts in relation to the advancing crack tip. Comparison of peripheral trabeculae adjacent to the trabecular fracture margin with trabeculae located further from the wound volume revealed no evidence of compressive trabecular buckling or cell collapse with permanent deformation (**Fig.3.6e**, thick arrow). In specimens with high resolution in the trabecular region, the free edges of fractured cells along the trabecular fracture margin did not appear compressed; rather, the crack appeared to have crossed one cell width at a time through the cellular

solid. When the section is parallel to the cell-axis this process leaves clearly discernible bisected cells along the trabecular fracture margin showing no signs of deformation (**Fig.3.6e**, thin arrows). In-line fracture between angulated cortical fracture edges and trabeculae, coupled with bisection of trabeculae by a single crack, is consistent with propagation of a trans-laminar fracture through the three layers of the sandwich bone from its origin at the outer cortical surface.

Peripheral trabeculae around the wound channel were apparently unaffected by the perforation event in all five velocity groups and regardless of absorbed energy (**Fig.3.6f**). Trabecular attachments to the inner and outer cortical plates also remained undamaged up to the trabecular fracture margin (**Fig. 3.6e**, circled), suggesting that significant deformation of the cortical layers outside the impact location did not occur. Such structural integrity in the regions immediately around the wound channels indicates that projectile perforation from 139 m/s to 897 m/s in sandwich bones is characterised by an extremely localised material response. One specimen in V_4 and three in V_5 lacked the conoidal internal structure and demonstrated a "blown out" morphology when viewed from the front, with significant fracture and elevation of the outer cortical plates. Although the exact cause of this morphology was unclear, a hydraulic bursting effect in the fluid contained within the trabecular bone is plausible. Eight wounds allowed analysis of how irregularity of the cortical entry wound related to the shape of the internal bevel. Irregular cortical entry wounds corresponded to a matching irregularity of the internal bevel in only two specimens, from groups V_2 and V_3, respectively; in the other 6 specimens, irregular entry wounds did not result in irregular internal bevels. Analysis through the depth of the bone revealed that the fine details of cortical irregularity were lost in the trabecular fracture margin through the depth of the wound channel. This shape- deletion process is illustrated in **Fig.6g-h** for a 335.55 m/s perforation event. In this specimen, the external cortical plate displays an oval- irregular entry wound (**Fig.6g**); however, the finer irregular details are lost by the trabecular fracture margin at approximately mid-depth in the trabecular lamina of the sandwich structure (**Fig.3.6h**).

3.4.5. Relationship between inner cortical plate fragments and internal fracture morphology

Observed relationships between the bevel and inner cortical plate fragments were consistent with trans-laminar fracture forming a distinct tri-layered conoidal structure during impact. Cross-sectional views indicated that the internal bevel was fully formed underneath retained fragment cones (**Fig.3.7a**, arrows); this hidden bevel was found in all five V_1 specimens where fragment cones obscured all or part of the exit. Sectional analysis verified that the counterpart to these inner cortical plate fragments was the exit cortical fracture edge of the internal bevel, with the two separated by the trans-laminar fracture when it reached the inner cortical plate (**Fig.3.7a**, large arrow). Morphologically, inner cortical plate fragments with counterpart relationship to the internal bevel thus formed the floor of the conoidal wound volume. A structure corresponding to this feature was observed in high-speed video (**Fig.3.3a**), fully displaced from the wound and moving ahead of the projectile before its subsequent fragmentation. In

some sections, an accessory fracture (**Fig.3.7b,** thin arrow) was located peripheral to the trans-laminar fracture producing the conoidal wound (**Fig.3.7b**, thick arrow). In such cases, the presence of an angulated exit cortical fracture edge (**Fig.3.7b**, thick arrow) indicated that the accessory fracture must have formed secondarily to the trans-laminar fracture.

Additional evidence supporting formation of a distinct tri-layered conoidal structure was provided when the inner cortical plate fragments were in close proximity to the bevelled edge from which they were derived. **Fig.3.7c** and **d** show a photograph and three-dimensional view of such a fragment on the inner cortical plate of a V_2 specimen impacted at 333 m/s; the line across the fragment in **Fig.3.7d** corresponds to the y-z view visible in **Fig.3.7e**. In y-z section (**Fig.3.7e**), the bevel appeared as a marked conoidal fracture in the trabecular layer with the fragment forming a partial floor to this edge of the wound. Part-counterpart relationships between exit cortical fracture edge and fragment meant the latter would slot in and out of the internal bevel in the parent bone. Observation of the whole wound from the right demonstrated the internal bevel running *underneath* the fragment (**Fig.3.7f**), which is thus accurately interpreted as a fragment of the cortical floor of the conoidal wound. Part-counterpart association between inner cortical plate fragments and wound were often so clear that the intact floor could be visualised even when the fragments had been significantly displaced (**Fig. 3.7g**). The conoidal fracture residing above lower cortical floor fragments and the part-counterpart relationships between them and the internal bevel was often striking (**Fig. 3.7h**). When inner cortical plate fragments showed minimal downwards displacement, the bevelled edge from which they derived was shielded from contact with a cortical shear plug or accumulated material (**Fig.3.7i**, arrows).

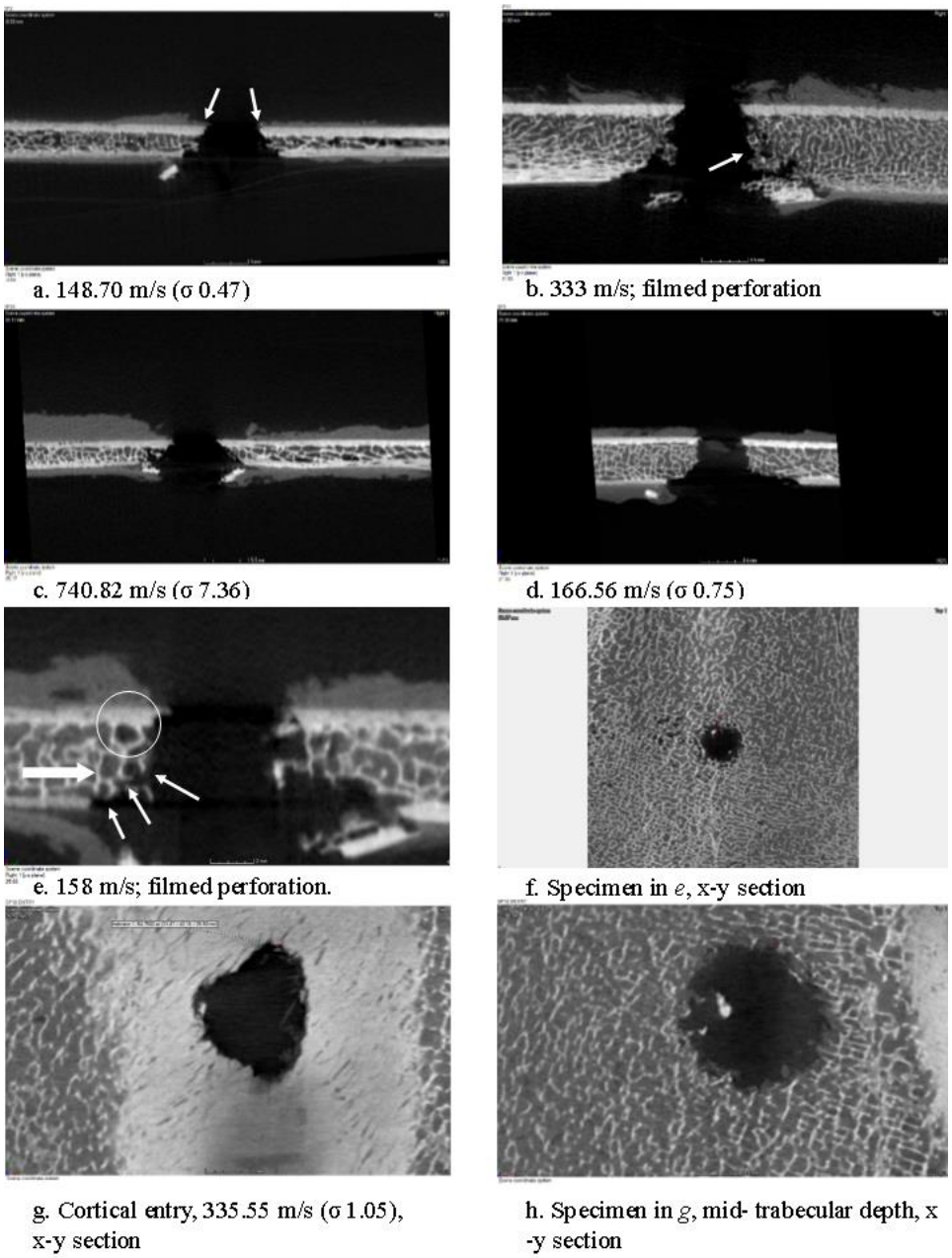

Fig.3.6 µ-CT cross- sections of projectile wounds. **a-c**; y-z views of conoidal morphology with bilateral angulation of entry cortical fracture edges (highlighted with arrows in a); trabecular intrusion shown in **b** (arrow); **d**, y-z section showing atypical wound cross-section; **e**, fracture morphology consistent with crack propagation one cell width at a time through trabeculae (thin arrows), y-z section. Note bilateral angulation of entry cortical fracture edges, lack of collapse of trabecular cells (thick arrow) and intact trabecular attachments to cortex (circle); **f**, x-y section of specimen seen in **e** showing localisation of wound in trabecular field; **g** x-y section of cortical entry wound in cortex (C); **h** x-y view of specimen shown in **g** showing loss of cortical irregularity by mid-trabecular depth; **f-h** show view looking into wound from above. Incident velocities provided with standard deviations in parentheses; velocities in **b**, **e** and **f** determined using time gate.

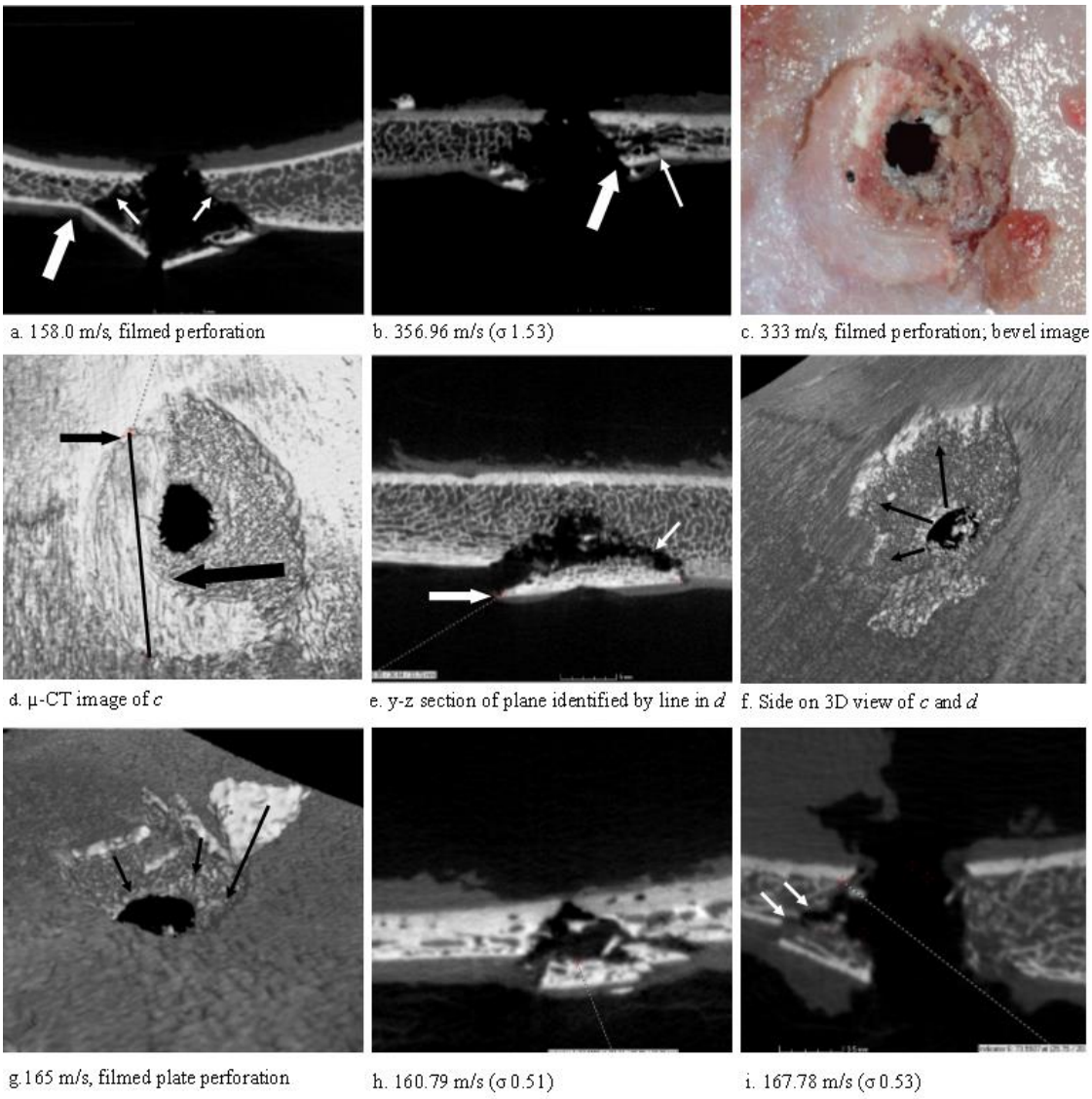

Fig.3.7 µ-CT images of inner cortical plate damage. **a**, x-z (transverse) cross-section of fragment cone with bevel concealed under fragments (arrows); large arrow marks the exit cortical fracture edge; **b**, accessory cortical fracture (thin arrow) outside the exit cortical fracture edge (thick arrow), y-z section. **c**. Photograph of C-shaped inner cortical plate fragment partially covering internal bevel after a 333 m/s perforation; **d**, µ-CT 3D view of fragment shown in **c**; black line shows plane of slice visible in **e**; **e,** y-z view of C-shaped fragment, viewed in direction of arrow shown in **d**; note the conoidal internal bevel above the fragment and the close approximation between bevel and fragment at right of image, with just over 1 mm separation in the region identified by the arrow; **f**, 3D view looking under C-shaped fragment in **c-e**; viewed from the right side, the internal bevel can be seen running underneath the fragment (arrows).**g,** 3D view looking into a conoidal wound from V_1; fragments moved in direction of arrows would partially re-form the floor of the wound; **h**. Marked conoidal fracture and counterpart fragments, y-z section; **i**; x-z section of bevelled edge (arrows) protected behind inner cortical plate fragment.

3.5. Discussion

The anatomical complexity of the human head makes detailed analyses of the terminal ballistics of this region challenging. In order to elucidate the fracture processes operative during perforation of the sandwich bone component of the head, the current study perforated pig scapulae with spherical steel projectiles and utilised a combination of µ-CT and high-speed videography for subsequent fracture analysis. While experimental conditions in the current work resulted in simpler projectile-tissue interactions than would be operative during perforation of the living bio-system, analysis of fracture morphology does not support the view that plug and spall is responsible for conoidal wound formation, as previously proposed [9-14]. Displaced inner cortical plate fragments were often in such close approximation to the bevel that a shear plug could not have been involved in bevel formation. Distinct part-counterpart relationships between inner cortical plate fragments and the internal bevel were also inconsistent with bevel formation by shear plugging. Finally, shear plug involvement in bevel formation was ruled out when the bevel was shielded behind inner cortical plate fragments. These previous features are, however, consistent with wound formation by propagation of a trans-laminar fracture through the sandwich bone.

In addition to morphological features that are inconsistent with plug and spall, fundamental penetration mechanics dictates that shear plugging will not occur in all perforation events within the same material. Shear plugging is sensitive to impact angle and projectile tip shape, and is commonly associated with blunt ended projectiles [22]; projectile velocity is also a contributing factor [23]. During plug formation intense shear occurs in a cylindrical zone under and around the projectile [24]; as a result, shear plugging is associated with cylindrical plugs of approximately the same diameter as the impactor [22, 23], resulting in cylindrical perforating channels through the material. Although data for trabecular bone are lacking, cylindrical shear channels have been reported subsequent to impact in a variety of foam cores in synthetic sandwich panels [25]. Such a morphology is inconsistent with the observed morphology of conoidal wounds in sandwich bones. The contention of Symes *et al* [10] that a plug of bone is pushed into the brain ahead of the projectile was not supported by the present study; projectile emergence from the inner cortical plate occurred in the absence of a sheared cortical plug in all filmed perforation events.

At present, the only other study to utilise µ-CT to visualise the internal morphology of perforating projectile wounds to sandwich bones is that of Kieser *et al* [14], who reported funnel shaped wound channels consisting of a vertical tunnel through the outer cortical layer and a conoidal bevelled region beneath this. In direct contrast, the present study found few examples where two such regions existed through the wound cross-sections. Rather than exhibiting vertical walls, the entry cortical fracture edges typically exhibited angulation suggestive of cone crack formation under the impacting projectile. Significantly, the crack induced at the cortical surface propagated through the sandwich bone without regard for the change in bone type at the upper or lower cortical-trabecular transitions. The possibility that cone cracks might form in the cortical layers of sandwich bones is supported by existing

literature; cone crack formation during indentation or impact is common in brittle materials [26-28] including glass, ceramics, and hard polymers [24], and has also been demonstrated in the cortex of long bones subsequent to projectile impact [29]. A principle failure mechanism in ceramics subjected to ballistic impact is the formation of a *ceramic conoid* due to cone crack propagation; a separated conoidal volume of ceramic, flaring in the direction of projectile travel, and typically undergoing fragmentation once formed [30]. Similarity between the bevel and such conoidal fractures in other brittle materials was previously noted by Klepinger [31], although this author ultimately contended that the bevel in entry wounds was formed by shards of bone breaking free from the inner surface.

Compact bone may be classified as a bioceramic composite [32], and conoidal wounds in sandwich bones resemble observed conoidal damage in non-biogenic ceramics to a remarkable degree with the exception that there is an intervening layer of a brittle cellular solid running through the centre of the impacted structure through which the crack must propagate. However, formation of cone cracks in cellular solids is not without precedent; cone cracks have previously been reported in low density Polyethylene Terephthalate (PET) foams subsequent to impact [25], and morphological evidence revealed by µ-CT suggests the involvement of cone cracks in projectile wound formation through sandwich bones. It has been established that cone cracks propagate into materials along lines of tensile stress initiating at the material surface [26] and that, when subjected to tensile stress, brittle open cell solids fail by propagation of a crack that hops one cell at a time through the material [33]. Observed trabecular fracture morphology in the present series was consistent with such a tensile failure mode; trabecular cells along the wound channel appeared to be bisected by a fracture crossing from one cell edge to another. Once initiated in the trabeculae, tensile fracture of one cell leads to greater load being borne by other cells [34]; provided enough energy is available, the fracture will thus propagate catastrophically through the entire layer [35]. Accordingly, it might reasonably be postulated that conoidal wounds are produced when a cone crack from the outer cortex propagates into and crosses the trabecular and inner cortical layers. Significantly, this process would account for the often straight-edged morphology of the trabecular fracture margin and for the lack of evidence for compression with permanent deformation of trabecular cells lining the wound channel, a feature also noted by Kieser *et al* [14].

An issue of central importance to the cone crack hypothesis is the question of how such a fracture crosses the upper and lower interfaces between cortices and trabeculae. Whether a given fracture will arrest, be deflected by or cross a given interface between two materials is determined by the angle of the fracture relative to the interface, the difference in elastic moduli between the two materials, and the presence of a third interface material sandwiched between the other two [36, 37]. When considering crack propagation from cortical to trabecular bone, the latter component may be eliminated due to lack of interface material between bone types. The relationship between fracture angle and the probability of a fracture crossing or deflecting an interface is analogous to the process of skimming a stone over water; the more acute the angle, the greater the probability that the fracture will

be deflected along the interface, rather than penetrating it [38]. In the present analysis no crack deflection was observed at the interfaces between cortical and trabecular bone, suggesting that cortical fracture angles are above the critical limit for crack deflection at the interfaces.

The relative elastic moduli of the two materials is of particular importance to crack behaviour at an interface; when a fracture approaches an interface with a material of lower elastic modulus, crack velocity increases significantly [39] and the crack is thus more likely to propagate into the second material. Although there is a wide range of reported values for the elastic modulus of trabecular bone in the literature, Keaveny *et al* [40] summarised data for elastic moduli determined using ultrasound methods and found values approximately 20 percent lower than that for cortical bone. More recent analyses have suggested that the elastic modulus of trabecular bone is lower than cortical bone, but only slightly [40, 41]. In sandwich bones, direct continuity between cortices and trabeculae and abundant cortical-trabecular connections, coupled with elastic modulus mismatch, would enhance the probability of a given fracture propagating into the trabecular layer from the outer cortex. Based upon internal and external fracture morphology and the above theoretical considerations, a novel mechanism for conoidal wound formation through sandwich bones is described below and in diagrammatic form in **Fig.3.8**:

1. Projectile impact initiates the formation of a cone crack within the outer cortical plate.
2. The cortical cone crack propagates across the upper cortical-trabecular transition via trabecular attachments that are in line with the cortical tensile stress. Tensile failure causes propagation of the crack across the trabecular cells one cell width at a time and produces a relatively straight-edged trabecular fracture margin. Local inhomogeneities in trabecular composition and differences in trabecular orientation may cause the crack to deviate and result in trabecular intrusion into the wound channel. High tensile stresses begin formation of stellate fractures on the inner cortical plate before projectile exit.
3. The cone crack propagates from the lower trabeculae through to the inner cortical layer via trabecular attachments in line with the tensile stress trajectory.
4. Propagation of the fracture to the lower cortical table completes formation of the internal bevel and results in formation of a conoidal volume of bone consisting of all three layers of the sandwich bone separated from the parent bone by the bevel. This structure remains intact during low velocity impacts.
5. Kinetic energy and stress waves associated with high-velocity impacts result in the instantaneous collapse and fragmentation of the formed conoidal volume. The floor of this volume forms *inner cortical plate fragments* which undergo elevation and eversion during projectile exit, leaving fragment cones at low velocity. At higher velocity, these fragments are largely ejected with soft tissue components, although some may remain *in-situ* due to incomplete trans-laminar fracture or retention within soft tissue. Trans-laminar fracture results in part-counterpart relationships between these retained fragments and the internal bevel.

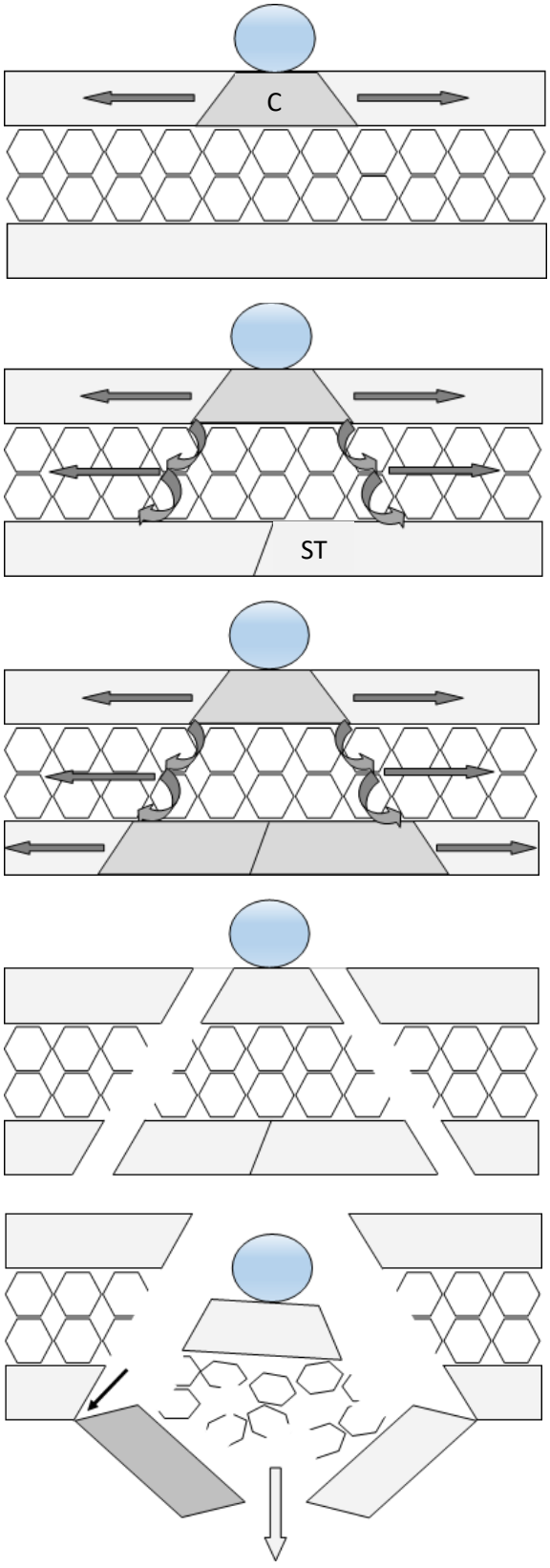

Step 1. Projectile impact initiates formation of a cone crack (C) under tension (arrows) in the outer cortical plate.

Step 2. The cone crack enters the trabecular layer via trabeculae orientated along the lines of tensile stress; under tension, the crack jumps from one cell strut to another (curved arrows). Compressive stress passing through the sandwich bone results in tensile failure of the inner cortical plate and formation of a stellate fracture radiating from the centre (angulated line ST).

Step 3. The cone crack follows lines of tensile stress into the inner cortical plate.

Step 4. Crack propagation through the entire sandwich structure results in temporary formation of a bioceramic conoid, separated from the parent bone by the internal bevel.

Step 5. During higher velocity impacts, trabeculae undergo stress- wave induced cell collapse. As the conoidal volume compresses, full failure of the inner cortical plate occurs in the centre at the stellate fracture (open arrow). After impact, some of the cortical floor may remain as *inner cortical plate fragments* (dark grey section of inner plate). Trans-laminar fracture results in part-counterpart relationships between these retained fragments and the internal bevel (solid arrow).

Fig.3.8 Novel mechanism for conoidal wound formation through sandwich bones

According to this mechanism, the internal bevel is the counterpart to the missing bone volume which, if intact, would slot in and out of the parent bone. The intact conoidal bone volume produced by this mechanism would be identical to the ceramic conoids produced in engineering ceramics subjected to ballistic impact, where a conoid of material is separated from the parent ceramic by the conoidal fracture [30]. In bone, such a conoidal volume may thus reasonably be termed a *bioceramic conoid*. Once initiated, cone cracks will propagate at the speed of sound for the material in which they are propagating, with conoid formation typically only taking a few microseconds in engineering ceramics [42]. Whilst the plug and spall hypothesis proposes that the bevel is created during projectile exit [9-12], the cone crack hypothesis suggests it is created *at the moment of impact*; the bevel is then revealed by subsequent conoid fragmentation. Additional evidence that bevel formation is due to trans-laminar fracture arises from the observation that bevels are interrupted at pre-existing fractures or sutures; this process, known as crack arrest, occurs when the energy driving fracture dissipates at the discontinuity [43].

Although the cone crack hypothesis suggests that wound formation is driven by tensile stress, this does not preclude the simultaneous operating of other failure modes through the wound volume; indeed, most cracks in bone are formed under a mixture of stresses [44]. Observation of stellate fracture patterns in the inner cortical plate confirms that a compressive stress transfers through the conoid during perforation, resulting in eventual tensile failure there. High-velocity perforation also undoubtedly involves additional mechanisms such as stress wave induced trabecular cell collapse [45], delamination within cortical bone [19] and possibly heating effects [14]. Previous Scanning Electron Microscope analysis of entry cortical fracture edges in bovine (*Bos taurus*) sandwich bones has identified fracture surfaces produced by tensile failure [19]. However, further fracture surface characterisation in both human and non-human bone is required to test the hypothesis that wound formation is driven by tensile stress and also to establish the contribution of additional failure modes to projectile wounding.

In the present experiment no intact bioceramic conoids were produced and fracture through the sandwich bones was often incomplete, with portions of the conoid floor remaining attached to the exit cortical fracture edge. The rarity of intact bioceramic conoids reported in case work suggests a particular set of circumstances must combine to form them; kinetic energy absorption must be low enough to prevent fragmentation and trans-laminar fracture must entirely separate the conoid from the parent bone. In brittle materials, plug fragmentation is likely to occur at velocities 5-10% above the minimum perforation velocity [22]; with higher velocity impacts it is therefore to be expected that much of the bioceramic conoid would undergo fragmentation. Such behaviour is also consistent with engineering ceramics, where fragmentation is similarly restricted to the separated conoid [24]. Impact data generated in the present study revealed that incident velocity and energy absorption were positively correlated. The law of conservation of energy dictates that both greater fragmentation and greater energy utilisation in fragment ejection must occur as velocity increases, with the latter process becoming particularly significant at higher velocities [46]. A positive correlation between incident velocity and energy

absorption has also been found in synthetic sandwich panels, where it is thought to be a characteristic of such structures [47, 48].

It is generally held that perpendicular entry wounds tend to be circular or oval in shape [5] and also that areas of bevel elongation indicate projectile trajectory [6, 7]. The current study substantiated the high frequency of circular wounds, which accounted for just under half of all cortical entry shapes. Whilst oval and irregular wounds were more common at higher velocities, circular wounds were present in the lowest and highest velocity groups. Variation in cortical entry wound shape subsequent to perpendicular impact with spherical, non-deforming projectiles suggests the importance of intrinsic biological factors, such as bone microarchitecture, in determining wound shape. The frequency of bevel asymmetry was interesting; of fourteen circular wounds, twelve (85.71%) exhibited asymmetrical bevelling. Across all cortical entry shapes, asymmetrical bevelling was far more common than symmetrical bevelling, accounting for 82.76% of bevels. These findings are in accordance with previously published data for entry wounds in human crania [21], where only fifteen percent of bevels were classed as symmetrical; an exact correlation between trajectory and bevel asymmetry was found in only five out of thirty nine entry wounds. In light of these findings, these authors highlighted the importance of intrinsic anatomical features in determination of bevel shape.

Observation of projectile exit in the present analysis suggested that the bevel and its symmetry are determined before projectile exit has occurred, with accessory fractures outside the conoidal wound potentially contributing to apparent bevel asymmetry. The cone crack hypotheses predicts that bevel shape would be determined by the initial angle of the cone crack, which differs around the cortical entry wound, and the subsequent crack path through the trabecular network. In synthetic materials, cone cracks become steeper with a decrease in Poisson's ratio [49] and with an increase in velocity [26]. Although further work is required to investigate relationships between velocity and cone angle in bone, overlap between angles across the velocity groups suggests that material factors might supersede loading rate in determining the angles achieved. Upon establishment of the cone angles in the outer cortex, final bevel shape would be determined by the subsequent path of the cone crack through the trabecular layer and inner cortex. High frequency of bevel asymmetry with perpendicular impacts suggests caution should be applied when using this feature to make trajectory determinations in the absence of an exit wound or other directionality indicators.

A number of authors have noted that irregular cortical entry wounds do not always result in irregular internal bevels [13, 21]. These findings were supported by the present study; irregular or partially irregular entry shape was lost by the internal bevel in 80 % of irregular wounds. µ-CT analysis revealed that fine details of cortical irregularity are deleted by approximately mid-depth in the trabecular layer. This phenomenon is consistent with the hypothesis of wound formation by trans-laminar cone crack propagation; minor deviations in crack path through individual trabeculae and differences in trabecular orientation in relation to the advancing crack would have a distorting effect as it propagated downwards, resulting in a deletion of information relating to entry wound shape as depth increased.

Despite lack of production of intact bioceramic conoids, comparison of plug morphology produced by low velocity impacts [15-17] with residual fracture morphology subsequent to medium and high-velocity impacts reveals similarities that are indicative of a common fracture process. Whilst overlap in external morphology between conoidal wounds produced by blunt and projectile trauma has been reported previously [50-52], this is the first report of wounds inflicted at 150 m/s being identical internally to those produced at 850 m/s. These shared internal and external morphological features suggest that conoidal wounds form a distinct category of trauma characterised by trans-laminar crack propagation and bioceramic conoid production. In cross-section, such conoidal wounds may be diagnosed by angulated entry cortical fracture edges in all or parts of the section and by evidence for crack propagation through all three layers of the sandwich bone. Further work utilising low velocity impacts is required to confirm their wider role in wound formation. The hypothesis that trans-laminar fracture underlies formation of all conoidal wounds raises interesting research challenges for enhanced differential diagnosis.

In addition to overlap between trauma types, wound diagnosis is complicated by taphonomic agencies including rodent gnawing [53] and carnivore scavenging [54]. Diagnosis may also be complicated by deliberate anthropogenic activities, particularly the use of fire [55, 56]. Traumatic wounds must also be differentiated from psuedotraumatic defects [57] such as missing sutural ossicles, which can combine with other fractures to create defects resembling those produced by traumatic events [58]. Cross-sectional microanatomy revealed by µ-CT provided a number of features that might be of diagnostic value. Sandwich bone response to projectile perforation was found to be extremely localised. Damage localisation is due to the short contact time between impactor and target, resulting in kinetic energy absorption over a small area [59]. Localisation of damage is also a characteristic feature of impacted cellular solids [45], and internal examination of perforated sandwich bones revealed intact peripheral trabeculae even at the highest velocities. Conoidal wounds exhibited angulation of the entry cortical fracture edges, trans-laminar fracture through the trabeculae which crossed from one cell edge to another, lack of sandwich layer delamination, and lack of permanent collapse of trabecular cells. Further work with lower velocity impact events is needed to detect when such features appear; comparative work with psuedotraumatic defects is also essential. Elucidation of the taphonomic resistance of any identified diagnostic indicators is also critical if they are to be of use in skeletal remains subjected to deposition in ecosystems.

Acknowledgements

We are indebted to Dr David Wood, Andrew Roberts, David Miller and Alan Peare for their considerable technical input and for operation of the gas guns and projectile housing. We would also like to extend our thanks to Kerrie Smith for the error propagation formula and Dr Keith Rogers and George Adams for their assistance and advice with micro-computerised tomography.

Conflict of Interest

The authors declare that they have no conflict of interest.

Ethical approval

This study was approved by the ethics committee of Cranfield University.

3.6. References

[1] Maiden N (2009) Ballistics reviews: mechanisms of bullet wound trauma. Forensic Sci Med Pathol 5:204-209 https:// doi.org/10.1007/s12024-009-9096-6

[2] Aarabi B, Tofighi B, Kufera JA, Hadley J, Ahn ES et al (2014) Predictors of outcome in civilian gunshot wounds to the head. J Neurosurg 120:1138-1146

[3] Mota A, Klug WS, Ortiz M, Pandolfi A (2003) Finite-element simulation of firearm injury to the human cranium. Comput Mech 31: 115-121 https://doi.org/ 10.1007/s00466-002-0398-8

[4] Snell R S (1995) Clinical Anatomy. Lipincott Williams and Wilkins, Maryland.

[5] Berryman HE, Symes SA (1998) Recognising gunshot and cranial trauma through fracture interpretation. In Reichs, K J (ed) Forensic Osteology: advances in the identification of human remains. Charles C Thomas Publishers, Springfield, pp 333-352

[6] Rhine S, Curran BK (1990) Multiple gunshot wounds to the head: An anthropological review. J. Forensic Sci. 35 (3): 1236-1245

[7] Spitz WU (2006) Injuries by gunfire. In Spitz WU, Spitz DJ, Clark R (eds) Spitz and Fisher's medicolegal investigation of death: guidelines for the application of pathology to crime investigation, Charles C Thomas Publishers, Springfield. [Online] Available from: Proquest Ebook Central (accessed 9.11.17)

[8] Hull D (1999) Fractography: observing, measuring and interpreting fracture surface topography. Cambridge University Press, Cambridge

[9] Komar DA, Buikstra JE (2008) Forensic anthropology: contemporary theory and practice. Oxford University Press Inc., New York.

[10] Symes SA, L'Abbé EN, Chapman EN, Wolff I, Dirkmaat DC (2012) Interpreting traumatic injuries to bone in medicolegal investigations. In Dirkmaat DC (ed) A companion to forensic anthropology, Wiley- Blackwell Publishing, West Sussex

[11] Christensen AM, Passalacqua NV, Bartelink EJ (2014) Forensic anthropology: current methods and practice. Academic Press, Oxford

[12] Peterson BL (1991) External beveling of cranial gunshot entrance wounds. J. Forensic Sci. 36 (5): 1592-1595

[13] Kimmerle EH, Baraybar JP (2008). Skeletal trauma: identification of injuries resulting from human rights abuses and armed conflict. CRC Press, Florida.

[14] Kieser JA, Tahere J, Agnew C et al (2011) Morphoscopic analysis of experimentally produced bony wounds from low velocity ballistic impact. Forensic Sci Med Pathol 7:322-332 https:// doi.org 10.1007/s12024-011-9240-y

[15] Murphy MS, Gaither C, Goycochea E, Verano JW, Cock G (2010) Violence and weapon-related trauma at Puruchuko-Huaquerones, Peru. Am J Phys Anthropol 142:636-649

[16] Murphy MS, Spatola B, Weathermon R (2014) Allies today, enemies tomorrow: a comparative analysis of perimortem injuries along the biomechanical continuum. In Martin DL, Anderson CP (eds) Bioarchaeological and forensic perspectives on violence: how violent death is interpreted from skeletal remains, Cambridge University Press, Cambridge, pp 261-288

[17] Bird CE, Fleischman JM (2015) A rare case of an intact bone plug associated with a gunshot exit wound. J. Forensic Sci. 60 (4): 1074-1077

[18] Smith MJ, Brickley MB, Leach SL (2007) Experimental evidence for lithic projectile injuries: improving identification of an under-recognised phenomenon. J. Archaeol. Sci. 34: 540-553

[19] Rickman JM, Smith MJ (2014) Scanning Electron Microscope analysis of gunshot defects to bone: an underutilised source of information on ballistic trauma. J. Forensic Sci. 59 (6): 1473-1486 https:// doi.org 10.1111/1556-4029.12522

[20] Currey J D (2002) Bones: structure and mechanics. Princeton University Press, New Jersey

[21] Quatrehomme G, İşcan MY (1998) Analysis of bevelling in gunshot entrance wounds. Forensic Sci. Int. 93: 45-60

[22] Zukas JA (1982). Penetration and perforation of solids. In Zukas JA, Nicholas T, Swift HF, Greszczuk LB, Curran DR (eds) Impact dynamics, John Wiley and Sons, Inc., USA, pp 155- 214

[23] Backman ME, Goldsmith W (1978) The mechanics of penetration of projectiles into targets. Int J Engng Sci 16:1-99

[24] Crouch IG (2016) An introduction to armour materials. In Crouch IG, Arthur J (eds) The Science of armour materials, available from ProQuest Ebook central

[25] Hassan MZ, Cantwell WJ (2012) The influence of core properties on the perforation resistance of sandwich structures: an experimental study. Composites: Part B 43: 3231-3238

[26] Knight CG, Swain MV, Chaudhri (1977) Impact of small steel spheres on glass surfaces. J Mater Sci 12:1573-1586

[27] Chen SY, Farris TN, Chandrasekar S (1995) Contact mechanics of Hertzian cone cracking. Int J Solids Structures 2 (3/4): 329-340

[28] Lawn BR (1998) Indentation of ceramics with spheres: a century after Hertz. J Am Ceram Soc 81 (8): 1977-1994

[29] Kieser DC, Riddell R, Kieser JA, Theis J, Swain MV (2013) Bone micro-fracture observations from direct impact of slow velocity projectiles. J Arch Mil Med 2(1): e15614 https:// doi.org 10.5812/jamm.15614 (Accessed 8/3/2015)

[30] Zaera R, Sánchez-Gálvez V (1998) Analytical modelling of normal and oblique ballistic impact on ceramic/ metal lightweight armours. Int J Impact Engng 21 (3): 133-148

[31] Klepinger LL (2006) Fundamentals of forensic anthropology. John Wiley & Sons, New Jersey

[32] Olszta MJ, Cheng X, Jee SS, Kumar R *et al* (2007) Bone structure and formation: a new perspective. Mater Sci Eng R Rep 58: 77-116

[33] Gibson LJ, Ashby MF (1988) Cellular solids: structure and properties. Pergamon press, Oxford

[34] Kaplan SL, Hayes WC, Stone JL (1985) Tensile strength of bovine trabecular bone. J Biomech 18 (9): 723-727

[35] Tomar V (2009) Insights into the effects of tensile and compressive loadings on microstructure dependent fracture of trabecular bone. Eng Fract Mech 76: 884-897

[36] Imbeni V, Kruzic JJ, Marshall GW, Marshall SJ, Ritchie RO (2005) The dentin-enamel junction and the fracture of human teeth. Nat Mater https:// doi.org 10.1038/nmat1323

[37] Zimmermann EA, Gludovatz B, Schaible E, Busse B, Ritchie RO (2014) Fracture resistance of human cortical bone across multiple length scales at physiological strain rates. Biomaterials 35: 5472-5481

[38] He M-Y, Hutchinson JW (1989) Crack deflection at an interface between dissimilar elastic materials. Int J Solids Structures 25 (9): 1053-1067

[39] Mencík J (2010) Mechanics of components with treated or coated surfaces. Klewer Academic Publishers, Netherlands.

[40] Keaveny TM, Morgan EF, Yeh OC (2004) Bone biomechanics. In Kutz M (ed) Standard handbook of biomedical engineering and design, McGraw- Hill Professional, USA, pp 8.1-8.23

[41] Bayraktar HH, Morgan EF, Niebur GL, Morris GE, Wong EK, Keaveny TM (2004) Comparison of elastic and yield properties of human femoral trabecular and cortical bone tissue. J Biomech 37: 27-35

[42] Kaufmann C, Cronin D, Worswick M, Pageau G, Beth A (2003) Influence of material properties on the ballistic performance of ceramics for personal body armour. Shock and Vibration 10: 51-58

[43] Madea B, Staak M (1988) Determination of the sequence of gunshot wounds of the skull. J. Forensic Sci. Soc 28: 321-328

[44] Zimmermann EA, Launey ME, Barth HD, Ritchie RO (2009) Mixed mode fracture of human cortical bone. Biomaterials 30: 5877-5884

[45] Zou Z, Reid SR, Tan PJ, Li S, Harrigan JJ (2009) Dynamic crushing of honeycombs and features of shock fronts. Int J Impact Eng 36: 165-176

[46] Abrate S (1998) Impact on composite structures. Cambridge University Press, Cambridge

[47] Skvortsov V, Kepler J, Bozhevolnaya E (2003) Energy partition for ballistic penetration of sandwich panels. Int J Impact Eng 28: 697-716

[48] Hou W, Zhu F, LU G, Fang D-N (2010) Ballistic impact experiments of metallic sandwich panels with aluminium foam core. Int J Impact Eng 37: 1045-1055

[49] Chaudhri MM (2015) Dynamic fracture of inorganic glasses by hard spherical and conical projectiles. Philos Trans R Soc Lond A 373: 20140135 https:// doi.org 10.1098/rsta.2014.0135

[50] Spatola BF (2015). Atypical gunshot and blunt force injuries: wounds along the biomechanical continuum. In Passalacqua NV, Rainwater CW (eds) Skeletal trauma analysis: case studies in context. John Wiley & Sons, West Sussex, pp 7-26

[51] Quatrehomme G, Piercecchi-Marti M, Buchet L, Alunni V (2015) Bone bevelling caused by blunt trauma: a case report. Int J Legal Med 130 (3): 771-775 https:// doi.org/10.1007/s00414-015-1293-0

[52] Vermeij EJ, Zoon PD, Chang SBCG et al (2012). Analysis of microtraces in invasive traumas using SEM/EDS. Forensic Sci. Int. 214 (1): 96-104

[53] Nawrocki SP (2009) Forensic taphonomy. In Blau S, Ubelaker DH (eds) Handbook of Forensic Anthropology and Archaeology, Left Coast Press, California, pp 284-294

[54] Moraitis K, Spiliopoulou C (2010) Forensic implications of carnivore scavenging on human remains recovered from outdoor locations in Greece. J Forensic Leg Med 17: 298-303

[55] Pope EJ, Smith O'BC (2004) Identification of traumatic injury in burned cranial bone: an experimental approach. J. Forensic Sci. 49 (3): 1-10

[56] Tümer AR, Karacaoğlu E, Keten A, Ünal M (2012) Postmortem burning of the corpses following homicide. J Forensic Leg Med 19: 223-228

[57] Loe L (2009) Perimortem trauma. In Blau S, Ubelaker DH (eds) Handbook of Forensic Anthropology and Archaeology, Left Coast Press, California, pp 263-283.

[58] Machado MPS, Simões MP, Gamba TO, Flores IL et al (2016) A Wormian bone, mimicking a gunshot entrance wound of the skull, in an anthropological specimen. J. Forensic Sci. 61 (3): 855-857 https:// doi.org 10.1111/1556-4029.13043

[59] Cantwell WJ, Morton J (1989) Comparison of low and high velocity impact response of CFRP. Composites 20 (6): 545-551

CHAPTER 4, PAPER 3

(Published in the *International Journal of Legal Medicine* 133 (2019): 1443-1459)

Crack propagation through sandwich bones due to low-velocity projectile impact

John M Rickman* (MSc), Dr James Shackel**

4.1. Abstract

Projectile impact in sandwich bones typically results in formation of conoidal wounds exhibiting a larger region of damage on the inner cortical plate termed the bevel. To date, a number of hypotheses have been put forward to explain the formation of this wound type. The plug and spall hypothesis suggests that the conoidal morphology is produced by a two- phase mechanism of shear plug formation followed by internal bevel production during projectile exit. In contrast, the cone crack hypothesis suggests that such wounds are produced by cone crack propagation through the three laminae of the sandwich bone, resulting in the formation of bioceramic conoids consisting of all three bone laminae. In order to test these hypotheses, 28 non-human sandwich bones were impacted with 6 mm carbon steel spheres at velocities ranging from 26 m/s to 96 m/s. Impacts were filmed utilising high-speed videography and fracture morphology analysed using micro-computerised tomography (µ-CT). Sequential increase in velocity successfully captured the genesis of conoidal wounds. Low-velocity impact produced circular depressed fractures in the outer cortex exhibiting angulated cortical fracture edges. An increase in velocity resulted in translaminar fracture and production of one intact and three fragmentary bioceramic conoids. At the highest velocities, conoids were fragmented and lost in the ejecta plume, with attached fragments undergoing dynamic movement during and after perforation. Significantly, projectile exit was not required for bevel production. The implications of these findings in wound interpretation are discussed.

Cranfield Forensic Institute

Cranfield University, Defence Academy of the United Kingdom

Shrivenham

SN6 8LA

*Corresponding author email address: j.m.rickman@cranfield.ac.uk

*Phone: 01793785531

*ORCID: 0000-002-1188-8805

**Email address j.shackel@cranfield.ac.uk

**Phone: 01793785747

Keywords

Skeletal trauma; projectile trauma; bevelling; forensic anthropology; fracture; trajectory determination

4.2. Introduction

The conoidal fracture expressed in sandwich bones subsequent to projectile impact is an intriguing traumatic feature upon which critical diagnostic and trajectory determinations are based [1-4]. Morphologically, this wound type consists of a conoidal wound volume bordered by a fracture edge through all three layers of the sandwich bone, extending from the entry point in the outer cortex and across the intervening trabeculae to the inner cortical lamina [5]. Such conoidal fracture morphology dictates that the region of missing bone in the inner cortical lamina has a larger surface area than that missing from the opposing cortical entry wound. The bony layers composing this flaring, termed the *internal bevel* in entry wounds and *external bevel* in exit wounds [1, 6], are rarely formally defined; however, it is accepted that the conoidal fracture extends in the direction of projectile travel and thus indicates the entry or exit status of the wound [6, 7]. Further diagnostic emphasis has been placed on the symmetry of the bevel, with regions of bevel elongation considered to indicate the trajectory of the projectile through the bone [2, 3, 8], although full correlation between these variables has been disputed [5; 9]. Despite the importance of such determinations in forensic contexts, there is still no consensus in the literature as to the mechanisms underlying formation of this conoidal wound type, and multiple medicolegal cases have now demonstrated that this feature is not unique to projectile impact [10].

In material terms, bone is a bioceramic composite [11] with hierarchical organisation [12-14]. At the macroscopic level, the sandwich bones of the neurocranium are constructed of outer and inner layers of cortical bone separated by an intervening trabecular layer of variable thickness, sometimes termed the *diploë* [15]. Fractures through such a sandwich bone may be confined to a single layer (*intra-laminar*), cross one or more layers (*trans-laminar*) or pass between layers (*inter-laminar*, or *delamination*) [5]. These fractures may be further classified according to mechanism; *mode 1* failure indicates a tensile, crack opening mode whilst *mode 2* refers to in-plane shear, which occurs in the absence of crack opening [16].

For descriptive purposes, the current paper utilises nomenclature developed from the micro-computerised tomographic (μ-CT) analysis presented previously by the present authors [5]. In this scheme (**Fig.4.2**), a single conoidal entry wound in a sandwich bone is considered to consist of a *cortical entry* in the outer cortical layer and a *cortical exit* in the inner cortical layer, the two encompassing the upper and lower borders of an internal conoidal *wound volume*. *Entry cortical fracture edges* form the walls of the *cortical entry* whilst the *cortical exit* is bound by the walls of the *exit cortical fracture edge*. The *trabecular fracture margin* is formed by the free edges of fractured trabeculae, and *peripheral trabeculae* are those trabeculae up to 3 mm peripheral to this margin. This entry cortical fracture edge is typically angulated and the crack producing this cortical fracture margin crosses with little to no deviation across the trabeculae and into the inner cortex as a *translaminar fracture surface*. Such continuous translaminar fracture renders definition of the layers composing the internal bevel an

arbitrary process; however, the present paper defines the internal bevel as a conoidal wound volume encompassing the *exit cortical fracture edge* and *trabecular fracture margin*.

The plug and spall hypothesis is the most widely cited mechanism for production of this wound type, appearing in multiple standard texts considering the subject of osseous gunshot wounds [e.g. 3, 7, 17]. This hypothesis (see **Fig.4.1)** proposes that conoidal wound formation is a two-phase process involving *plug formation in the outer cortex* and then *bevel production.* In the first phase, projectile impact shears a plug or disc of cortical bone from the outer cortical layer [3, 18, 19] (**Fig.4.1.a**). This shear plug is then theorised to move ahead of the projectile through the sandwich structure (**Fig.4.1.b**), with some interpretations also suggesting that fractured material accumulates ahead of the projectile/ plug combination [19]. In the second phase, the internal bevel is believed to be formed by a blow-out process involving fracture or "spall" around the plug during projectile exit (**Fig.4.1.c.**) [3, 7, 18], with plug-induced shear through the trabeculae posited as a specific mechanism for trabecular failure [4]. Kieser et al [19] utilised µ-CT to analyse wound cross-sections and proposed that the resultant wound profile due to cortical plug production was funnel shaped, with the neck of the funnel in the external cortex (**Fig.4.1.d**). According to the plug and spall hypothesis, the dominant fracture mechanism is considered to be mode 2 (*in-plane shear*). The plug and spall hypothesis, as described above, involves several key assumptions:

1. Plug production through in- plane shear is independent of projectile tip shape and construction, since conoidal wounds are not restricted to certain projectile designs.
2. The disc of sheared bone does not fragment during transit through the sandwich structure.
3. The projectile must pass through the trabeculae and then exit the bone for the bevel to form

Despite wide usage of this hypothesis, there appears to be no published evidence supporting the role of a cortical plug in wound formation. Shear plugging itself is sensitive to multiple factors including target material characteristics, projectile tip shape, velocity, and angle of impact [20], and thus it will not occur with all impacts in a given material. Recognition of the high contact stresses developed during impact raises the question as to how a shear plug could participate in perforation without itself being destroyed during the impact event. Analysis of high-speed footage of projectile exit through pig sandwich bones has revealed no evidence for an intact disc of cortical bone exiting ahead of the projectile [5]. Furthermore, cross-sectional analysis has demonstrated that the bevel still forms when it is shielded behind bone fragments retained on the inner cortical plate, effectively ruling out bevel production due to contact with a disc of cortical bone in those regions [5].

In an alternative hypothesis based upon a µ-CT and high-speed video analysis (**Fig.4.2**), Rickman and Shackel [5] proposed that the conoidal wound in sandwich bones is produced by cone crack formation under tension in the outer cortex; this cone crack was then theorised to propagate through the trabecular lamina one cell width at a time before finally entering the inner cortex. According

to this scheme the crack propagates through the tri-laminar sandwich bone as if it were a homogeneous solid, resulting in production of a conoidal structure consisting of all three layers of the sandwich bone, separated from the parent bone by the conoidal fracture, or bevel. This tri-layered plug, or *bioceramic conoid*, would be identical to the *ceramic conoids* produced during impact of non-biogenic ceramics [21] but with the addition of a layer of trabecular bone running between cortical plates. Morphological evidence in support of the cone crack hypothesis and bioceramic conoid formation at higher velocities included angulation of the entry cortical fracture edges, apparent trans-laminar fracture through the sandwich structure, and part-counterpart relationships between fragments of inner cortical plate and the internal bevel. Unlike the plug and spall theory, the cone crack hypothesis does not assume that projectile exit is required to produce the bevel. Rather, the bevel is theorised to form at the moment of impact by a cone crack propagating at the speed of sound through the material from outer to inner cortical plates. Unlike the plug and spall theory, the cone crack hypothesis suggests that the fracture driving wound formation is primarily a crack opening, mode 1 (*tensile*) process.

A significant complication when studying plugs during high velocity impact arises from the fact that plug fragmentation in brittle materials occurs as little as ten percent beyond the minimum perforation velocity [20]; accordingly, their possible formation above this threshold must be inferred from residual fracture morphology. At present, evidence of intact projectile-induced bioceramic conoids in sandwich bones is limited to a few reports in the archaeological and forensic literature of tri-layered plugs that demonstrate part-counterpart relationships with their parent bone [22-24]. However, while these valuable finds indicate that conoidal plugs can be produced during at least some projectile impacts, it is not yet clear if their production underlies the formation of all conoidal wounds. To date, no published accounts of their experimental formation could be identified and, accordingly, there is much to be learned about how these structures form and about their possible wider role in conoidal wound formation in sandwich bones.

An alternative approach to the study of crack propagation from post-perforation fracture morphology is to utilise a series of low-velocity increments in an attempt to capture crack propagation through the depth of the structure. Although the assumption that low and high velocity impacts elicit identical fracture behaviours may not always be met due to both strain rate and shock wave effects, this technique was successfully utilised by Kieser *et al* [25] to capture the formation of butterfly fractures in deer femora, a fracture type typical of higher velocity impacts in long bone shafts. Significantly, these authors also reported cone crack propagation in the compact bone. Although informative footage of long bone projectile perforation has been captured by high-speed videography [26-28], visualisation of fracture processes in sandwich bones is currently limited to high velocity tangential impacts to synthetic analogues [29] and perpendicular impacts to pig scapulae [5]. To further test the plug and spall and cone crack hypotheses, the present study utilises a combination of µ-CT and high-speed videography to capture crack propagation processes in non-human sandwich bones subjected to a series of incremental low-velocity impacts between 25 m/s (metres per second) and 100 m/s. Fracture

processes are described and their significance in relation to wound diagnosis and interpretation are then discussed.

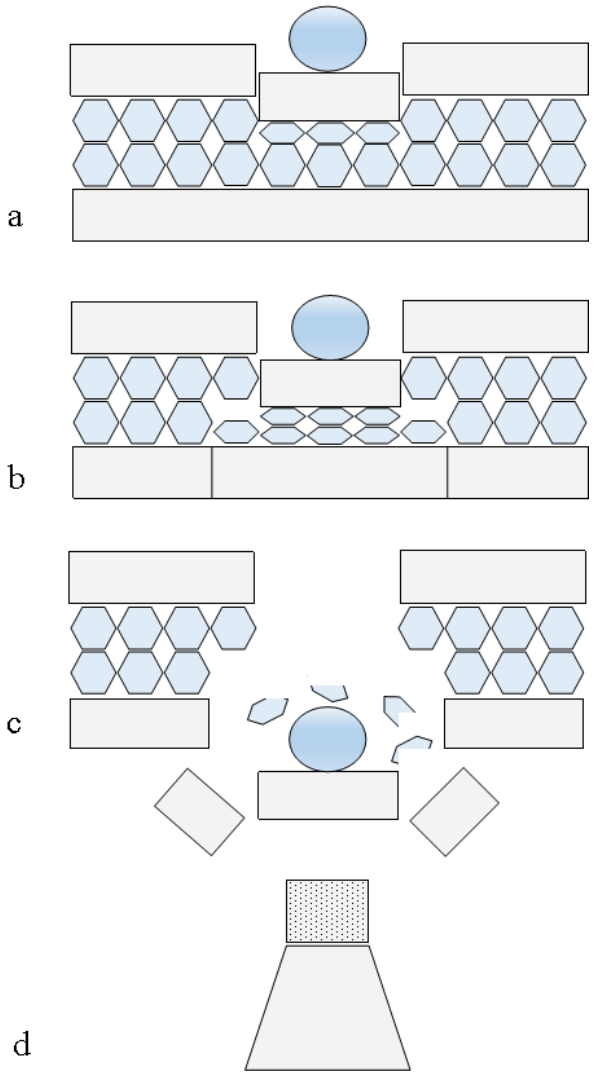

Fig.4.1. The plug and spall hypothesis; **a**, projectile impact shears a plug of cortical bone from the outer cortical layer; **b,** projectile and sheared plug move through the trabecular layer, signified by hexagons; note cell collapse and densification due to compressive stresses; **c**, projectile and shear plug blast out the exit to produce the internal bevel; **d**, wound volume profile in section as proposed by Keiser *et al* [19]; wound is funnel shaped, with vertical neck in the outer cortex (dotted region) and conoidal region through the trabecular layer and internal cortical layer.

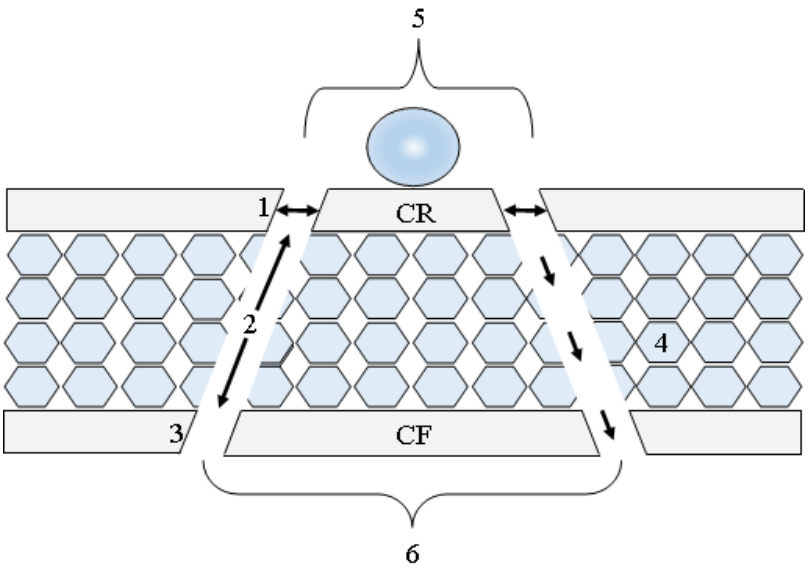

Fig.4.2 The cone crack hypothesis and formation of a tri-layered plug or *bioceramic conoid*; projectile impact elicits cone crack formation under tension in the outer cortical layer (horizontal double headed arrows); crack then propagates under tension through the trabecular cells and through the inner cortical layer (three arrows descending at right); nomenclature for cross-sectional anatomy presented in [5]; **1**, *entry cortical fracture edge*; **2**, *trabecular fracture margin*; **3**, *exit cortical fracture edge*; **4**, *peripheral trabeculae*; **5**, *cortical entry*; **6**, *cortical exit*; the bevel is here defined as the trabecular fracture margin (**2**) and exit cortical fracture edge (**3**); intact bioceramic conoid has a cortical roof (CR) and a cortical floor (CF)

4.3. Methods

4.3.1. Sample type and shooting methodology

Adult domestic pig (*Sus scrofa*) scapulae derived from the food chain were selected as proxies for human bones due to the fact they exhibit bevelled wounds when subjected to ballistic impact. Specimens were prepared according to the methods presented in [5]. In brief, only specimens with a layer of soft tissue in the infraspinous fossa, which was selected due to its larger size, were utilised. The glenoid, neck and spine were removed using a band saw, as was a section of cartilage on the anatomically dorsal surface. A target region of the infraspinous fossa no less than 40 mm from any edge was then selected and marked. During impact, specimens were secured in a specially constructed steel clamp that allowed full adjustment for different specimen sizes (**Fig.4.3**). All specimens were impacted with the ventral region forming the apex, the broader dorsal region forming the base, and the infraspinous fossa facing outwards.

Surface hardened 6 mm carbon steel spherical projectiles (Atlas Ball and Bearings, UK) weighing 0.885 grams were selected to prevent yaw or deformation from influencing fracture behaviour. These projectiles were fired from a compressed air powered gas gun capable of achieving a velocity range of approximately 25 m/s to 150 m/s. In order to achieve desired incident velocities for

the 6 mm spheres, a calibration curve of pressure versus velocity was created in a series of test shots. During the bone impacts, a muzzle-target distance of 60 cm was chosen to prevent discharged air from influencing fracture processes.

Incident (pre-impact) velocity, residual (post-impact) velocity and energy absorption values were determined by placing a Phantom V12 camera to the side of the specimens with a scale in the image. Impact data was then calculated using Phantom Cine Viewer (Vision Research, Inc.); to allow for variation in velocity measurements, projectile velocity was taken as the mean of three velocity determinations for each specimen. Assuming that energy is not utilised in projectile deformation and that energy lost due to frictional heating is minimal, energy absorption(ΔE) by the bone in joules (J) was then determined using the following formula:

$$\frac{m\left(v_1^2\text{-}v_2^2\right)}{2}$$

Where *m* is the mass of the projectile in grams, V_1 is the incident velocity and V_2 the residual velocity in metres per second (m/s). In order to derive a standard deviation for the individual energy absorption values, which were calculated from the mean of three velocities, the error propagation formula presented in Rickman and Shackel [5] was utilised. Inner cortical plate behaviour was captured in all impacts using a Phantom V12 12 camera facing the inner plate and recording at 40,000 frames per second.

To determine velocities associated with internal crack formation, initial tests were conducted with six specimens divided into three pairs with selected target velocities of 30 m/s, 40 m/s and 50 m/s. Actual achieved test velocities were 26 m/s and 29 m/s (group 1), 35 m/s and 37 m/s (group 2), and 47 m/s and 49 m/s (group 3). µ-CT examination revealed that internal cracking was restricted to the specimen impacted at 47 m/s; accordingly, velocities above 50 m/s were selected for subsequent analysis. In the latter experiments, a more refined inter-shot variation of 1-2 m/s was achieved by noting the velocity of the first shot at each selected velocity; all subsequent shots were then discharged with the same air pressure. Utilising this method, specimens were impacted between 54-55 m/s (group 4), 57-58 m/s (group 5), 74-75 m/s (group 6), and 95-97 m/s (group 7). The number of specimens impacted across these velocities is provided in **Table 4.1**. Following Goldsmith [30], *penetration* was considered to occur if the projectile rebounded and induced surface damage to the specimen (including soft tissue) or if it embedded in the target; *perforation* occurred if the projectile exited the sandwich bone.

In order to remove the concealing effect of soft tissue when observing fracture, soft tissue was dissected away from the outer and inner cortical layers of six additional specimens. Footage of entry and exit was then obtained by placing the Phantom V12 12 camera at the rear of each specimen and the Phantom V12 camera at the front; both cameras were then set to record on the same trigger. Although

lack of a camera mounted to the side meant that incident velocities could not be determined from imaging of the projectile, the calibration curve allowed velocity estimation to within approximately 1-2 m/s. Inner cortical plate behaviour during projectile re-bound was captured using four specimens impacted at approximately 57 m/s. To view the full perforation process at higher velocity, two final specimens were impacted at approximately 150 m/s. Post- impact analysis revealed that a technical fault in the trigger time of one camera had resulted in a variable delay between front and rear footage, preventing full camera synchronisation; however, valuable data on fracture processes was obtained.

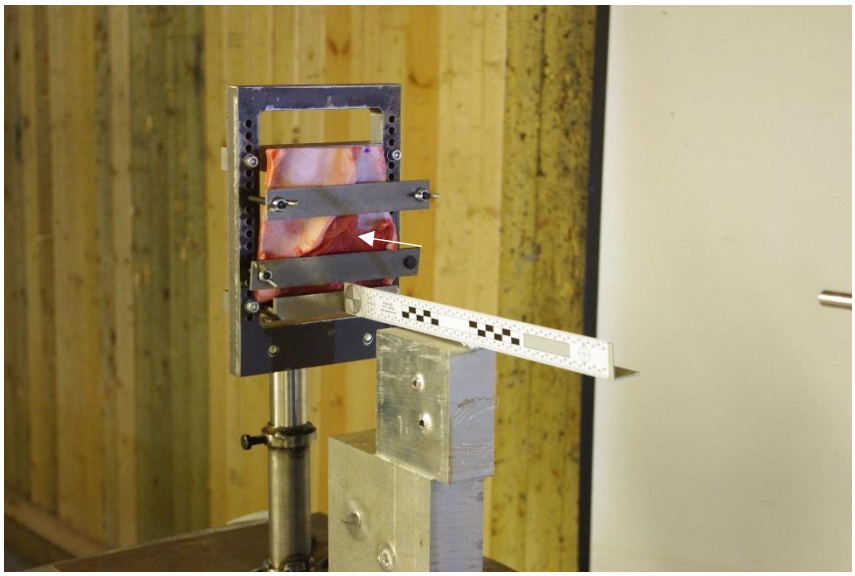

Fig.4.3 Machined specimen mounted in adjustable clamping apparatus; target area in the infraspinous fossa indicated by arrow

4.3.2. Micro-Computerised Tomography (µ-CT)

Specimens were wrapped in cling film, mounted in foam blocks and held securely in place using tape. The impact area of the fleshed specimens was identified and scanned in a Nikon X-Tec XT H 225 scanner at 75 kV, 90 µA and 2.25 magnification, resulting in a voxel size of 89 microns. Scan data was reconstructed using CT Pro 3D; the radius of reconstruction was reduced from 100% to 95-90% in order to remove edge artefacts produced by rotation of the flat plate around the damage area. Reconstructed volumes were analysed in VGStudeo MAX version 2.2 (Volume graphics, Germany). The simple registration function was utilised to orientate specimens across the middle of the screen with the cortical entry facing upwards. Bone surfaces were identified using the surface determination function. Distance and angle measuring tools were set to recognise and attach to the bone surface using the snap to surface function, allowing precise placement of the tool. The depth of depressed fractures at the impact location was obtained by placing a line across the cortical entry and then dropping a distance measuring tool from this to the most compressed region of cortex.

4.3.3. Cortical entry shape and bevel symmetry

Cortical entry shape was classed as circular, oval, or irregular; entries were further classed as circular-irregular or oval- irregular if there was irregularity in part of their otherwise symmetrical margin. Bevel symmetry was determined using µ-CT scans in 3D view and by descending through the wound to the exit cortical fracture edge (ExCF). *Asymmetrical bevels* were defined as those presenting a deviation in the ExCF resulting in a more pronounced bevel margin in one or more areas; in *symmetrical* bevels, the ExCF showed no such deviation.

4.4. Results

A total of 28 specimens were impacted and filmed, with side on camera footage available for 22 of these**; s**ummary data for these 22 impacts is provided in **Table 4.1**. Energy absorption values could not be calculated in the two group one specimens; in one, projectile re-bound was not captured, while in the other the projectile immediately re-bounded off the clamp. **Fig.4.4.** shows the relationship between incident velocity, energy absorption and whether impact resulted in re-bound, penetration or perforation for the remaining 20 specimens. Across these impacts, absorbed energy ranged from 0.48 J to 4.08 J. An increase in incident velocity resulted in a steep increase in energy absorption. In specimens retaining soft tissue, a total of 16 impacts resulted in penetration, with 14 of these undergoing rebound. Two impacts at the highest velocities in the series (at 94 m/s and 96 m/s) resulted in embedment. In total, perforation was observed in 6 specimens and was found to initiate at 58 m/s. Greater absorbed kinetic energy above this threshold resulted in perforation in five of the seven impacts between 73-96 m/s.

Measurement data taken from the four specimens impacted between 94-96 m/s suggested factors that might have determined whether projectile penetration or perforation occurred (**Table 4.2)**. Apical and basal total thicknesses, apical and basal trabecular thicknesses and apical cortical thicknesses were greater in the two embedding impacts. This general trend for a thicker outer cortex in the embedding impacts also existed for the basal side of the wound, although there was overlap between the 96 m/s perforation and 96 m/s embedment. Apical and basal thicknesses of the inner cortical layers were also greater in the two embedding impacts. The thickness of the trabecular lamina in relation to whole bone thickness did not appear to influence projectile behaviour, with one perforating impact actually having a proportionally thicker trabecular layer than the two embedding impacts. Projectile embedment was associated with greater energy absorption in both cases.

Table 4.3 details external wound morphology in the 6 perforated fleshed specimens. The majority of entries were circular (n=3) or circular-irregular (n=2). The single irregular entry occurred at the lowest incident velocity and in a very thin specimen (0.9 mm at its thinnest point). The majority of bevels (n=4) were asymmetrical. Only one of the three circular entries exhibited symmetrical bevelling.

Group	Incident velocity (m/s) (n)	Penetration	Perforation	Ring crack/ compressed cortical disc	Angulated entry cortical fracture edges	Tri-layered bioceramic conoid (I= intact; F= fragmentary)	Longitudinal plane; mean apical EnCF angle	Longitudinal plane; mean basal EnCF angle
1	26 (1)	S	-	-	-	-	-	-
	29 (1)	S	-	-	-	-	-	-
2	35 (1)	S	-	-	-	-	-	-
	37 (1)	S	-	-	-	-	-	-
3	47 (1)	SB	-	1	1	0	-	-
	49 (1)	S	-	0	0	0	-	-
4	54-55 (3)	3 SB	-	3	3	0	55.31 (2) *49.24-61.37*	64.82 (2) *52.57-77.07*
5	56-58 (6)	4 SB; 1 S	1	4	4	1 I	50.33 (3) *36.74-62.70*	47.00 *36.34-53.37*
6	73-75 (3)	-	3	3	3	3 F	45.94 *44.17-48.97*	39.42 *27.28-49.34*
7	94-96 (4)	2, E	2	-	4	0	44.44 *31.19-57.99*	53.05 (3) *31.98-70.28*
Total	22	16	6	11	15	4		

Table 4.1 Summary data for n= 22 impact events; n = number of specimens; velocities from 26 m/s to 49 m/s were grouped into three pairs of initial test shots with the velocity indicated; S = penetration of soft tissue only; SB = penetration of soft tissue and bone; E = projectile embedded in bone; EnCF = entry cortical fracture edge; absence of cracks or cracks that were too small for accurate measurement in the longitudinal plane resulted in the mean entry cortical fracture edge angle being determined from the sample size indicated in parentheses (groups 4, 5 and 7); angle range indicated in Italics

Incident velocity (m/s)	Projectile behaviour	Total bone thickness (TB), apical (mm)	Total bone thickness (TB), basal (mm)	Outer cortical thickness, apical (mm)	Outer cortical thickness, basal (mm)	Inner cortical thickness, apical (mm)	Inner cortical thickness, basal (mm)	Trabecular thickness (T), apical (mm)	Trabecular thickness (T), basal (mm)	Trabecular proportion (T/TB), apical	Trabecular proportion (T/TB), basal	Energy absorbed (J)
94	Embedment	5.74	6.20	1.34	0.96	0.85	0.92	3.35	4.06	0.58	0.65	3.90 (0.01)
96	Embedment	5.80	6.34	1.04	0.92	0.99	0.72	3.55	4.55	0.61	0.72	4.08 (0.01)
91	Perforation	4.17	4.05	0.71	0.62	0.62	0.47	2.95	2.82	0.71	0.70	2.65 (0.01)
96	Perforation	1.92	3.09	0.99	0.92	0.51	0.68	0.51	1.48	0.27	0.48	3.15 (0.0002)

Table 4.2 Projectile behaviour and energy absorption (J) in relation to total bone thickness, thickness of the outer and inner cortical layers and trabecular thickness; data derived from µ-CT using y-z (longitudinal) sections; each thickness measured as close to the wound volume as possible; standard deviation for energy absorbed in parentheses was calculated using the error propagation formula in [5]

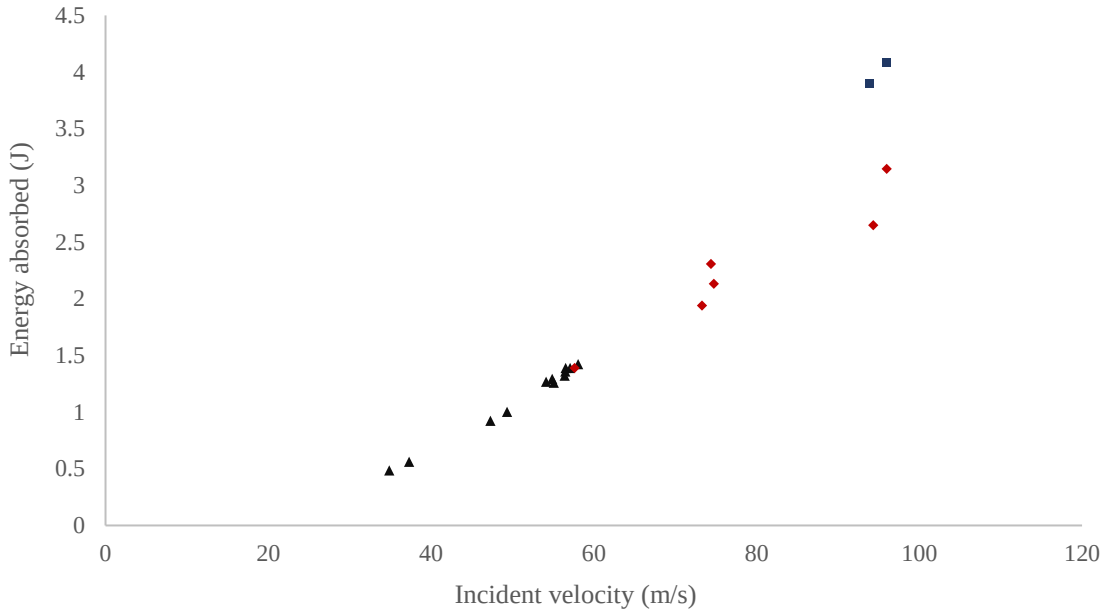

Fig.4.4 Relationship between incident velocity (m/s), energy absorption (J) and projectile behaviour during impact; re-bound (triangles); perforation (diamonds) and penetration (squares).

4.4.1. External and internal fracture morphology

Rebound impacts between 26-58 m/s resulted in splitting and retraction of the periosteum at the impact site. In all impacts between 26 m/s to 37 m/s, damage was entirely limited to soft tissue. Rebound impacts induced between 47 m/s- 58 m/s resulted in partial or full penetration of the outer cortical plate. Penetration was associated with formation of a *cortical entry* bordered by a circular, ring-type crack and a compressed disc of cortex located immediately under the impact location (**Fig.4.5a)**. Compressed cortical discs and ring type cracks were present in the outer cortex of 8 of the 10 rebound impacts between 47 m/s- 58 m/s. The two remaining specimens in this velocity range exhibited no signs of fracture despite one being the highest velocity impact resulting in rebound at 58 m/s.

The flaws giving rise to the ring- type cracks were below the limit of resolution of the µ-CT in all but one specimen, where a crack emanated from a nutrient foramen in the outer cortical plate before taking a circular course and completing a semi-circular fracture at the impact location (**Fig.4.5b**). In cross-section, specimens exhibited various degrees of compression of the cortical disc, ranging from minimal (**Fig.4.5c**; incident velocity 47 m/s, approximately 0.38 mm compression) to just over a millimetre (**Fig.4.5d,** incident velocity 54 m/s**,** approximately 1.19 mm compression). Despite being bent from above downwards, plastic deformation occurred without signs of tensile fracture on the inner aspect of the cortical discs (e.g., **Fig.4.5d**). No specimens exhibited any sign of the disc being displaced downwards as an intact shear plug into the trabeculae. Trabecular cells underneath one heavily compressed cortical disc had undergone a degree of cell collapse, resulting in some densification of the cellular solid (**Fig.4.5d**).

Cross-sectional analysis of the compressed cortical discs revealed that fracture of the sandwich bone was restricted to the outer cortical layer in all but one specimen (discussed below). In cross-section, the cortical walls of the circular cracks were angulated with respect to the cortical surface in cone crack fashion, and presented a relatively straight (e.g. **Fig.4.5e**) or gently curving edge (e.g. **Fig 4.5f**). These angulated fracture surfaces were morphologically identical to those seen in fully formed conoidal wounds and may thus be termed *entry cortical fracture edges* (**Fig.4.5 c-e**). Mean apical and basal angles of these fracture edges together with ranges are presented in **Table 4.1.** Mean apical and basal angles showed a general decrease with velocity, although the highest velocity impacts in group 7 resulted in higher basal angles than those in group 6. There was great variation in the angles both within and across groups and around the perimeter of a single cortical entry. For example, whilst the apical angle in one specimen impacted at 57 m/s was 62.70^{o}, the angle on the left side of the same entry was 45.59^{o}. Angulation of the entry cortical fracture edge was evident in a perforated specimen where the impact site consisted entirely of cortical bone and was only 0.9 mm thick at its thinnest point.

When internal cracking was restricted to the outer cortex, the angulated cracks were open and their formation must therefore have involved a tensile (*mode 1*) cracking component (**Fig.4.5c-f**). An additional in-plane shear (*mode 2*) component to failure of the cortical discs was indicated in some specimens by a slight downward displacement of their lateral fracture surfaces with respect to the entry cortical fracture edge (**Fig.4.5e**, arrow**).** In one specimen, an angulated crack without associated in-plane shear was observed (**Fig.4.5f**, arrow), suggesting that shear, if it occurs, must follow initial crack opening under tension. Fracture morphology in the outer cortices was thus suggestive of mode 1 or mixed mode 1-2 cracking processes if shear was operative during the impact event.

Two impacts resulted in projectile embedment in the sandwich bone. Although these specimens represented difficult samples for µ-CT scanning with the projectiles left *in situ*, scans without removing the spheres to preserve fracture integrity captured details of the penetration process. In section, angulated entry cortical fracture edges were observed in both impacts (**Fig.4.5g-h**). Neither specimen exhibited an intact cortical shear plug beneath the projectile. Instead, the cortical disc in both cases had been fractured and displaced laterally by the projectile with the fragments so formed remaining in close proximity to the outer cortical layer from which they were derived. Trabecular cell collapse and associated densification of the cellular solid occurred in both impacts but was particularly prominent in the 91 m/s embedment (**Fig.4.5h,** labelled D). Tensile failure of the inner cortical plate was observable in the 96 m/s impact as a vertically orientated crack approximately in-line with the centre of the embedded sphere (**Fig.4.5h**). The latter specimen exhibited a clear internal conoidal morphology despite lack of projectile exit. Bisected trabecular cells consistent with a tensile fracture crossing from one cell edge to another were present on the right of the conoidal volume (**Fig.4.5h**, arrows). The large separation of the lower right portion of the conoidal volume from the parent bone appears to have occurred as the projectile compressed the densified trabecular bone downwards (**Fig.4.5h**).

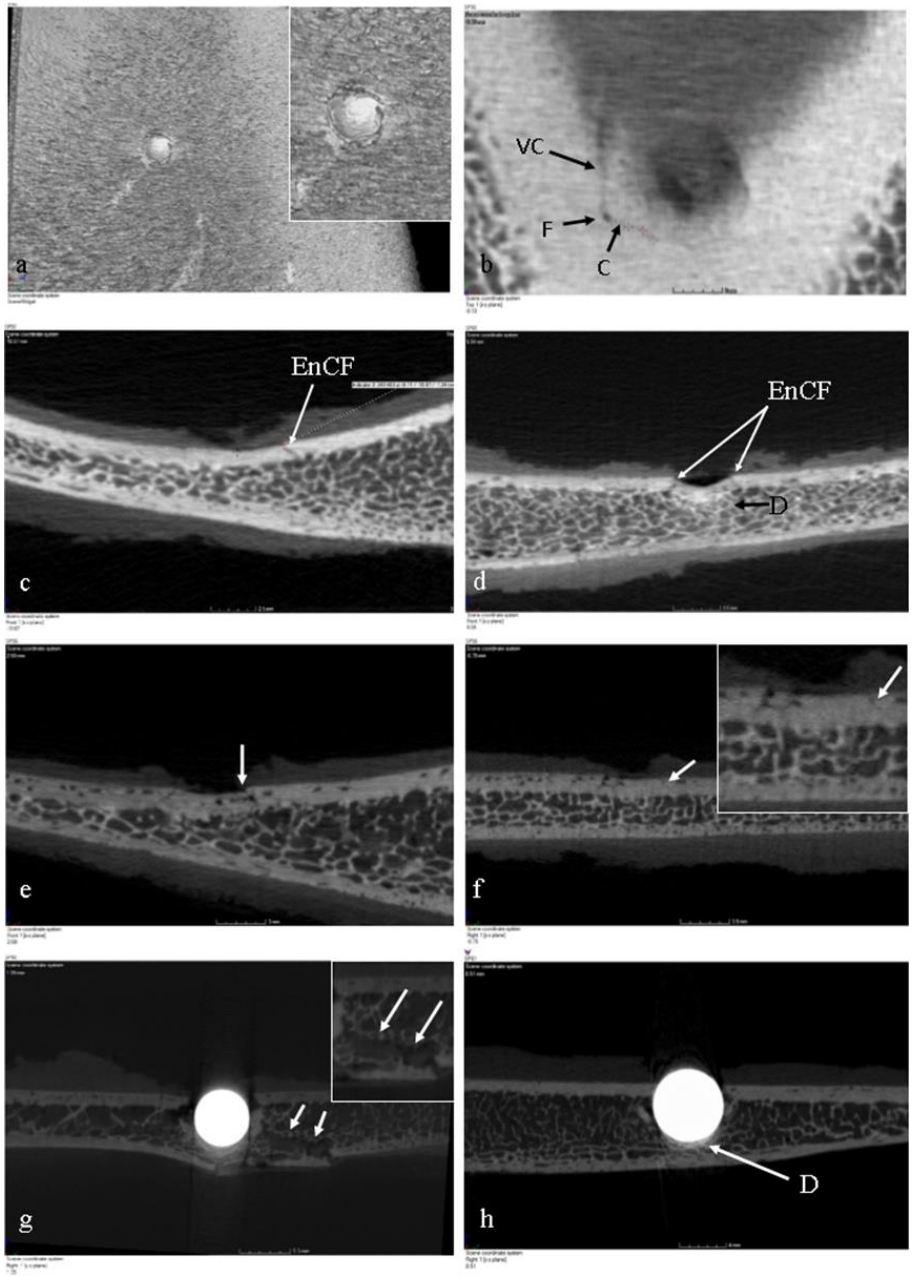

Fig.4.5 µ-CT cross-sections of compressed cortical discs and two projectiles embedded *in-situ***; a,** example of compressed disc of cortical bone at the impact site; **b**, ring crack (C) originating from nutrient foramen (F) with vascular canal (VC) running vertically; c, transverse section of ring crack in *b* showing incipient conoidal wound formation with the presence of an angulated entry cortical fracture edge (EnCF); note minimal compression of the cortex under the impact point; **d**, example of cortical disc showing more extensive compression with some densification (D) of the trabecular cells; note bilateral angulation of the EnCF and crack opening adjacent to the compressed disc; **e**, downward movement of the lateral portion of a compressed cortical disc in relation to the EnCF, indicating a mode 2 (in -plane shear) failure component; **f**, example of mode 1 tensile failure without evidence of in plane shear; **g**, cross-section of projectile embedment with projectile in-situ; wound exhibits bilateral angulation of the EnCF with the cortical disc having fractured in the mid-line and displaced laterally; note formation of a conoidal wound volume despite lack of projectile exit, tensile fracture of inner cortical plate and evidence of crack hopping one cell edge to another (white arrows); **h**, cross-section of second projectile embedment showing bilateral angulation of the EnCF, midline fracture of the cortical disc and densification (D) of the trabecular cells

Four impacts, at 57 m/s, 73 m/s, 74 m/s and 75 m/s, respectively, resulted in the formation of tri-layered bioceramic conoids (**Fig.4.6 a-h**). At 57 m/s, rebound impact left a structurally intact conoidal volume; fragmentation in the three higher velocity perforating impacts resulted in the retention of fragmentary components only. In all cases, the cortical disc derived from the outer cortex was still present in either intact or partially intact form and clearly formed the roof of the conoid. In the rebound impact, this conoidal roof had been compressed downwards without tilting into the trabecular layer, where it contrasted starkly with the spongy bone around it (**Fig.4.6a**). The conoid remained partially attached at one edge to the inner cortical layer, but translaminar fracture had otherwise separated it from the parent bone. Angulated cone fracture propagation without deviation through the sandwich layers was apparent and resulted in a distinct part-counterpart relationship between conoid and conoidal wound (**Fig.4.6, a-c**). In section, the outer cortical layer of this conoid was compressed by approximately 1.05 mm and in one part a delamination in the outer cortical layer was visible (**Fig.4.6c**). In this region, the upper border of the entry cortical fracture edge exhibited little to no angulation and the conoidal crack flared approximately mid-depth in the trabecular layer (**Fig.4.6c**, arrow). The relationships between the fracture morphology of this specimen and a typical conoidal perforating wound are illustrated in more detail in **Fig.4.6b**. Despite formation due to rebound impact, this specimen had a cortical entry (CE) and cortical exit (CEx) and a fully formed internal bevel (IB). The inner cortical plate in this specimen had failed in tension, resulting in the production of radial fractures emanating from a central point in a stellate pattern (**Fig.4.6d,** thin arrows). These radial fractures arrested at the exit cortical fracture edge, which must therefore have formed first (**Fig.4.6d**, thick arrow). Stellate fracture was detectable in cross-section as an angulated crack in the inner cortical plate (**Fig.4.6b**, labelled S).

In both the 73 m/s and 75 m/s impacts the fragmentary conoidal volume was tilted and compressed below the inner cortical layer (**Fig.4.6, e-h**). The conoidal structure exhibited better preservation in the 75 m/s impact (**Fig.4.6, e-g**). Viewed from above, the cortical roof of the conoid was visible through the cortical entry wound (**Fig.4.6e**). The conoid fragments remained attached to the inner cortex on one side (**Fig.4.6f**) and exhibited a tensile fracture that bisected it into two halves. Adjustment of the cross-sectional plane so that it was perpendicular to the displaced three-layered structure confirmed its status as a partial conoid with stellate fracture (**Fig.4.6g**). In the 73 m/s and 74 m/s impacts, the cortical disc forming the roof of the fragmentary conoid was again visible through the cortical entry wound, with the most intact morphology resulting from the 73 m/s impact (**Fig.4.6h**, CR). The presence of a fragmentary conoid in the latter is demonstrated well in cross-section, where both upper and lower cortical components of the structure are readily apparent (**Fig.4.6h**). A single trabecular connection between cortical layers in both the 73 m/s and 74 m/s specimens confirmed that the structures consisted of an entire tri-layered segment of sandwich bone (see **Fig.4.6h**, Tr).

Two higher velocity impacts at 91 m/s and 96 m/s resulted in perforation without retention of any tri-layered fragments. In these specimens, inner cortical plate fragments exhibited part-counterpart relationships with the exit cortical fracture edge and retained some attached trabeculae (**Fig.4.6, i**, **j**).

These fragments were therefore identical to the lower portion of the intact bioceramic conoid illustrated in **Fig.4.6, a-c**, with their upper parts having been fragmented and ejected. In the 91 m/s impact, some parts of the section through the conoidal wound presented a cleanly fractured edge on one side but exhibited protrusion of the trabeculae into the conoidal wound volume on the other due to alteration in the path of translaminar fracture (**Fig.4.6i,** arrow).

4.4.2. High-speed footage of the outer cortical plate

Front on footage of impact at approximately 57 m/s was obtained for four dissected specimens. In this series, rebound occurred in three cases and embedment in the fourth. In all four specimens impact resulted in a deformation pulse causing vibration at the free specimen edges. In two of the rebound impacts and the embedment, projectile impact resulted in a pulse of elastic deformation in the cortex immediately around the impact point, with rebound occurring during the recoil phase of cortical deformation. Estimated rebound times at approximately 58 m/s, taken as the time difference between the frames capturing initial contact and retrograde movement, were 227.23 μs, 227.24 μs and 136.34 μs, respectively. During rebound impacts, projectiles partially penetrated the outer cortex (**Fig.4.7b**), with the compressed cortical discs so formed visible as a whitened region of cortex (**Fig.4.7c**). μ-CT analysis of the specimen illustrated in **Fig.4.7a-c** revealed a vertically orientated fracture in the cortical disc just adjacent to the mid-line (**Fig.4.7d**). Cross-sectional fracture morphology revealed bilateral angulation of the entry cortical fracture edges (**Fig.4.7e, f**), identical in form to that observed in impacted fleshed specimens; densification of the trabeculae was also apparent (**Fig.4.7f,** labelled D**)**. In the penetrated specimen, the projectile fractured the outer cortical layer before moving in a retrograde direction and embedding at a depth of approximately half its diameter in the sandwich bone.

Impact at approximately 150 m/s in two defleshed specimens resulted in full perforation, with a deformation pulse visible at the specimen edges in only one of these. Unlike the 58 m/s impacts, the cortex around the impact site showed no visible signs of elastic deformation. Cortical behaviour under the projectile was captured in one specimen, where a semi-circular section of fractured cortex was visible to the right of the projectile (**Fig.4.7g**). Rather than descending with the projectile through the sandwich structure as a shear plug, this fragment folded downwards as the projectile completed perforation (**Fig.4.7h**). Such behaviour was consistent with this fragment being part of the originally circular cortical roof of a bioceramic conoid, identical in morphology to the fractured discs resulting from both embedding (**Fig.4.5, g and h**) and rebound impact (**Fig.4.7 d-f**). Fracture and ejection of the cortical roof left an approximately circular cortical entry (**Fig.4.7i**).

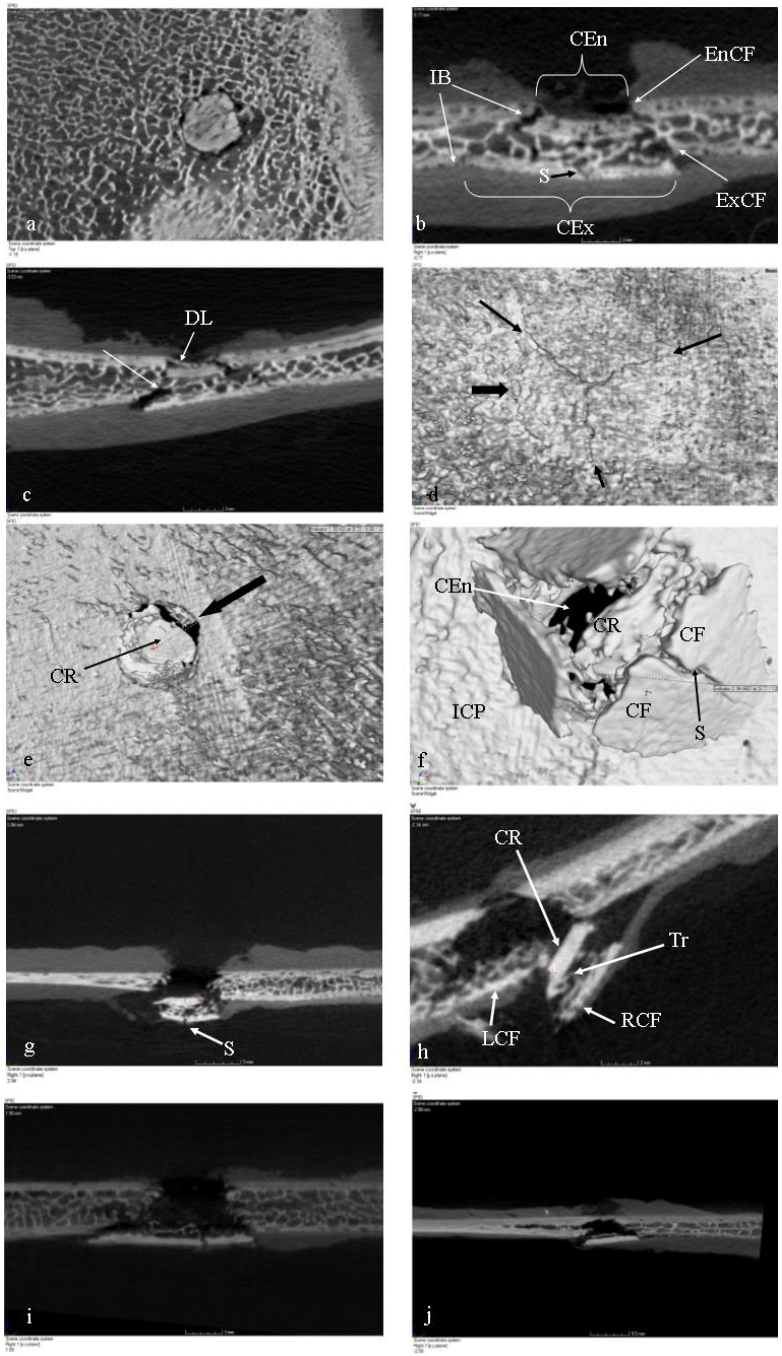

Fig.4.6 Bioceramic conoid morphology; *a-d* intact conoid produced by a 57 m/s impact; **a**, cortical roof of conoid compressed into the trabecular layer; **b**, longitudinal section of conoid showing relationships with typical perforating conoidal projectile wound; CEn, cortical entry; CEx, cortical exit; EnCF, entry cortical fracture edge; ExCF, exit cortical fracture edge; IB, internal bevel; S, stellate fracture; **c**, transverse section showing delamination (DL) of upper cortical layer and flaring of the conoidal crack within the trabeculae (arrow); **d**, inner cortical plate showing exit cortical fracture edge (large black arrow) and radial fractures of stellate fracture pattern (small black arrows); **e-g**, fragmented conoid produced by a 75 m/s impact; **e**, view through cortical entry showing depressed cortical roof of conoid and entry cortical fracture edge (arrow); **f**, conoid fragment viewed from inner cortical plate; CR cortical roof; CF, cortical floor; S, stellate fracture; CEn, cortical entry; ICP, inner cortical plate; **g**, cross-section perpendicular to the conoid fragment visible in **f**; **h**, fragmented conoid produced by 73 m/s impact; CR, cortical roof; Tr, trabecular connection between cortical roof and cortical floor of fragmentary conoid; LCF, left cortical floor and RCF, right cortical floor corresponding to fragments visible in **Fig.8 j-l**; recoil resulted in the cortical roof (CR) being in line with the left cortical floor (LCF); **i-j**, structures consistent with being the inner cortical vestiges of bioceramic conoids formed by 91 m/s (**i**) and 96 m/s impacts (**j**)

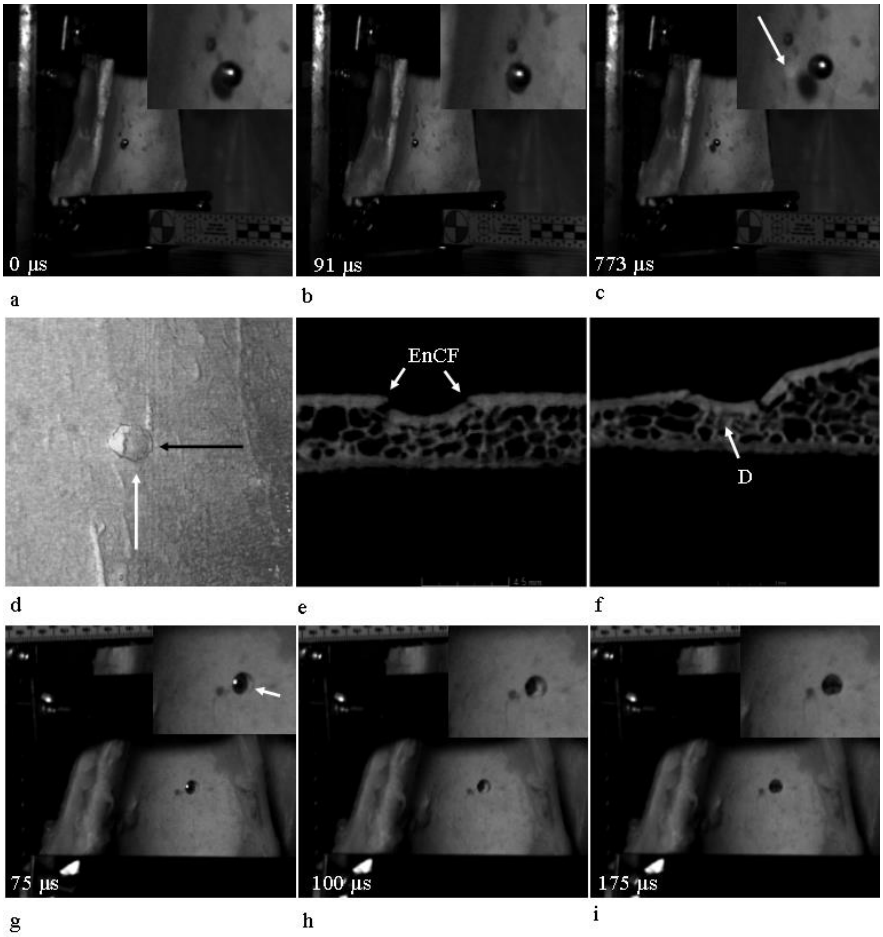

Fig.4.7 Rebound and perforating impacts to defleshed outer cortical plates; **a-c**, rebound impact resulting from impact at approximately 57 m/s; **a**, pre-impact; **b**, maximum projectile penetration; **c**, rebound revealing compressed cortical disc (arrow); **d-e**, µCT images of specimen in **a-c**; **d**, three-dimensional view of compressed cortical disc revealing vertical fracture; **e**, section of impact area at approximately mid-cortical entry (direction of section indicated by black arrow in **d**); note angulated entry cortical fractures edges (EnCF) and compression of cortical disc; **f**, section through region of vertical fracture within the cortical disc (direction of section indicated by white arrow in **d**); note densification of trabeculae (D); **g-i**, perforating impact at approximately 150 m/s, indicated times are from the pre-impact frame (not shown); **g**, projectile has perforated the outer cortical plate, which has fractured and displaced downwards (arrow in enlargement); **h**, projectile has completed exit of the outer cortical plate, revealing fractured and displaced cortical disc still in the process of fragmentation and ejection; **i**, final morphology of cortical entry

4.4.3. High-speed footage of the inner cortical plate

There was no evidence of an intact shear plug arising from the outer cortical layer in any of the impact events. In contrast, observation of the inner cortical plate revealed a common fracture process between impacts that resulted in intact or fragmentary conoid production and higher velocity impacts that did not. During formation of an intact bioceramic conoid (illustrated in **Fig.4.8, a-c**), the tri-layered structure elevated with respect to the inner cortical plate, and the conoid floor simultaneously underwent stellate fracture due to high tensile stresses there (**Fig.4.8a**). As impact proceeded, the conoid then underwent recoil in relation to the exit cortical fracture edge (**Fig.4.8c**). The time taken to reach maximal elevation, measured from the frame prior to damage initiation, was 175 µs; the total time taken to reach maximum recoil was 600 µs.

Perforating impact resulting in partial fragmentation of a bioceramic conoid is illustrated in **Fig.4.8, d-f**. Impact again resulted in elevation of the conoid floor and stellate fracture (**Fig.4.8e**, arrow). Subsequently, the inner cortical plate fragments formed by stellate fracture then went through a process of elevation and eversion, resulting in their trabecular surfaces facing outwards (**Fig.4.8.f**), with some then being ejected. Projectile exit occurred through the aperture created by the inner cortical plate fragments before full eversion. The sequence of elevation, stellate fracture, fragment eversion and ejection occurred in the absence of residual tri-layered fragment morphology at 91 m/s and 96 m/s (**Fig.4.6i, j**), and was also seen in dissected specimens impacted at approximately 150 m/s where fragments were ejected. A sequence of images of capturing the exit process is provided for a defleshed specimen impacted at approximately 150 m/s in **Fig.4.8, g-i**.

Retained inner cortical plate fragments underwent considerable dynamic movement which in one case resulted in unusual fragment positions after impact (**Fig.4.8 j-l).** In this specimen, also illustrated in cross-section in **Fig.4.6h**, two large conoid fragments were produced to the left and right of the cortical exit, with the right fragment retaining the tri-layered morphology. During impact, the conoid elevated and underwent stellate fracture (**Fig.4.8.j**, arrow). Although soft tissue partially obscures the bone in the high-speed footage ((**Fig.4.8k)**, a feature consistent with the left fragment (black arrow) could be seen elevating adjacent to the right tri-layered fragment (white arrow). Subsequent to projectile exit, fragment recoil resulted in the right fragment covering the left (**Fig. 4.8l**). In cross-section this process resulted in the outer cortex of the tri-layered fragment being level with the inner cortex of the left fragment (**Fig.4.6h**).

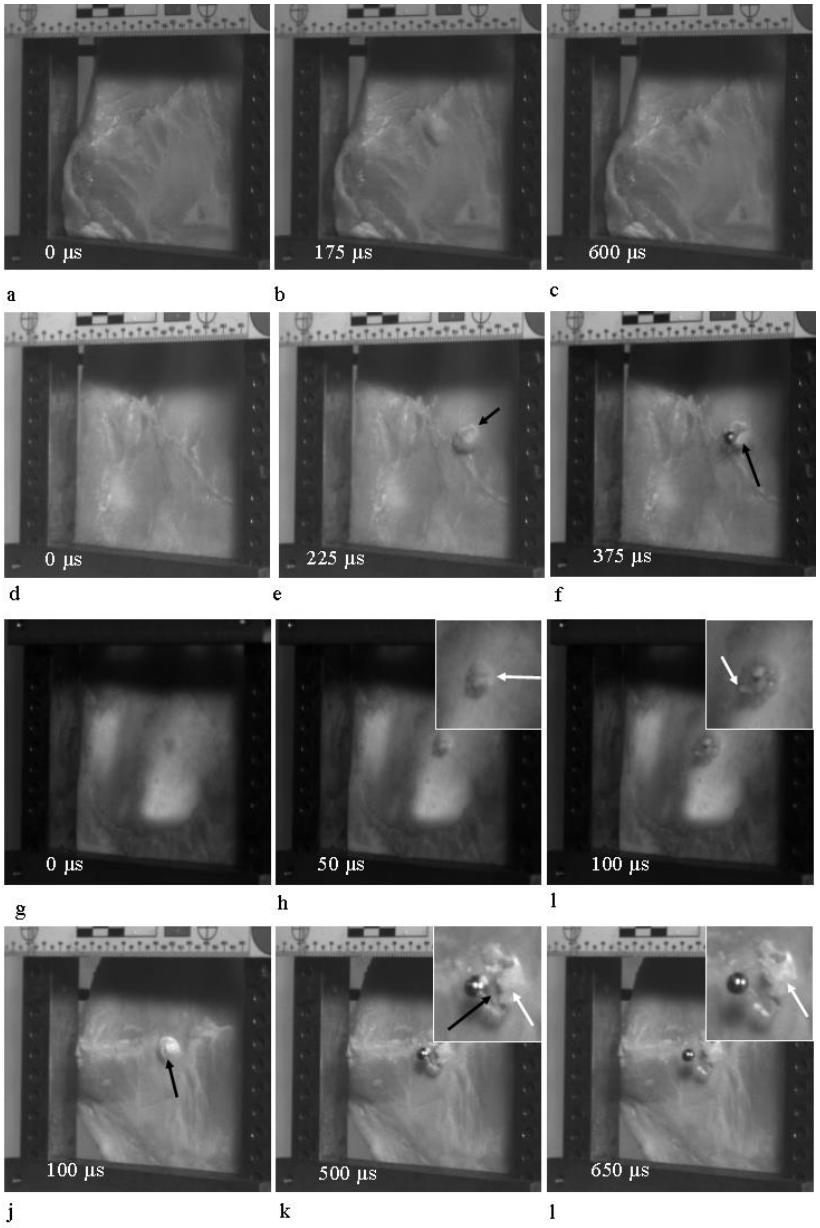

Fig.4.8 High-speed footage of conoid behaviour viewed from inner cortical plate; all times from frame prior to visible damage; **a-c**, damage sequence capturing intact bioceramic conoid behaviour during 57 m/s re-bound impact; **a**, pre-impact; **b**, maximum conoid elevation; **c**, final damage pattern resulting from recoil of conoid; **d-f**, 75 m/s perforation that resulted in partial conoid fragmentation; **d**, pre-impact; **e**, early elevation of conoid floor with stellate fracture (arrow) forming inner cortical plate fragments; **f**, eversion of inner cortical plate fragments (arrow); **g-i**; perforation sequence in dissected specimen, approximately 150 m/s; *g*, pre-impact; **h**, elevation and stellate fracture (arrow); **i**, inner cortical plate fragment elevation and eversion (arrow); **j-l**; dynamic movement of conoid fragments during a 73 m/s impact; **j**, stellate fracture of conoid floor (arrow) with central aperture between inner cortical plate fragments; **k**, enlargement shows left cortical floor fragment (black arrow) adjacent to right cortical floor fragment (white arrow); **l**, enlargement shows right fragment has recoiled over left fragment resulting in sectional view visible in **Fig.4.6h**.

4.5. Discussion

Projectile perforation is a complex event and the exact mechanisms involved depend upon multiple factors such as target material properties, projectile design, and incident velocity [20]. Failure modes can also compete during penetration, with the ultimate mechanism determined by material and projectile characteristics [31]. The complex hierarchical organisation of bone also dictates that failure can occur at multiple length scales, introducing a complexity to failure processes that is not typical of synthetic composites [32]. In order to test the plug and spall and cone crack hypotheses, the present study therefore utilised a simplified experimental model consisting of non-human sandwich bones impacted with spherical projectiles. Low-velocity impacts induced using this system successfully captured the genesis of conoidal wounds, at least with the projectile-target combination utilised. Impacts between 26-96 m/s resulted in rebound, penetration and perforation, with projectile embedment apparently associated with greater bone thicknesses. Multiple aspects of fracture morphology induced by this range of projectile behaviours did not substantiate the contention that a cortical shear plug participates in perforation and instead were consistent with a tensile, cone cracking process resulting in production of tri-layered bioceramic conoids.

The initial phase of wound formation in rebound impacts below 58 m/s was the production of permanently compressed discs of cortical bone in the outer cortex identical in form to those described in the compact bone of deer femora subjected to sub-100 m/s impact [25]. Although seemingly consistent with shear plug formation when present in sandwich bones, cross-sectional fracture morphology revealed no evidence of these discs being driven through the remaining two sandwich layers, as predicted by the plug and spall hypothesis [4, 7, 18, 19]. In two embedding impacts and high-speed footage of one perforation, the cortical disc underwent fracture in the approximate mid-line and then underwent downward displacement during projectile passage. In four specimens, the cortical disc clearly formed the roof of a bioceramic conoid that displaced downwards as a unit consisting of all three sandwich layers. Significantly, the intact bioceramic conoid induced at 57 m/s shared multiple features with the plugs described in human material by Murphy et al [22], Murphy et al [23] and Bird and Fleishman 2015 [24]. Shared structural features included stellate fracture of the inner cortical plate, compression of the outer cortical plate, minimal to no trabecular compression and part-counterpart relationship with the internal bevel in the parent bone. Such morphological correspondence is highly indicative of common fracture processes in human and pig sandwich bones subjected to projectile impact.

A central component of the plug and spall hypothesis is that perforation of the outer cortical layer and bevel formation are separate events, with bevel formation suggested to occur during projectile exit [e.g. 3, 7, 18, 33, 34]. However, the present study confirms that bevel formation occurs *in the absence of projectile exit*; indeed, a fully formed conoidal wound was produced by a rebound impact. Numerous lines of evidence now converge to support the hypothesis that production of tri-layered bioceramic conoids is central to conoidal wound formation regardless of incident velocity. In addition

to morphological correspondence between experimentally and non-experimentally produced bioceramic conoids, cross-sectional fracture morphology induced by impacts below 100 m/s is identical to that described for impacts between 150-897 m/s [5].

The fragmentary nature of three of the conoids formed in the current experiment, coupled with identical deformation and fracture behaviour in perforated specimens lacking conoids, strongly suggests that their absence subsequent to higher velocity impacts is not due to lack of formation but to their complete comminution and ejection, as predicted by the cone crack hypothesis [5]. Incident velocity apparently need not be great to fragment the conoidal volume, with comminution occurring between 73 m/s-75 m/s. Comminution appears to initiate with midline fracture and downward displacement of the conoidal roof. Subsequently, trabecular cells undergo the process of cell collapse resulting in densification of the trabecular layer. Finally, projectile exit elevates the inner cortical plate fragments and the majority of the conoidal volume is then ejected. Interestingly, the formation of intact conoids highlights a notable difference between biological and synthetic sandwich structures; while outer and inner laminae are perforated separately in the latter [35], intact conoid formation does not involve perforation of *either* layer.

Previous case reports have described conoidal wounds induced by low-velocity impact that are macroscopically identical to those induced at high velocity [36-38], raising a significant diagnostic challenge. The current study indicates that increasing velocity imparts a sequence to conoid behaviour that may assist in such diagnoses. Production of intact conoids was rare, with total fragmentation of the conoidal structure being the norm above 90 m/s. Conoid vestiges produced by impacts in the 73-75 m/s range consisted of variably comminuted outer and inner cortical layers with retained trabecular connections. As velocity increased, conoid collapse from above downwards resulted in loss of the tri-layered morphology, leaving retained inner cortical plate fragments with attached trabeculae as the only vestige of their formation. This morphological data supports the contention of Bird and Fleishman [24] that the retention of intact conoids (termed “plugs” in their article) is consistent with a relatively low-velocity impact event; however, it extends the diagnostic value of these features down to the *fragment* level. Accordingly, in cases where attached fragments or bony ejecta are retained it may prove beneficial to search for the vestiges of a tri-layered morphology.

Numerous features of fracture morphology were consistent with a cone cracking failure mode. The first stage in cone crack formation during indentation or impact of brittle materials is the initiation of a surface crack from flaws at or slightly outside the contact radius of the projectile in the region of highest tensile stress; this crack then curves around in a circle to produce a *ring crack* [39-41]. While the origin of the circular crack in the outer cortex was not captured in all specimens, in one a fracture appeared to originate from a nutrient foramen located in the outer cortex before following a circular path delineating the indented cortical disc. Although a larger sample capturing the origin of such cracks is required to draw definitive conclusions, fracture morphology in this case was inconsistent with a shear failure mode and instead suggested the cortical disc was formed as a result of ring cracking.

During cone crack formation, increasing contact pressure from the projectile results in the ring crack flaring to form a cone within the tensile stress field [41]. Similarly, in the present series all fractured specimens exhibited crack angulation, initiating either in the outer cortical layer, the trabecular layer, or both through different parts of the cross-section. Significantly, these angulated cracks were open and in close approximation suggesting the predominance of a tensile, crack opening failure mode. An additional tensile contribution to wound formation appears to arise when the projectile compresses the conoidal volume downwards relative to the trabecular fracture margin, a process that enhances separation of the conoid from the parent bone.

The establishment of projectile trajectory is often a critical aspect of medicolegal investigations [42], with the results of such analyses potentially influencing the outcome of criminal trials [2]. In this regard, the findings presented herein have considerable significance for our understanding of the factors underlying bevel morphology and thus the information that can be gathered from it. At present, prevailing theory indicates that regions of asymmetrical bevelling reflect the trajectory of the projectile [2, 8]. However, work addressing this proposed relationship with human skeletal material reported a poor correlation between these variables [9]. Bevel asymmetry was also found to be more common than bevel symmetry in experimentally induced perpendicular projectile wounds in pig sandwich bones [5]. The current analysis suggests this trend extends below 100 m/s, with 4/6 perforating wounds between 58-96 m/s classified as having an asymmetrical bevel despite resulting from perpendicular impact.

Whilst projectile trajectory in all likelihood does play a part in determining bevel symmetry, the finding that bevel formation occurs in the absence of perforation indicates it is but one of a number interacting factors underlying bevel shape. The production of bioceramic conoids in the present study confirms that a principle determinant of bevel symmetry must be the path of the translaminar fracture through the sandwich bone subsequent to its origin in the outer cortex. This path will be influenced by material factors such as Poisson's ratio, which is a key determinant of cone crack angle [43], the orientation of the trabecular struts in relation to the advancing crack tip [5] and the presence and distribution of cortical features altering crack direction, such as the cement sheaths of secondary osteons [32]. Loading rate may also play a part in fracture path, with cracks at lower loading rates tending to follow tortuous routes through regions of least resistance and cracks at high loading rates showing no such preference [44-46]. Further quantitative analyses of bevel symmetry and the potential influence of impact angle on this variable are required to quantify the accuracy of bevel shape in trajectory determinations.

The position of retained bone fragments is another indicator that has been utilised to establish trajectory, based on the assumption that their orientation results from direct interaction with the projectile [47]. However, unusual fragment positions can also enhance the challenge of trajectory determination and how the wound is interpreted in general. For example, Kieser [48] reported a keyhole entry with the outer cortical layer adjacent to the cortical entry compressed inwards rather than outwards as expected for a keyhole entry wound [49]. The results of high-speed videography may help explain such unusual

fragment placements. Observation of impact revealed that kinetic energy imparted to attached fragments results in their dynamic motion and oscillation after the projectile has exited the specimen. Such fragment behaviour in one impact event resulted in the outer cortical layer of one conoid fragment residing below the inner cortical layer of another. When considering fragment position in trajectory determination it must therefore be kept in mind that their final placement is not necessarily due to a *direct* interaction with the projectile; rather, it might represent their resting position after dynamic movement has ceased.

The presence and location of bevelling is fundamental to the determination of the entry or exit status of projectile wounds [1, 7], and in this regard it is significant that some authors have noted its absence in thin areas of bone that lack a trabecular layer [6, 9, 34]. While the trabecular fracture margin and exit cortical fracture edge will be absent in such bones, the translaminar fracture resulting in bevel formation typically begins as an angulated crack in the outer cortical layer. This angulated crack was restricted to the outer cortical layer in 7 specimens and was also present in a perforated specimen consisting entirely of cortical bone, indicating it forms independently of the trabecular lamina. The possibility therefore arises that cross-sectional analysis may be able to identify the entry or exit status of wounds in thin cortical bone that lacks bevelling. Interestingly, images of angulated entry cortical fracture edges have been captured using Multidetector Computed Tomography (MDCT) [50], suggesting they can be detected *in-situ* during post-mortem analysis.

While the present work focused specifically on sandwich bones, it is important to consider conoidal fracture in a wider skeletal context; at present, it is not clear if this mechanism is responsible for conoidal wound formation during impact in all bone types. For example, Huelke et al [51, 52] attributed conoidal wound formation in the femoral epiphyses to temporary cavitation of fluid located in the interstices of the trabeculae. Although the formation and dynamic behaviour of bioceramic conoids was captured by the current experimental model, further research is required to confirm that incident kinetic energy drives a process of translaminar fracture and bioceramic conoid formation in human material. Finally, whilst spherical projectiles are ideal for eliminating confounding variables such as deformation on the impact process, future analyses should seek to address the influence of projectile design on perforation mechanisms.

Ethical approval

This study was fully approved by the ethics committee of Cranfield University.

Conflict of interest

The authors report no conflict of interest.

Acknowledgements

We are indebted to Alan Peare for running the compressed airgun and high-speed cameras and also for his technical input. We would also like to extend our sincere thanks to Gary Cooper for the design and manufacture of the clamping apparatus.

4.6. References

[1] Berryman HE, Symes SA (1998) Recognising gunshot and cranial trauma through fracture interpretation. In Reichs, K J (ed) Forensic Osteology: advances in the identification of human remains. Charles C Thomas Publishers, Springfield, pp 333-352

[2] Rhine and Curran (1990) Multiple gunshot wounds to the head: An anthropological review. J Forensic Sci 35 (3): 1236-1245

[3] Komar DA, Buikstra JE (2008) Forensic anthropology: contemporary theory and practice. Oxford University Press Inc., New York.

[4] Kimmerle EH, Baraybar J P (2008). Skeletal trauma: identification of injuries resulting from human rights abuses and armed conflict. CRC Press, Florida.

[5] Rickman JM, Shackel, J (2018) A novel hypothesis for the formation of conoidal wounds in sandwich bones. Int J Legal Med (2018) https://doi.org/10.1007/s00414-018-1946-x

[6] Di Maio VJM (1999) Gunshot wounds: practical aspects of firearms, ballistics and forensic techniques. CRC Press, Florida

[7] Symes SA, L'Abbé EN, Chapman EN, Wolff I, Dirkmaat DC (2012) Interpreting traumatic injuries to bone in medicolegal investigations. In Dirkmaat DC (ed) A companion to forensic anthropology, Wiley- Blackwell Publishing, West Sussex

[8] Spitz WU (2006) Injuries by gunfire. In Spitz WU, Spitz DJ, Clark R (eds) Spitz and Fisher's medicolegal investigation of death: guidelines for the application of pathology to crime investigation, Charles C Thomas Publishers, Springfield. Available from: Proquest Ebook Central (accessed 8.8.17)

[9] Quatrehomme G, İşcan MY (1998) Analysis of bevelling in gunshot entrance wounds. Forensic Sci. Int. 93: 45-60

[10] Rickman JM, Smith MJ (2014) Scanning Electron Microscope analysis of gunshot defects to bone: an underutilised source of information on ballistic trauma. J Forensic Sci 59 (6): 1473-1486 https:// doi.org 10.1111/1556-4029.12522

[11] Olszta MJ, Cheng X, Jee SS, Kumar R *et al* (2007) Bone structure and formation: a new perspective. Mater Sci Eng R Rep 58: 77-116

[12] Rho JY, Kuhn-Spearing L, Zioupos P (1997) Mechanical properties and the hierarchical structure of bone. Med Eng Phy 20: 92-102

[13] Fratzl P, Weinkamer R (1998) Nature's hierarchical materials. Prog Mater Sci 52: 1263-1334

[14] Weiner S, Wagner HD (1998) The material bone: structure-mechanical function relations. Annu Rev Mat Sci 28: 271-298

[15] Gray H (1997) Gray's Anatomy. The Promotional Reprint Company, London

[16] Hull D (1999) Fractography: observing, measuring and interpreting fracture surface topography. Cambridge University Press, Cambridge

[17] Christensen AM, Passalacqua NV, Bartelink EJ (2014) Forensic anthropology: current methods and practice. Academic Press, Oxford

[18] Peterson BL (1991) External beveling of cranial gunshot entrance wounds. J Forensic Sci 36 (5): 1592-1595

[19] Kieser JA, Tahere J, Agnew C et al (2011) Morphoscopic analysis of experimentally produced bony wounds from low velocity ballistic impact. Forensic Sci Med Pathol 7:322-332 https:// doi.org 10.1007/s12024-011-9240-y

[20] Zukas JA (1982). Penetration and perforation of solids. In Zukas JA, Nicholas T, Swift HF, Greszczuk LB, Curran DR (eds) Impact dynamics, John Wiley and Sons, Inc., USA, pp 155- 214

[21] Zaera R, Sánchez-Gálvez V (1998) Analytical modelling of normal and oblique ballistic impact on ceramic/ metal lightweight armours. Int J Impact Engng 21 (3): 133-148

[22] Murphy MS, Gaither C, Goycochea E, Verano JW, Cock G (2010) Violence and weapon-related trauma at Puruchuko-Huaquerones, Peru. Am J Phys Anthropol 142:636-649

[23] Murphy MS, Spatola B, Weathermon R (2014) Allies today, enemies tomorrow: a comparative analysis of perimortem injuries along the biomechanical continuum. In Martin DL, Anderson CP (eds) Bioarchaeological and forensic perspectives on violence: how violent death is interpreted from skeletal remains, Cambridge University Press, Cambridge, pp 261-288

[24] Bird CE, Fleischman JM (2015) A rare case of an intact bone plug associated with a gunshot exit wound. J Forensic Sci 60 (4): 1074-1077

[25] Kieser DC, Riddell R, Kieser JA, Theis J, Swain MV (2013) Bone micro-fracture observations from direct impact of slow velocity projectiles. J Arch Mil Med 2(1): e15614 https:// doi.org 10.5812/jamm.15614

[26] Amato JJ, Lawrence BJ, Lawson NS, Norman R (1974) High velocity missile injury. Am J Surg 127: 454-459

[27] Amato JJ, Syracuse D, Seaver PR, Rich N (1989) Bone as a secondary missile: an experimental study in the fragmenting of bone by high velocity missiles. J Trauma 29 (5): 609-612

[28] Ragsdale BD, Josselson A (1988) Experimental gunshot fractures. J Trauma 28 (No.1 suppl): S109-S115

[29] Thali MJ, Kneubuehl BP, Zollinger U, Dirnhoffer R (2002) A study of the morphology of gunshot entrance wounds, in connection with their dynamic creation, utilising the "skin-skull-brain" model. Forensic Sci Int 125: 190-194

[30] Goldsmith W (1960) Impact: the theory and physical behaviour of colliding solids. Edward Arnold Publishers, London

[31] Wilkins ML (1978) Mechanics of penetration and perforation. Int J Engng Sci 16: 793-807

[32] Currey J D (2002) Bones: structure and mechanics. Princeton University Press, New Jersey

[33] Dodd MJ (2006) Terminal ballistics: a text and atlas of gunshot wounds. CRC Press, Taylor and Francis Group, Florida

[34] Loe L (2009) Perimortem trauma. In Blau S, Ubelaker DH (eds) Handbook of Forensic Anthropology and Archaeology, Left Coast Press, California, pp 263-283.

[35] Abrate S (1998) Impact on composite structures. Cambridge University Press, Cambridge

[36] Vermeij EJ, Zoon PD, Chang SBCG et al (2012). Analysis of microtraces in invasive traumas using SEM/EDS. Forensic Sci. Int. 214 (1): 96-104

[37] Spatola BF (2015). Atypical gunshot and blunt force injuries: wounds along the biomechanical continuum. In Passalacqua NV, Rainwater CW (eds) Skeletal trauma analysis: case studies in context pp 7-26

[38] Quatrehomme G, Piercecchi-Marti M, Buchet L, Alunni V (2015) Bone bevelling caused by blunt trauma: a case report. Int J Legal Med 130 (3): 771-775 https:// doi.org/10.1007/s00414-015-1293-0

[39] Zeng K, Breder K, Dowcliffe DJ (1992) The Hertzian stress field and formation of cone cracks- I. theoretical approach. Acta Metall Mater 40 (10): 2595-2600

[40] Chen SY, Farris TN, Chandrasekar S (1995) Contact mechanics of Hertzian cone cracking. Int J Solids Structures 2 (3/4): 329-340

[41] Lawn BR (1998) Indentation of ceramics with spheres: a century after Hertz. J Am Ceram Soc 81 (8): 1977-1994

[42] Berryman HE, Gunther WM (2000) Keyhole defect production in tubular bone. J Forensic Sci 45 (2): 483-487

[43] Chaudhri MM (2015) Dynamic fracture of inorganic glasses by hard spherical and conical projectiles. Philos Trans R Soc Lond A 373: 20140135 https:// doi.org 10.1098/rsta.2014.0135

[44] Piekarski K (1970) Fracture of bone. J Appl Phys 41 (1): 215-223

[45] Pope MH, Outwater JO (1972) The fracture characteristics of bone substance. J Biomech 5: 457-465

[46] Pechníková M, Mazzerelli D, Poppa P, Gibelli D, Baggi ES, Cattaneo C (2015) Microscopic pattern of bone fractures as an indicator of blast trauma: a pilot study. J Forensic Sci 60 (5): 1140-1145

[47] Ubelaker DH (1996) The remains of Dr Carl Austin Weiss: Anthropological analysis. J Forensic Sci 41 (1): 60-79

[48] Kieser J (2012) Biomechanics of bone and bony trauma. In Kieser J, Taylor T, Karr D Forensic Biomechanics. John Wiley & Sons, United Kingdom

[49] Dixon DS (1982) Keyhole lesions of the skull and direction of fire. J Forensic Sci 23 (3): 555-566

[50] Harcke HT, Levy AD, Getz JM, Robinson SR (2008) MDCT analysis of projectile injury in forensic investigation. AJR Am J Roentgenol 190 (2): W106-W111

[51] Huelke DF, Buege LJ, Harger JH (1967) Bone fractures produced by high velocity impacts. Am J Anat 120: 123-132

[52] Huelke DF, Harger JH, Buege LJ, Dingman HG, Harger DR (1967) Bone fractures produced by high velocity impacts. J Biomech 1: 97-103

CHAPTER 5, PAPER 4

A quantitative analysis of projectile entry wounds in sandwich bones; impact dynamics and wound morphometrics

John M Rickman*, Dr Jon Painter**, Dr Rachael Hazael***

5.1. Abstract

Projectile injuries to the cranium represent a significant cause of mortality in civilian populations; however, much remains to be understood about the dynamic absorption of energy by the sandwich bones of the cranial vault. The relationship between quantitative aspects of sandwich bone wound morphology and the energetics of impact is also largely unexplored. The present study utilised non-human sandwich bones to generate impact dynamics data using 6 mm spherical projectiles at velocities ranging from 35 m/s to 897 m/s. Wound morphology was quantified by calculating the surface area of missing bone from the cortical entry and cortical exit (bevel); relative exit size was calculated as the ratio between the two. The percentage of energy absorbed by flat bones was found to decrease with increasing velocity according to a power function. A linear relationship was found between incident and residual projectile velocity and between incident and residual projectile kinetic energy, whilst the relationship between velocity and energy absorption was described by a power function. There was a moderate correlation between exit size and velocity and between exit size and energy absorption, but entry size was not influenced by those variables. The significance of the results in relation to synthetic materials, different bone types and existing injury models is discussed.

Cranfield Defence and Security

Cranfield University

Defence Academy of the United Kingdom

Shrivenham, SN6 8LA

*Corresponding author email address: j.m.rickman@cranfield.ac.uk

*Phone: +44 (0) 1793 785531

*ORCID: 0000-002-1188-8805

**Email address j.d.painter@cranfield.ac.uk

**Phone: +44 (0) 1793 785392

***Email address rachael.hazael@cranfield,ac,uk

***Phone +44 (0) 1793 785414

Keywords

Projectile trauma; sandwich bones; impact dynamics; wound morphology; bevelling

5.2. Introduction

Projectile perforation of the cranial sandwich bones due to use of firearms is of considerable significance to forensic and clinical practice, with a mortality rate of 90% reported in civilian settings [1]. This trauma type is also of particular importance to forensic anthropologists; such high mortality rates appear to be coupled with involvement in bone trauma, with one analysis of post-mortem homicide reports finding that 92.6% of ballistic trauma victims exhibited bone wounds [2]. From a clinical viewpoint, a more detailed understanding of the mechanisms underlying ballistic wounding of the cranium will inform treatment protocols and the surgical methods used to repair damaged tissues [3]. The amount of energy lost by a given projectile during the perforation event reveals critical information about how a given material fails during impact [4]. At present, little is known about the relationships between pre-impact or incident velocity and kinetic energy absorption during sandwich bone perforation, or between those variables and wound size and morphology. In addition to the obvious clinical and forensic relevance of this information, such data has considerable significance for the continuing development of synthetic alternatives to bone for projectile trauma experimentation. Although some consider existing synthetic substitutes to be suitably analogous to bone during ballistic impact [5-9], recent research has questioned the biofidelity of synthetic materials when subject to impacts of various loading rates [10-12).

During projectile perforation of sandwich bones the absorbed kinetic energy is utilised to perform the mechanical work of fracture, fragmentation and fragment ejection, and it is these processes that produce the final, or *terminal*, fracture morphology. In sandwich bones, the typical terminal morphology is a *conoidal wound*, with the cone flaring in the direction of projectile travel [13]. Previous morphological analysis of such conoidal wounds has indicated that projectile impact at both low and high velocity results in the momentary formation of a tri-layered plug or *conoid* of bone by a process of trans-laminar fracture through the sandwich bone [13], with conoid fragmentation reported to occur above 90 m/s [14]. Determination of critical impact dynamics data is needed to reveal how this wound formation mechanism manifests energetically.

To date, the most extensive series of investigations shedding preliminary light on the energetics of bone penetration are those of Huelke *et al* [15-17] and Harger and Huelke [18], all using human long bones impacted with spherical projectiles fired from a gas gun apparatus. Early findings with 6.35 mm spheres in this series suggested a linear relationship between projectile velocity and kinetic energy absorption during penetration of the distal femur [15]. Later work with the same femoral region demonstrated a quadratic relationship for both 6.35 mm and 10.31 mm spheres, with the larger sphere losing more energy at any given velocity [16]. Results were slightly more complex for femoral shaft penetration, with a quadratic relationship reported for 6.35 mm spheres and a linear relationship for 10.31 mm spheres [17], although penetration of the latter through osteoporotic shafts was also described by a quadratic function. While the amount of energy lost increased in absolute terms with velocity, data

derived from the epiphyseal impacts indicated that the proportion of available kinetic energy lost during perforation decreased with increasing velocity [15, 16]. Subsequent work comparing 6.35 mm steel spheres with 6.35 mm tungsten carbide spheres that were 2.18 times heavier revealed that mass had little effect on the amount of energy expended [18]. In contrast, at identical impact velocities the 10.31 mm spheres always lost more energy and caused more damage than the two smaller spheres, suggesting that calibre is the determining factor in the extent of bone damage [18].

To date, the only study providing kinetic energy absorption data for sandwich bones is that of Tang *et al* [19], who utilised Finite Element Analysis (FEA) to simulate penetration of the human mandible by 6.3 mm steel spheres and 7.62 mm spitzer tipped bullets at three impact angles (45º, 67.5º and 90º) and three impact velocities (400 m/s, 734 m/s, and 1109,185 m/s). Although experimental verification of the findings was not performed, their data suggests a linear relationship between velocity and energy absorption for both projectile types impacting at an angle of 45º. At all impact velocities and for both projectile types, 45º impact resulted in the highest energy absorption and 90º the lowest. In common with Huelke *et al* [15, 16], higher velocity impact resulted in greater absolute energy absorption but a lower proportion of energy loss in relation to available pre-impact kinetic energy.

A relatively simple analytical approach to begin addressing the important question of if or how the impact dynamics data discussed above might influence wound size is to determine the relationship between those parameters and the surface area of damage in the target material, an approach that is common in synthetic materials that might be subject to impact in service [e.g. 4, 20]. It might seem intuitive that, for a given calibre, greater absorbed kinetic energy would manifest in a larger damage area; in reality, however, the picture is more complex. A qualitative increase in wound size as a function of velocity has been reported in the distal human femur [15. 16] and diaphysis [17] impacted with steel spheres. Using their FE model for perforation of the human mandible, Tang *et al* [19] reported a qualitative increase in wound size with velocity with both spheres and spitzer-tipped projectiles. A quantitative increase in bevel size with velocity has been reported in polyurethane spheres, although this study utilised multiple calibres and two different tip-shapes across the velocity series [9]. Working with synthetic long bone shafts, Kneubuehl [21] reported that 9 mm full metal jacket (FMJ) handgun bullets could cause more damage than high-velocity FMJ 7.62 NATO rifle bullets when both were in stable flight. The latter finding was attributed to the inverse relationship between projectile-shaft contact time and velocity, which allows less time for energy absorption by the synthetic material.

Quantitative analysis of surface areas may also yield information of relevance to the biofidelity of synthetic bone substitutes. Morphometric analysis of entry wounds in a forensic series has suggested the existence of a correlation between the surface area of the entry wound and that of the associated internal bevel, and has also indicated highly variable bevel/ entry surface area ratios in cranial material ranging from 1.00 (no bevelling) in an occipital to 6.41 in a temporal bone [22]. Although sample derivation from a case series means it is difficult to isolate variables that might influence such relationships, data such as this lends itself to comparison with projectile fractures in synthetic bone.

Preliminary work with Polyurethane Bone Substitutes (PBS) has revealed differences in bevel morphology and size between synthetic and real bone [11]. Experimental acquisition of further baseline morphometric data from real bone would be advantageous for enhanced testing of synthetic bone biofidelity.

Considering the above, the present paper presents an analysis of the impact dynamics of non-human sandwich bones perforated by spherical projectiles at a series of increasing velocities. It then considers the relationships between projectile velocity, absorbed kinetic energy and wound size. Preliminary data provided by this work will assist in future tests of the accuracy of FE models and the biofidelity of synthetic sandwich bone analogues and will also provide a quantitative morphological basis for wound description in clinical and forensic contexts.

5.3. Methods

The current paper presents impact dynamics data that was derived during a previous experimental series that utilised pig scapulae and spherical projectiles to create wounds for analysis with micro-computerised tomography [13, 14]. The methods utilised therein are thus only briefly described again here along with more detailed descriptions of methodology unique to the present analysis.

5.3.1. Nomenclature

A single bevelled fracture consists of a *cortical entry* in the outer cortical plate and a *cortical exit* in the inner cortical plate, with the bevel being composed of the fracture edge running across the trabeculae and inner cortical plate [13].

5.3.2. Projectile type

Surface hardened 6 mm steel spherical projectiles (Atlas Ball Bearings, UK) were utilised in order to eliminate the effects of yaw and projectile deformation on impact dynamics.

5.3.3. Sample

Adult pig (*Sus scrofa domesticus*) scapulae were utilised as experimental models for human cranial sandwich bones due to their formation of internally bevelled wounds when subjected to impact. The infraspinous fossa was selected as the target area with the lateral surface facing outwards. For impact, the glenoid, neck and spine were cut away on a bandsaw to leave an approximately rectangular section of the scapular body large enough to allow the impact site to be 40-50 mm from any edge. For comparative purposes, specimens were placed into eleven groups, each utilising a different target perforation velocity either below 100 m/s (groups pre-fixed V_L) or between 150 m/s -850 m/s (groups pre-fixed V). Mean target group velocities for each group are provided together in **Table 5.1**. Velocities achieved by typical handgun and rifle ammunition were found in groups V_2 and V_5, respectively. During the ballistic tests, all specimens were clamped with the broader dorsal scapular margin forming the base.

Velocity group	Target velocity (m/s)
VL_1	30
VL_2	40
VL_3	50
VL_4	54-58*
VL_5	70
VL_6	100
V_1	150
V_2	350
V_3	450
V_4	650
V_5	850

TABLE 5.1 Target velocities for each velocity group; *amalgamated groups 4 and 5 from Rickman and Shackel [14]

Projectiles in groups V_1-V_3 were mounted in plastic sabots and propelled by a 21.3 mm calibre compressed air gas gun; high-speed footage of these groups was obtained using a Phantom V12 camera (Vision research Inc., New Jersey) operating at 55000 frames per second. To prevent intact sabots impacting the bone in the confined space of the gas gun chamber, a sabot stripper located at the exit of the barrel fragmented the sabots immediately upon exit. Initial shots in groups $V_{4\text{-}5}$ were carried out with a 30 mm helium powered gas gun but in 10 of these (one in V_4 and one in V_5) the fragmented plastic sabots had extensively damaged the perforation site and covered the wound channel with a fine black powder. Subsequently, a further 13 specimens were prepared for groups $V_{4\text{-}5}$ and impacted in an indoor shooting range with sabot mounted projectiles being propelled by an Enfield number three proof housing fitted with a 7.62 mm barrel. To achieve velocities below 100 m/s in V_L groups, a compressed air powered gas gun fitted with a 6 mm barrel was utilised. Footage for V_L and the new V_4 and V_5 groups was obtained on a Phantom V12 12 camera operating between 37-40,000 frames per second. Camera selection was based only upon availability during the experimental period.

To capture tissue behaviour during projectile entry and exit, two bones from V_1 and two from V_2 had cameras placed at either the front or rear during impact. In these specimens, incident velocity could still be estimated using the gas gun's time gate. Residual velocity could not be calculated due to lack of side-on footage; these four specimens were thus unavailable for energy absorption calculations. High-speed footage from both cameras was analysed using Phantom camera control software. To compensate for blurring of projectile edges in high velocity footage, frames with the best view of the projectile were selected for measurement. Incident and residual velocities were then calculated three times on separate days; the mean of these measurements was taken as the velocity and then utilised for subsequent impact dynamics analyses.

5.3.4. Calculating kinetic energy and energy absorption

The kinetic energy of a projectile, *E*, is utilised in tissue wounding processes and is a function of projectile mass (*m*) and velocity (*v*). Projectile kinetic energy, in joules (J), is provided by:

Eq.1:

$$\frac{mv^2}{2}$$

Where *m* is projectile mass in kilograms and *v* is velocity in metres per second (m/s). If the projectile retains sufficient kinetic energy to exit the perforated structure and does not lose mass during perforation (e.g. during fragmentation), the kinetic energy absorbed by the tissue (ΔE) is the difference between the incident (E_i) and residual (E_r) kinetic energies and is provided by the following term:

Eq.2:

$$\frac{m\,(v_1^2 - v_2^2)}{2}$$

Where v_1 is the incident velocity and v_2 the residual velocity. Since a single kinetic energy absorption figure was calculated from the mean of three velocity measurements, the error propagation formula presented in Rickman and Shackel [13] was utilised to provide a standard deviation for absorption values:

Equation 3:

$$[\sigma_{\Delta E}]^2 = \left[\frac{{v_1}^2 - {v_2}^2}{2}\right]^2 [\sigma_m]^2 + \left[\frac{mv_1}{2}\right]^2 [\sigma_{v_1}]^2 + \left[\frac{mv_2}{2}\right]^2 [\sigma_{v_2}]^2$$

Where σ is the standard deviation, *m* is the mass of the projectile in kilograms, v_1 is the incident velocity and v_2 the residual velocity. The standard deviation associated with the kinetic energy absorbed for each individual impact is the square root of $[\sigma_{\Delta E}]^2$.

5.3.5. Quantitative analysis of wound morphology

To remove soft tissue without harming bone fracture surfaces specimens were cold water macerated by immersing in water for 7 days. Specimens were left immersed in plastic tubs, with lids half open to allow aeration, under a fume hood. Residual soft tissue was then carefully dissected away from the specimens, taking care not to forcibly remove fragments that remained attached to the cortical plates. Fragments adherent in soft tissue were photographed before and after removal. After cleaning, specimens were left to air dry in a fume cupboard for 7 days before being placed in sealable plastic bags and stored in a freezer to prevent further bone degradation. For photography, sand was placed in a sealable bag which was then wrapped in black cloth to enhance contrast with the bones. To ensure the specimens were as level as possible they were first rested on a rubber disk placed on top of the sand-

filled bag. A bubble level was then placed on the specimen as close as possible to the hole and the specimen orientated on top of the deformable sandbag until the bubble indicated the specimen was level.

Images were taken using a Canon EOS 200D camera fitted with an EF-S 60 mm macro lens placed on a tripod with extendable boom arm and ball head mount. A second bubble level on the rear of the camera allowed it to be orientated so it was in line with the bubble level indicator on the specimen and thus on the same approximate plane as the entry or exit. For scale, a measuring tape was cut small enough to ensure it fitted on the specimen without being raised by areas of bone curvature. To prevent camera shake, pictures were taken remotely by Wi-Fi using the Canon Camera Connect Ap. Quantitative data was gathered in ImageJ (version 1.52a; 64 bit), with the scale in each image being used to provide the number of pixels per millimetre for subsequent numerical analysis.

Mean surface area of entry and exit in mm^2 was calculated using the wand edge detection tool in ImageJ, which automatically delineates the fracture edges with a yellow line. The wand tool was set to 8- connected with a tolerance of 30; mean surface area was calculated from two measurements per specimen. Whilst this tool worked well with the start contrast between the entry cortical fracture edge and black background, on the exit side there was no contrast due the medially situated bevel. Accordingly, after the wand tool had auto- fitted a line the "brush" function was utilised to manually move it to the most peripheral fracture edge visible. Although the bevel is a three-dimensional structure, the present paper follows Quatrehomme and İşcan [22] and quantifies the extent of bevelling using the ratio of exit surface area divided by entry surface area. Accordingly, a ratio of 1.0 means there is no bevelling (that is, a cylindrical wound channel) whilst a higher value indicates more extensive bevelling.

5.4. Results

5.4.1. Projectile-bone interactions and impact dynamics

A total of fifty specimens were impacted and filmed in lateral view. Two specimens from V_4 and one from V_5 were subsequently excluded due to off target perforation events through thicker bone regions. Projectile re-bound was not captured in footage of the two specimens composing VL_1, and this group was thus also excluded from subsequent analysis. The total range of impact velocities across the 45 remaining specimens was 35 m/s to 897 m/s. Summary impact dynamics data from Rickman and Shackel [13, 14] combined with current morphometric data is presented in **Table 5.2**. Specimens impacted in groups $V_{1\text{-}3}$ exhibited variable amounts of small plastic sabot fragments embedded in soft tissue on the entry side. Whilst an effect of sabot impact on wound size cannot be ruled out, plastic sabot fragments were spread across wounds of all shapes, sizes and at variable impact velocities. For example, one specimen in V_2 (incident velocity 333 m/s, see **Fig.5.5**) had a circular entry with a mean surface area of 25.67 mm^2, whilst the largest circular V_1 cortical entry (incident velocity 161 m/s) had a mean surface area of 28.29 mm^2. Groups $V_{2\text{-}3}$ and V_5 displayed large group means for both entry and exit (**Table 5.2**). Larger entry surface areas in these groups were attributable to additional fragments

whose periphery formed part of the damaged area, to re-entrant geometries along the fracture edges, or to irregular wound shapes. All groups exhibited larger mean exit surface areas than entry surface areas.

The relationship between projectile incident velocity and residual velocity was linear (**Fig**.**5**.**1**), as was the relationship between incident kinetic energy and residual kinetic energy (**Fig.5.2**). The latter relationship indicates that the incremental energetic cost of perforation was essentially constant and independent of total available incident kinetic energy. In both graphs, fluctuation in the data is likely attributable to variation in incident velocity and, to a greater extent, the intrinsic biological features of the specimens. Bone exhibits considerable natural variation in tissue parameters such as mineralisation and histological structure, in addition to variation in absolute and relative thickness of the three laminae composing the sandwich bone. Such biological variation will influence the mechanical properties of the impacted region, including fracture toughness and work of fracture. The energy utilised to fracture bone and eject material (absorbed energy, ΔE) increased with increasing velocity according to a power function, although the relationship was not quadratic ($y= 0.0045x^{1.4045}$) (**Fig.5.3**). No plateaux in energy absorption was seen within the range of velocities achieved in this experiment, indicating that further work of fracture could be performed during higher velocity impacts beyond those achieved with small arms. Within a single group there was considerable variation between incident velocity and the kinetic energy absorbed by the specimens. For example, in V_1 the lowest velocity 149 m/s impact resulted in 5.18 J (standard deviation 0.03) of kinetic energy being absorbed, whilst a higher velocity impact at 168 m/s absorbed only slightly more at 5.26 J (standard deviation 0.07). Similarly, the maximum energy absorbed within V_5 (87 J, standard deviation 4.04) was produced by the second highest velocity impact (885 m/s); the highest velocity impact itself (897 m/s) resulted in only 67 J (standard deviation 4.43) of energy being absorbed.

Whilst increased incident velocities resulted in greater absolute energy absorption, the proportion of available incident kinetic energy utilised to effect target penetration or perforation was inversely related to incident velocity, with data for all impacted specimens being described by a negative power function ($y = 1027.7x^{-0.596}$) (**Fig.5.4**). Percentage energy absorbed showed the most rapid decline between groups VL_2 and V_1, ranging between incident velocities of 35 m/s to 168 m/s. Excluding two impacts where the projectiles embedded (resulting in 100% absorption), percentage kinetic energy absorption across the specimens decreased from a maximum of 97.93% (incident velocity 57 m/s) in VL_2 to a minimum of 16.76% (incident velocity 871 m/s) in V_5. Across the velocity groups, mean percentage energy absorbed decreased from 90.24 % in VL_2 (mean incident velocity 36 m/s) to 19.70 % in V5 (mean incident velocity 863 m/s). Above 741 m/s all impacts utilised less than a quarter of available incident kinetic energy to effect target perforation. Since there can never be zero energetic cost to perforate, levelling off at the highest incident velocities indicated the possible approach of the minimal energetic cost of perforation for this target-material combination.

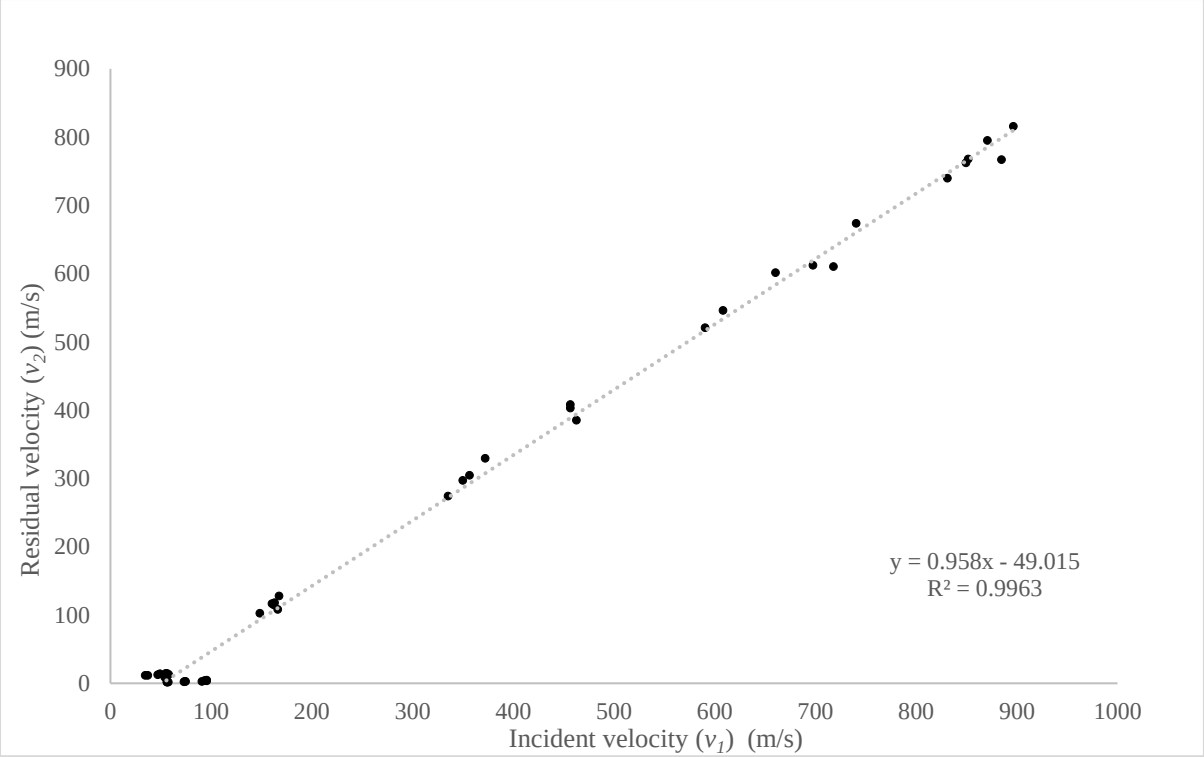

Fig.5.1 Projectile esidual velocity as a function of incident velocity during impact of sandwich bones by 6 mm surface hardened steel spheres, n=45

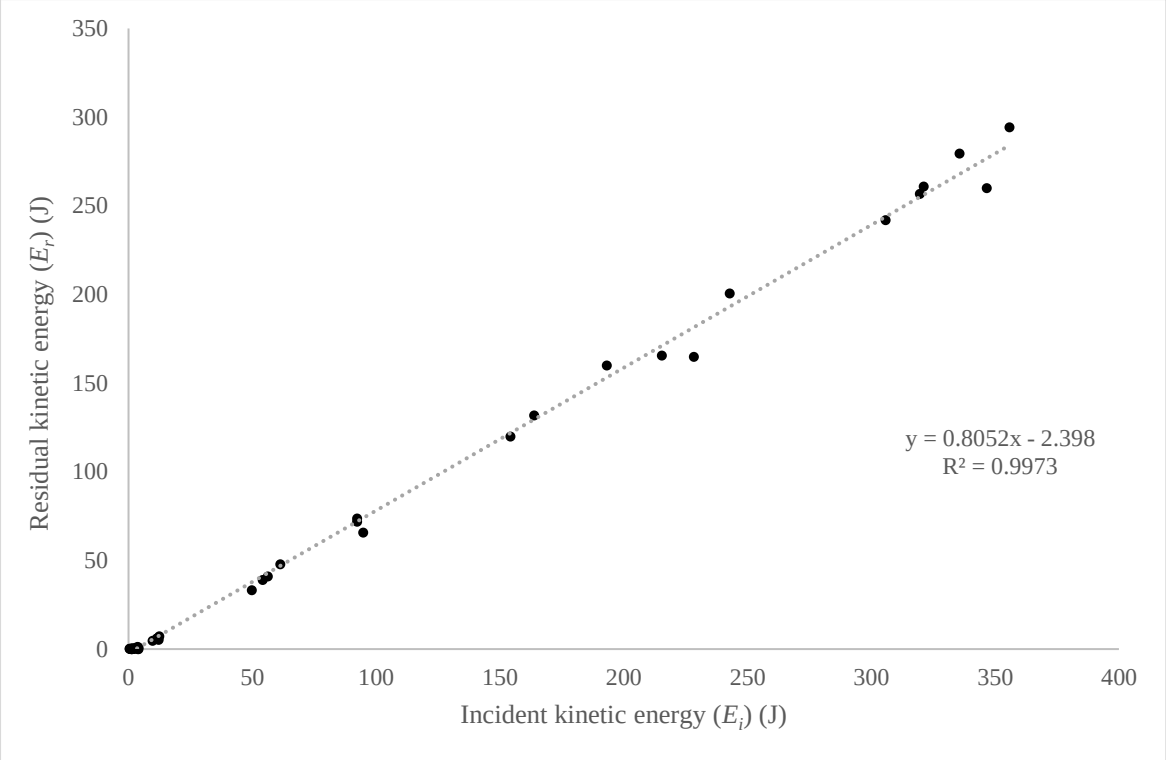

Fig.5.2 Projectile residual kinetic energy (J) as a function of incident kinetic energy (J) subsequent to perforation of sandwich bones by 6 mm surface hardened steel spheres; n=45

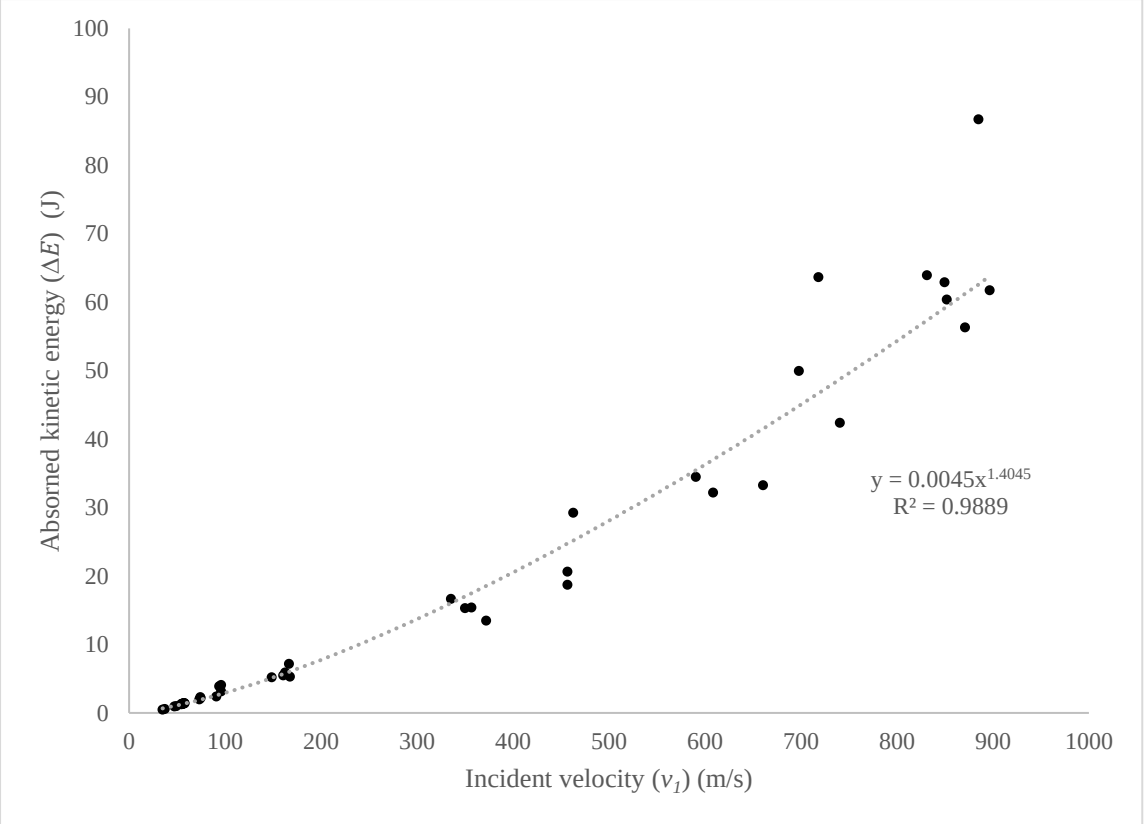

Fig.5.3 Kinetic energy absorption as a function of incident velocity during impact of sandwich bones by 6 mm surface hardened steel spheres; n=45

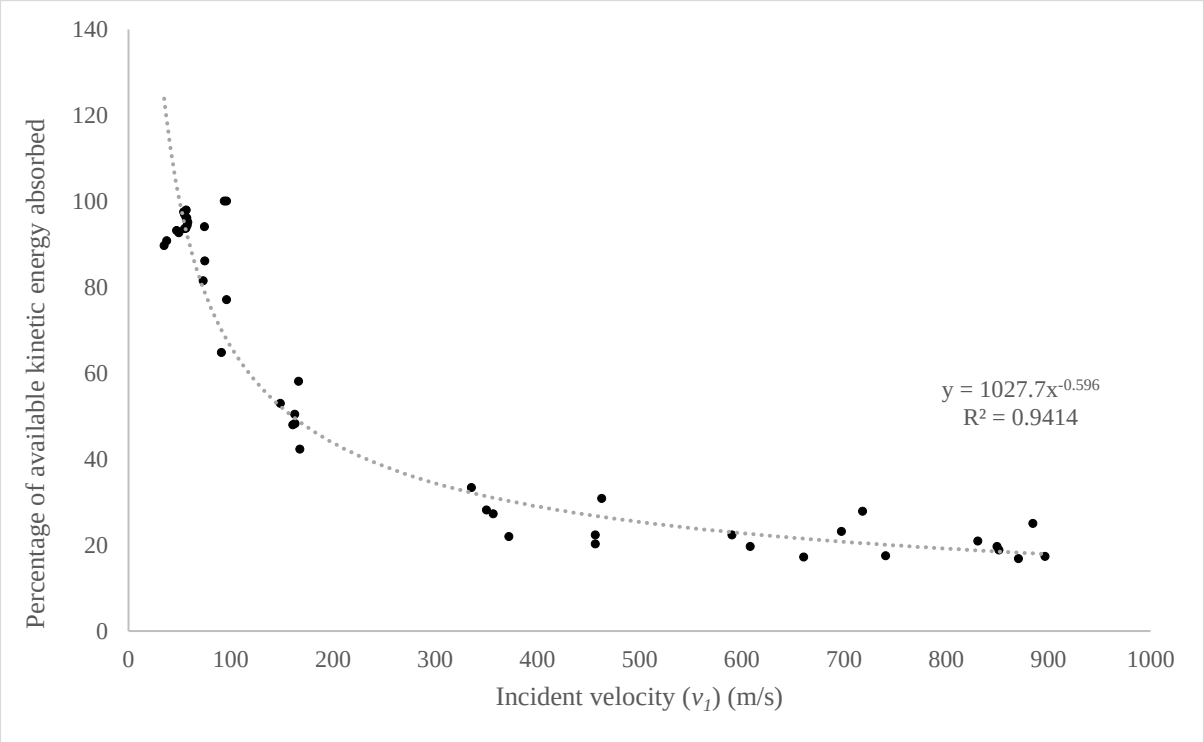

Fig.5.4 Percentage of available incident kinetic energy absorbed as a function of incident velocity; n=45

Velocity group (n)	V_1 (m/s)	V_2 (m/s)	Mean E_i (J)	Mean E_r (J)	Mean ΔE (J)	Mean % kinetic energy loss ($\Delta E / E_i$) x100	Mean SA Cortical entry (mm^2)	Mean SA Cortical exit (mm^2)
VL_2 (2)	36.12 (1.22)	11.27 (0.06)	0.58 (0.04)	0.056 (0.001)	0.52 (0.04)	90.24 (0.55)	-	-
VL_3 (2)	48.33 (1.04)	12.84 (0.52)	1.03 (0.04)	0.07 (0.01)	0.96 (0.04)	92.95 (0.27)	-	-
VL_4 (9)	56.29 (1.24)	11.49 (2.19)	1.40 (0.06)	0.06 (0.02)	1.34 (0.06)	95.70 (1.50)	66.94** (n=1)	-
VL_5 (3)	74.17 (0.61)	25.85 (5.69)	2.43 (0.04)	0.31 (0.12)	2.12 (0.15)	87.22 (5.21)	28.60 [25.11-33.35]	105.38 [89.30-129.76]
VL_6 (4)	94.24 (2.06)	49.99* (4.02)	3.93 (0.17)	1.11* (0.18)	3.38 (0.68)	85.47 (15.17)	28.29 (n=2) [28.21-28.37]	121.44** (n=1)
V_1 (6)	161.63 (6.84)	114.23 (8.72)	11.58 (0.95)	5.80 (0.88)	5.78 (0.72)	49.98 (5.32)	25.85 (n=8) [24.34-28.72]	131.83 (n=8) [50.86-238.26]
V_2 (4)	353.75 (15.24)	301.04 (22.68)	55.45 (4.77)	40.27 (6.06)	15.18 (1.31)	27.68 (4.68)	70.57 (n=5) [25.67-146.00]	229.07 (n=5) [95.54-330.03]
V_3 (3)	458.93 (2.88)	398.56 (9.79)	93.20 (1.17)	70.33 (3.43)	22.87 (4.58)	24.48 (4.57)	127.98 [89.22-168.76]	266.59 [189.94-341.28]
V_4 (5)	655.24 (55.18)	577.83 (42.01)	191.06 (31.93)	148.37 (21.12)	42.69 (13.78)	22.04 (4.02)	27.09 (n=3) [20.80-35.30]	189.58 {n=3) [128.76-241.65]
V_5 (7)	846.69 (51.75)	759.73 (45.37)	318.24 (37.38)	256.19 (29.80)	62.05 (13.14)	19.43 (2.86)	41.94 (n=4) [29.16-59.52]	314.23 (n=5) [157.26-853.49]

TABLE 5.2 Summary data for n=45 impacts from Rickman and Shackel [13] and Rickman and Shackel [14] for all velocity groups coupled with morphometric data; standard deviation in parentheses; *excludes two specimens where the projectile embedded; **figure represents the mean of two measurements for the single specimen; a total of 6 specimens were impacted in V_2 but two were utilised for front and rear filming, respectively

5.4.2. Quantitative analysis of wound morphology

A total of 31 fully perforated specimens from velocity groups VL_4-V_5 were photographed for quantitative analysis. Of these, 29 specimens provided data on the surface area of the cortical entry, whilst 28 specimens yielded data on the surface area of the cortical exit. In total, 26 specimens yielded surface area data for both the entry and the associated exit. One specimen in V_4 and three specimens in V_5 displayed extensive damage encompassing curved bone which prevented quantitative analysis. The following pairs of variables were analysed for correlation; incident velocity versus cortical entry surface area (SA); **1**, incident velocity versus cortical exit SA; **2**, absorbed energy versus entry SA; **3**, absorbed energy versus exit SA; **4**, entry SA versus exit SA; **5**, exit/entry ratio versus incident velocity; and **6**, exit/entry ratio versus absorbed energy. Since no variable combinations involving incident velocity or energy absorbed could be bivariate normally distributed, Spearman-Rank correlation (r_s) was utilised. A Kolmogorov-Smirnov test for normality for the cortical entry and cortical exit surface areas revealed that entry SA was not normally distributed; accordingly, r_s was also utilised to analyse this correlation.

5.4.2.1. Surface areas of the cortical entry and associated cortical exit and their relationships with absorbed kinetic energy and incident velocity

The results of Spearman's Rank correlation coefficient analysis of surface area relationships are presented in **Table 5.3**. Across the range of incident velocities utilised there was a weak and non-significant correlation between the surface area of the cortical entry and the surface area of the associated exit, (r_s = 0.311, n=26). Across the series the correlation between cortical entry size and incident velocity was weak and not significant (r_s=0.309, n=29). Cortical exit surface area was found to be moderately correlated with incident velocity, and this result was highly significant (r_s = 0.559, p <0.01, n=28). The correlation between absorbed kinetic energy and the surface areas of the cortical entries was weak and not significant (r_s= 0.270, n=25). However, the correlation between absorbed kinetic energy and the surface area of the cortical exit was moderate and highly significant (r_s = 0.581, p <0.01).

	Cortical entry and cortical exit surface areas	Incident velocity (m/s) and cortical entry surface areas (mm^2)	Incident velocity (m/s) and cortical exit surface areas (mm^2)	ΔE (J) and cortical entry surface areas (mm^2)	ΔE (J) and cortical exit surface areas (mm^2)	Incident velocity and exit/entry ratio	ΔE (J) and exit/entry ratio
r_s	0.311	0.309	0.559*	0.27	0.581*	0.055	0.028
n	26	29	28	25**	24**	26	22

TABLE 5.3 Spearman-Rank correlation analysis of surface areas; *significant at p=<0.01; **four specimens excluded due to utilisation in filming from front or rear

5.4.2.2. Cortical exit/ entry ratios and extent of bevelling

All 26 perforated specimens exhibited bevelling, with the exit/entry ratio ranging from 1.78 in a 350 m/s impact to 10.38 in a 333 m/s impact; the mean ratio across all specimens was 4.48 (standard deviation 2.54). Across all specimens and incident velocities, there was no correlation between the exit/entry ratio and incident velocity or between that ratio and absorbed energy (**Table 5.3**). Mean exit/entry ratio across the velocity groups ranged from 2.09 in V_3 to 6.59 in V_4 (**Table 5.4**). Across the greatest range of incident velocities for which data was available, between group VL_4 (mean incident velocity 74 m/s) and V_5 (mean incident velocity 847 m/s), the mean exit/entry ratio differed by only 0.7. Within groups, there was considerable variation in the extent of bevelling even when the incident velocities were similar. For example, in group V_1 a 163 m/s impact resulted in a ratio of 2.78 whilst a 167 m/s impact resulted in a ratio of 8.65. Similarly, two impacts in V_2 occurred at an identical incident velocity of 333 m/s; however, whilst the first of these impacts resulted in a ratio of 10.38, the second resulted in a ratio of only 3.46.

	VL_5 (n=3)	V_1 (n=8)	V_2 (n=5)	V_3 (n=3)	V_4 (n=2)	V_5 (n=4)
Mean exit/entry ratio (s)	3.78 (1.21)	5.21 (2.86)	4.33 (3.51)	2.09 (0.06)	6.59 (4.16)	4.49 (0.91

TABLE 5.4 Mean exit/entry ratio across 6 velocity groups (standard deviation in parentheses)

5.4.5. High-speed footage of tissue ejection

The kinetic energy imparted during impact resulted in simultaneous retrograde and anterograde tissue motion during the perforation event, resulting in a double cone ejection profile. Soft-tissue ejection dominated retrograde tissue movement whilst anterograde tissue ejection consisted of both bone fragments and soft tissue. Although the amount of tissue ejected during each impact was not quantified, tissue ejection was more much more explosive and extensive at the higher impact velocities. Footage capturing entry in two specimens, impacted at 158 m/s and 333 m/s respectively, revealed that retrograde soft tissue ejection begins when a highly accelerated column of soft tissue, recruited from a region larger than projectile calibre, subsequently expands radially to form the conical plume (**Fig.5.5**). Examination of the specimens during dissection revealed that the periosteum remained intact up to the edge of the cortical entry; soft tissue ejected from the entry side thus consisted almost entirely of striated muscle and connective tissue.

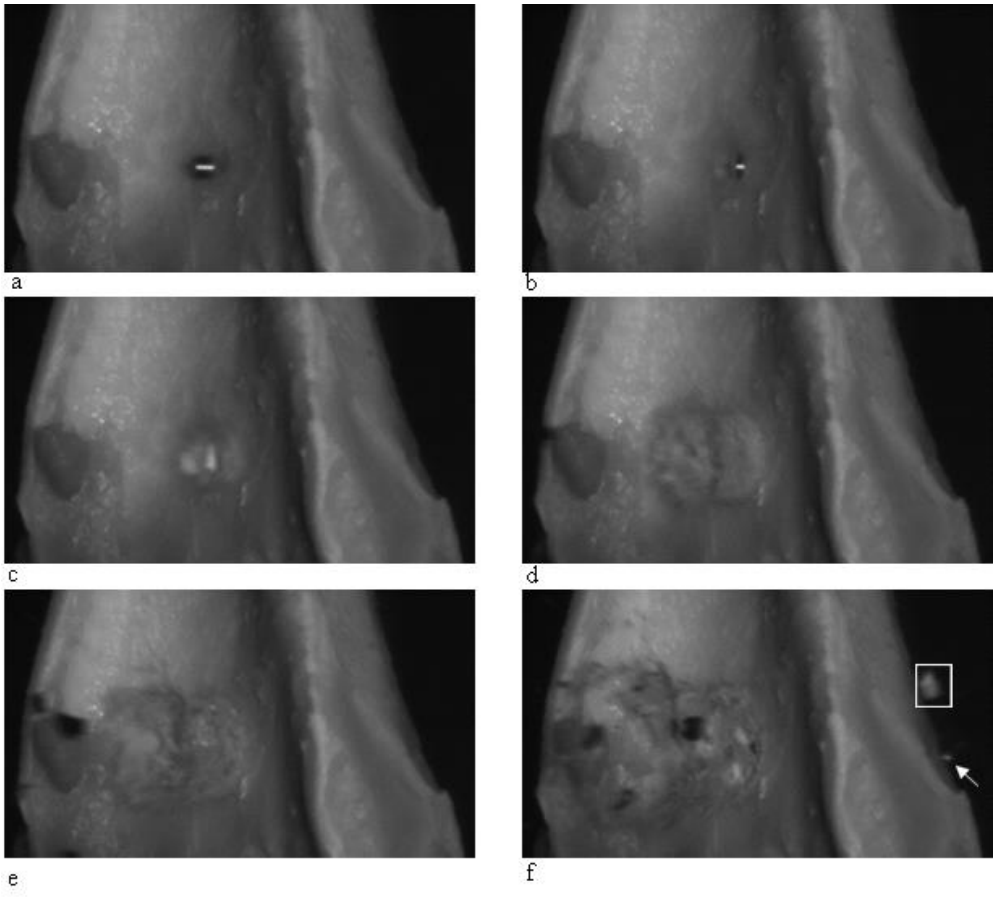

Fig.5.5 Tissue behaviour during a 333 m/s impact with a 6 mm surface hardened steel sphere. Total time of image sequence 272.68 μs. The plume begins as an elongated cylinder before adopting a conoidal morphology with radial expansion. Black objects in **e** and **f** are sabot fragments impacting peripheral to the entry. **a**. pre-impact; **b**, initial contact with specimen; **c**, nascent retrograde soft tissue plume; **d**, elongation of soft tissue plume, pre-radial expansion; **e**, beginning of radial expansion; **f**, radial expansion and projectile exit (arrow) coupled with anterograde bone fragment ejection (square)

5.5. Discussion

In order to gather data on the dynamics of sandwich bone perforation by projectiles, the current investigation utilised pig scapulae as proxies for the sandwich bones of the human neurocranium; carbon steel spherical projectiles were utilised to eliminate the effects of yaw and deformation on the energetics of the impact process. While it is important to note that such an experimental model is less complex than the living bio-system, this experimental analogue provided useful preliminary impact data on which to base subsequent analyses with both synthetic and human material.

Analysis of high-speed footage revealed linear relationships between projectile incident and residual velocities and therefore between incident kinetic energy (E_i) and residual kinetic energy (E_r). The latter finding indicated that the energetic cost of perforation through sandwich bones was independent of the total kinetic energy possessed by the projectile, and is in accordance with tabulated data presented by Huelke *et al* [16] for human femoral epiphyses perforated with 10.3 mm and 6.4 mm

spheres. The presence of a linear function for E_i versus E_r in both sandwich bones and long bone epiphyses, which differ greatly in terms of absolute thickness, cortical thickness, and trabecular volume, suggests that this association may be a characteristic feature of bone perforation irrespective of bone type.

In terms of the relationships between pre-and post-impact projectile velocity and kinetic energy, bone appears to behave similarly to synthetic composite materials. For example, linear associations between incident and residual velocity have been reported in Carbon Fibre Reinforced (CFRP) plates [23], whilst linear relationships between incident and residual kinetic energy have been described in polyethylene fibre composites [24] and in natural fibre composites [25]. Interestingly, this relationship was also reported in balsa core sandwich structures with carbon fibre skins, where it was linked to damage localisation within the structure above the ballistic limit [20]. Damage localisation immediately adjacent to conoidal projectile wounds has also been demonstrated with µCT in non-human sandwich bones [13] and this is consistent with the linear relationship for E_i and E_r observed in the present study. In sandwich bones, damage localisation is satisfactorily explained by the mechanism underlying the formation of conoidal wounds. During perforation, projectile impact initiates a trans-laminar crack through the three bone layers that not only forms the bevel but also momentarily creates a conoidal plug of bone inside it [13, 14]. This trans-laminar crack would act to restrict fragmentation to the conoidal plug and thus result in damage localisation and the observed linear relationship for E_i and E_r.

During the impact event, a proportion of available incident kinetic energy is absorbed by the target material and utilised to effect perforation. The relationship between this percentage value and incident velocity will be affected by the physical characteristics of both projectile and target material, in addition to the angle of incidence between projectile and bone. Characterisation of this proportion allows both quantitative analyses of the effects of these variables and a comparative analysis of different projectile- bone combinations. In accordance with impact theory and published findings for both long bone epiphyses [15] and simulated sandwich bone impacts [19], an inverse relationship was detected in the present series. This inverse relationship is due to the reduced contact time between target and projectile at higher velocities, which dictates that relatively less kinetic energy can be absorbed by the material per unit time. Experimentally determined percentage energy loss values using spherical projectiles and real bone do not, therefore, substantiate the notion that bullets lose nearly all their energy during bone impacts [26]. The proportionally lower cost of perforation at higher velocities is of clinical significance in that it leaves the projectile with more kinetic energy to effect damage in deeper soft tissue structures along the wound track.

The percentages of kinetic energy utilised in perforation of pig scapulae reported here differ from values reported for other bone/ species combinations in the literature. In their FE model utilising 6.3 mm spheres perforating the human mandibular angle at 90 degrees, Tang *et al* (2012) reported percentage energy absorption values of 44.97% at 400 m/s and 32.63% at 734 m/s, respectively. In contrast, mean absorption values for pig sandwich bones in the present analysis were 24.48% at 458

m/s and 20.58% at 639 m/s. Differences are also apparent between pig sandwich bones and human femoral epiphyses perforated by 6.35 mm projectiles [16]. For example, whilst a 472 m/s epiphyseal perforation utilised 47.8% of incident kinetic energy, a 459 m/s pig scapula perforation utilised only 24.48%. In their FE model for the human parietal, Rodrigues *et al* [27] reported percentage absorption values of 14.2% for .380 auto (incident velocity 288 m/s), 10.8% for .40 Smith and Wesson (incident velocity 300 m/s) and 7.6% for 9 mm Luger projectiles (incident velocity 343 m/s). Absorption values for pig sandwich bone perforations at velocities bracketing the above were considerably higher, with mean percentage absorption values of 49.98 % at 162 m/s and 27.68% at 354 m/s.

Differences in percentage values may be attributable to several factors. Higher percentage losses reported for long bone epiphyses utilised by Huelke *et al* [16] are probably attributable to the thickness of the distal femur, which increases projectile-target contact time, and to a greater trabecular abundance in that bone region. Although target thickness was not provided for the FE models of Tang *et al* [19] or Rodrigues *et al* [27], bone thickness and calibre differences seem unlikely to fully account for why their results should differ so greatly from each other and from the present experimental model. Such disparity may reflect bone-specific differences operative during perforation or may suggest areas for further refinement of existing FE models. In their analysis, Rodrigues *et al* [27] attributed observed percentage absorption values to differences in projectile design and calibre; however, ordering their projectiles by velocity reveals the expected inverse relationship for percentage energy loss. Accordingly, while projectile characteristics, particularly calibre [18], undoubtedly play a large part in the proportional cost of perforation, further work holding incident velocity constant while altering projectile design variables is needed to elucidate any underlying signatures related to projectile construction.

The relationship between incident velocity and the amount of energy absorbed during impact (ΔE), and subsequent determination of how that energy is utilised to effect wounding, is critical to a complete understanding of projectile-tissue interactions. With the pig sandwich bone proxies utilised in the present analysis, the energy absorption profile was described by a power function across a gradation of velocities extending from 35 m/s to 897 m/s. This finding is similar to previously described literature for human long bones, which have yielded quadratic relationships for both epiphyseal [16] and osteoporotic diaphyseal perforation [17], but contrasts with the linear profile accepted for 10.31 mm spheres perforating non-osteoporotic femoral shafts in the latter series [17]. Although published data for sandwich bone energy absorption during ballistic perforation is lacking, the three energy absorption values developed by the human mandibular perforation model of Tang *et al* [19] for 6.3 mm spheres perforating at three velocities and at 45^0 suggest a linear relationship, although caution should be applied to this result due to the small number of velocities utilised. Based upon current data, it appears that in bone power energy absorption profiles are more common than linear profiles; further, while the exponent is variable, bone type does not seem to alter the general profile obtained, with power relationships generated by both long bones and sandwich bones.

A power relationship for energy absorption as a function of velocity indicates that higher velocity impacts are associated with a proportionally greater amount of energy utilised in the fracture, fragmentation, and fragment ejection than during lower velocity impacts. Although the relative role of each of these processes in energy re-distribution during perforation of pig sandwich bones was not established, data for ceramics and synthetic composites may be instructive. In ceramics, experimental work has shown that relatively little kinetic energy is utilised in the creation of new fracture surface area; rather, a much larger proportion of the kinetic energy is re-distributed as residual kinetic energy of fragments in the ejecta plume [28]. For brittle materials in general, up to half of the incident kinetic energy can be utilised in the acceleration and ejection of fragments [29], and the importance of fragment ejection in energy re-distribution has also been noted in synthetic composites [4]. However, although a relationship between energy input and liberated fracture surface area has been demonstrated in a bone substitute [30] and later in cortical bone [31], further work is required to establish how fragment size relates to velocity during projectile impact and whether subsequent ejection of this material accounts for the greatest proportion of utilised kinetic energy.

Bone in the living vertebrate cannot be considered in isolation due to its close association with soft tissue structures, particularly the skeletal musculature and, in the skull, underlying neurological tissues. Comparison of tissue ejection of fleshed specimens impacted at low and high velocity revealed soft tissue ejection both in the anterograde and retrograde directions, resulting in a "double plume" of ejection, a profile has also been noted for long bone impacts [1, 7]. Although soft tissue ejection in the current study was qualitatively more explosive and extensive at higher velocities, the relative contribution of soft tissue ejection to kinetic energy absorption during impact has yet to be quantified; further work is therefore required with fleshed and de-fleshed specimens to gather this important data.

In addition to impact dynamics data, the current study also quantified wound morphology utilising surface area measurements. Calculation of exit/entry ratios revealed bevelling in all twenty-six wounds where this value could be determined. Similar findings on the prevalence of bevelling have been reported by Quatrehomme and İşcan [22] in their analysis of gunshot entry wounds in a forensic series. In that study, which included 39 entry wounds in cranial and postcranial material, the authors reported an absence of bevelling in only four bones. However, whilst both analyses support the high prevalence of bevelling in projectile wounds, exit/entry ratios calculated in the current study were higher than that reported in Quatrehomme and İşcan [22]. The largest bevel in their series was an exit/entry ratio 7.70 in a clavicle and the smallest a ratio of 1.04 in a left occipital, with a mean ratio across all 39 wounds of 2.29. This compares to a maximum ratio of 10.38, a minimum ratio of 1.78 and a mean ratio of 4.48 across the twenty-six specimens in the present analysis.

Whilst it is unclear what specific factors may precipitate such variation in ratios, it is likely due to both extrinsic (*projectile-related*) and intrinsic (*bone-related*) variables. Specific details of the ammunition types that produced the 39 gunshot wounds analysed in Quatrehomme and İşcan [22] were unavailable in most cases, and it is possible that some of the variation in bevel ratios may be attributed

to different projectile characteristics including tip shape and construction (e.g. deforming versus non-deforming). Furthermore, experimental work examining the relationship between the intrinsic bone features and cortical entry size has revealed that both greater bone thickness [32] and bone mineral density [33] result in larger cortical entry sizes; these intrinsic factors would, therefore, influence bevel ratio. Finally, Quatrehomme and İşcan [22] noted that bevel morphology is likely influenced by numerous anatomical features present at or near the impacted cranial region including sutures and emissary veins. The scapulae utilised in the present study presented with relatively uniform outer and inner cortical plates devoid of conspicuous anatomical features that might interrupt bevel formation.

Recent years and growing case experience have led to the realisation that conoidal wounds may be produced by a variety of impacting objects in addition to projectiles [34-36], making differential diagnosis more complex in some cases. In light of this overlap, any wound with bevelling must currently be considered a gunshot injury in the absence of evidence to the contrary [36]. Whilst the process of defleshing, macro photography and analysis makes quantification of bevel size impractical in most contexts, minimum exit/ entry ratios of 1.04 [22] and 1.79 in the present study highlight the fact that projectiles can induce a limited amount of bevelling that may be hard to assess by eye. Quantification of exit and entrance size for diagnostic purposes may therefore be recommended in such cases where qualitative assessment of the presence or absence of bevelling is ambiguous.

In addition to showing variation between specimens, the exit/entry ratio showed only a weak and non-significant correlation with incident velocity and absorbed kinetic energy. These findings suggest that, with this projectile-target combination at least, the ratio must instead be determined by intrinsic features of the bone through which the translaminar crack front initiates and subsequently propagates. This interpretation is consistent with the finding that there was no significant correlation between the surface area of the cortical entry and the surface area of the associated cortical exit. Previous analysis of conoidal wounds has found that irregular cortical entry shape only rarely results in a corresponding irregular bevel, with irregularity being lost in the trabecular layer [13]. This loss of irregularity was also noted by both Kimmerle and Baraybar [37] in shrapnel impacts and by Quatrehomme and İşcan with projectile impacts [22]. Rickman and Shackel [13] proposed that deletion of irregularity was due to deviations in translaminar crack path due to material inhomogeneities in the sandwich bone, particularly trabecular strut orientation in relation to the propagating crack. Critically, this crack deviation mechanism would also de-couple entry wound size from bevel size and, additionally, contribute at least partially to the observed variation in exit/entry ratios.

It is important to note that the weak correlation between entry and exit surface areas presented here is in direct contrast to that provided by Quatrehomme and İşcan [22], who reported a strong and significant correlation between entry and exit surface areas. Why this difference should exist is not immediately clear but may reside in differences in bone type, shape and thickness as well as projectile design and construction. It may also originate from methodological differences, with Quatrehomme and İşcan [22] calculating surface areas using formulae for the shape of the entries and exits rather than

direct measurement of the fracture perimeter; sample size was also larger in the forensic series. Further analysis impacting a larger number of specimens at a constant velocity would prove informative in establishing the strength of correlation between these variables.

Previous analyses of the relationship between incident velocity (and thus absorbed energy) and the extent of bone damage have yielded contrasting results. Qualitative increase in wound or fracture size has been reported in both FE simulation of human mandible perforation [19] and in long bone impacts (15-17], whilst Taylor and Kranioti [9] reported a quantitative increase in bevel size (measured as a straight- line distance) in synbone spheres. In direct contrast, Kneubuehl [21] demonstrated with synthetic long bones that high-velocity impacts with 7.62 mm NATO rifle bullets can result in less damage than lower velocity impacts with 9 mm FMJ handgun bullets, a result attributed to reduced projectile-material contact time. It must of course be kept in mind when considering such findings that other variables, particularly calibre and projectile design, may have influenced observed damage patterns. The present study substantiates the findings of Taylor and Kranioti [9]; cortical exit surface area (i.e., the perimeter of the bevel) increased with an increase in both incident velocity and absorbed energy, although the correlation in both cases was only moderate. Given the moderate correlation between velocity and exit size and the number of additional intrinsic and extrinsic factors that might influence the latter, such as bone thickness and projectile design, this variable is unlikely to be a suitable candidate for determination of projectile velocity from fracture morphology.

Cortical entry size has been the subject of several analyses seeking to determine the reliability of calibre estimations based upon measurement of defect diameter [32, 33, 39]. In contrast to cortical exit size, the present study found weak and non-significant correlations between entry surface area and both velocity and absorbed energy, although it must be borne in mind that four specimens in groups V_4 and V_5 with extensive damage to the outer cortical plate could not be measured due to bone curvature (discussed further below). Accordingly, whilst cortical entry size may vary with projectile construction and impact angle [38], in addition to bone thickness [32] and mineral density [33], projectile velocity and absorbed energy did not predictably influence entry size when impact was achieved using non-deforming steel spheres. In some higher-velocity impacts, particularly in groups $V_{2\text{-}3}$ and V_5, complex fracture edges created accessory fragments and re-entrant geometries which increased entry surface area. While sabot fragment involvement cannot be fully ruled out in groups $V_{2\text{-}3}$, it cannot account for additional fracture surface area in group V_5 where there was no sabot contact. Additional research is therefore required to establish the intrinsic and/ or extrinsic factors that underlie such morphological diversity at the cortical entry.

Quantitative analysis of exit surface area may yield information pertaining to the formation of conoidal wounds in different bone types. According to the translaminar cone crack theory of conoidal wound formation in sandwich bones [13, 14], the conoidal volume of bone to be fragmented and ejected is defined at the moment of impact by the instantaneous propagation of a tensile cone crack in three-dimensions through the three bone laminae. However, in their analyses of the dynamics of impact to

femoral epiphyses, Huelke *et al* [15, 16] proposed that it was temporary cavitation that resulted in the formation of the conoidal wound and the more extensive damage observed at high velocity. Compelling evidence for this mechanism was provided by the fact that preliminary tests with dried femora exhibited a simple "drill hole" through the bone at velocities that produced extensive damage in normal femora [15].

This temporary cavitation theory has subsequently been used to explain how conoidal wounds form in sandwich bones [33], which have a much thinner trabecular layer than long bone epiphyses. Since high velocity impact can result in temporary cavities up to 12.5 times projectile calibre [39], it might reasonably be predicted that temporary cavitation would result in a large increase in exit surface area at high velocity due to the hydraulic bursting effect. The moderate correlation between incident velocity and the increase in surface area of the exit reported in the present study does not, therefore, substantiate this prediction. It is important to note, however, that four bones in the series did express an extreme amount of damage to both the internal and external cortical plates. This damage was so extensive that the damage encompassed the heavily curved edges of the scapulae, preventing accurate surface area determinations. In cross-section, all these specimens displayed an exceptionally thick trabecular lamina, raising the possibility that temporary cavitation might have occurred [13]. Interestingly, damage to both outer and inner cortical plates and trabeculae resulted in a double cone appearance, unlike the typical conoidal wound which flares in one direction only.

The current experimental work adopted a reductionist model and utilised the simplest projectile-target combination possible. Additional research needs to focus on the effects of projectile construction on the dynamics of impact in sandwich bones, particularly the effects of deformation and bullet shape on energy absorption profiles and quantitative wound morphology. To maximise the biofidelity of synthetic bone analogues it is critical that their dynamic behaviour match that of bone and, furthermore, that the damage morphology quantitatively replicate that observed in osseous tissue. Although several studies have found a good qualitative relationship between the behaviour of synthetic and real bone [5-9], quantitative studies are beginning to reveal some of the limitations of current synthetic systems [10-12, 40]. It is hoped that the fundamental impact data presented here will assist with the continued development of enhanced biomimetic materials for trauma experimentation.

5.6 Conclusions

1. Impact of surface hardened carbon steel spheres on porcine sandwich bones across an incremental velocity series resulted in linear relationships between incident and residual velocity and between incident and residual kinetic energy.
2. An increase in incident velocity resulted in an increase in absorbed kinetic energy according to a power function. This result is likely explained by the greater amount of fragmentation and particularly tissue ejection observed at higher incident velocities.

3. The proportion of kinetic energy lost by the projectile decreased with increasing incident velocity according to a power function.
4. Incident velocity and absorbed kinetic energy were found to moderately correlate with the surface area of the cortical exit. The correlation between the surface area of the cortical entry and both incident velocity and absorbed kinetic energy was weak and not significant.
5. The correlation between the surface area of the cortical entry and the associated exit was weak and not significant, indicating that deviations in crack path during formation of the bevel might de-couple entry size from exit size.
6. Bevelling, quantified as exit surface area/ entry surface area, was observed in all specimens. This ratio did not correlate with incident velocity or absorbed kinetic energy, indicating that intrinsic biological features of bone are paramount in determining this value.

Acknowledgements

We are indebted to Alan Peare, Andrew Roberts, Dr David Wood, and David Miller for setting up and operating the shooting and filming equipment. We are also indebted to Dr James Shackel for his help and advice concerning experimental ballistics.

Conflict of interest

The authors conform there is no conflict of interest.

Ethical approval

This study was carried out with full approval by the ethics committee of Cranfield University.

5.7. References

[1] Mota A, Klug WS, Otriz M, Pandolfi A (2003). Finite-element simulation of firearm injury to the human cranium. Comput. Mech 31: 115-121

[2] Fleiger A, Kölzer SC, Plenzig S, Heinbuch S, Kettner M, Ramsthaler F, Verhoff MA (2016). Bony injuries in homicide cases (1994-2014). A retrospective study. Int J Legal Med 130: 1401-1408

[3] Matoso IM, Freire AR, Santos LSdM, Deruge Junior E, Rossi AC, Prado FB (2014). Comparison of gunshot entrance morphologies caused by .40 caliber Smith & Wesson, .380-caliber, and 9 mm Luger bullets: a finite element analysis study. PLOS ONE 9 (10): e111192.https://doi.org/10.1371/journal.pone.0111192 [Online] Available at https://journals.plos.org/plosone/article?id=10.1371/journal.pone.0111192 (accessed 29/5/2015)

[4] Abrate S (1998) Impact on composite structures. Cambridge University Press, Cambridge

[5] Thali MJ, Kneubuehl BP, Zollinger U, Dirnhoffer R. (2002) The “skin-skull brain model”: a new instrument for the study of gunshot effects. Forensic Sci. Int 125:178-189

[6] Thali MJ, Kneubuehl BP, Zollinger U, Dirnhoffer R. (2002). A study of the morphology of gunshot entrance wounds, in connection with their dynamic creation, utilising the “skin-skull-brain model”. Forensic Sci. Int 125:190-194

[7] Thali MJ, Kneubuehl BP, Zollinger U, Dirnhoffer R (2003). A high-speed study of the dynamic bullet-body interactions produced by grazing gunshots with full metal jacketed and lead projectiles. Forensic Sci. Int 132: 93-98

[8] Kneubuehl BP, Thali MJ (2003). The evaluation of a synthetic long bone structure as a substitute for human tissue in gunshot experiments. Forensic Sci. Int 138:44-49

[9] Taylor SC, Kranioti EF (2018). Cranial trauma in handgun executions: experimental data using polyurethane proxies. Forensic Sci. Int 282:157-167

[10] Muccino E, Porta D, Magli F, Cigada A, Sala R, Gibelli D, Cattaneo C (2013). Applicability of cranial models in urethane resin and foam as a substitute for bone: are synthetic materials reliable? J. Forensic Sci. 58 (5): 1257-63 https://doi: 10.1111/1556-4029.12164

[11] Smith MJ, James S, Pover T, Ball N, Barnetson V, Foster B, Guy C, Rickman J, Walton V (2015). Fantastic plastic? Experimental evaluation of polyurethane bone substitutes as proxies for human bone in trauma simulations. Leg Med (Tokyo) 17: 427-435

[12] Raymond DE, Bir CA (2015). A biomechanical evaluation of skull-brain surrogates to blunt high-rate impacts to postmortem subjects. J. Forensic Sci. 60 (2): 370-373

[13] Rickman JM, Shackel, J (2019) A novel hypothesis for the formation of conoidal wounds in sandwich bones. Int J Legal Med 133: 501-519

[14] Rickman JM, Shackel, J (2019). Crack propagation due to low velocity projectile impact. Int J Legal Med 133: 1443-1459

[15] Huelke Df, Buege LJ, Harger JH (1967). Bone fractures produced by high velocity impacts. Am.J. Anat 20:123-132

[16] Huelke DF, Harger JH, Buege LG, Dingman HG, Harger DR (1968). An experimental study in bio-ballistics: femoral fractures produced by projectiles. J. Biomech. 1:97-105

[17] Huelke DF, Harger JH, Buege LG, Dingman HG (1968). An experimental study in bio-ballistics: femoral fractures produced by projectiles- II, shaft impacts. J. Biomech.1:313-321

[18] Harger JH, Huelke DF (1970). Femoral fractures produced by projectiles-the effects of mass and diameter on target damage. J. Biomech.1:487-493

[19] Tang Z, Tu W, Zhang G, Chen Y, Lei T, Tan Y (2012). Dynamic simulation and preliminary Finite Element Analysis of gunshot wounds to the human mandible. Injury, Int. J. Care Injured 43: 660-665

[20] Jover N, Shafiq B, Vaidya U (2014). Ballistic impact analysis of balsa core sandwich composites. Compos. Part B-Eng 67: 160-169

[21] Kneubuehl BP (2011). General wound ballistics. In Kneubuehl BP (Ed), Coupland RM, Rothschild MA, Thali MJ. Wound ballistics: basics and applications. Springer-Verlag Berlin, Heidelberg 87-161

[22] Quatrehomme G, İşcan MY (1998) Analysis of bevelling in gunshot entrance wounds. Forensic Sci. Int. 93: 45-60

[23] Wu E, Tsai C-Z (2000). Impact behaviour and analysis of CFRP laminated plates. In Reid SR, Zhou G (Eds) Impact behaviour of fibre-reinforced composite materials and structures. CRC Press, Woodhead Publishing Limited, Cambridge, England 212-238

[24] Lin LC, Bhatnagar A (1991). Ballistic energy absorption of composites-II. 23rd International SAMPE Technical Conference Oct 21-24 1991: 669-683

[25] Wambua P, Vangrimde B, Lomov S, Verpoest I (2007). The response of natural fibre composites to ballistic impact by fragment simulating projectiles. Compos. Struct. 77: 232-240

[26] Clasper and Hodgetts (1994). High velocity gunshot wound through bone with low energy transfer. Injury, Int. J. Care Injured 25 (4): 264-266

[27] Rodrigues LL, Costa ST, Rossi AC, Deruge Junior E, Prado FB, Freire AR (2018). Computational simulation of projectile injuries to human parietal bone using finite element analysis. Aust. J. Forensic Sci 51 (4): 446-454 http://doi.org/10.1080/00450618.2017.1416173

[28] Woodward RL, Gooch Jr WA, O'Donnell G, Perciballi WJ, Baxter BJ, Pattie SD (1994). A study of fragmentation in the ballistic impact of ceramics. Int. J. Impact Engng 15 (5): 605-618

[29] Woodward R, Baxter B, Pattie S, Mccarthy P (1991). Impact fragmentation of brittle materials. J. Phys. IV Colloque, 1991, 01, (C3), pp C3-259-C3-264 10.1051/jp4:1991336 jpa-00250478

[30] Beardsley CL, Bertsch CR, Marsh J.L, Brown TD (2002). Interfragmentary surface area as an index of comminution energy: proof of concept in a bone fracture surrogate. J. Biomech 35: 331-338

[31] Beardsley CL, Anderson DD, Marsh J.L, Brown TD (2005). Interfragmentary surface area as an index of comminution severity in cortical bone impact. J. Orthop. Res 23:686-690

[32] Ross AH (1996) Caliber estimation from cranial entrance defect measurements. J. Forensic Sci. 41 (4): 629-633

[33] Paschall A, Ross AH (2016). Bone mineral density and wounding capacity of handguns: implications for estimation of caliber. Int J Legal Med 131: 161-166

[34] Vermeij EJ, Zoon PD, Chang SBCG et al (2012). Analysis of microtraces in invasive traumas using SEM/EDS. Forensic Sci. Int. 214 (1): 96-104

[35] Spatola BF (2015). Atypical gunshot and blunt force injuries: wounds along the biomechanical continuum. In Passalacqua NV, Rainwater CW (eds) Skeletal trauma analysis: case studies in context.

[36] Quatrehomme G, Piercecchi-Marti M, Buchet L, Alunni V (2016) Bone bevelling caused by blunt trauma: a case report. Int J Legal Med 130 (3): 771-775 https:// doi.org/10.1007/s00414-015-1293-0

[37] Kimmerle EH, Baraybar J P (2008). Skeletal trauma: identification of injuries resulting from human rights abuses and armed conflict. CRC Press, Florida.

[38] Berryman HE, Smith OC, Symes SA (1995). Diameter of cranial gunshot wounds as a function of bullet caliber. J. Forensic Sci. 40 (5): 751-754

[39] Di Maio VJM (1999). Gunshot wounds: practical aspects of firearms, ballistics and forensic techniques. CRC Press, Boca Raton, Florida

[40] Henwood BJ, Appleby-Thomas G (2020). The suitability of synbone ® as a tissue analogue in ballistic impacts. J. Mater. Sci 55: 3022-3033

CHAPTER 6, PAPER 5

(Paper submitted to the *International Journal of Legal Medicine*)

A Scanning Electron Microscopy study of projectile entry fractures in cortical bone; genesis and microarchitectural features

John M Rickman*, Dr Jonathan Painter**, Dr Rachael Hazael***

6.1. Abstract

The present paper presents a Scanning Electron Microscope (SEM) analysis of the genesis and microarchitecture of experimentally induced cortical entry fractures in porcine scapulae impacted at velocities ranging from 54 m/s to 897 m/s. SEM observation was conducted on polyurethane replicas cast from negative silicone moulds. Analysis of the sequence of fracture processes operative during projectile impact revealed the presence of ring cracks at the site of impact, confirming that penetration in sandwich bones is achieved by cone crack propagation. Despite impulsive loading, two forms of plastic deformation were identified in the cortical bone surrounding the entry fracture up to a maximum velocity of 871 m/s. Microscopic radial and concentric cracks were associated with projectile impact and the role of pores and pits as stress concentrators was captured. Possible underlying mechanisms for the observed plastic deformation are described, and the diagnostic utility of SEM analysis is presented.

Cranfield Forensic Institute, Cranfield University, Defence Academy of the United Kingdom,

Shrivenham SN6 8LA

****Centre for Defence Engineering, Cranfield University, Defence Academy of the United Kingdom, Shrivenham, SN6 8LA*

*Corresponding author email address: j.m.rickman@cranfield.ac.uk

*Phone: +44 (0) 1793 785531

*ORCID: 0000-002-1188-8805

**Email address j.d.painter@cranfield.ac.uk

**Phone: +44 (0) 1793 785392

***Email address rachael.hazael@cranfield,ac,uk

***Phone +44 (0) 1793 785414

Keywords

Forensic anthropology, projectile trauma, ring cracking, cone cracking, plastic deformation, shock waves, hydroxyapatite crystals

6.2. Introduction

The typical fracture produced by perpendicular projectile impact in tri-layered sandwich bones exhibits a circular hole in the outer cortical layer (the *cortical entry*) and a bevel flaring in the direction of projectile travel on the exiting side [1-2]. This unique fracture type is composed of distinct morphological sub-components which for the purposes of discussion are identified and defined in **Fig.6.1** [3]. Recent work indicates that conoidal fractures are produced by propagation of a Hertzian cone crack through the three-laminae of the sandwich bone [3-4]. This translaminar fracture mechanism results in the production of tri-layered conoids of bone that typically undergo comminution during high-velocity impact, although traces may remain in the form of cortical roof and floor fragments (**Fig.6.1**). The correlation between this distinct conoidal fracture morphology and bullet involvement led to it being considered diagnostic of ballistic impact quite early in skeletal trauma analyses [2], and it is largely still considered so today [5]. However, recent case reports of conoidal fractures resulting from low-velocity impacts that did not involve bullets, discussed below, have partially reduced the diagnostic utility of this fracture morphology in identifying gunshot trauma. In addition, in skeletonised and/or fragmentary material, multiple factors can add considerable complexity to the differential diagnoses of perforating holes in skeletal elements [6].

In the first instance, potential sites of gunshot trauma in skeletonised remains must be differentially diagnosed from holes arising from congenital abnormalities, disease, and surgical alteration [7]. Taphonomic inputs can further muddy the diagnostic waters by masking or mimicking gunshot trauma. For example, animal trophic activities may damage fracture margins [8], whilst exposure to fire may produce bevelled defects resembling conoidal wounds [9-10]. Differential diagnosis may be challenging in thinner cranial bones, such as the sphenoid, which do not exhibit bevelling [6]. In such cases, a gunshot wound may be identical to holes created by other mechanisms such as the punctures created by mammalian [11] and avian scavengers [12]. Finally, fragmentation may make diagnosis difficult if only a small portion of a penetrating defect is recovered [13, 14, 15].

The cone cracking mechanism underlying bevel formation does not require projectile perforation and is also independent of impact velocity [3-4]. This common fracture mechanism across loading rates explains why bevelling has been described subsequent to lower velocity impacts with a range of implements including a bike lock [16], umbrella tip [17] and umbrella vane [5], and dictates that the cortical entry/bevel combination is not diagnostic of high-velocity trauma. The diagnostic value of radial and concentric cracks is limited by the fact they are not always present with ballistic trauma; accordingly, their absence cannot rule out bullet involvement [5]. This diagnostic complexity, coupled with a deficit in diagnostic techniques, means that current practice is to assume all traumatic bevelled perforations are gunshot wounds in the absence of evidence to the contrary [5]. Overlap of this magnitude between trauma types is readily explained by the biomechanical continuum, a concept which

considers a given traumatic fracture to be the product not just of weapon type but of multiple interacting factors such as the applied force, the surface area of the impacting object, and the rate of acceleration or deceleration [18].

The biomechanical continuum is an important concept because it highlights that sharp, blunt and projectile trauma are not absolute categories into which all traumatic features can or should be placed [19]. However, these traditional categories remain critical to law enforcement agencies due to their role in eliminating or reducing the number of potential weapons underlying a given traumatic feature [20]. It is therefore essential that further research be undertaken to investigate techniques that may be applied to enhance differential diagnosis when bones expressing a hole of ambiguous aetiology are recovered. Such techniques may be derived from one of two categories:

1. The detection of trace evidence associated with firearm discharge and/or bullet contact with bone (gunshot residue, GSR)
2. Analysis of bone trauma morphology including fracture characteristics, cortical surface features (topography) or other alterations in bone structure or organisation

To date, the majority of investigations have been conducted in the first category, and the detection of GSR on bone has proven to be quite a powerful diagnostic technique [13, 14, 15, 21]. However, the presence of trace signatures on bone is dependent on projectile type [22], firing distance [23] and taphonomic exposure [13, 21], and an absence of GSR does not rule out bullet involvement. The exacting requirements of proof in legal settings also dictates that GSR is of no use if environmental contamination cannot be ruled out [15].

At present there is no macroscopic method to accurately determine projectile velocity from bone trauma morphology, in large part due to the multiple intrinsic and extrinsic factors that determine the nature and extent of fracture [24]. However, when considering the utility of alteration in bone morphology as a diagnostic indicator it is important to note that bone is a complex hierarchical material with seven levels of organisation spanning from the nanoscale (hydroxyapatite crystals and collagen fibres) to the macroscale (the whole bone) [25]. Whilst analysis at the macroscale can reveal important information about skeletal trauma it cannot, in isolation, detect alterations at microstructural scales. In the first instance, fracture propagation does not just occur through the macrostructural features of bone; rather, the crack tip propagates through the microstructural features of bone. Moreover, high-velocity projectile impact exposes bone to a unique set of conditions characterised by extreme stresses acting in short time spans [26], shock-wave propagation [27-28] and frictional heating [28]. Considering these intense conditions, it is reasonable to ask if there might be a scale at which high-velocity impact results in detectable changes in bone structure and/ or morphology that would enable enhanced differential diagnosis of gunshot trauma.

At present, our understanding of the microstructural features of cortical entry fractures is limited and the analyses that have been conducted have all utilised a narrow range of impact velocities. Scanning Electron Microscopy (SEM) formed a prominent component of all these studies due to its great depth of field, high resolution, and large magnifying power which make it eminently suitable for surface analysis. Speeter and Ohnsorge [29] impacted 49 human femora and found that shot direction was recorded at the microscopic scale in both cortical and trabecular bone. Significantly, these authors also reported striated abrasions resembling bullet rifling marks in the cortical bone. Gaîdash *et al* [30] utilised SEM and atomic force microscopy (AFM), in addition to spectroscopic and nanohardness measurements, to analyse cortical entry fractures in human bones. These authors reported an increase in porosity of the cortical bone, which they termed shock- wave osteoporosis, and a decrease in bone hardness towards the perforated region which they attributed to shock-wave induced changes in the mineral phase of the bone matrix. More recently, Keiser *et al* [31] impacted pig ribs with .22 handgun bullets and analysed the wound perimeter with SEM. These authors described areas of smoothed cortical bone on the entry cortical fracture edge (EnCF) which they attributed to frictional melting of the hydroxyapatite.

Rickman and Smith [6] utilised SEM to analyse experimentally induced conoidal wounds in bovine scapulae with two types of rifle ammunition (soft point and full metal jacket, FMJ) and a captive bolt gun. Large microcracks were observed emanating from the EnCF in both soft point and FMJ wounds, and entry-exit and side to side directionality were recorded in deviations of microscopic bone fragments. Although the loading rates experienced during high-velocity impacts should result in brittle fracture [32], a notable morphological feature produced by the FMJ projectiles and captive bolt impacts was a conspicuous plastic deformation of sections of the perimeter of the cortical entry in the direction of projectile travel. The mechanism or mechanisms underlying this paradoxical plastic deformation currently remain unknown, as does the full extent of its distribution around a single cortical entry.

In order to examine the micro-morphology of cortical entry fractures and to identify features that might be of potential diagnostic utility, the present paper presents the findings of an SEM analysis of projectile fractures induced in the cortical bone of porcine sandwich bones at impact velocities ranging from 54 m/s to 897 m/s. Since the fracture mechanisms operative during cortical entry formation may themselves be of diagnostic utility, the sequence of fracture events occurring during penetration and perforation are presented. This is followed by an analysis of the effects of projectile impact on cortical bone at and adjacent to the cortical entry. The significance of these findings in relation to differential diagnosis are then discussed.

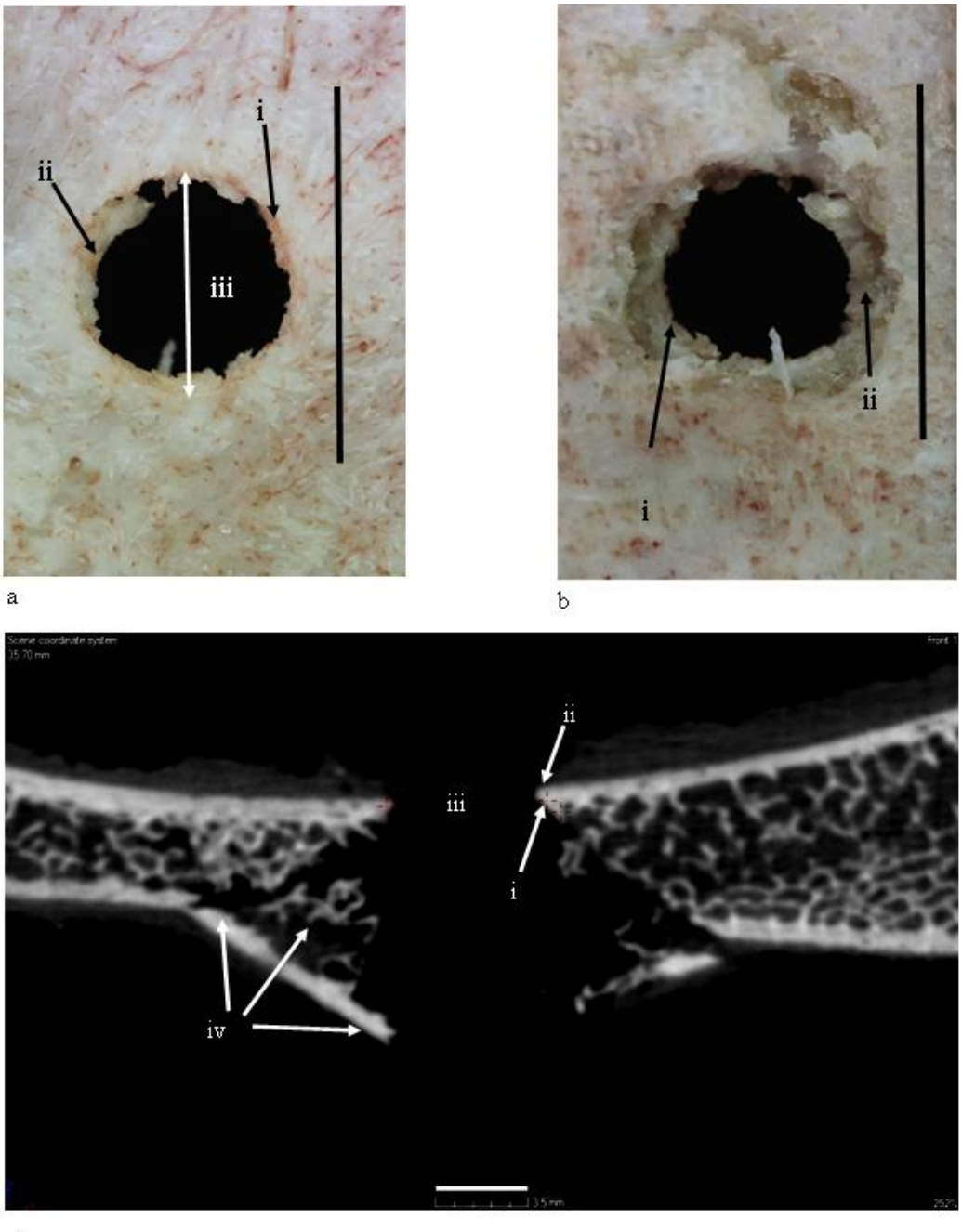

Fig.6.1 Key nomenclature for the components of a bevelled fracture in sandwich bones; **a-b**, 163 m/s perforating impact (scales bars 10 mm); **a**, **i**, apex of the entry cortical fracture edge (EnCF); the top edge of EnCF where the cortical fracture edge and cortical surface meet; the EnCF itself runs under the apex and is not visible from above; **ii**, cortical roof fragment; fragmentary component of the conoid roof remaining *in situ* after fragmentation and ejection of the bulk of the conoidal volume; the distal edge faces the cortical entry and the medial edge the cortical surface; **iii**, cortical entry; delineated in cross-section by the EnCF and in surface view by the apex of the EnCF; **b**, same cortical entry as in seen in **a** but from the bevel side; **i**, EnCF angling away from the apex; **ii**, underside of the cortical roof fragment

seen in **a**; **c**, 158 m/s perforating impact, µCT cross-sectional view showing internal structure; (scale bar 3.5 mm) i, EnCF, ii, apex of the EnCF, iii, cortical entry; iv, fragment of conoid

6.3. Methods

6.3.1. Sample, shooting equipment and specimen preparation

The specimens utilised for SEM analysis formed part of a previous experimental series that was subjected to micro-computerised tomographic (µCT) and videographic analyses; detailed descriptions of methodology can therefore be found elsewhere [3, 4]. Adult (12-14 month) porcine (*Sus scrofa domesticus*) scapulae were selected for impact due to their sandwich construction and the fact they express conoidal fractures when impacted by projectiles. Histologically, artiodactyl bone is largely of fibrolamellar organisation and thus differs from the secondary osteons found in adult human bone. However, the laminated morphology of fibrolamellar bone is broadly comparable to the layered, fibrous sheets of bone that form the superficial layer of cranial vault bones [33]. Scapulae were sourced from animals humanely killed as part of the food chain. The infraspinous fossa was chosen for the target area due to its larger size, and only specimens with a covering of soft tissue in this fossa were selected. Each scapula was machined on a bandsaw to provide relatively uniform plates for impact. Specimen size after cutting was determined by scapula dimensions and robusticity but was typically 12 cm high by 13 cm wide; all specimens were large enough to ensure the selected impact point was a minimum of 3 cm from an edge to eliminate shock-induced edge effects. Specimens were stored frozen prior to impact and defrosted the day of the experiment.

To eliminate confounding variables introduced by projectile shape and deformation on perforation mechanisms, 6 mm surface hardened carbon steel spheres were utilised (Atlas Bearings LTD, UK). A compressed air gun with 6 mm barrel was utilised to impact specimens from 54m/s to 96 m/s, whilst a 21.3 mm calibre gas gun using sabot-mounted projectiles impacted specimens from 149-168 m/s. Incident velocities from 333 m/s to 897 m/s were achieved using the 21.3 mm gas gun (333 m/s) or an Enfield number 2 projectile housing (591-897 m/s), again using sabot mounted projectiles. All impacts were filmed from the side with a scale for determining incident (pre-impact) and residual (post-impact) velocities. Individual velocities for each impact were calculated from three repeat measurements in Phantom Cine viewer software.

Subsequent to impact, specimens were photographed and re-frozen to prevent soft tissue degradation while specimens awaited analyses. Previous µCT comparison of pre-and post-freeze damage architecture in control specimens revealed no difference in fracture patterns after freezing [3]. For SEM analysis, specimens were defleshed by cold water maceration in open plastic tubs under a fume hood. Bulk soft tissue was carefully removed prior to immersion to leave as little as possible for the maceration period. Specimens were photographed prior to an immersion of 7 days. After this period, soft tissue was carefully removed using a scalpel, metal scraper, and plastic and wood implements; only the latter two were used in closer proximity to the cortical entry. Great care was taken to avoid tool

marks on the bone by avoiding their use in an area of approximately 1-1.5 cm around the cortical entry. After cleaning, specimens were photographed, air dried for 7 days and then re-frozen to prevent further degradation of the organic and mineral phases while other specimens underwent maceration. In total 26 specimens were utilised for analysis; 22 of these were perforated specimens whilst four were depressed factures caused by re-bound impact (two impacted fleshed and two impacted defleshed for filming). One perforated specimen was utilised as a test bone to perfect the replication technique.

6.3.2. SEM negative moulding and positive casting

All machined specimens were too large to fit in the SEM chamber and it was therefore necessary to make replicas of the cortical entries for analysis in the SEM. Replication was achieved using Isomark T-2 grey silicone impression material (Isomark LTD, Leicestershire, United Kingdom). T-2 was selected as its longer working life (3 minutes at 20^{o}C) which allowed multiple specimens to be replicated before the silicone cured in the applicator nozzle. Silicone was applied using the 50 ml cartridge system and applicator gun with attached mixing nozzle.

In order to cast both the EnCF and surrounding cortical surface, it was necessary to form a floor to the cortical entry. Testing revealed that the most cost effective and simple material for this purpose was adhesive wall putty, which is readily available from stationary suppliers. Loose cortical floor fragments that obstructed cortical entry access via the bevel were removed where possible. A portion of putty was rolled into a ball and one end then rolled tighter until it was just slightly larger than the cortical entry. A round- ended clay sculpting tool was then used to form a slight indentation in the end of the elongated portion. The putty was then introduced through the bevel and, viewing from the cortical entry side, pushed into place such that the edges of the putty indentation approximated the lower aspect of the EnCF. Larger gaps between putty and EnCF, which sometimes formed due to irregularity in bone morphology on the bevel side, were removed as much as possible by very carefully placing a round ended sculpting tool through the cortical entry and gently nudging the putty to reduce the size of the gap. At all times, great care was taken not to touch the EnCF with the tool or putty.

Specimens were subsequently placed on a flat surface and the T-2 introduced as close to the putty floor as possible; enough was added to create a raised protrusion of T-2 approximately 5 mm or more above the cortical entry. A square section of clear 0.5 mm thick plastic measuring 15 mm x 15 mm was then used as a cover slip to gently press down on the T-2. This gentle pressure ensured the impression material spread over the cortical surface and also provided a flat back to the negative mould. To ensure that curing had occurred, a small quantity of T-2 was placed on the cortical surface of the specimen without a cover slip, thus enabling its hardness to be felt. The mould was photographed in position and, when cured, the top was marked with a coloured dot. When removing the moulds, the putty was detached first to prevent pinching of the negative mould against the bone; the silicone moulds were then carefully removed and placed in small re-sealable plastic containers.

Negative silicone moulds were cast to positive replicas using Easy Flo 60, a two part (A and B) cold curing polyurethane resin (Polytek Development Corp, Pennsylvania). Positive replicas were cast in circular pots with a removable floor. Negative moulds were stuck to the removeable pot base using double sided sticky tape; to maintain specimen orientation, the top of the replicated entry fracture was marked on the outside of the pot with a sticky label. Equal parts A and B were mixed and gently stirred for one minute before pouring into the pots; the resin was then allowed to cure for 90 minutes. To enable orientation in the SEM, the top of the cortical entry was marked on the reverse side of the replica after curing. Positive replicas were then stored in individual plastic containers and left to fully cure for 7 days before analysis. Replicas were analysed in a Hitachi SU 3500 SEM in variable pressure mode (80 Pa) with and acceleration voltage 20 kV; working distance depended on replica height but was typically between 8-12 mm. Replicas were examined in both 3D backscattered electron (BSE-3D) and backscattered electron topographic (BSE-TOPO) mode utilising Hitachi's 5 segment backscatter detector. Typical cortical surface features with which fractures and other failure mechanisms interacted were examined and documented using areas of cortex peripheral to the cortical entry.

6.3.3. Nomenclature for analysis

To accurately convey the orientation of structural features in the SEM images the nomenclature presented in **Fig.6.1** was utilised for analysis. The *entry cortical fracture edge* (EnCF) meets the cortical surface at the *apex* (**Fig.6.1a, c**), which defines the cortical entry when viewed from above. When viewed from below (**Fig.6.1b**) and in cross- section (**Fig.6.1c**) the cortical entry is circumscribed by the EnCF. The tri-layered conoid formed by impact consists of a *cortical roof* and *cortical floor* with the trabeculae in between [4]. This conoid typically undergoes comminution but can leave behind traces in the form of cortical roof and floor fragments. When present, the *medial edge* of cortical roof fragment faces the EnCF, whilst the *distal edge* faces into the cortical entry.

6.4. Results

6.4.1. Cortical surface features

The cortical surface of *Sus* scapulae presented varying degrees of *sculpturing* consisting of ridges combining to form a distinct tessellated pattern. This sculpturing varied from minimal (e.g., **Fig.6.2 a** and **b**) to pronounced (e.g., **Fig.6.2.c**) across specimens. The cortex was punctuated intermittently by cortical pits (with a floor) and cortical pores (leading to a lumen), occasionally associated with a channel running along the cortical surface. Porosity varied across specimens, with some displaying few pores and some presenting with an abundance of them. The cortical surface showed no abrupt topographic change in slope from one region to another and there were no distinct muscle attachment points in the outer cortical plate of any specimens.

6.4.2. Casting artefacts; recognition and causation

Air bubble artefacts were introduced during the positive casting stage due to both the mixing process and exothermic curing. Small air bubbles, when present, were easily differentiated from cortical pores by their sharp edge and lack of internal morphology and did not influence feature identification. Larger air bubbles occasionally formed in portions of the cortical entry and, when present, prevented replication of surface detail and feature identification. Comparison of micrographs to macro photographs indicated that these larger bubbles may be associated with re-entrant geometries or large pores or depressions along the EnCF. Detail replication adjacent to these larger bubble artefacts was normal.

6.4.3. Genesis of the cortical entry in sandwich bones

Rebound impact (impact velocities from 54-57 m/s) resulted in the formation of depressed discs of cortical bone, with previous work with μCT indicating that these form the cortical roof of tri-layered conoids if there is sufficient energy to drive fracture through all three sandwich bone laminae [4]. In all four rebound specimens both plastic deformation and Hertzian fracture were operative under the impacting sphere and both processes were responsible for formation of the concavity. Plastic deformation was often pronounced, with the plastically deformed zones descending steeply downwards to the base of the compressed region (**Fig.6.2, a-b**). Plastic deformation occurred without formation of visible microcracks at the cortical surface, suggesting cracking was either too small to detect with the impression media or that an alternative failure mechanism is operative in the cortical bone.

Fracture in the compressed region in 3 of the 4 rebound impacts took the form of distinct circumferentially orientated *ring cracks* which occupied parts of the circumference, rather than completely encircling it (**Fig.6.2, a-b**). Impact resulted in multiple generations of ring cracks extending from inside to outside of the cortical discs (**Fig.6.2b**), with each ring crack formed successively at the widening contact radius of the projectile as it penetrated deeper into the cortex. In the fourth specimen, nascent concentric ring cracks less than 400 microns in length were observed emanating from cortical pores near the edge of the compressed region, indicating these had acted as stress concentrating flaws during impact (**Fig.6.2c**). Separation of cortex at the ring cracks contributed to the observed compression of the cortical roof. Apparent ring cracks were also preserved on a section of cortical roof fragment resulting from a 96 m/s perforating impact (**Fig.6.2d,** black arrows at right). Radial cracks arising normal to the apex of the EnCF were observed in one fleshed 54 m/s rebound impact (5 cracks) and one defleshed 57 m/s impact (2 cracks). All were less than 500 μm in length apart from one large, approximately 1 mm crack in the cortex peripheral to the EnCF in the defleshed impact.

Initial failure of the cortical roof in both rebound and perforating impacts occurred via a fracture arising normal to the free fracture margin of the roof; this process was observed in both a rebound impact (**Fig.6.3a**) and in the cortex of a relatively intact tri-layered conoid. In the latter case, the conoid had been displaced downwards and tilted so that the cortical roof was lower than the inner cortical layer (**Fig.6.3b**). Despite this displacement, the surface sculpturing was not altered due to contact with the

projectile. The same was true of the cortical surfaces of the two defleshed specimens subjected to rebound impact.

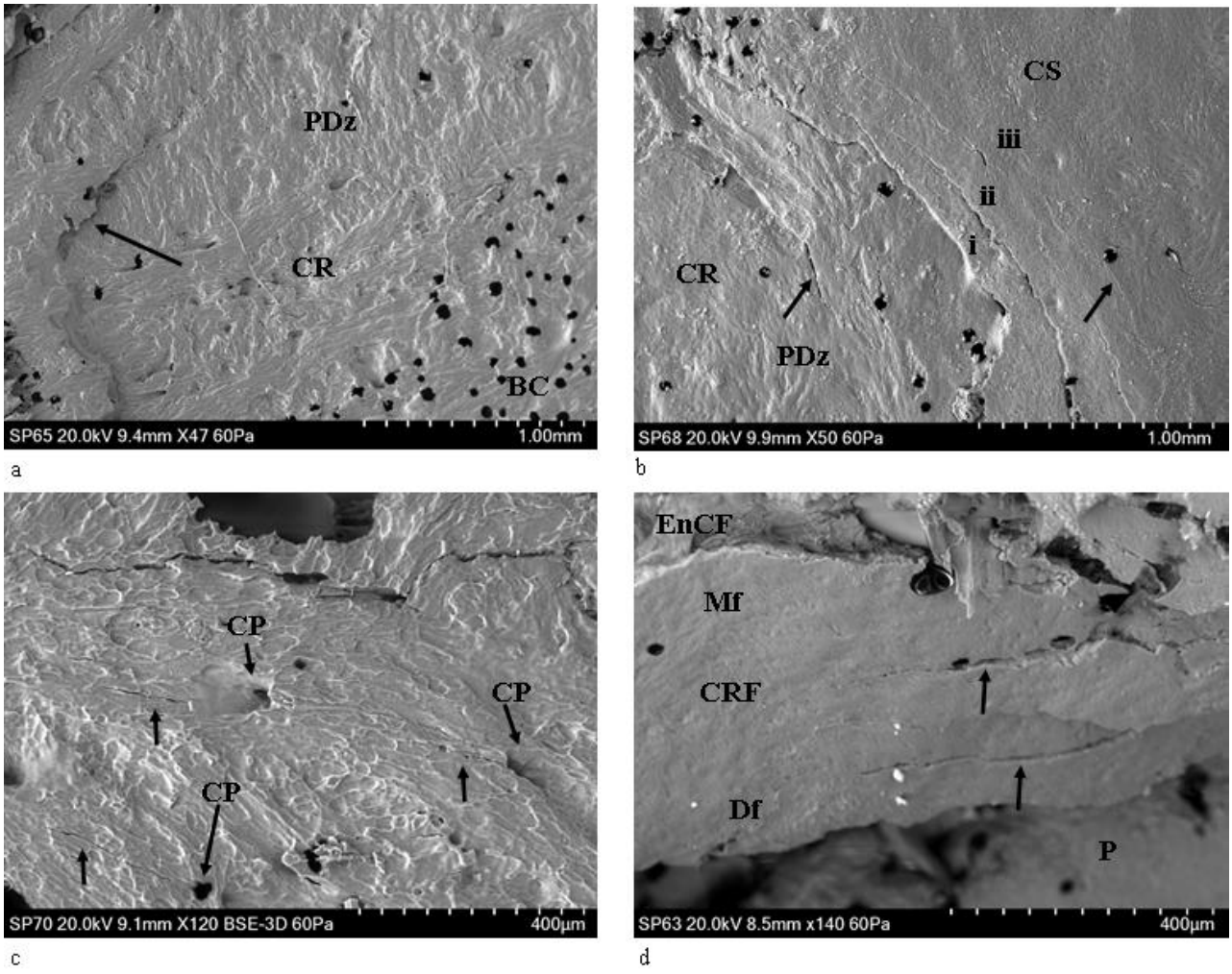

Fig.6.2 Genesis of the cortical entry in sandwich bones; plastic deformation and ring cracks (CS, cortical surface; CR, cortical roof; CRF, cortical roof fragment; Mf, medial fracture edge of cortical roof fragment; Df, distal fracture edge of cortical roof fragment; P, putty used to seal the floor of the entry); **a**, 54 m/s rebound impact (fleshed specimen), CS located just out of view top left and across the top of the micrograph; micrograph indicates extensive plastic deformation is involved in formation of the concavity (PDz); a ring crack is visible at left (arrow) with the base of the concavity located at the bottom right (BC); **b**, 57 m/s rebound impact, (fleshed specimen), micrograph of the right edge of a depressed fracture showing three generations of larger ring cracks (annotated i-iii); and two smaller cracks (arrowed); deformation forming the cavity occurs both along the ring crack fracture margins and in plastically deformed zones without visible fracture; **c**, ~57 m/s impact (defleshed specimen) showing cortical surface adjacent to impact site (located along top of micrograph); concentrically orientated nascent ring cracks (white arrows) can be seen arising from cortical pores (CP); **d**, 96 m/s perforating impact; cortical roof fragment with the distal edge displaced downwards into the cortical entry and displaying concentric fractures consistent with ring cracking during the initial stages of impact (arrows)

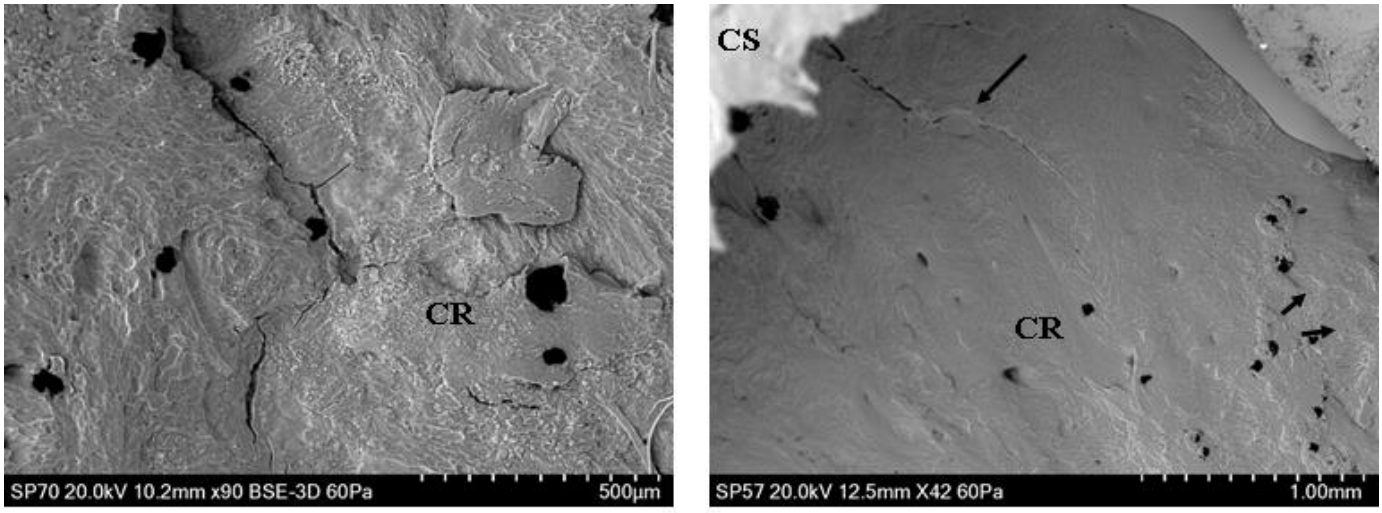

a b

Fig.6.3 Genesis of the cortical entry in sandwich bones; failure of the cortical roof (CS, cortical surface; CR, cortical roof); **a**, ~57 m/s rebound impact (defleshed specimen); surface of cortical roof showing vertically orientated fracture dividing the roof into two halves; fracture resulted from tensile failure of the inner surface of the cortical plate under compressive loading; **b**, 75 m/s perforating impact, view of the cortical roof of a nearly intact conoid displaced downwards so it is beneath the cortical surface and protruding from the inner cortical plate; the surface has not been modified by impact but bears a fracture ending before the mid-section (arrow)

Examination of the medial margin of both the cortical roof and cortical roof fragments in perforating impacts revealed some degree of stepping of the fracture edges resulting from mode I, tensile failure during cone crack propagation across the lamellae composing the fibrolamellar bone. This stepped morphology was observed on the margin of the cortical roof resulting from both rebound (**Fig.6.4a**) and perforating impacts (**Fig.6.4, b-d**). The stepped edges were either composed of pointed, overlapping lamellar components (**Fig.6.4, b-c**) or presented a more uniform stepped morphology (**Fig. 6.4d**). The pointed lamellar morphology is illustrated in **Fig.6.4b**, which shows the lower right margin of the cortical roof of the intact conoid seen in **Fig.6.3b**. In this part of the conoid the stepped region was angled to match the corresponding angulation of the EnCF, and the overlapping pointed lamellar fracture edges produced a complex fracture surface. This morphology may have resulted from the plane of the crack in relation to the lamellar structure in that region or from a pull-out process as the conoid was compressed downwards. Stepped fracture margins with pointed fracture edges were also observed on a smaller scale in a fragment of cortical roof resulting from a 94 m/s impact; in this specimen, the pointed ends of the lamellae revealed the differing orientations of individual lamellae in successive layers (**Fig.6.4c**, black arrows).

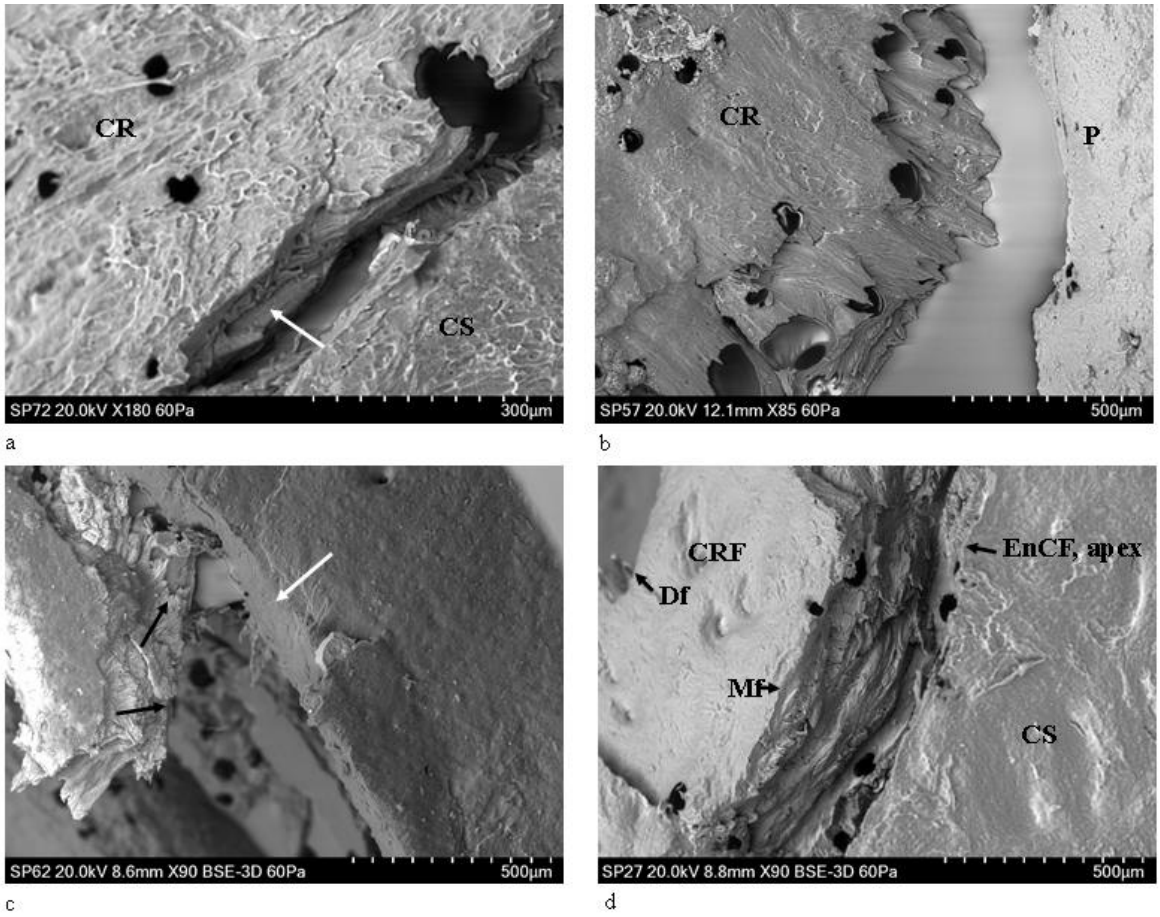

Fig.6.4 Genesis of the cortical entry in sandwich bones; stepping of the cortical roof (CS, cortical surface; CR, cortical roof; CRF, cortical roof fragment; Mf, medial fracture edge of cortical roof fragment; Df, distal fracture edge of cortical roof fragment; P, putty used to seal the cortical entry for negative moulding; EnCF, entry cortical fracture edge); **a**, ~57 m/s rebound impact (defleshed specimen), mode I (tensile, crack opening) fracture mode indicated by stepping of the fracture edge across lamellar planes inside the cortical roof (arrow); **b**, ~75 m/s perforating impact showing right fracture edge of the cortical roof of the nearly intact conoid seen in **Fig.6.3b**, complex stepped morphology resulting from mode I fracture across lamellae; fracture edge is angulated to match the corresponding angulation of the EnCF; **c,** 94 m/s perforating impact, cortical roof fragment with the distal surface facing upwards and displaying internal lamellae on the medial side orientated in different planes (highlighted by the small arrows); large arrow indicates an area of smooth bone consistent with being surface-modified plastic deformation; **d**, 161 m/s perforating impact showing cortical roof fragment with pronounced stepping across the lamellae of the medial fracture margin.

6.4.4. Plastic deformation of the cortex

In addition to the plastic deformation seen in the rebound impacts, analysis of the apex of the EnCF and adjacent cortical surface revealed that the cortex underwent plastic deformation in perforating impacts, including two at over 850 m/s. Plastic deformation in this region occurred in two distinct forms, which were identifiable based upon morphology and location. *Surface-modified plastic deformation (SPD)* (**Figs.6.5-6.6**) was characterised by loss of surface sculpturing and varying extents of downward deformation (bending) without visible fracture. SPD was entirely restricted to the *projectile-bone interface*, being found only at the apex of the EnCF and the surfaces of cortical roof fragments inside the cortical entry. *Peripheral plastic deformation* involved the cortical surface peripheral to the apex, with the cortical surface typically remaining unmodified or partially modified (**Fig.6.7**). These different types of plastic deformation are discussed below.

6.4.4.1 Surface-modified plastic deformation

In total, SPD was identified in 18 of the 21 perforated specimens spanning a velocity range from 73 to 871 m/s. SPD, which was localised around the apex rather than occupying the full circumference, was characterised by the gradual loss of surface sculpturing at the apex of the EnCF with an eventual *transition zone* where the ridges blended with smooth areas of cortical bone at the projectile-bone interface. This transition zone is illustrated in specimens impacted at 74-75 m/s **Fig.6.5, a-b** and in specimens impacted at 148-333 m/s in **Fig.6.6, a-b**. Additional features of SPD, present to varying extents in each affected region, were a compressed, deformed cortex and down-bending in the absence of visible fracture. These features are illustrated in a 96 m/s impact in **Fig.6.5 c** and in a 591 m/s and 609 m/s impact in **Fig.6.6 c-d,** respectively. The down-bending associated with SPD resulted in a ductile morphology at the apex of the EnCF. **Fig.6.5d** shows a cortical roof fragment where bending was extensive enough to allow it to descend into the cortical entry without visible fracture at the top edge (**B** in the image). Areas of SPD sometimes showed circumferential fractures running along the modified cortical surface (**Fig.6.6c**); these were indistinguishable from ring cracks when they were of large size.

Fig.6.3 Genesis of the cortical entry in sandwich bones; failure of the cortical roof (CS, cortical surface; CR, cortical roof); **a**, ~57 m/s rebound impact (defleshed specimen); surface of cortical roof showing vertically orientated fracture dividing the roof into two halves; fracture resulted from tensile failure of the inner surface of the cortical plate under compressive loading; **b**, 75 m/s perforating impact, view of the cortical roof of a nearly intact conoid displaced downwards so it is beneath the cortical surface and protruding from the inner cortical plate; the surface has not been modified by impact but bears a fracture ending before the mid-section (arrow)

The contrast between the cortical surface in the immediate cortical landscape and SPD along the apex is illustrated in **Fig.6.6d**. In this example, the cortical surface adjacent to the apex was markedly sculpted; this morphology contrasted greatly with the region of SPD which showed complete loss of sculpturing, bending without visible fracture and a compressed, smoothed appearance.

6.4.4.2 Peripheral plastic deformation (PPD)

PPD was detected in 7 of the 21 perforated specimens with an impact velocity range of 73 m/s to 591 m/s. In common with SPD, PPD did not occupy the full circumference of the cortical entry and was localised in distribution. PPD was characterised by down bending of the cortex a variable distance peripheral to the apex of the EnCF with little to no alteration to cortical sculpturing. As a result of this process, the apex was characteristically lower than the cortical surface. The sloping associated with PPD imparted a ductile morphology to the periphery of the cortical entries in affected regions (**Fig.6.7**). PPD was identified at the attached ends of cortical roof fragments (**Fig.6.7, a-b**) and diffusely around the margins of the apex (**Fig.6.7, c-e**). The slope induced by plastic deformation varied from being gradual (**Fig.6.7a**) to steep, and in the latter case the area where bending initiated could be easily identified as a distinct fold (**Fig.6.7, b-f**). The ductile morphology induced by PPD when it occupied a larger portion of the circumference of the cortical entry is shown in **Fig.6.7c**, where the bending at left is approximately 1 mm long. **Fig.6.7d** shows an image of a specimen impacted at 570 m/s, which exhibited a very steep deformed region. In this case the fold was well defined, and the slope steep enough for the apex of the EnCF to nearly contact the putty which was situated lower than the outer cortical plate (located at the right of the image). Continuity of the cortical surface to a deformed region is shown in **Fig.6.7e**, which shows a small area of PPD from above and at x300 magnification in a specimen impacted at 591 m/s. Topographic view of the same region highlights both the extent of sloping and the continuity of the cortical surface across it (**Fig.6.7f**).

6.4.5. Cortical morphology when SPD and PPD were absent

Neither SPD or PPD were distributed uniformly around the whole circumference of the cortical entries and when absent the EnCF presented with abrupt edges (**Fig.6.8a**) or complex edges with re-entrant geometries between fragmented cortical components (**Fig.6.8b**).

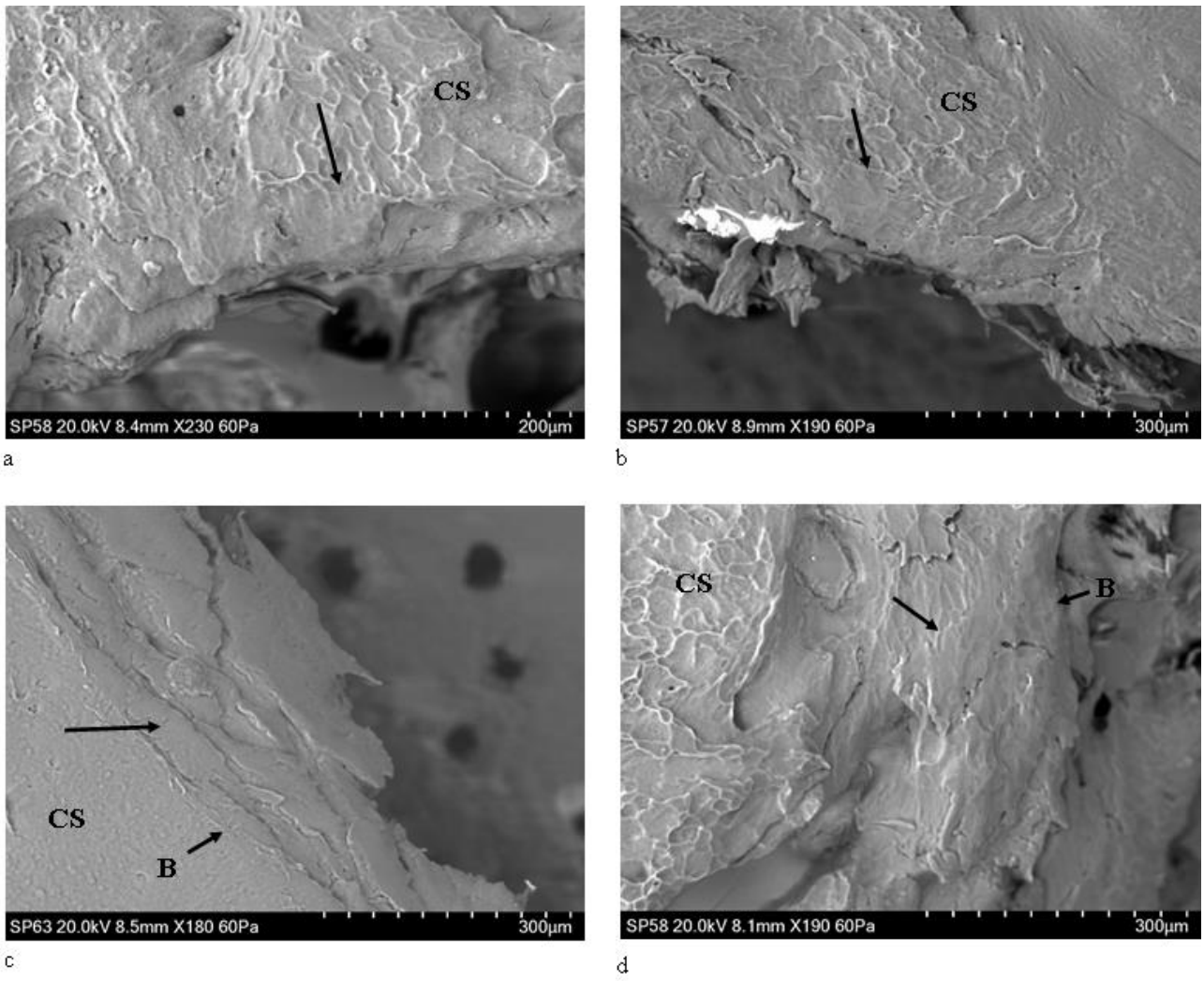

Fig.6.5 Surface-modified plastic deformation (SPD), 74-96 m/s perforating impacts (CS, cortical surface); **a**, 74 m/s impact showing SPD with transition of cortical sculpturing to smooth zone (black arrow); **b**, 75 m/s impact showing area of SPD with cortical sculpturing fading out at the point indicated by the arrow; bending results in a ductile morphology at the apex of the EnCF; **c**, 96 m/s impact with SPD showing compressed, deformed cortex (top black arrow) and bending without fracture (B) leading to a ductile morphology; **d**, same specimen as in **a** showing SPD on a descending fragment of cortical roof, arrow indicates the point at which cortical sculpturing fades; bending at B is extensive enough to allow the fragment to descend into the cortical entry without fracture

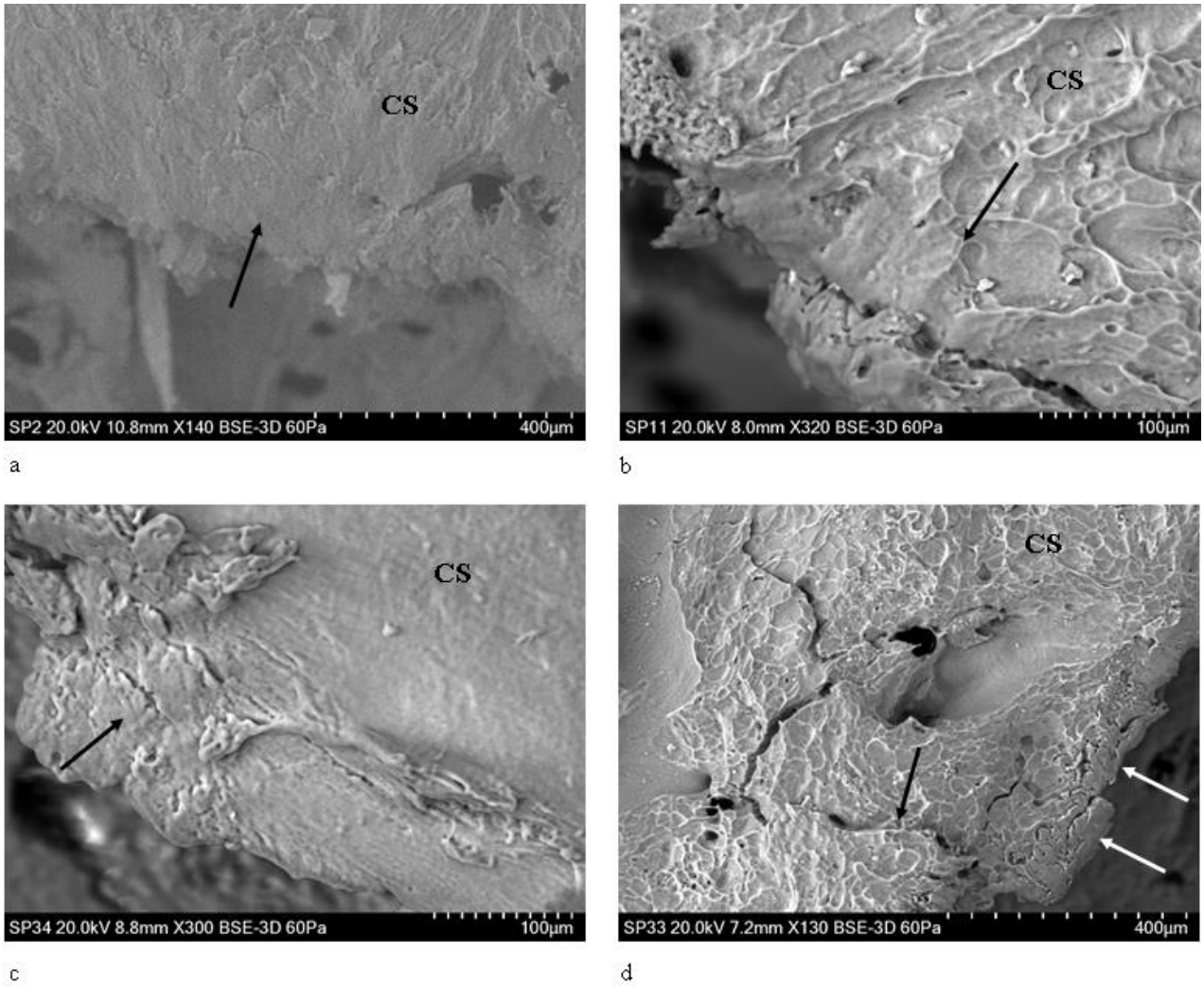

Fig.6.6 Surface modified plastic deformation (SPD), 149-609 m/s perforating impacts (CS, cortical surface); **a**, 148 m/s impact showing loss of surface detail (arrow); **b**, 333 m/s impact showing SPD with transition of cortical sculpturing (arrow), **c**, 591 m/s impact showing SPD (black arrow) with small transverse fractures; **d**, 609 m/s impact showing SPD along the apex of the EnCF (lower white arrows) in relation to the immediate cortical landscape; note the radial crack emanating from the EnCF (black arrow).

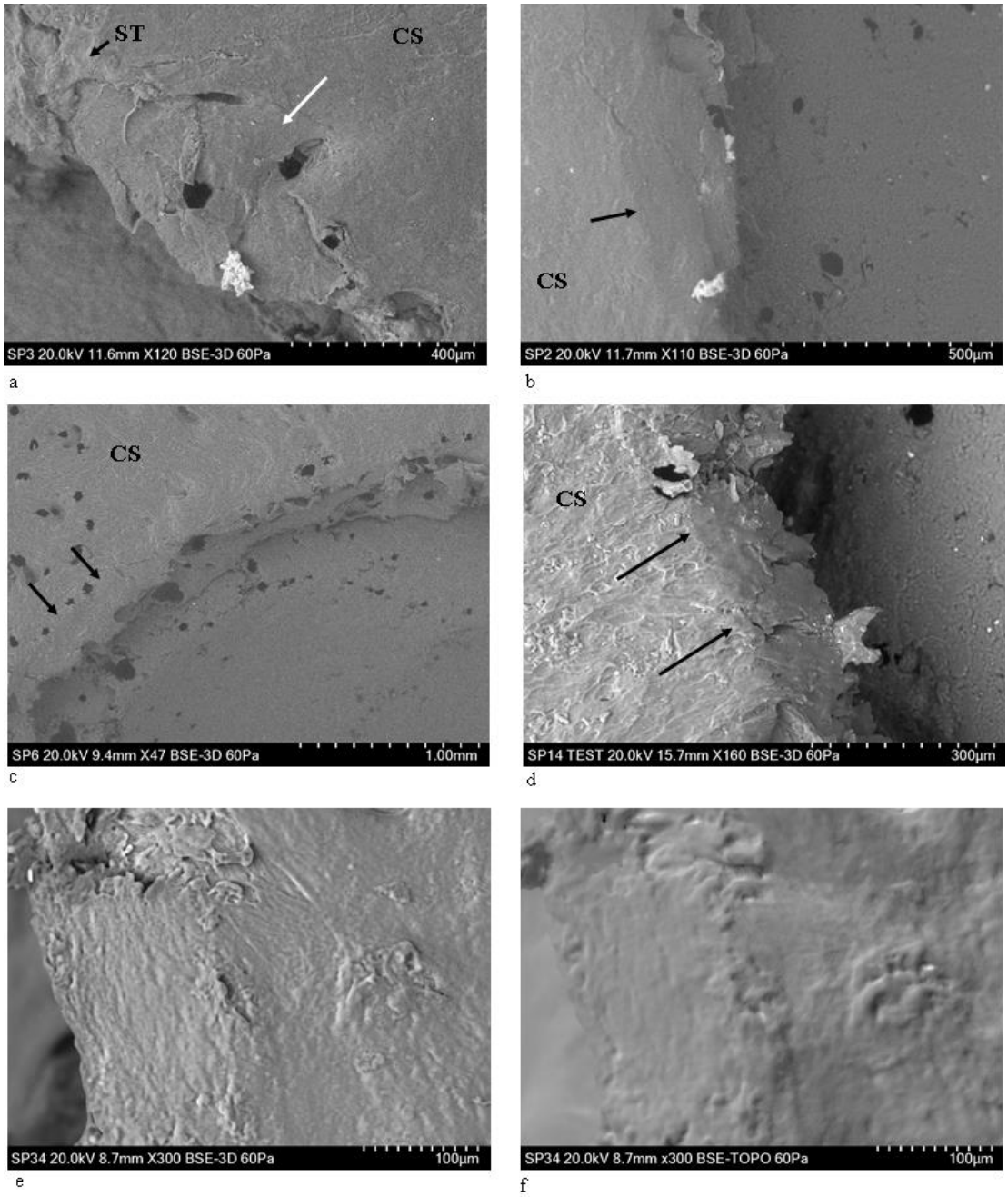

Fig.6.7 Peripheral plastic deformation and associated ductile morphology (perforating impacts), (CS cortical surface; ST, soft tissue); **a**, 163 m/s impact showing small area of plastic deformation with intact surface sculpturing; note that the CS is continuous with the bent section of bone (white arrow); **b**, 149 m/s impact, area of plastically deformed bone with intact surface sculpturing and fold identified by arrow; this area is at the lower edge of a section of cortical roof fragment; **c**, 165 m/s impact showing margin of cortical entry with cortical bending due to plastic deformation, particularly at the area identified by black arrows; **d**, 570 m/s impact; area of plastic deformation with the fold identified by arrows; note that this region combines pronounced cortical sloping with some surface modification; **e**, 591 m/s impact, showing continuity of the cortical surface with the plastically deformed region; **f**, topographic view of **e** confirming bending of the cortex

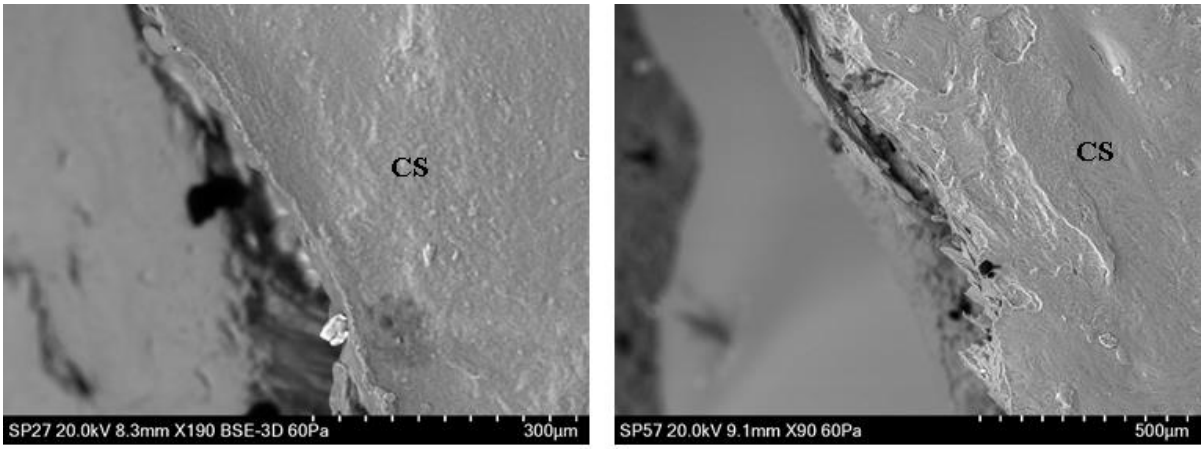

Fig.6.8 Apex of the EnCF in non-plastically deformed zones, perforating impacts (CS, cortical surface); **a**, 161 m/s impact, abrupt and straight-edged apex; **b**, 75 m/s impact showing more complex fracture morphology with re-entrant geometries; both fracture edges seen here differ markedly from zones of SPD and PPD

6.4.6. Radial cracks; perforating impacts

Radial cracks were observed in 19 of the 21 perforated specimens across the velocity series (illustrated for impacts from 591-871 m/s in **Fig.6.9, a-d**). Radial cracks were identified in 12 of the 14 impacts between 58-168 m/s and in all 7 impacts between 333-897 m/s. Radial cracks followed both relatively straight (**Fig.6.9, a-b**) and tortuous (**Fig.6.9c**) paths. Tortuosity was not clearly associated with velocity; for example, the tortuous crack in Fig.9c was associated with a 609 m/s impact, whilst the straight crack in **Fig.6.9b** was created by an 850 m/s impact. Some of the radial cracks exhibited uncracked ligament bridging despite high impact velocity (e.g., white arrow in **Fig.6.9a**). Radial cracks ranged from being narrow (**Fig.6.9a**) to open (**Fig.6.9, b-d)** and occasionally exhibited bifurcations along their path (**Fig.6.9,c-d**, arrows). Estimates of crack length using the scale in the images indicated that radial cracks >1 mm in length were more common in high-velocity impacts. Of the 14 perforated specimens impacted between 58-168 m/s, only three possessed radial cracks longer than 1 mm (impacted at 58 m/s, 165 m/s, and 167 m/s, respectively). In contrast, a total of 4 out of 6 specimens impacted between 333-897 m/s had radial cracks greater than 1 mm in length (impacted at 591 m/s, 850 m/s, 885 m/s and 897 m/s).

6.4.7. Circumferential cracks and cracks arising from cortical stress concentrators

Circumferential cracks were identified in a total of 9/14 impacts between 58-168 m/s and 4/7 impacts between 333-897 m/s. These cracks were found both near the apex of the EnCF (**Fig.6.10, a-b**) and further away in the cortical landscape; in one case, a concentric crack was found approximately 1.5 mm from the cortical entry. Unlike the rebound impacts, circumferential cracks in the perforating impacts did not appear to form concentric generations but were dispersed diffusely around the cortical entry. Cortical pits and pores acted as stress concentrators during impact and were detected as the origin for some circumferential (**Fig.6.10c**) and radial (**Fig.6.10d**) cracks. In elliptical pores, stresses acting

normal to the major axis resulted in cracking at each end due to concentration of stresses there (**Fig.6.10e**). Pore and pit cracks did not always occur in isolation, with an example of a linked pore-crack complex occurring in an 871 m/s impact (**Fig.6.10f**). Cortical pore cracking occurred both near the apex of the EnCF (**Fig.6.10a and b**) and more distant, with the pore in **Fig.6.10e** being over 1 mm away from it.

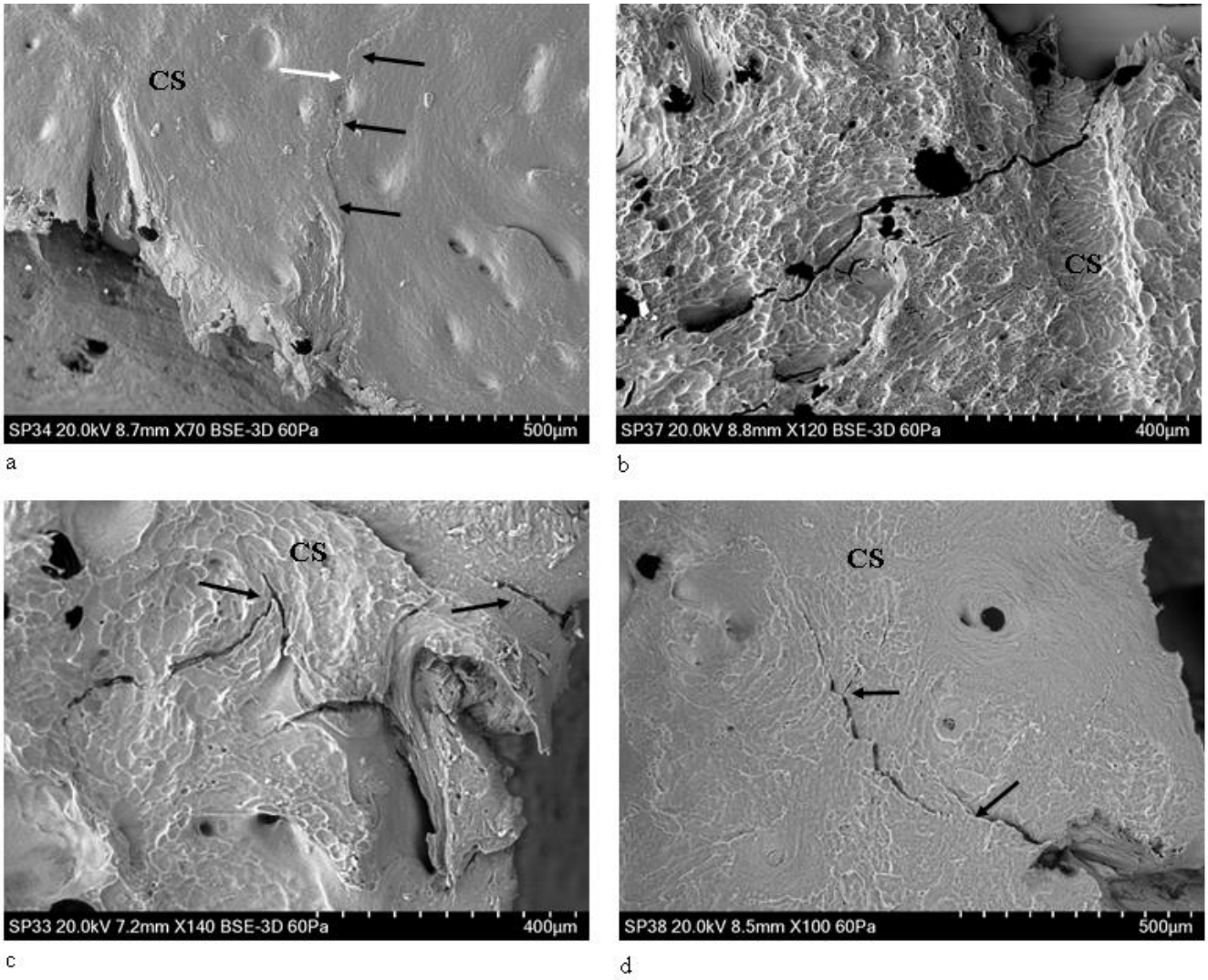

Fig.6.9 Radial cracks originating from the entry cortical fracture edge, perforating impacts (CS, cortical surface)**; a**, 591 m/s impact, narrow crack crossing cortical pit and showing a small ligament bridge (white arrow); **b**, 850 m/s impact showing large, wide radial crack crossing cortical furrow; **c**, 609 m/s impact showing crack with a bifurcation (left arrow) and a separate straight radial crack inside a cortical furrow (right arrow); **d**, 871 m/s impact, long radial crack with two points of bifurcation (arrows)

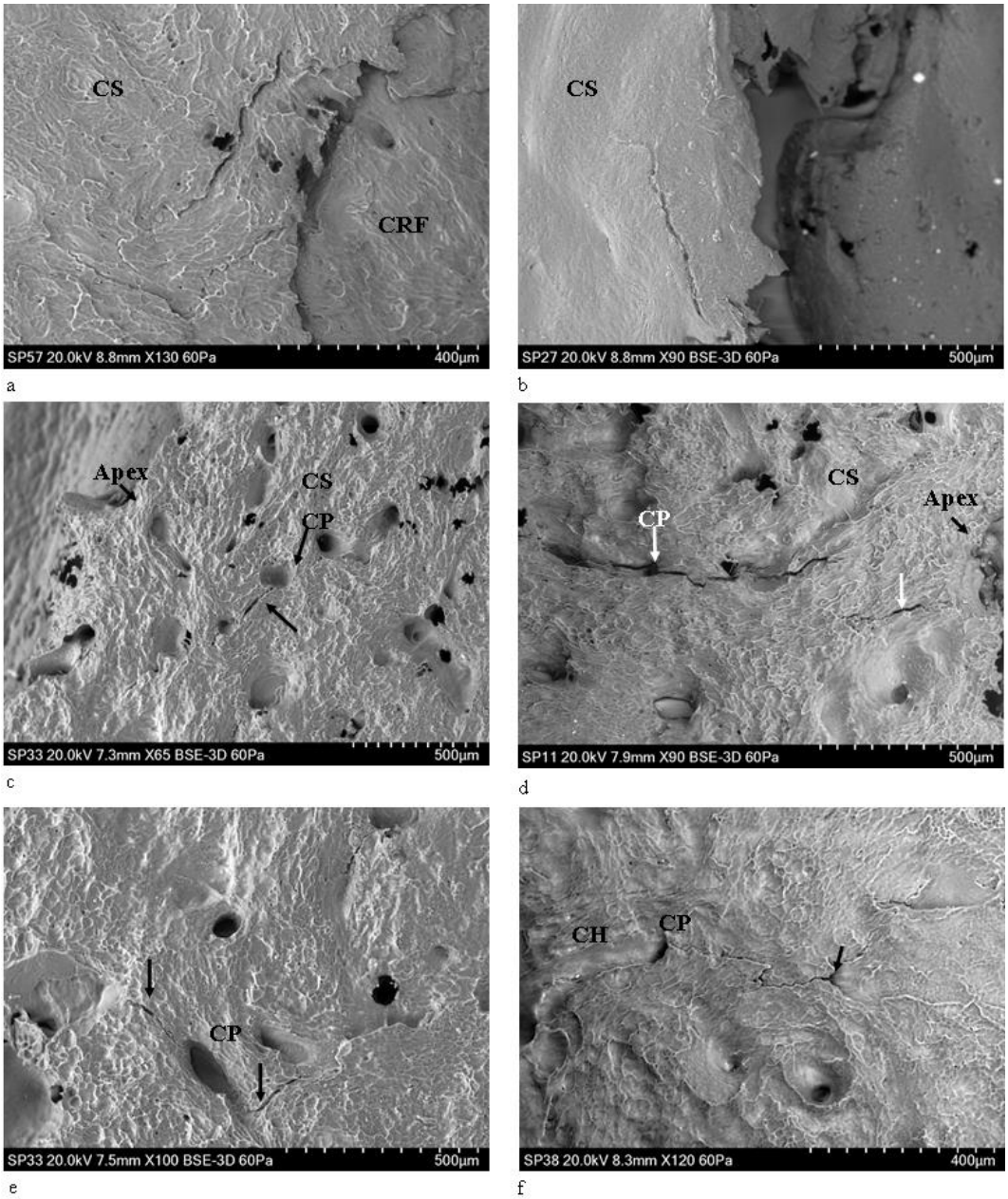

Fig.6.10 Concentric cracking and cracks arising from cortical stress concentrators, perforating impacts (CS, cortical surface, CR, cortical roof; CRF, cortical roof fragment, CP, cortical pore; CH, channel); **a**, 75 m/s impact showing concentric crack adjacent to a fragment of cortical roof; **b**, 161 m/s impact with concentrically orientated crack near the EnCF; **c**, 609 m/s impact showing concentric crack arising from cortical pit adjacent to the apex of the EnCF; **d**, 333 m/s perforating impact, large radially orientated crack adjacent to the apex and associated with a cortical pore; note the smaller radially orientated crack (lower arrow) that arises within the cortex not a pore; **e**, same specimen as in **b**, showing elliptical cortical pore with the major axis running upwards from right to left; stresses acting normal to this axis resulted in stress concentrating at the tips of the elliptical cavity and resulted in cracking at both ends; **f**, 871 m/s perforating impact showing crack associated with a cortical pore/ channel complex and extending to a smaller pore-type structure at right (arrow)

6.5. Discussion

A central tenet of the present paper was that the process of projectile trauma analysis and diagnosis will be enhanced when the penetration mechanisms and their associated morphological characteristics are defined at multiple hierarchical scales of bone organisation. SEM analysis of perforating impacts from 58 to 897 m/s revealed that at the microscopic scale the cortical entry and surrounding cortical surface are characterised by varying degrees of SPD and PPD, by radial cracks emanating at or near to the apex, by circumferential cracks running parallel to the apex, and by pore/ pit-crack complexes up to 1.5 mm from the apex. Areas of apex lacking plastic deformation were either abrupt or exhibited complex re-entrant geometries. Evidence for tensile, mode I failure due to impact consisted of stepped fracture edges on the medial edge of intact cortical roofs in rebound impacts and cortical roof fragments in perforating impacts. It is interesting to note that peripheral plastic deformation, radial cracks and concentric cracks have been identified around a perforating fracture to a human parietal [6], indicating that at least three of the features observed here also occur in human compact bone. Although further work is required to establish the prevalence of these features in human bone, their potential as diagnostic indicators is readily apparent. For example, whilst GSR cannot be utilised as diagnostic evidence when environmental contamination cannot be ruled out [15], the presence of GSR with a combination of the above microscopic features might substantiate projectile involvement. Similarly, these features may be of use when only a small fragment of a perforating hole is recovered or when differentially diagnosing intact holes of ambiguous aetiology.

In concurrence with previous evidence that conoidal projectile wounds in sandwich bones are created by cone cracking [3-4], SEM analysis of rebound impacts in the present study confirmed the formation of ring cracks in compact bone impacted by spherical projectiles. Ring cracks are shallow, circular cracks that form normal to the surface at the edge of the impactor contact radius which, at a certain load (P), then propagate into the material whilst flaring outwards to form a cone crack [34]. Ring cracks themselves originate from surface flaws activated by the high tensile stresses present at the edge of the contact circle [35]. Although the flaws giving rise to the ring cracks in this study were too small to be identified in three cases, in one rebound impact nascent concentric ring cracks were observed originating from cortical pits and pores adjacent to the apex. Ring cracks in cortical bone are identical in form to those produced by indentation or impact in other ceramics [34, 36] and thus emphasise the importance of the mineral phase of bone in determining the dominant penetration mechanism.

Analysis of the impact site across specimens indicated that there were differences in the number of generations of ring cracks formed during penetration. In three rebound impacts, several generations of ring cracks were formed as the projectile penetrated progressively deeper into the cortex. Fractures consistent with being two generations of ring cracks were also preserved in a cortical roof fragment resulting from a 96 m/s impact. In contrast, SEM analysis of the intact cortical roof of the conoid produced at 74 m/s did not show any ring cracks (see [4] for μCT cross-sectional analysis of this conoid). Ring cracks large enough to detect with μCT were also absent from a second conoid resulting

from a 57 m/s impact in the same experimental series [4] and are not present in the images of intact conoids reported in the literature [37, 38, 39]. Variation in ring crack number and distribution around the impact site has also been demonstrated in other ceramic materials including dense alumina [34] and coarse alumina subjected to repeated load cycles [36].

In bone conoids, absence of multiple generations of ring cracks may be explained by compression brought about by plastic deformation and fracture of the cortical roof, both of which have been observed in cross-section [4]. Plastic deformation can occur in brittle materials during indentation [40], with experimental work in ceramics indicating that inelastic deformation occurs before fracture if the projectile radius is below a critical value [41]. Theoretically, compression due to plastic deformation and/ or fracture would cause immediate contact with a wider projectile radius and thus result in only one ring crack. In support of this hypothesis, four of the five conoids described from the archaeological and forensic literature displayed a compressed cortical roof [37, 38, 39], as did the two most intact conoids in our previous experimental series [4]. This hypothesis cannot not fully explain lack of multiple ring cracks, however, as the rebound impacts exhibited both plastic deformation and more than one generation of ring crack. In addition to compression, it is therefore likely that bone parameters such as cortical thickness, mineralisation and geometry at the site of impact, in addition to the angle of incidence of the projectile in relation to the bone, may be involved in determining the ring cracking behaviour of the cortical roof.

In addition to plastic deformation of the cortical roof in rebound impacts, plastic deformation in the form PPD and SPD was observed in perforating impacts induced from 74 m/s to 971 m/s. Whilst permanent deformation identical in form to PPD has been previously been observed in bovine scapulae impacted with a captive bolt and 7.62 x 51 mm NATO full metal jacket projectiles [6], to the best of our knowledge this is the first study to report bending associated with loss of surface sculpting in the form of SPD. These plastic deformation morphotypes differed both in their location and appearance. Whilst SPD was restricted to the projectile-bone interface at the apex, PPD started in the cortex adjacent to it and where present imparted a distinct dish-shaped morphology to the cortical entry. Interestingly, no cortical entries displayed SPD or PPD around their entire circumference; accordingly, a given cortical entry might express areas of plastic deformation that contrast sharply with abrupt, non-deformed edges.

The presence of plastic deformation of any kind around fractures induced at higher velocities is surprising and suggests involvement of different plastic mechanisms to those operative at lower loading rates. In material terms, bone is a semi-brittle solid whose viscoelastic properties impart strain rate sensitivity to its failure behaviour [42, 43]. Thus, whilst low strain rates allow bone to deform in the plastic part of the stress-strain curve, high strain rates apply energy too quickly for the viscous mechanisms to respond and the bone fractures in brittle fashion [2, 32, 44, 45]. Accordingly, mechanisms that allow bone to deform in the plastic portion of the curve, including slip within and between mineralised collagen fibrils [46, 47, 48, 49] and microcracking [50], cannot account for plastic

deformation during impulsive loading. The questions therefore arise as to how plastic deformation is occurring between 74 m/s-871 m/s and if the mechanisms are the same for SPD and PPD.

One possible underlying mechanism for the observed ductility that has some experimental support is softening of the mineral phase in the cortical bone surrounding the impact site. Previous analysis utilising nanohardness measurements of cortical entries in human sandwich bones has indicated a loss of hardness from 61.1 ± 1.6 kg/mm^2 in a control specimen to 47.7 ± 0.9 kg/mm^2 in cortical bone adjacent to the entry [30]. These authors attributed the softening to shock-induced phase changes and resultant amorphization of hydroxyapatite (HA) crystals. The latter process was also considered to cause an increase in the size of nanopores around the collagen fibres, disrupting their organisation and resulting in increased porosity of the bone matrix. Reversible pressure-induced structural change has been demonstrated experimentally in pure HA crystals at 20 kilobars (kbar), with reversal occurring during decompression at a pressure of 22 kbar [51]. Later analysis of HA with X-ray diffraction (XRD), Fourier transform infrared (FTIR) and SEM has demonstrated a transition from crystalline to fully amorphous phase at 10 Gigapascals (GPa), or 100 kbar pressure [52]. The effect of shock waves may also be more apparent in bone than other tissues due to its density, which results in high amplitude reflections [27].

Whilst softening of the mineral phase may account for the ductility observed in the present study, any proposed mechanism must also account for the fact plastic deformation was localised around the cortical entry. It is established that ceramics can undergo plastic deformation during shock loading through a process termed micro-plasticity, which in polycrystalline ceramics occurs due to deformation within and between crystals [53]. Experimental modelling of this process has demonstrated that microplasticity originates in localised sites that coalesce with an increase in strain, with subsequent microplastic evolution being determined by crystal orientation with respect to the applied load [53]. Significantly, this model also predicted that 2% of the ceramic must be undergoing microplasticity for plastic deformation to be observed macroscopically [53]. Although this model was not based on a nanocrystalline ceramic such as bone, a similar sensitivity to crystal orientation may explain the localised plastic deformation around the cortical entry, with collagen fibre and thus crystal orientation varying between bone lamellae around the circumference of the EnCF. Direction-specific behaviour such as this is consistent with the anisotropic nature of bone as a material [42]. Shock waves initiated by high-velocity impact also reflect at interfaces and cavities within the bone, a process that results in waves both reinforcing and cancelling cancel each other out [42]. The highly heterogeneous nature of bone and resultant complexity in shock wave behaviour around the impact site would also contribute to the localisation process. Further systematic analysis of the crystal structure in deformed and non-deformed regions of the cortical entry is necessary to confirm the distribution of shocked HA crystals in each region, and additional nanohardness investigations might also prove instructive.

Until the precise mechanisms underlying these plastic deformation types are elucidated it is only possible to speculate as to whether they are formed in the same way. However, restriction of areas of

SPD to the projectile-bone interface, that is, at the apex and on cortical roof fragments, is suggestive of it being caused by *direct close interaction* with the projectile. SPD was characterised by gradual loss of surface sculpturing resulting in smooth regions of bone, often with compressed appearance, and by bending of affected regions resulting in a ductile morphology. Similar areas of smooth bone at the EnCF have been observed in a previous SEM analysis of porcine ribs impacted with .22 bullets and were attributed to melting of the bone due to frictional heating [31]. However, although a portion of the available incident kinetic energy will be turned into frictional heat, it is not currently known what temperatures might be generated during perforation of cortical bone or if the contact time is sufficient to allow heat to transfer. Although data is lacking for bone, published data for synthetic materials provides some insight into the temperatures that can be created by impact. Thermographic analysis of the penetration of ultra-high molecular weight polyethylene with fragment simulated projectiles captured a temperature at the site of impact of 200^{o}C, with thermal energy accounting for half of the lost incident kinetic energy during perforation [54].

The effects of heat on bone chemistry are complex but what is clear is that temperatures must be high and sustained to bring about change to the crystal structure. Experimental work has shown that bone morphology remains normal up to 185^{o}C and that melting of HA only occurs at temperatures exceeding 800^{o}C [55]. Furthermore, a change in HA crystal structure has been reported to occur only in the first fifteen minutes of heating at 500^{o}C [56]. Combined, this data suggests that the smooth areas of bone reported previously [31] and categorised as SPD in the present study are unlikely to result from melting of the hydroxyapatite. As an alternative hypothesis, it is speculated that the observed morphology of SPD is the result of shock-induced softening coupled with a physical scraping and crushing effect at the projectile-bone interface. Maximum stress wave intensity at the apex of the EnCF and extreme physical disruption of the HA crystals may account for the gradual loss of cortical sculpturing at the apex, with alteration in crystal structure at the nano scale leading to morphological change at the micro scale.

Apart from one specimen impacted at 885 m/s that exhibited two macroscopic radial fractures, impacted porcine scapulae did not show the large radial or concentric fractures that are commonly associated with gunshot entry and exit sites in human crania. These fracture types are also typically absent in bovine scapulae subjected to ballistic impact [6] but have been documented in bovine ribs [57]. Radially and concentrically orientated cracks were identified around the cortical entry at the microscopic scale in both re-bound and perforating impacts, but whilst the radial cracks may be analogous to those seen macroscopically in human material the concentric cracks are not. Concentric cracks associated with ballistic trauma in human crania originate under tension in the endocranium as a result of temporary cavitation within the brain [58], whilst the microscopic fractures originated in the outer cortical plate in the absence of cavitational effects. Although further quantitative work is required, preliminary analysis indicated that radial cracks over 1 mm in length were more common with higher velocity impacts. An increase in crack length such as this is consistent with the greater absolute amounts

of kinetic energy absorbed at higher impact velocities, which allows greater work of fracture. Uncracked-ligament bridging was observed in cortical cracks from 54 m/s up to the highest impact velocity of 897 m/s. This phenomenon, which occurs when a secondary crack initiates slightly ahead of a primary crack with a segment of cortex between the two, is a well-documented toughening mechanism in bone [49]; however, this appears to be first time it has been observed adjacent to projectile perforation sites.

The microscopic radial cracks observed in the present study may have some taphonomic significance. Calcination of cortical entries in bovine ribs by heating at 800^{o} C resulted in the nucleation of large radial cracks from the apex that were not there before heating [57]. Heating drill holes in the same bone type and subjecting them to the same temperature did not result in radial cracking, and as a result the authors speculated that injury related fractures, such as ballistic impact, induced areas of weakness which they termed *loci minoris resistentiae* [57]. Although they did not speculate as to what the cause of this weakness might be, thermal expansion of microscopic radial cracks emanating at or near the EnCF would explain the additional macroscopic radial cracks during heating.

Whilst previous cross-sectional analysis with μCT has demonstrated damage localisation through the depth of the conoidal fracture, Finite Element Modelling of von Mises stresses has demonstrated that the stress field does radiate some distance from the cortical entry [59, 60, 61, 62, 63]. SEM analysis in the present study indicates that this stress field is sufficient to nucleate cracks from cortical pits and pores in the immediate cortical environment around the cortical entry. Crack nucleation from these cortical features followed predictable physical laws, with cracks emanating from the ends of ellipsoidal pores or pits where the stress concentration is highest [41]. Further quantitative analysis controlling for pit/ pore density should seek to address if the abundance of these small cracks around a given cortical is related to the magnitude of the stress field.

The present paper sought to begin addressing the question as to whether there is a level of bone organisation where the energy inputs and contact stresses associated with high-velocity projectile trauma might manifest structurally. In this regard, the presence of plastic deformation and the indication that this is associated with a structural change at the level of individual HA crystals is significant. Plastic deformation was induced by both low and high-velocity impacts and therefore future analyses should seek to characterise the precise changes to crystal structure and/or orientation that are occurring both in PPD and SPD, and then establish if there is a quantitative relationship between the degree of structural change and absorbed kinetic energy during the impact event. Further analyses of radial crack length and tortuosity are also necessary. Resolution with the negative-positive casting process was in the order of microns, confirming the utility of this process in the examination of traumatic fractures. Further work should seek to develop techniques to reduce artefact formation and allow enhanced quantitative analyses. The findings of the present study indicate that a comprehensive understanding of projectile trauma must include analysis across lower scales of organisation. Differential diagnosis will be

enhanced when the failure mechanisms and associated morphological characteristics are defined and documented across multiple hierarchical scales.

Acknowledgements
We are indebted to Andrew Roberts, Dr David Wood, David Miller and Alan Peare for operating the shooting and filming speed cameras. We would also like to extend our thanks to Adrian Mustey for his advice with the positive casting process. Finally, we are also indebted to Dr James Shackel for his input on terminal ballistics.

Conflict of interest
The authors conform there is no conflict of interest.

Ethical approval
This study was fully authorised by the ethics committee of Cranfield University.

6.6. References

[1] DiMaio VJM (1999) Gunshot wounds: practical aspects of firearms, ballistics and forensic techniques. CRC Press, Florida

[2] Berryman HE, Symes SA (1998) Recognising gunshot and cranial trauma through fracture interpretation. In Reichs, K J (ed) Forensic Osteology: advances in the identification of human remains. Charles C Thomas Publishers, Springfield, pp 333-352

[3] Rickman JM, Shackel, J (2018) A novel hypothesis for the formation of conoidal wounds in sandwich bones. Int J Legal Med (2018) 133: 501-519

[4] Rickman JM, Shackel, J (2018). Crack propagation due to low-velocity projectile impact. Int J Legal Med 133: 1443-1459

[5] Quatrehomme G, Piercecchi-Marti M, Buchet L, Alunni V (2016) Bone bevelling caused by blunt trauma: a case report. Int J Legal Med 130 (3): 771-775 https:// doi.org/10.1007/s00414-015-1293-0

[6] Rickman JM, Smith MJ (2014) Scanning Electron Microscope analysis of gunshot defects to bone: an underutilised source of information on ballistic trauma. J Forensic Sci 59 (6): 1473-1486 https:// doi.org 10.1111/1556-4029.12522

[7] Kaufman MH, Whitaker D, McTavish J (1997) Differential diagnosis of holes in the calvarium: application of modern clinical data to palaeopathology. J. Archaeol. Sci. 24: 193-218

[8] Nawrocki SP (2009) Forensic taphonomy. In Blau S, Ubelaker DH (eds) Handbook of Forensic Anthropology and Archaeology, Left Coast Press, California, pp 284-294

[9] Hausmann R, Betz P (2002) Thermally induced entrance wound-like defect of the skull. Forensic Sci. Int. 128: 159-161

[10] Tsokos M (2011) Heat-induced post-mortem defect of the skull simulating an exit gunshot wound of the calvarium Forensic Sci Med Pathol 7: 227-228

[11] Pokines JT (2014) Faunal dispersal, reconcentration, and gnawing damage to bone in terrestrial environments. In Pokines JT, Symes SA (eds) Manual of forensic taphonomy. CRC Press, Taylor and Francis group, Florida pp 201-248

[12] Pokines JT, Baker SE (2014) Avian taphonomy. In Pokines JT, Symes SA (eds) Manual of forensic taphonomy. CRC Press, Taylor and Francis group, Florida pp 427-446

[13] Taborelli A, Gibelli D, Rizzi A, Andreola S, Brandone A, Cattaneo C (2012) Gunshot residues on dry bone after decomposition- a pilot study. J Forensic Sci 59 (5): 1281-1284

[14] Amadasi A, Brandone A, Rizzi A, Mazzarelli D, Cattaneo C (2012) The survival of metallic residues from gunshot wounds in cremated bone: a SEM-EDX study. Int J Legal Med 126: 525-531

[15] Amadasi A, Gibelli D, Mazzarelli D, Porta D, Gaudio D, Salsarola D, Brandone A, Rizzi A, Cattaneo C (2015) Assets and pitfalls of chemical and microscopic analyses of gunshot residues in skeletonized bodies: a report of five cases. Int J Legal Med 129: 819-824

[16] Vermeij EJ, Zoon PD, Chang SBCG, Keereweer I, Pieterman R, Gerretsen RRR (2012). Analysis of microtraces in invasive traumas using SEM/EDS. Forensic Sci. Int. 214 (1): 96-104

[17] Spatola BF (2015). Atypical gunshot and blunt force injuries: wounds along the biomechanical continuum. In Passalacqua NV, Rainwater CW (eds) Skeletal trauma analysis: case studies in context. John Wiley & Sons, West Sussex, pp 7-26

[18] Kroman A (2010) Rethinking bone trauma: a new biomechanical continuum based approach. 62nd Annual Meeting of the American Academy of Forensic Sciences, Chicago, Illinois

[19] Kroman A, Symes SA (2013) Investigation of skeletal trauma. In DiGangi EA, Moore MK (eds) Research Methods in Human Skeletal Biology, Academic Press, Waltham, Massachusetts pp 219-239

[20] Berryman HE, Shirley NR, Lanfear AK (2012) Low-velocity trauma. In Tersigni-Tarrant MA, Shirley NR (eds) Forensic Anthropology: An introduction, CRC Press, Taylor and Francis group, Florida pp 271-290

[21] Lindström AC, Hoogewerff J, Athens J, Obertova Z, Duncan W, Waddell N, Kieser J (2015) Gunshot residue preservation in seawater. Forensic Sci. Int. 253: 103-111

[22] Amadasi A, Merli D, Brandone A, Cattaneo C (2014) Chromatic variation in soot soiling: a possible marker for gunshot wounds in burnt bone. J Forensic Sci 59 (1): 195-198

[23] Fischbeck HJ, Ryan SR, Snow CC (1986) Detection of bullet residue in bone using Proton-Induced X-ray Emission (PIXE) analysis. J Forensic Sci 31 (1): 79-85

[24] Berryman HE (2019) A systematic approach to the interpretation of gunshot trauma. Forensic Sci. Int. 301: 306-317

[25] Weiner S, Wagner HD (1998) The material bone: structure-mechanical function relations. Annu Rev Mat Sci 28: 271-298

[26] Kieser J (2013) Biomechanics of bone and bony trauma. In Kieser J, Taylor T, Karr D Forensic Biomechanics. John Wiley & Sons, United Kingdom

[27] Backman ME, Goldsmith W (1978) The mechanics of penetration of projectiles into targets. Int J Engng Sci 16:1-99

[28] Kneubuehl BP (2011) Wound ballistics of bullets and fragments. In Kneubuehl BP (ed), Coupland RM, Rothschild MA, Thali MJ Wound Ballistics: Basics and Applications pp 163-252

[29] Speeter D, Ohnsorge J 1973 Investigations for determination of shot direction in bones with Scanning Electron Microscopy. Z Rechtsmedizin 73:137–43

[30] Gaîdash AA, Bashirov RS, Kolkutin VV, Tolmachev IA, Tyurin MV, Bozhchenko AP, Denisov AV (2010) New data on the morphogenesis of gunshot injuries to bone. СУДЕБНО-МЕДИЦИНСКАЯ ЭКСПЕРТИЗА ((Forensic Medical Examination) 4, 2010

[31] Kieser JA, Tahere J, Agnew C, Kieser DC, Duncan W, Swain MV, Reeves MT (2011) Morphoscopic analysis of experimentally produced bony wounds from low-velocity ballistic impact. Forensic Sci Med Pathol 7:322-332

[32] Smith OC, Berryman HE, Symes SA, Francisco JT, Hnilica V (1993) Atypical gunshot exit defects to the cranial vault. J Forensic Sci 38 (2): 339-343

[33] Zhi-Jin Z, Jia-Zhen Z (1991) Study on the microstructures of skull fracture. Forensic Sci. Int. 50:1–14

[34] Lawn BR (1998) Indentation of ceramics with spheres: a century after Hertz. J Am Ceram Soc 81 (8):1977-1994

[35] Warren PD, Hills DA, Dai DN (1995) Mechanics of Hertzian cracking. Tribol.Int 28 (6): 357-362

[36] Guiberteau F, Padture NP, Cai H, Lawn BR (1993) Indentation fatigue: a simple cyclic Hertzian test for measuring damage accumulation in polycrystalline ceramics Philos. Mag A 68 (5): 1003-1016

[37] Murphy MS, Gaither C, Goycochea E, Verano JW, Cock G (2010) Violence and weapon-related trauma at Puruchuko-Huaquerones, Peru. Am J Phys Anthropol 142:636-649

[38] Murphy MS, Spatola B, Weathermon R (2014) Allies today, enemies tomorrow: a comparative analysis of perimortem injuries along the biomechanical continuum. In Martin DL, Anderson CP (eds) Bioarchaeological and forensic perspectives on violence: how violent death is interpreted from skeletal remains, Cambridge University Press, Cambridge, pp 261-288

[39] Bird CE, Fleischman JM (2015) A rare case of an intact bone plug associated with a gunshot exit wound. J Forensic Sci 60 (4): 1074-1077

[40] Frank FC, Lawn BR (1967) On the theory of Hertzian fracture. Proceedings of the Royal Society 299: 291-306

[41] Pfeiffer W, Rombach M (1999) Macroscopic and microscopic residual stresses in ceramics due to contact loading Adv. X-ray Anal. 41: 495-500

[42] Currey J D (2002) Bones: structure and mechanics. Princeton University Press, New Jersey

[43] Abdel-Wahab AA, Alam K, Silberschmidt VV (2011) Analysis of anisotropic viscoplastic properties of cortical bone tissues. J Mech Behav Biomed Mater 4 (5): 807-820

[44] Symes SA, L'Abbé EN, Stull KE, Lacroix M, Pokines JT (2014) Taphonomy and the timing of bone fractures. In Pokines JT, Symes SA (eds) Manual of forensic taphonomy. CRC Press, Taylor and Francis group, Florida pp 341- 362

[45] Morgan EF, Unnikrisnan U, Hussein AI (2018) Bone mechanical properties in healthy and diseased States. Annu Rev Biomed Eng 20: 119-143

[46] Gupta HS, Wagermaier W, Zickler GA, Raz-Ben Aroush D, Funari SS, Roschger P, Wagner HD, Fratzl P (2005) Nanoscale deformation mechanisms in bone. Nano Lett 5 (10): 2108-2111

[47] Gupta HS, Seto J, Wagermaier W, Zaslansky P, Boesecke P, Fratzl P (2006) Cooperative deformation of mineral and collagen in bone at the nanoscale. PNAS 103 (47): 17741-17746

[48] Gupta HS, Fratzl P, Kerschnitzki M, Benecke G, Wagermaier W, Kirchner HOC (2007) Evidence for an elementary process in bone plasticity with an activation enthalpy of 1eV. J. R. Soc. Interface 4: 277-282

[49] Ritchie RO, Buehler MJ, Hansma P (2009) Plasticity and toughness in bone. Phys Today 62: 41-47

[50] Zioupos P, Hansen U, Currey JD (2008) Microcracking damage in relation to strain rate in human cortical bone tensile failure. J. Biomech 41: 2932- 2939

[51] Xu J, Gilson DFR, Butler IS, Stangel I (1996) Effect of high external pressures on the vibrational spectra of biomedical materials: calcium hydroxyapatite and calcium fluoroapatite. J. Biomed. Mater. Res 30: 239-244

[52] Vaidya SN, Karunakaran C, Pande BM, Gupta NM, Iyer RK, Karweer SB (1997) Pressure-induced crystalline to amorphous transition in hydroxylapatite J. Mater. Sci 32: 3213- 3217

[53] Zhang KS, Wu MS, Feng R (2005) Simulation of microplasticity-induced deformation in uniaxially strained ceramics by 3-D Voronoi polycrystal modelling. Int. J. Plast 21: 801-834

[54] Papantonakis MR, Furstenberg R, Nguyen V, Moser A, Kendziora, McGill RA (2014) Infrared imaging analysis of ballistic impacts of composite armor materials. In Colbert FP, Sheng-Jen H (eds) Thermosense: Thermal Infrared Applications, Proc. of SPIE Vol. 9105, 91050B [Online] Available at https://www.spiedigitallibrary.org/conference-proceedings-of-spie?SSO=1 (accessed 4/2/2015)

[55] Shipman P, Foster G, Schoeninger M (1984) Burnt bones and teeth: an experimental study of colour, morphology, crystal structure, and shrinkage. J. Archaeol. Sci. 11: 307-325

[56] Hiller JC, Thompson TJU, Evison MP, Chamberlain AT, Wess TJ (2003) Bone mineral change during experimental heating: an X-ray scattering investigation. Biomaterials 24: 5091-5097

[57] Collini F, Amadasi A, Mazzucchi A, Porta D, Regazolla VL, Garofalo P, Di Blasio A, Cattaneo C (2015) The erratic behaviour of lesions in burnt bone. J. Forensic Sci. 60 (5): 1290-1294

[58] Smith O, Berryman HE, Lahren CH (1987) Cranial fracture patterns and estimate of direction from low velocity gunshot wounds. J Forensic Sci 32 (5): 1416-1421

[59] Chen Y, Miao Y, Xu C, Zhang G, Lei T, Tan Y (2010) Wound ballistics of the mandibular angle: a preliminary Finite Element Analysis and experimental study. J. Biomech 43: 1131-1137

[60] Tang Z, Tu W, Zhang G, Chen Y, Lei T, Tan Y (2012). Dynamic simulation and preliminary Finite Element Analysis of gunshot wounds to the human mandible. Injury, Int. J. Care Injured 43: 660-665

[61] Matoso IM, Freire AR, Santos LSdM, Deruge Junior E, Rossi AC, Prado FB (2014). Comparison of gunshot entrance morphologies caused by .40 caliber Smith & Wesson, .380-caliber, and 9 mm Luger bullets: a finite element analysis study. PLOS ONE 9 (10): e111192.https://doi.org/10.1371/journal.pone.0111192 [Online] Available at https://journals.plos.org/plosone/article?id=10.1371/journal.pone.0111192 (accessed 29/5/2015)

[62] Costa ST, Freire AR, Matoso RI, Daruge Júnior E, Rossi AC, Prado FB. Computational approach to identify different injuries by firearms. J Forensic Sci 62 (2): 361-368

[63] Rodrigues LL, Costa ST, Rossi AC, Deruge Júnior E, Prado FB, Freire AR (2018). Computational simulation of projectile injuries to human parietal bone using finite element analysis. Aust. J. Forensic Sci 51 (4): 446-454 http://doi.org/10.1080/00450618.2017.1416173

CHAPTER 7, DISCUSSION

7.1. Review of the research objectives; the impact of key findings and their contribution to knowledge

This body of work was borne from an analysis of the literature that revealed the difficulties that can be encountered when attempting to differentially diagnose and accurately interpret projectile trauma in skeletal material. Given the importance of this trauma type in forensic anthropology, and forensic pathology more widely, it was therefore significant that review of the literature in Chapter 2 (Paper 1), indicated that a consensus had not been reached as to how conoidal wounds form in sandwich bones and, additionally, that there were few empirical investigations into the underlying fracture mechanisms which might shed light on that important question. Chapter 2 also highlighted that conoidal wounds can be formed by both low and high velocity impacts, a diagnostic challenge only enhanced by the fact there is no accurate method to determine velocity from macroscopic analysis of fracture morphology at and around the site of perforation [1]. The aim of the research was therefore to facilitate the forensic interpretation of conoidal entry wounds in sandwich bones by empirically investigating the fracture processes underlying their genesis and by carrying out a detailed examination of their morphology at different hierarchical scales. This discussion re-introduces the research objectives and discusses the impact of key findings relating to them.

7.1.1. Objective 1; Enhance the description, analysis, and classification of conoidal wounds by developing a detailed nomenclature for their morphological components (**Chapters 3, 4 and 6**).

In order to accurately interpret and describe the morphology of conoidal wounds, Paper 2 utilised µ-CT to produce cross-sectional slices in transverse (y-z), longitudinal (x-z) and depth (x-y) planes to develop a nomenclature for observable component parts and to define the laminae composing the bevel. This nomenclature, published for the first time in the *International Journal of Legal Medicine* [2] and again with one addition in Chapter 4 [3], represents the first formal naming system for conoidal wounds and will facilitate forensic anthropologists and pathologists tasked with analysing this fracture type in medico-legal cases. This nomenclature will also enable enhanced communication between practitioners when collaboration is required for wound interpretation or differential diagnosis and, additionally, when describing wound morphology in court settings. The nomenclature derived from µ-CT analysis was critical to subsequent work with the SEM in Chapter 6, Paper 5, with the latter also necessitating the inclusion of the additional terms *projectile bone interface* and *apex*. These additional terms were critical in enabling discussion of novel morphological changes observed with SEM that revealed important information relating to compact bone behaviour under impulsive loading and may be of diagnostic value (see objective 6).

7.1.2. Objective 2; determine the fracture mechanisms underlying the genesis of conoidal wounds using a combination of high-speed videography and morphological analysis with micro-computerised tomography (µ-CT) (Chapters 3 and 4).

Chapter two (Paper 1) revealed that conoidal wounds have been utilised in forensic contexts for both differential diagnosis of projectile trauma [4, 5] and as entry-exit [4, 6] and side to side directionality indicators using bevel asymmetry [7, 8]. However, in order to fully understand what information can and cannot be derived from conoidal wounds, as well as the accuracy of any derived information such as side-side trajectory determinations, the fracture mechanisms underlying their formation must be defined and understood. A considerable gap in knowledge at the start of this research was a lack of empirical work testing proposed hypotheses, with the only published experimental work utilising µ-CT to examine conoidal post-formation; this analysis did not, therefore, confirm that the proposed processes actually occurred during perforation [9].

In order to further examine how conoidal wounds are formed, the present work utilised high-speed videography to capture the penetration process and coupled this with subsequent morphological analysis using µ-CT (Chapters 3 and 4). Based upon this coupled analytical approach, Chapter 3, Paper 2 proposed a novel hypothesis for the formation of conoidal wounds that was consistent with their cross-sectional structure and the fracture processes observed during the penetration event. Unlike the plug and spall hypothesis, which posits that the shear plug is derived from the outer cortical layer only [10], Paper 2 suggested that impact results in trans-laminar cone crack propagation and production of tri-layered conoids that simultaneously fragment at high velocity. In addition to strong morphological evidence and a firm foundation in the behaviour of other ceramic materials subjected to impact, this interpretation was also consistent with the morphology of recovered tri-layered plugs reported in the literature [11-13], which were hitherto considered to be a low velocity variation of plug and spall [13].

Significantly, the first phase of this research revealed that the bevel is formed early during impact and before projectile exit. This observation, and the cone crack hypothesis in general, is likely to have a significant impact on forensic practice due its implications with regards to the accuracy of trajectory determinations from bevel asymmetry. Although conventional theory posits that asymmetry is determined by the path of the projectile through the sandwich structure [7, 8], genesis of the translaminar cone crack in the outer cortical layer and its propagation from above downwards dictates that crack path through the three laminae must also be a factor in any observed asymmetry. Loss of the shape of the cortical entry in the trabecular layer indicated that crack deviation was particularly prevalent during propagation across the differently orientated trabecular cell struts, which essentially deleted the finer details of entry shape by approximately mid-trabecular depth. Further support for the role of crack path in determining bevel asymmetry was the greater frequency of asymmetrical bevels despite perpendicular impact. As highlighted in Chapter 3, Paper 2, this change in understanding of how

the bevel forms means investigators should apply caution to trajectory determinations utilising bevel asymmetry if there is a lack of additional evidence, particularly an exit wound.

In addition to suggesting how conoidal wounds form, cross-sectional analyses in Paper 2 revealed a striking localisation of damage around the conoidal fracture. This feature, which was subsequently revealed to manifest energetically in Chapter 5, Paper 4, is significant for two reasons. Firstly, this finding reveals novel information about the behaviour of sandwich bones during impact that will be of utility in the development and verification of both computer simulated and synthetic models. Secondly, damage localisation may be of diagnostic value if perforations caused by other mechanisms such as carnivore punctures, lytic disease conditions and erosive weathering do not exhibit damage localisation in the trabeculae. Further analytical work examining such perforations with µ-CT 3is required to characterise and define their cross-sectional morphology in order to judge the value of damage localisation in fracture classification and differential diagnosis (see Chapter 7).

Despite a lowest perforation velocity of 139 m/s, no intact conoids were produced in Paper 2 and their existence was inferred from the part-counterpart relationships between cortical floor fragments and their associated bevel and from observation of high-speed footage. This lack of intact conoids with which to test the hypothesis that tri-layered conoids underlie conoidal wound formation led directly to the experimental work presented in Chapter 4, Paper 3. Whilst low-velocity impact experiments had previously demonstrated the formation of cone cracks in the compact bone of non-human long bones [14], prior to the work presented in Paper 3 there was no data available on their formation in sandwich bones. This second phase of published research was therefore significant in that it demonstrated, for the first time, both cone crack formation and the production of tri-layered conoids in sandwich bones. Conoid morphology was entirely consistent with the structure of those reported in the literature [11-13], and with the fragmentary conoid components resulting from high-velocity impacts presented in Chapter 3 (Paper 2). In combination, this data indicated that conoidal wounds are formed during both low and high-velocity impact through a process of trans-laminar cone crack propagation and tri-layered conoid production. Significantly, this research demonstrated that projectile exit is not required for bevel formation, ruling out plug and spall in conoidal wound formation and underlining the importance of trans-laminar crack path in determining ultimate bevel shape and symmetry.

The research findings in Chapters 3 and 4 are starting to have a demonstrable impact on the forensic anthropological community. Publication of both papers resulted in communication from Dr Angi Christensen, Forensic Anthropologist at the Federal Bureau of Investigation Laboratory in Quantico, Virginia, and later with Dr Hugh Berryman at Middle Tennessee State University. This has resulted in us subsequently writing a collaborative paper on forensic fractography which is currently *in press* in the journal *Forensic Anthropology*. This paper includes a review of the research presented in Chapters 3 (Paper 2) and 4 (Paper 3) and presents the nomenclature developed in Paper 2 as a system for naming their component parts. It is hoped that inclusion of the current research findings in this

medium will facilitate dissemination of the results within the forensic anthropological community and in so doing enhance analyses of conoidal wounds.

7.1.3. Objective 3a; generate and interpret impact dynamics data to establish how sandwich bones behave during perforation and to determine how that behaviour is influenced by the fracture mechanisms identified in objective 2 (Chapter 5).

The energy that is absorbed during the perforation of any material is utilised in large part to drive the failure mechanisms that allow the projectile to penetrate, pass through and exit the material and, in brittle materials, to accelerate and eject fragments. As such, impact dynamics data on the energetics of impact can reveal critical information about these mechanisms and it was, therefore, important to generate this data in the present research. Previous work on the impact dynamics of bone dated back to the late 1960s and 1970s and focused entirely on human long bones [15-18], leaving a considerable gap in our understanding of how sandwich bones behave dynamically and if that behaviour resembles that of long bones.

Impact dynamics data presented in Paper 4 captured the process of damage localisation energetically and provided additional support for the cone crack hypothesis. Damage localisation manifested in the energetics data as a linear relationship between incident kinetic energy (E_i) and residual kinetic energy (E_r), a feature reported previously in composite sandwich panels [19]. In Paper 4 it was proposed that propagation of the trans-laminar cone crack isolates the conoid from the rest of the bone, resulting in both the linear E_i versus E_r profile and the damage localisation pattern described in Chapter 3, Paper 2. The relationship between the energetics of impact and underlying fracture mechanisms clearly demonstrates the utility of impact dynamics data in contributing to our understanding of the behaviour of bone under the extremely high loading rates that characterise high-velocity perforation.

In common with data for the human femoral epiphyses [16] and femoral shafts impacted with 6.35 mm spheres [17], the relationship between incident velocity and absorbed kinetic energy was described by a power function. Significantly, this similarity in energy absorption profiles between bone types of such different shape, thickness and trabecular abundance indicated that bone material behaviour during impact is the main determinant of the profile obtained, rather than bone type. Paper 4 presented the hypothesis that the power relationship was a manifestation of increased energy being utilised in the creation and ejection of fragments with increasing velocity and thus absorbed kinetic energy. Although further work on fragment size and mass is required to test this theory, it is consistent with the known behaviour of other brittle materials [20, 21] and composites [22] and thus places bone in a wider context of material behaviour under impulsive loading.

This experimental series utilised the simplest projectile shape possible to eliminate such factors as projectile yaw and deformation from consideration in the energetics data. The results presented in Paper 4 thus represent an important baseline with which to observe the effects of key components of

projectile design on impact dynamics and bone behaviour. For example, utilisation of deforming spheres of the same mass and diameter as those selected in the current work would enable the effects of deformation on the relationship between E_i and E_r to be determined, and in turn provide valuable data on damage localisation and conoidal wound formation in the absence of, or prior to, examining the bone with virtual techniques. Similarly, whilst Paper 4 reported a negative relationship between the percentage of available kinetic energy absorbed and incident velocity, a finding in common with other studies ([15, 16, 23], deforming projectiles might be predicted to have higher percentage absorption values at any given velocity. At present, it is not clear what effects projectile design has on the dynamics of bone impact and this should therefore form an important body of future study.

In addition to analysis of key extrinsic variables on the perforation process, it is hoped that this impact dynamics data will also inform future tests of the biofidelity of synthetic materials used as bone analogues. Whilst a number of previous studies have considered how closely fracture morphology in synthetic models resembles that seen in real bone after projectile penetration [24-26], to the best of the author's knowledge no published study has developed detailed impact dynamics data for synthetic materials such as Synbone®; it is therefore not clear how closely the dynamic behaviour, and thus failure processes, of such materials compares to bone.

7.1.4. Objective 3.b. Carry out a quantitative morphological analysis of conoidal wounds to detect any relationships between morphology, incident velocity and absorbed kinetic energy (Chapter 5).

Chapter 2 (Paper 1) highlighted and reviewed the small number of quantitative analyses that have been carried out on conoidal wounds, with entry wounds being the single focus of only one study [8]. Although providing valuable information on morphology, the data provided could not be related to causal factors due to its derivation from a forensic case series rather than under controlled experimental conditions. Calculation of impact dynamics data for each impact in Chapter 5, Paper 4, provided the opportunity to relate such factors as incident velocity and absorbed kinetic energy to quantitative estimates of surface area and to investigate the relationship between the surface area of the cortical entry and cortical exit.

Morphometric analysis of conoidal entry wounds in the present research revealed several findings that are of forensic importance. Previous analyses of the relationship between incident velocity and wound size have either been qualitative [15-17, 23] or have utilised different calibres and projectile designs [25, 27]. Quantitative analysis controlling for projectile design variables in the present series revealed that in entry wounds incident velocity and absorbed kinetic energy were only moderately correlated with the surface area of the bevel, as defined by the exit cortical fracture edge. This moderate correlation, coupled with the number of variables that might influence exit size (such as projectile deformation), dictates that it is not a suitable candidate for velocity estimations. A further key

morphometric finding of the current series was that the correlations between cortical entry surface area and velocity/ absorbed kinetic energy were weak and not significant. Thus, whilst thicker bones [28] and higher mineral density [29] are associated with larger entry holes and may therefore suggest a larger projectile calibre than was actually involved, with non-deforming steel spheres projectile velocity and absorbed energy do not appear to predictably influence cortical entry size.

Following the work of Quatrehomme and İşcan [8] the extent of bevelling was quantified and assessed by calculating exit/ entry surface area ratios. This quantification revealed that conoidal wounds display variable extents of bevelling despite similar incident velocities. A particularly important finding was that this method detected even small amounts of bevelling (minimum ratio 1.79 in the present study) that would be difficult to assess by eye. Accordingly, in forensic case work where a perforation site presents difficulties in assessment of the presence or absence of bevelling, determination of the exit/ entry ratio may be of some assistance in making that determination.

7.1.5. Objective 4. Employ Scanning Electron Microscopy (SEM) to identify features associated with the genesis of conoidal wounds and to determine if projectile impact results in morphological changes at lower hierarchical scales that might be of diagnostic utility (Chapter 6).

Review of the literature in Chapter 2 (Paper 1) revealed that most analyses of conoidal wounds have been conducted at the macroscopic scale. Indeed, this is the scale upon which the biomechanical continuum was formulated [30] and has been subsequently utilised [12, 31]. The question therefore arose as to whether overlap between conoidal wounds caused by low- and high-velocity trauma, and between projectile wounds and holes produced by other agencies, is to some extent an artefact of the *scale* at which the fracture is observed. In other words, the hierarchical nature of bone means that macroscopic similarity does not necessarily preclude microscopic disparity. A central theme of this research was therefore that a comprehensive understanding of conoidal wounds, and a search for potential diagnostic indicators, must include an analysis of lower hierarchical scales of bone organisation.

In order to capture the genesis of conoidal wounds, Chapter 4 (Paper 3) presented cross-sectional analyses of specimens impacted between 25 m/s and 100 m/s. Penetrating rebound impacts below 60 m/s in this series resulted in the formation of approximately circular plastically deformed compressed regions of outer cortex which represented the initial phase of conoidal wound formation. Analysis with µ-CT in Chapter 4 (Paper 3) indicated that the circular cracks delineating the compressed cortical discs were morphologically consistent with being ring cracks. However, although the resolution of µ-CT was sufficient to capture the origin of one of these cracks at a nutrient foramen and to establish their angulated edge in cross-section, it was not possible to examine detailed features of cortical morphology in these compressed regions. Subsequent examination of the compressed cortical discs with SEM in Chapter 6 (Paper 5) conclusively demonstrated that these regions were characterised by the

presence of ring cracks, often forming multiple concentric generations as the projectile penetrated deeper into the cortex. These ring cracks, which are the forerunner to the cone crack which eventually propagates into the bone with increasing load, were identical in form to those observed with SEM in other ceramic materials subjected to loading with spherical indenters (e.g., [32, 33]. This finding represented the first description of multiple generations of ring cracks at the site of indentation in cortical bone and highlighted the ceramic behaviour of this bone type during projectile impact.

In addition to ring cracks, SEM examination captured other morphological features that yielded important information on the stresses operative during formation of the cortical entry. In concurrence with an initial experimental series with SEM [34], stepped fracture edges were observed along the medial edge of cortical roof fragments and along some regions of the EnCF. This stepping, which is the result of tensile (Mode 1) stresses causing fracture along different planes in the lamellae composing the cortical bone, reinforced the contention in Chapters 3 (Paper 2) that tension is a critical stress in the generation of the cortical entry. As indicated in Chapter 4 (Paper 3), an additional in-plane shear (Mode 2) component appears to be operative as penetration proceeds, resulting in mixed Mode 1-2 fracture [3]. The discovery of mixed-mode fracture during projectile impact is significant because it reveals that the stresses acting at the crack tip are complex and will vary in relation to such factors as bone shape at the impact site and the plane of the crack in relation to the sandwich bone lamellae. This picture of underlying complexity in the stresses driving fracture differs from other descriptions which have considered shear (Mode 2) stress to be dominant ([1, 35-37] Komar and Buikstra 2008; Kimmerle and Baraybar 2008; Symes *et al* 2012; Berryman 2019).

A particularly important finding of Chapter 6 (Paper 5) was the discovery of two distinct types of plastic deformation around the cortical entry. The significance of these two morphotypes, termed Surface-modified plastic deformation (SPD) and Peripheral plastic deformation (PPD), resides in what they reveal about the behaviour of the mineral phase of bone and in the potential diagnostic value of that behaviour. In accordance with the known amorphization behaviour of hydroxyapatite (HA) crystals when exposed to high pressure [38] and with reported shock-induced phase changes and softening detected around the cortical entry [39], Chapter 6 (Paper 5) hypothesised that both forms of plastic deformation were due to amorphization of the mineral phase allowing the larger scale bending of PPD and the surface modification associated with SPD. Significantly, confirmation of HA amorphization in plastically deformed zones would allow targeted analysis of the fracture margin and thus be of considerable diagnostic utility. In addition, further quantitative analysis for any correlation between incident velocity and extent of HA amorphization might be of assistance in estimating this important extrinsic variable.

7.2. Summary

The present body of research presented a novel hypothesis for the formation of conoidal entry wounds that is of great importance to the way that conoidal wounds are analysed and interpreted. Quantitative analysis of the energetics of impact yielded results in support of that hypothesis and provided important base-line data for future analyses of sandwich bone perforation by projectiles. Quantitative morphometric analysis of conoidal wounds in association with impact dynamics data highlighted how incident velocity and absorbed energy relate to conoidal wound morphology. SEM analysis in the final paper provided important data on the genesis of conoidal wounds and confirmed the presence of ring cracking at the site of impact. Finally, examination of the cortical entry and surrounding cortical environment with SEM led to the identification and description of two forms of plastic deformation and a proposed mechanism for their formation that may be of considerable diagnostic significance.

7.3. Areas for future research

This project utilised a simple projectile-target combination in order to isolate and observe the fundamental processes that are operative during formation of conoidal wounds and, as such, there remain multiple avenues of research that require further investigation. In addition, the research findings themselves have highlighted several potentially useful diagnostic indicators that necessitate additional experimental work to establish their potential efficacy. Areas of further investigation are set out under eight themes as a series of research questions below.

7.3.1. Theme 1. The influence of projectile design on penetration mechanisms, impact dynamics and morphology at different hierarchical scales

Projectile design represents a critical extrinsic factor in terminal ballistics with such features as tip shape, material and calibre varying widely cross different projectile types. This variation is exemplified by the difference between the pointed spitzer tipped bullet characteristic of rifle ammunition and the spherical projectiles utilised in the present series. This aspect of sandwich bone penetration contains the largest body of future research due to the number of variables involved. Further research questions relating to projectile design that would be investigated utilising a combination of high-speed videography, μ-CT and SEM analysis are presented below:

a. What are the effects of tip shape, projectile material and calibre on penetration and perforation mechanisms? How do these features influence the genesis of conoidal wounds?
b. Do tip shape, projectile material and calibre influence the dynamics of impact and wound morphometrics and, if so, how?
c. What effect, if any, does tip shape, projectile material and calibre have on the microscopic structure of the cortical entry? Can pointed projectile tip shape and type be determined from analysis of surface features and fracture morphology at lower hierarchical scales?

7.3.2. Theme 2. Further investigation of the impact dynamics and morphometrics of sandwich bones

The current research raised several questions relating to the dynamics of impact during the perforation of sandwich bones. Utilisation of the simple experimental model adopted in the present series will enable the influence of different factors on impact dynamics to be isolated and examined. Critical research questions that remain to be answered using this experimental model include:

a. How is absorbed kinetic energy distributed between the processes of fragmentation and fragment ejection?
b. What effect does a soft tissue covering of appropriate anatomical thickness have on the dynamics of impact?
c. What effect do intrinsic biological variables such as mineralisation, absolute thickness, and relative thickness of the three bony laminae have on impact dynamics and wound morphometrics?

7.3.3. Theme 3. The application of impact dynamics data for tests of the biofidelity of synthetic sandwich bone analogues

Recent years have seen a growing focus on synthetic alternatives to bone due to their ease of use and absence of ethical considerations. In order to enhance our understanding of the biofidelity of alternatives to bone, future research should focus on generating impact dynamics and morphometric data for synthetic analogues that can be compared to that presented in Chapter 5 (Paper 4). This research will be key to answering the following questions:

a. Do synthetic models exhibit the same dynamic behaviour as sandwich bones? If they do not, how does this difference manifest in failure mechanisms?
b. Do synthetic models exhibit similar relationships between incident velocity, absorbed kinetic energy and morphometric characteristics to sandwich bones?
c. Does alteration of projectile tip shape, type and calibre result in similar dynamic behaviour to that detected in section 1b, above?

7.3.4. Theme 4. Quantitative analysis of bevel asymmetry and the strength of correlation with trajectory

Given that bevel asymmetry is utilised as a trajectory indicator it is critical that further research is undertaken to quantitatively examine bevel shape and its relationship to trajectory under controlled experimental conditions. Bevel asymmetry lends itself to simple quantitative measures such as the ratio of the longest to shortest dimension measured across the centre of the cortical entry (aspect ratio or asymmetry index). Further research should seek to examine the following:

a. What are the asymmetry indices of the experimental series generated in the current body of work where impact was perpendicular to the outer cortical plate?
b. By varying the angle of the outer cortical plate in relation to the direction of projectile travel, is there a correlation between impact angle and direction and extent of bevel asymmetry?
c. Do asymmetry indices from perpendicular impacts fall within the bounds of those resulting from tangential impacts or do they form distinct groups?
d. How do anatomical features such as bone shape, foramina and muscle attachments influence bevel symmetry?

7.3.5. Theme 5. Further analysis of diagnostic signatures

The current research has demonstrated that lower hierarchical scales of bone organisation may yield important diagnostic information relating to projectile trauma. Further experimental analysis with SEM and additional techniques such as X-Ray diffraction and nanoindentation is required to investigate the following important questions:

a. Is there a detectable change in HA crystal structure in plastically deformed regions compared to non-plastically deformed regions around the cortical entry?
b. Is there a detectable difference in HA crystal structure between regions of SPD and PPD?
c. Is there a relationship between any change in HA crystal structure and incident velocity and absorbed kinetic energy?
d. Do nanohardness measurements substantiate previous findings by Gaîdash *et al* [39] of a softening of cortical bone around the cortical entry? If so, do plastically deformed regions exhibit lower nanohardness values and do those values differ between regions of SPD and PPD?
e. Is there a quantitative relationship between the length of radial cracks emanating from or near to the EnCF and incident velocity or absorbed kinetic energy?

7.3.6. Theme 6. Comparative analysis of conoidal wounds in human material

The present body of work utilised non-human sandwich bones and further research is therefore required to examine the microscopic structure of conoidal wounds in human material. This research would be centred on the experimental findings of the research highlighted in *Themes 1 and 4.* Key research questions include:

a. How do the fractographic features of the cortical entry in human bone compare to those observed in non-human material?
b. Does human cortical bone exhibit plastic deformation in the form of SPD and PPD?
c. Dependant on the findings of Theme 4, does human cortical bone exhibit changes in HA crystal structure and nanohardness around the cortical entry?

7.3.7. Theme 7. Analysis of perforations in sandwich bones produced by taphonomic and disease processes

In order to assess the potential diagnostic utility of such features as damage localisation and potential changes in HA crystal structure it is critical that further research examines the structure of perforations produced by other mechanisms. Pertinent research questions include:

a. Does the pressure generated by punctures induced at low loading rates, such as by carnivore canines, result in changes to HA crystal structure?
b. Is plastic deformation detectable at the microscale around non-projectile perforations?
c. What is the extent of damage localisation around non-projectile perforations, particularly in the trabecular lamina?
d. Is SEM investigation of non-projectile perforations of any utility in differential diagnosis?

7.3.8. Theme 8. Analysis of the taphonomic resistance of macroscopic and microscopic morphological features

In forensic anthropological contexts skeletonised remains recovered in outdoor environments will have undergone exposure to multiple taphonomic inputs such as weathering, scavenging and fragmentation. Further research is required to determine:

a. Does exposure to deposition in different environments alter such morphological features as the symmetry of bevelling or the size of the cortical entry?
b. How does deposition in different environments alter HA crystal structure?
c. How does deposition in different environments alter the microstructure of the cortical entry? How resistant are such features as PPD and SPD to processes such as weathering and burial in soils of different chemistry?

7.4. References

[1] Berryman HE (2019) A systematic approach to the interpretation of gunshot trauma. Forensic Sci. Int. 301: 306-317

[2] Rickman JM, Shackel, J (2018) A novel hypothesis for the formation of conoidal wounds in sandwich bones. Int J Legal Med (2018) 133: 501-519

[3] Rickman JM, Shackel, J (2018). Crack propagation due to low-velocity projectile impact. Int J Legal Med 133: 1443-1459

[4] Berryman HE, Symes SA (1998) Recognising gunshot and cranial trauma through fracture interpretation. In Reichs, K J (ed) Forensic Osteology: advances in the identification of human remains. Charles C Thomas Publishers, Springfield, pp 333-352

[5] Quatrehomme G, Piercecchi-Marti M, Buchet L, Alunni V (2016) Bone bevelling caused by blunt trauma: a case report. Int J Legal Med 130 (3): 771-775 https:// doi.org/10.1007/s00414-015-1293-0

[6] Di Maio VJM (1999). Gunshot wounds: practical aspects of firearms, ballistics and forensic techniques. CRC Press, Boca Raton, Florida

[7] Spitz WU (2006) Injuries by gunfire. In Spitz WU, Spitz DJ, Clark R (eds) Spitz and Fisher's medicolegal investigation of death: guidelines for the application of pathology to crime investigation, Charles C Thomas Publishers, Springfield. [Online] Available from: Proquest Ebook Central (accessed 9.11.17)

[8] Quatrehomme G, İşcan MY (1998) Analysis of bevelling in gunshot entrance wounds. Forensic Sci. Int. 93: 45-60

[9] Kieser JA, Tahere J, Agnew C, Kieser DC, Duncan W, Swain MV, Reeves MT (2011) Morphoscopic analysis of experimentally produced bony wounds from low-velocity ballistic impact. Forensic Sci Med Pathol 7:322-332

[10] Peterson BL (1991) External beveling of cranial gunshot entrance wounds. J. Forensic Sci. 36 (5): 1592-1595

[11] Murphy MS, Gaither C, Goycochea E, Verano JW, Cock G (2010) Violence and weapon-related trauma at Puruchuko-Huaquerones, Peru. Am J Phys Anthropol 142:636-649

[12] Murphy MS, Spatola B, Weathermon R (2014) Allies today, enemies tomorrow: a comparative analysis of perimortem injuries along the biomechanical continuum. In Martin DL, Anderson CP (eds)

Bioarchaeological and forensic perspectives on violence: how violent death is interpreted from skeletal remains, Cambridge University Press, Cambridge, pp 261-288

[13] Bird CE, Fleischman JM (2015) A rare case of an intact bone plug associated with a gunshot exit wound. J. Forensic Sci. 60 (4): 1074-1077

[14] Kieser DC, Riddell R, Kieser JA, Theis J, Swain MV (2013) Bone micro-fracture observations from direct impact of slow velocity projectiles. J Arch Mil Med 2(1): e15614 https:// doi.org 10.5812/jamm.15614

[15] Huelke Df, Buege LJ, Harger JH (1967). Bone fractures produced by high velocity impacts. Am.J. Anat 20:123-132

[16] Huelke DF, Harger JH, Buege LG, Dingman HG, Harger DR (1968). An experimental study in bio-ballistics: femoral fractures produced by projectiles. J. Biomech. 1:97-105

[17] Huelke DF, Harger JH, Buege LG, Dingman HG (1968). An experimental study in bio-ballistics: femoral fractures produced by projectiles- II, shaft impacts. J. Biomech.1:313-321

[18] Harger JH, Huelke DF (1970). Femoral fractures produced by projectiles-the effects of mass and diameter on target damage. J. Biomech.1:487-493

[19] Jover N, Shafiq B, Vaidya U (2014). Ballistic impact analysis of balsa core sandwich composites. Compos. Part B-Eng 67: 160-169

[20] Woodward R, Baxter B, Pattie S, Mccarthy P (1991). Impact fragmentation of brittle materials. J. Phys. IV Colloque, 1991, 01, (C3), pp C3-259-C3-264 10.1051/jp4:1991336 jpa-00250478

[21] Woodward RL, Gooch Jr WA, O'Donnell G, Perciballi WJ, Baxter BJ, Pattie SD (1994). A study of fragmentation in the ballistic impact of ceramics. Int. J. Impact Engng 15 (5): 605-618

[22] Abrate S (1998) Impact on composite structures. Cambridge University Press, Cambridge

[23] Tang Z, Tu W, Zhang G, Chen Y, Lei T, Tan Y (2012). Dynamic simulation and preliminary Finite Element Analysis of gunshot wounds to the human mandible. Injury, Int. J. Care Injured 43: 660-665

[24] Smith MJ, James S, Pover T, Ball N, Barnetson V, Foster B, Guy C, Rickman J, Walton V (2015). Fantastic plastic? Experimental evaluation of polyurethane bone substitutes as proxies for human bone in trauma simulations. Leg Med (Tokyo) 17: 427-435

[25] Taylor SC, Kranioti EF (2018). Cranial trauma in handgun executions: experimental data using polyurethane proxies. Forensic Sci. Int 282:157-167

[26] Henwood BJ, Appleby-Thomas G (2020). The suitability of synbone ® as a tissue analogue in ballistic impacts. J. Mater. Sci 55: 3022-3033

[27] Kneubuehl BP (2011). General wound ballistics. In Kneubuehl BP (Ed), Coupland RM, Rothschild MA, Thali MJ. Wound ballistics: basics and applications. Springer-Verlag Berlin, Heidelberg 87-161

[28] Ross AH (1996) Caliber estimation from cranial entrance defect measurements. J. Forensic Sci. 41 (4): 629-633

[29] Paschall A, Ross AH (2016). Bone mineral density and wounding capacity of handguns: implications for estimation of caliber. Int J Legal Med 131: 161-166

[30] Kroman A (2010) Rethinking bone trauma: a new biomechanical continuum based approach. 62nd Annual Meeting of the American Academy of Forensic Sciences, Chicago, Illinois

[31] Spatola BF (2015). Atypical gunshot and blunt force injuries: wounds along the biomechanical continuum. In Passalacqua NV, Rainwater CW (eds) Skeletal trauma analysis: case studies in context. John Wiley & Sons, West Sussex, pp 7-26

[32] Guiberteau F, Padture NP, Cai H, Lawn BR (1993) Indentation fatigue: a simple cyclic Hertzian test for measuring damage accumulation in polycrystalline ceramics Philos. Mag A 68 (5): 1003-1016

[33] Lawn BR (1998) Indentation of ceramics with spheres: a century after Hertz. J Am Ceram Soc 81 (8):1977-1994

[34] Rickman JM, Smith MJ (2014) Scanning Electron Microscope analysis of gunshot defects to bone: an underutilised source of information on ballistic trauma. J Forensic Sci 59 (6): 1473-1486 https:// doi.org 10.1111/1556-4029.12522

[35] Komar DA, Buikstra JE (2008) Forensic anthropology: contemporary theory and practice. Oxford University Press Inc., New York.

[36] Kimmerle EH, Baraybar JP (2008). Skeletal trauma: identification of injuries resulting from human rights abuses and armed conflict. CRC Press, Florida.

[37] Symes SA, L'Abbé EN, Chapman EN, Wolff I, Dirkmaat DC (2012) Interpreting traumatic injuries to bone in medicolegal investigations. In Dirkmaat DC (ed) A companion to forensic anthropology, Wiley- Blackwell Publishing, West Sussex

[38] Xu J, Gilson DFR, Butler IS, Stangel I (1996) Effect of high external pressures on the vibrational spectra of biomedical materials: calcium hydroxyapatite and calcium fluoroapatite. J. Biomed. Mater. Res 30: 239-244

[39] Gaîdash AA, Bashirov RS, Kolkutin VV, Tolmachev IA, Tyurin MV, Bozhchenko AP, Denisov AV (2010) New data on the morphogenesis of gunshot injuries to bone. СУДЕБНО-МЕДИЦИНСКАЯ ЭКСПЕРТИЗА ((Forensic Medical Examination) 4, 2010

APPENDIX 1

Published paper:

A novel hypothesis for the formation of conoidal projectile wounds in sandwich bones

John M Rickman* (MSc) and Dr James Shackel

Corresponding author address:

Cranfield Defence and Security

Cranfield University

Defence Academy of the United Kingdom

Shrivenham

SN6 8LA

*Corresponding author email address: j.m.rickman@cranfield.ac.uk

*Phone: 01793785531

*ORCID: 0000-002-1188-8805

International Journal of Legal Medicine
https://doi.org/10.1007/s00414-018-1946-x

ORIGINAL ARTICLE

A novel hypothesis for the formation of conoidal projectile wounds in sandwich bones

John M. Rickman[1] · James Shackel[1]

Received: 9 April 2018 / Accepted: 10 October 2018

Abstract
When perforated by a projectile, sandwich bones typically exhibit wounds with a distinct conoidal morphology that is widely utilised both in wound diagnosis and trajectory determinations. However, the dynamic fracture mechanisms underlying this intriguing wound type have yet to be experimentally verified. The most frequently quoted hypothesis for their formation, plug and spall, is difficult to reconcile with the conoidal morphology exhibited by such wounds. The present article carries out a high-speed videographic and micro-computerised tomographic (μ-CT) analysis of perpendicularly produced projectile wounds induced from 139.15 to 896.84 metres per second (m/s) in pig scapulae. Fundamental data on energy absorption, wound shape and bevel symmetry are presented. Cross-sectional fracture morphology revealed by μ-CT raises the novel hypothesis that tensile stresses induced by the projectile in the outer cortex elicit cone crack formation and that this cone crack then propagates catastrophically through the entire sandwich structure. This process results in the momentary formation of a bioceramic conoid, a conoidal volume of bone consisting of all three sandwich bone layers separated from the parent bone by the internal bevel. Fragmentation of the separated volume leaves the conoidal wound behind as its counterpart. The significance of this hypothesis in terms of differential diagnosis and interpretation of bevel shape is discussed.

Keywords Skeletal trauma · Projectile injuries · Forensic anthropology · Forensic pathology · Fracture · Sandwich bones

The potential of a bullet to incapacitate is determined by impact location and thus the anatomical structures damaged along the bullet tract [1], in addition to the amount of energy absorbed by those impacted tissues. In this regard, gunshot wounds to the cranial vault are exceptionally lethal. Mortality data summarised by Aarabi et al. [2] suggest that up to 71% of victims die at the scene of the shooting, whilst in the USA a 90% mortality rate has been reported in civilian settings [3]. From a forensic perspective, gunshot wounds to the sandwich bones of the skull are thus of considerable interest. In cross-section, sandwich bones are tri-layered structures consisting of two layers, or *laminae*, of cortical bone enclosing a lamina of trabecular bone [4]. Perpendicular entry wounds to such bones typically consist of a circular fracture in the outer cortical layer and a larger cone-shaped area of damage involving the trabeculae and inner cortical layer termed the *bevel* [5], resulting in what may be described as a *conoidal wound*. Such conoidal wounds characteristically flare in the direction of projectile travel, resulting in an *internal bevel* in entry wounds and an *external bevel* in exit wounds [5]. Further trajectory determinations are based on areas of bevel elongation, which are thought to correspond to the specific direction of projectile passage [6, 7]. However, despite the clear importance of such determinations, the fracture mechanisms underlying formation of conoidal wounds remain unclear. In addition, the layers forming the bevel and other cross-sectional features of their microanatomy have to date received no formal definitions.

A significant step in establishing how conoidal wounds form in sandwich bones is identification of the bony layers through which critical fractures propagate to produce the final morphology. The cortical layer of the sandwich bone first impacted by the projectile is here defined as the *outer cortical layer* and its counterpart the *inner cortical layer*. The region where the trabecular bone meets a cortical layer is here defined

✉ John M. Rickman
j.m.rickman@cranfield.ac.uk

James Shackel
j.shackel@cranfield.ac.uk

[1] Cranfield Defence and Security, Cranfield University, Defence Academy of the United Kingdom, Shrivenham SN6 8LA, UK

Published online: 18 October 2018

as the *cortical-trabecular transition*, with one such region under the outer cortical layer and another above the inner cortical layer. In this paper, a crack propagating through a sandwich bone is defined as *inter-laminar* if it passes between layers and separates them (the process of *delamination*), *intra-laminar* if it occurs within a layer and *trans-laminar* if it crosses a layer (Fig. 1). Cracks are further classified as *mode 1* if produced by tensile stress (crack opening) and *mode 2* if produced by in plane shear, i.e. by one part sliding past another with no crack opening [8]. At present, the most widely accepted theory for conoidal wound formation is plug and spall [e.g. 9–11], which proposes that high tensile stresses initiated under the impacting projectile cause the shearing of a plug of bone from the outer cortical layer of the sandwich bone, which then moves ahead of the projectile through the other bone layers. According to this hypothesis, conoidal wound formation is a shear plugging process consisting of two phases:

1. Projectile entry through the outer cortical layer with associated shear plug formation
2. Bevel production during the process of projectile exit

Critically, this hypothesis proposes that bevel production occurs secondarily to plug formation; however, the specific biomechanical processes underlying bevel production by this cortical plug differ across the literature. Peterson [12] suggested that the cortical disc of bone is pushed through the trabecular layer and then blows out the bevel on the inner layer. Komar and Buikstra [9], Symes et al. [10] and Christensen et al. [11] suggested that spall, or fracture, produces the internal bevel without speculating on the stresses involved, whilst Kimmerle and Baraybar [13] suggested that bevelling is created by the plug shearing through the trabeculae. Kieser et al. [14] used micro-computerised tomography to analyse cross-sections of pig ribs perforated by 0.22 handgun projectiles and reported a clear transition between a vertically walled channel through the outer cortical layer and the conoidal bevel beneath. Utilising this interpretation of the wound cross-section, these authors suggested that the sheared cortical plug, together with accumulated fractured material ahead of it, causes internal bevel production through a process of brittle fracture. These theories notwithstanding, it remains unclear as to why, specifically, a conoidal morphology is formed by the plug and spall mechanism, and nor is it clear how a cortical plug could withstand the massive stresses of the impact event without itself fragmenting during the perforation process.

An implicit assumption of the plug and spall hypothesis is that trans-laminar fracture is limited to the outer cortical layer, resulting in production of a plug consisting solely of cortical bone. However, recent descriptions of conoidal wounds associated with intact tri-layered bone plugs in both archaeological and recent material raise the intriguing hypothesis that all three layers of the sandwich bone might fracture as a unit during projectile impact due to trans-laminar fracture propagation through the entire structure. The first description of such plugs was provided by Murphy et al. [15] who described frontal and parietal plugs associated with perforating wounds of unknown aetiology in archaeological material. Murphy et al. [16] later described two more entry wound plugs in a parietal (produced by impact with a train) and occipital (produced by a cross-bow bolt), and Bird and Fleischman [17] later provided additional information on a frontal bone exit wound plug produced by low-velocity bullet impact. Significantly, these tri-layered bone plugs are conoidal and the hole they fit into in their parent bone is bevelled accordingly, internally for an entry [15, 16] and externally for an exit [17]. The compressive side of the plug in the outer cortical layer may exhibit compressive damage, whilst the tensile side of the plug in the inner cortical layer is often characterised by radial fractures emanating from a central point, a process resulting in a distinct *stellate fracture* pattern. Although this limited number of reports testifies to tri-layered plug formation during at least some low energy impacts, it is currently unknown if their production is fundamental to conoidal wound formation or if these rare examples are atypical in nature.

A number of questions may be posed in relation to the mechanisms underlying conoidal wound formation. Firstly, what plugging mechanisms are operative during projectile perforation of sandwich bones; i.e. is trans-laminar fracture isolated to the outer cortical plate or does it involve all three layers? Secondly, is the same plugging mechanism operative at different velocities? Thirdly, if a role for tri-layered plugs is suggested by conoidal wound morphology, by what mechanisms are they formed? Fourthly, how might these mechanisms influence wound morphology? Fifthly, does projectile impact initiate internal damage peripheral to the conoidal wound? In order to begin to address these questions, the present paper presents the findings of a high-speed video and micro-computerised tomographic (μ-CT) analysis of a series of experimentally induced projectile wounds inflicted at a series of increasing velocities to porcine scapulae. Gross wound morphology is described and basic data on energy absorption by sandwich bones during perforation is established. Based on this investigation, a nomenclature for the cross-sectional microanatomy of projectile wounds is developed and a novel theory for the formation of conoidal wounds is presented.

Methods

Projectile type and characteristics

Projectile yaw (deviation from horizontal flight) and deformation significantly affect the amount of energy absorbed during tissue penetration. In order to eliminate the effects of these

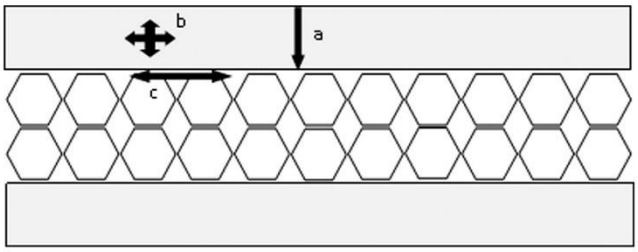

Fig. 1 Fracture classification scheme utilised for cracks in sandwich bones; outer cortical layer (top rectangle), inner cortical layer (bottom rectangle) and trabecular layer represented by hexagons. (a) *Trans-laminar fracture* crosses a lamina. (b) *Intra-laminar fracture* occurs within a lamina and may occur in any direction. (c) *Inter-laminar fracture* or *delamination* occurs between laminae

variables on fracture processes, surface hardened carbon steel spheres (Atlas Ball and Bearings Co. Ltd., UK) were utilised. Sphere weight and calibre were calculated from 24 spheres. Projectile calibre was measured using digital sliding callipers measuring to one hundredth of a millimetre. To determine projectile hardness, four spheres were ground and polished, mounted in polyester resin and then tested in a HWDM Indentec Micro indenter (Indentec Ltd., UK); ten readings were taken for the surface hardened exterior and ten for the core of each projectile. Mean hardness for each region was calculated from all four projectiles. Mean Vickers hardness values and projectile specifications are presented in Table 1. High Vicker's hardness and observation of high-speed footage indicated that projectile deformation could be eliminated from consideration in wounding processes.

Sample selection

Given both the rarity and ethical implications of utilising human bone, this material was considered unsuitable for preliminary investigation. The scapulae of large domesticated artiodactyls, including the cow (*Bos taurus*) and pig (*Sus scrofa*), are sandwich bones that exhibit internally bevelled wounds when subjected to ballistic impact. As such, their suitability as surrogates for the human cranium in experimental ballistic work has been discussed previously [18, 19]. Pig scapulae are smaller and therefore easier to machine, store and secure during testing than cow scapulae and were therefore selected for this experiment.

Sample preparation and velocity groups

Frozen pig scapulae were obtained from animals killed humanely as part of the food chain; samples were only taken from animals 12–14 months of age to ensure ossification of the target region. Specimens were stored frozen in sealed plastic bags at all times apart from when being prepared and impacted. The infraspinous fossa was selected as the impact region due to its larger size; only specimens with soft tissue in this region were utilised. Selected shot direction was lateral to medial, allowing the bevel to form in the flatter subscapular plate. In order to create specimens with a relatively uniform plate configuration, frozen specimens were machined on a bandsaw to approximately 120 mm height; as much of the scapular spine as possible was also removed (Fig. 2).

Target location in the scapulae was chosen to be 40–50 mm from the nearest edge; once selected, the location was marked with an ink dot. In order to examine wounds inflicted across a series of velocities and to allow comparison of impact data, fleshed specimens were allocated into one of five velocity groups. Each velocity group was allocated a target impact velocity; V_1 (150 m/s), V_2 (350 m/s), V_3 (450 m/s), V_4 (650 m/s) and V_5 (850 m/s), with groups V_2 and V_5 encompassing muzzle velocities of common handgun and rifle ammunition, respectively. To capture examples of soft and hard tissue behaviour during projectile exit, the camera was moved to face the rear of selected specimens. Using this mechanism, exit was filmed in one fleshed V_1 specimen and one fleshed V_2 specimen. To fully visualise bone fracture behaviour during exit, five additional specimens were defrosted and soft tissue dissected away from the inner cortical plate (group D); these specimens were impacted between 139–146 m/s. All specimens were defrosted slowly at room temperature in their sealed bags before the ballistic tests.

Table 1 Projectile characteristics, standard deviations in parentheses

Material	Mean surface hardness (Vickers) ($n = 10$)	Mean core hardness (Vickers) ($n = 10$)	Mean diameter (mm) ($n = 24$)	Mean weight (g) ($n = 24$)
Surface hardened carbon steel	717 (33.75)	455 (28.13)	5.98	0.885

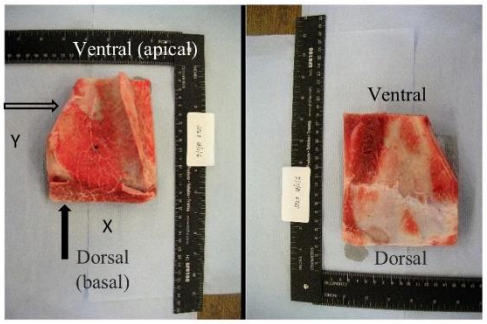

a.Lateral aspect b. Medial aspect

Fig. 2 Machined plate of sandwich bone with soft tissue covering orientated in shooting position. Anatomically ventral portion of scapula formed the apex of the plate during shooting. Letters x and y in **a** denote the axes utilised in μ-CT analysis; z-axis (not shown) refers to the depth of the specimen. Longitudinal (y-z) section indicated by open arrow; transverse (x-z) section indicated by closed arrow; x-y section descends through the depth of the plate. **a** Lateral aspect. **b** Medial aspect

Shooting equipment and high-speed filming

The response of bone to loading is strongly influenced by the direction in which it is loaded; that is, bone is anisotropic [20]. In order to reduce the influence of loading direction on wounding patterns, all specimens were mounted with the broad, anatomically dorsal region acting as the base and the narrower ventral region acting as the apex. Specimens in groups V_1–V_3 were impacted using a compressed air powered 21.3-mm calibre gas gun with a 12-cm muzzle-target distance; projectiles were held in a plastic holder (sabot) during firing which fragmented on a metal sabot stripper after exiting the barrel. To approach the desired velocities in the last two velocity groups, an initial round of 12 impacts across groups V_4 and V_5 utilised a 30-mm helium powered gas gun; however, in all but two impacts high-velocity plastic sabot fragments were found to have damaged the impact area. Accordingly, a further 13 specimens in groups $V_{4\text{-}5}$ were prepared and impacted using an Enfield number three proof housing with a 7.62-mm barrel; projectiles were sabot mounted and fired from a cartridge using a muzzle-target distance of 3.80 m to prevent sabots from impacting the specimens. Projectile perforation in defleshed V_6 specimens was achieved using a compressed air-powered gas gun, capable of velocities approaching 150 m/s.

Phantom high-speed cameras were utilised to obtain high-speed footage of all impacts (Vision research, New Jersey). A Phantom v12 camera operating at 55009 frames per second was utilised for both side and exit footage in the gas gun experiment. Specimen location during exit filming in the gas gun chamber prevented lateral placement of a second camera for velocity determination; accordingly, velocity was determined using the gas gun's time gate. High-speed footage for V_4 and V_5 was obtained using a Phantom v1212 camera at 37000 frames per second. V_6 exit footage was obtained using a Phantom v1212 camera at 40,000 frames/s, whilst lateral footage was obtained using a Phantom v7 camera operating at 5500 frames/s. Differences in cameras utilised were based solely on equipment availability and the maximum frame rate possible was utilised for each experimental set up. A millimetre scale was placed in view of the camera during filming to allow subsequent velocity determinations. To calculate incident (pre-impact) and residual (post-impact) projectile velocities, the camera was placed to the side of the impacted specimens. Velocities were then determined using Phantom Cine Viewer on a laptop. To allow for variation in the estimation of velocity caused by blurring of the projectile edges, the frame offering the best view of the projectile was selected and a clear location on the projectile noted. Velocity determinations were made using the same frame and location on the projectile on three separate occasions; projectile velocity was taken to be the mean of these three determinations.

Kinetic energy and energy absorption calculations

The kinetic energy, E, in joules, of a projectile of mass m (in kilogrammes) and velocity v (in metres per second, m/s) is given by:

$$\frac{mv^2}{2} \tag{1}$$

During penetration, the kinetic energy of the projectile is transferred to the tissues and utilised to do mechanical work, manifested as tissue wounding. If the projectile retains kinetic energy and exits the impacted body, and if there is no change in mass of the projectile, the kinetic energy absorbed (ΔE) is equal to the difference between the incident kinetic energy (E_i) and residual kinetic energy (E_r) and is given by:

$$\frac{m\left(v_1^2 - v_2^2\right)}{2} \tag{2}$$

where V_1 is the incident velocity and V_2 the residual velocity. E_i, E_r and ΔE were calculated for each perforation event and the mean of these values determined for each velocity group. The amount of energy utilised to perforate the bone in relation to available incident kinetic energy was expressed as a percentage using the formula $\Delta E/E_i \times 100$. In order to determine the error associated with ΔE values for each individual perforation event, which was calculated from the mean of three velocity determinations, an error propagation formula was generated. The error propagation formula propagates the standard deviations of the projectile velocity and mass measurements in order to provide a standard deviation for the energy absorbed, $[\sigma_{\Delta E}]^2$:

$$[\sigma_{\Delta E}]^2 = \left[\frac{{v_1}^2-{v_2}^2}{2}\right]^2 [\sigma_m]^2 + \left[\frac{v_1}{2}\right]^2 [\sigma_{v_1}]^2 + \left[\frac{v_2}{2}\right]^2 [\sigma_{v_2}]^2 \quad (3)$$

where σ is the standard deviation and m is the mass of the projectile in kilogrammes, v_1 is the impact velocity and v_2 the residual projectile velocity. The standard deviation associated with the kinetic energy absorbed for each individual impact is calculated by taking the square root of $[\sigma_{\Delta E}]^2$.

Impacted specimen analysis and micro-computerised tomography

In order to retain structural features critical to morphological analysis such as displaced bone fragments, soft tissue was left in situ for scanning. Long scan times and large sample size necessitated re-freezing impacted bones to prevent soft tissue decomposition prior to scanning. After impact, the bones were placed into a sealable bag, wrapped in protective tissue and frozen.

For μ-CT analysis, specimens were scanned in an X-Tec XT H 225 μ-CT (Nikon, Japan). In order to maximise resolution, the wound region was selected and observed at 75 kV, 90 μA and 2.25 magnification, giving a voxel size of 89 μm. The scanned volumes were manually reconstructed using Nikon's CT Pro 3D software; to eliminate edge artefacts, the radius of reconstruction was reduced from 100 to 90–95% depending on specimen size and the location of the wound. Volumes were analysed in VGStudeo MAX version 2.2 (Volume graphics, Germany). In order to allow comparison of x-z (transverse) and x-y (longitudinal) planes in VGStudeo MAX, a simple registration was carried out; each sectional plane was orientated so that the specimen occupied the centre of the screen with the cortical entry wound uppermost. In order to use the software's measuring tools, the bone surfaces were identified and highlighted using the surface determination function, which allows the user to specify the background and the material of interest.

Controls

To determine if re-freezing impacted bones resulted in damage alteration, a shot control was μ-CT scanned pre- and post-freezing to allow comparison of damage areas. Surface determination and simple registration were performed on pre- and post-freeze scans. Three damaged and displaced cortical bone regions in the pre-freeze scan were selected and the software's measuring tool utilised to measure the straight line distance in millimetres between two readily identifiable points in each of these damaged areas. To aid identification of the same landmarks in the post-freeze scan, an image of each location in the pre-freeze scan was saved as a JPEG file. The post-freeze scan was then opened and landmarks identified using the appropriate JPEG image; straight line distances between the same points were then measured and compared to pre-freeze measurements.

Gross wound morphology

Cortical entry wounds were classified as circular, oval, irregular or a combination of these; circular-irregular or oval-irregular wounds were classified as wounds with irregularity occurring in part of the otherwise symmetrical wound margin. Based on cross-sectional views obtained using μ-CT, the internal bevel was defined as a fracture surface encompassing the trabeculae and the fracture edge of the inner cortical layer. Following Quatrehomme and İşcan [21], internal bevels were defined as symmetrical if the bevel formed an evenly distributed wound margin and asymmetrical if any part of the perimeter was noticeably more pronounced. Preliminary μ-CT analysis indicated that the internal bevel is present beneath retained inner cortical plate fragments and these were thus considered part of the bevelled area when determining bevel symmetry. The relationship between the shape of the cortical entry wound and the shape of the internal bevel was assessed utilising μ-CT in both sectional and three-dimensional views.

Results

A total of 47 specimens were perforated; 13 specimens from groups V_{4-5} were excluded from analysis due to plastic sabot damage in the 30-mm gas gun chamber or off target impacts when using the projectile housing apparatus. Of the remaining 34 sandwich bones, only the fully fleshed specimens ($n = 29$) were scanned in the μ-CT and utilised for subsequent computerised analysis. A total of seven inner plate cortical exits were filmed, five with soft tissue removed and two with soft tissue in situ.

Controls

Comparison of pre- and post-freeze wounds suggested that freezing did not alter gross wound structure. Differences in measurements between pre-freeze and post-freeze scans were 30 μm, 10 μm and 10 μm, respectively. Such sub-millimetre differences between pre-and post-freeze measurements are likely attributable to small variation in surface determinations between scans, to fine differences in placement of each end of the measurement tool and to the possibility that the selected post-freeze measurement location did not fully correspond exactly to the pre-freeze measurement location.

Kinetic energy absorption and gross wound morphology

The total range of impact velocities was 139.15 m/s to 896.84 m/s; all specimens were fully perforated. Mean incident kinetic energies and mean absorbed kinetic energies are provided for each velocity group in Table 2. Mean absorbed kinetic energy in group V_5 was 10.73 times greater than in group V_1. An increase in incident kinetic energy resulted in an increase in the amount of energy absorbed. The percentage of available incident kinetic energy absorbed during perforation was inversely related to velocity; whilst just under half of incident kinetic energy was absorbed during perforation in V_1, less than a quarter was absorbed in V_5.

Observation of soft tissue post-impact revealed a dusting of sabot fragments in the soft tissue around the perforation site. Whilst some wound irregularity due to sabot impact cannot be fully ruled out, their presence around both circular and irregular wounds suggested any such effects were absent or minimal. Table 3 provides sample data on gross wound morphology across the five velocity groups. Only group V_1 exhibited the same entry wound shape in all perforated specimens, with all being circular. Increased incident velocity resulted in greater variation in cortical entry wound shape between specimens and an increase in occurrence of irregular wounds. Despite this general trend, there was overlap in entry wound morphology across groups V_2–V_5. In total, the majority of wounds (48.26%) were circular, followed by irregular (27.59%), circular-irregular (13.79%), oval-irregular (6.90%) and oval (3.45%). The majority of wounds exhibited asymmetrical bevelling (82.76%), whilst symmetrical bevelling was present in only 17.24% of wounds. The high frequency of bevel asymmetry meant that, of the 14 circular entry wounds, only two (in group V_1) exhibited a symmetrical bevel. Excluding four specimens across V_4 and V_5 where extensive cortical plate damage prevented accurate analysis, irregular cortical entry shape was lost by the internal bevel in 8/10 of the remaining irregular or partially irregular wounds.

There was variation in the extent of damage within groups at higher velocity; for example, whilst one specimen in V_4 and three specimens in V_5 exhibited considerable internal and external cortical plate damage at the impact location, other specimens in these groups showed far less damage despite similar energy absorption values. For example, in V_5 one specimen was perforated at 851.92 m/s, absorbed 60.39 J of energy and exhibited extensive damage to both external and internal plates; another, impacted at 871.02 m/s and absorbing 56.32 J, presented with a neat circular entry with a slightly depressed top margin.

Table 2 Mean incident kinetic energy (E_i), mean residual kinetic energy (E_r), mean absorbed kinetic energy (ΔE) and mean percentage kinetic energy absorbed

Velocity group	E_i (J)	E_r (J)	ΔE (J)	Percentage	Range ΔE (J)
D ($n=5$)[a]	8.93 (0.27)	3.72 (1.06)	5.21 (1.07)	58.37 (12.11)	3.32–6.40
V_1 ($n=6$)[b]	11.58 (0.95)	5.80 (0.88)	5.78 (0.72)	49.98 (5.32)	5.18–7.13
V_2 ($n=4$)[b]	55.45 (4.77)	40.27 (6.06)	15.18 (1.31)	27.68 (4.68)	13.46–16.63
V_3 ($n=3$)	93.20 (1.17)	70.33 (3.43)	22.87 (4.58)	24.48 (4.57)	18.72–29.24
V_4 ($n=5$)	191.06 (31.93)	148.37 (21.12)	42.69 (13.78)	22.04 (4.02)	32.18–63.65
V_5 ($n=7$)	318.24 (37.38)	256.19 (29.80)	62.05 (13.14)	19.43 (2.86)	42.38–86.72

All energy data in joules with standard deviations in parentheses

[a] Group D specimens had soft tissue dissected from the inner cortical plate prior to perforation, resulting in an unquantified reduction in energy absorption

[b] Two specimens from $n=8$ in V_1 and two of $n=6$ specimens in V_2 were utilised for perforation filming in a confined gas gun chamber that would not fit two high-speed cameras; velocities could thus not be determined from lateral high-speed footage

High-speed footage of inner plate perforation and μ-CT imaging of exit damage

Observation of the inner cortical plate during projectile exit at × 4 magnification failed to detect the ejection of a disc of bone corresponding to a sheared plug from the outer cortical layer, although fragmentation of such a structure once formed cannot be ruled out. High-speed footage revealed that tensile stellate fracture of the inner cortical plate was a significant component of the exit process. This fracture type, consisting of numerous radial cracks emanating from a central region of the exit, was clearly observed in three out of the five defleshed specimens and in both fleshed specimens; projectile exit was out of frame in two defleshed perforation events but an apparent stellate fracture was visible in a detached circular fragment in one of these (see below). Figure 3 shows a typical example of projectile exit in a defleshed inner plate at 142.51 m/s, with Fig. 3a showing the plate just before exit is initiated (designated time 0). The first indication of the perforation event was a small circular elevation of the cortex in the region that will form the location of the bevelled exit (Fig. 3b); although small, this elevation was detectable when compared to the non-perforated inner plate (Fig. 3a). Within 25 μs, the elevation had increased in height and exhibited three radial fractures emanating from its apex (Fig. 3c), forming a distinct stellate fracture that demarcated at least three triangular bone fragments (highlighted in Fig. 3d). As projectile exit proceeded, the cortical fragments elevated (Fig. 3e) and then

Table 3 Entry wound shape and bevel symmetry for $n = 29$ sandwich bone perforation events. Morphology determined in fleshed specimens using μ-CT in order to preserve fragile fractured elements on the inner cortical plate

Velocity group	Circular	Oval	Irregular	Circular-irregular	Oval-irregular	Bevel symmetry	
						S	A
V_1	8					2	6
V_2	1		2	2	1	2	4
V_3			2	1		0	3
V_4	3	1	1			0	5
V_5	2		3	1	1	1	6
Total	14	1	8	4	2	5	24
Percentage	48.26	3.45	27.59	13.79	6.90	17.24	82.76

S symmetrical, *A* asymmetrical

everted, resulting in their internal faces being uppermost (Fig. 3f). Cortical fragments were then either detached from the inner plate to form larger components of the ejecta plume or remained in situ. Measured from time zero to when the projectile was fully visible, the exit process took a total of 0.225 s at 142.51 m/s.

The crack forming the perimeter of the region of stellate fracture, here designated the *exit cortical fracture edge*, formed the cortical margin of the internal bevel. The radial tensile cracks composing the stellate fracture always arrested at this edge, a phenomenon also clearly visible in μ-CT images of perforated inner cortical plates (see Fig. 4). This crack arrest process indicates that the internal bevel must form very early during perforation and before radial crack production and dictates that bevel shape and symmetry is largely determined before the projectile has exited the bone. In one 142.52 m/s perforation, an approximately circular structure consisting of a fractured inner plate of cortical bone was captured moving ahead of the projectile (Fig. 4a). This removed circular section corresponded in part-counterpart fashion to the bevelled exit beneath it, and it thus represented the cortical floor of the conoidal wound volume (Fig. 4a, thick arrow). The central portion of this circular plate presented a faint rhomboidal pattern with a centrally located apex, indicating stellate fracture had initiated but not completed there (Fig. 4a, thin arrow). In this specimen, fracture of the inner cortical plate during bevel formation allowed displacement of a complete disc of cortical bone. Due to the angle of observation, it was not clear if this circular structure was composed of all three sandwich bone layers. Observation of exit in fleshed specimens at both low (168 m/s) and moderate (333 m/s) velocity revealed the same sequence as observed in defleshed specimens. A small elevation appeared, which then grew in height; the walls of this elevation, although covered in soft tissue, were clearly triangular in shape and formed by stellate fracture (Fig. 4b). The fragments then proceeded through the processes of elevation and eversion before being ejected.

A series of μ-CT images of inner cortical plate damage morphology is provided in Fig. 4c–f. Triangular fragments on the inner plate of specimens in V_1 and V_2 were often left in an elevated position forming *fragment cones* (Fig. 4c–d), and when present the region of convergence of the elevated fragments represented the point of projectile exit (Fig. 4d–e). Subsequent to higher velocity impacts in groups V_2–V_5, inner plate fragments remained confined within the margin of the exit cortical fracture edge but often presented with semi-lunar or rectangular form (Fig. 4f, thin arrow), with a fractured distal border indicating loss of material in the ejecta plume (Fig. 4f).

μ-CT fracture analysis of projectile wounds

μ-CT analysis revealed a number of internal morphological features of perforating wounds to sandwich bones and the following nomenclature was developed for analysis. An annotated cross-section typical of perforations across the series is shown in the y-z (longitudinal) plane in Fig. 5. In cross-section, the conoidal morphology of such perforating wounds is readily apparent. The *cortical entry wound* (1) is delineated by an *entry cortical fracture edge* (2). The fractured edges of the trabeculae are discernible and form a *trabecular fracture margin* (3). The *peripheral trabeculae* (4) may be classified as trabeculae up to 3 mm peripheral to the trabecular fracture margin. The *cortical exit wound* (5) is delineated by an *exit cortical fracture edge* (6). In current terminology, the *trabecular fracture margin* and *exit cortical fracture edge* would together constitute the *internal bevel* (7); however, in-line fracture between the entry cortical fracture edge and the trabecular fracture margin immediately beneath it makes the definition of what layers constitute the internal bevel somewhat arbitrary. The *cortical entry wound* and *internal bevel* together constitute the *wound volume* (8). Although *trabecular intrusion* into the wound volume was observed in some sections (see Fig. 6b), a distinct feature of the wound volume in

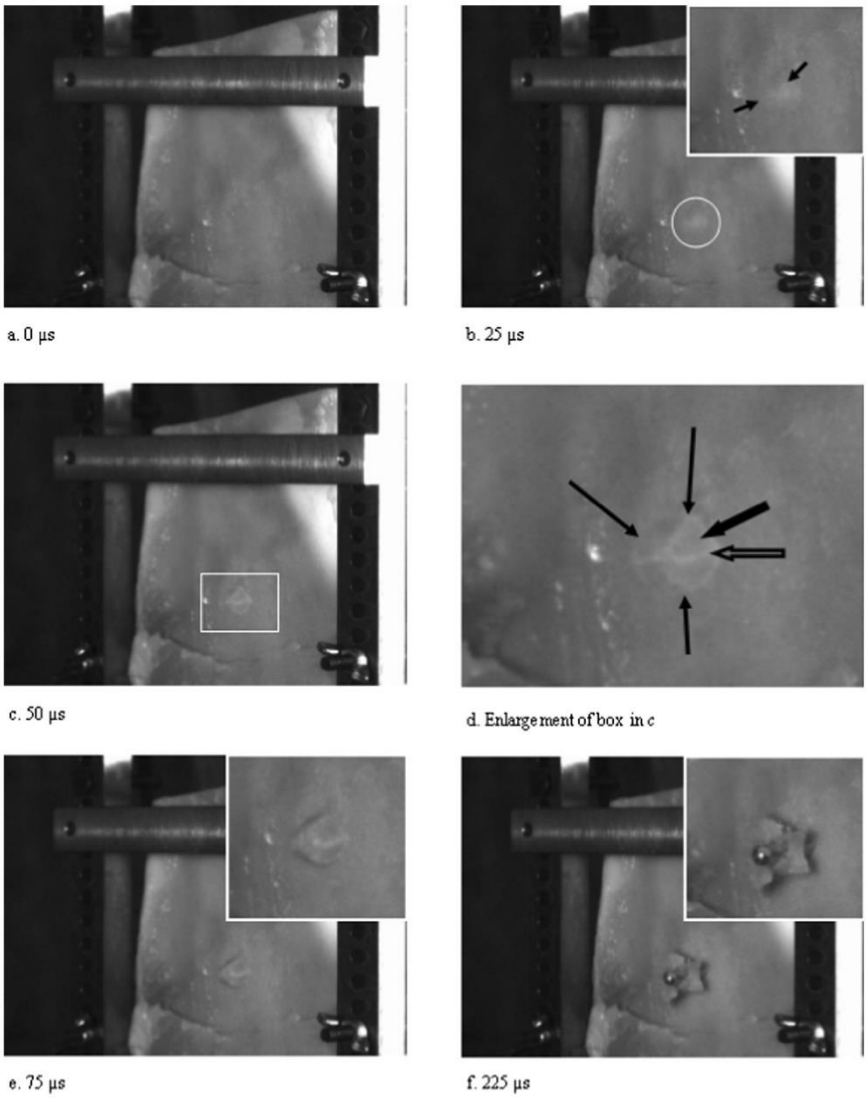

Fig. 3 Projectile exit, soft tissue removed, incident velocity 142.51 m/s (σ 0.61); **a** Pre-impact. **b** Initial cortical elevation visible as whiter region; enlargement inset shows faint indications of stellate fracture (arrows). **c** Fracture cone (highlighted). **d** Enlargement of fracture cone. Note example of radial fracture (large open arrow) and inner cortical plate fragment (large closed arrow). Thin arrows denote margin of external bevel, the *exit cortical fracture edge*; note that radial fractures arrest at this feature. **e** Plate elevation. **f** Plate eversion

the trabecular region is an abrupt border formed by the free edges of fractured trabecular cells.

In section, a characteristic feature of the entry cortical fracture edges is their angulation with respect to the cortical surface, a structure conforming to the typical cone crack morphology observed in impacted non-biogenic brittle materials such as ceramics (Fig. 6a–c). This cone crack type morphology was observed in 25 specimens across the five velocity groups; only four specimens with extensive damage to both cortical layers did not exhibit bilateral angulation at some

point in the cross-section. Mean cortical angles of the entry cortical fracture edge were obtained using the angle measuring tool in VGStudeo MAX; the y-z plane (longitudinal) was utilised to avoid any effects induced by curvature of the scapular fossae in the transverse direction. Results for the apical and basal sides of the wounds are presented in Table 4. Mean cortical angles differed on each side of the wound, with mean basal angles showing less variation than mean apical angles. Individual cortical angles showed considerable overlap across the velocity groups with no apparent association with velocity.

Analysis of fracture propagation at the upper cortical-trabecular interface revealed that, rather than adopting an inter-laminar course, the crack initiated in the outer cortex entered the trabeculae and extended through to the exit cortical fracture edge on the same side, producing a continuous trans-laminar fracture margin through the wound channel and resulting in an internal conoidal symmetry (Fig. 6a–c, e). This conoidal symmetry and common fracture edge through the three layers was found in all velocity groups and was thus independent of the absorbed kinetic energy. Lack of inter-laminar fracture at the cortical-trabecular interfaces meant that no specimens showed any evidence of delamination of the sandwich structure around the circumference of the wound channel. Pronounced intra-laminar fracture between cortical layers, produced by lateral deviation of the crack tip *within* the trabecular region, was observed in two thin specimens in groups V_1 and V_5 and one thicker specimen in V_1. The latter specimen, perforated at 166.56 m/s, deviated markedly from the typical wounding pattern (Fig. 6d). In longitudinal (y-z) section, this wound presented with a cylindrical wound channel to approximate mid-trabecular depth; at this point, the trabecular fracture margins deviated laterally in conoidal fashion to create a shallow internal bevel. Cylindrical morphology in the proximal part of the wound is indicative of shear in this region, whilst the conoidal portion is suggestive of a tensile cone cracking failure mode.

Although some deviations in trans-laminar crack path through the sandwich structures were visible, a characteristic feature of the wound cross-sections was a remarkably straight fracture edge (Fig. 6a–c). Deviations in the crack path from linearity may be attributed to inhomogeneities in bone microstructure and in particular to the orientation of trabecular struts in relation to the advancing crack tip. Comparison of peripheral trabeculae adjacent to the trabecular fracture margin with trabeculae located further from the wound volume revealed no evidence of compressive trabecular buckling or cell collapse with permanent deformation (Fig. 6e, thick arrow). In specimens with high resolution in the trabecular region, the free edges of fractured cells along the trabecular fracture margin did not appear compressed; rather, the crack appeared to have crossed one cell width at a time through the cellular solid. When the section was parallel to the cell-axis, this process left clearly discernible bisected cells along the trabecular fracture margin showing no signs of deformation (Fig. 6e, thin arrows). In-line fracture between angulated cortical fracture edges and trabeculae, coupled with bisection of trabeculae by a single crack, is consistent with propagation of a trans-laminar fracture through the three layers of the sandwich bone from its origin at the outer cortical surface.

Peripheral trabeculae around the wound channel were apparently unaffected by the perforation event in all five velocity groups and regardless of absorbed energy (Fig. 6f). Trabecular attachments to the inner and outer cortical plates also remained undamaged up to the trabecular fracture margin (Fig. 6e, circled), suggesting that significant deformation of the cortical layers outside the impact location did not occur. Such structural integrity in the regions immediately around the wound channels indicates that projectile perforation from 139 to 897 m/s in sandwich bones is characterised by an extremely localised material response. One specimen in V_4 and three in V_5 lacked the conoidal internal structure and demonstrated a "blown out" morphology when viewed from the front, with significant fracture and elevation of the outer cortical plates. Although the exact cause of this morphology was unclear, a hydraulic bursting effect in the fluid contained within the trabecular bone is plausible. Eight wounds allowed analysis of how irregularity of the cortical entry wound related to the shape of the internal bevel. Irregular cortical entry wounds corresponded to a matching irregularity of the internal bevel in only two specimens, from groups V_2 and V_3, respectively; in the other six specimens, irregular entry wounds did not result in irregular internal bevels. Analysis through the depth of the bone revealed that the fine details of cortical irregularity were lost in the trabecular fracture margin through the depth of the wound channel. This shape- deletion process is illustrated in Fig. 6g–h for a 335.55m/s perforation event. In this specimen, the outer cortical plate displays an oval-irregular entry wound (Fig. 6g); however, the finer irregular details are lost by the trabecular fracture margin at approximately mid-depth in the trabecular lamina of the sandwich structure (Fig. 6h).

Relationship between inner cortical plate fragments and internal fracture morphology

Observed relationships between the bevel and inner cortical plate fragments were consistent with trans-laminar fracture forming a distinct tri-layered conoidal structure during impact. Cross-sectional views indicated that the internal bevel was fully formed underneath retained fragment cones (Fig. 7a, arrows); this hidden bevel was found in all five V_1 specimens where fragment cones obscured all or part of the exit. Sectional analysis verified that the counterpart to these inner cortical plate fragments was the exit cortical fracture edge of the internal bevel, with the two separated by the trans-laminar fracture when it reached the inner cortical plate (Fig. 7a, large

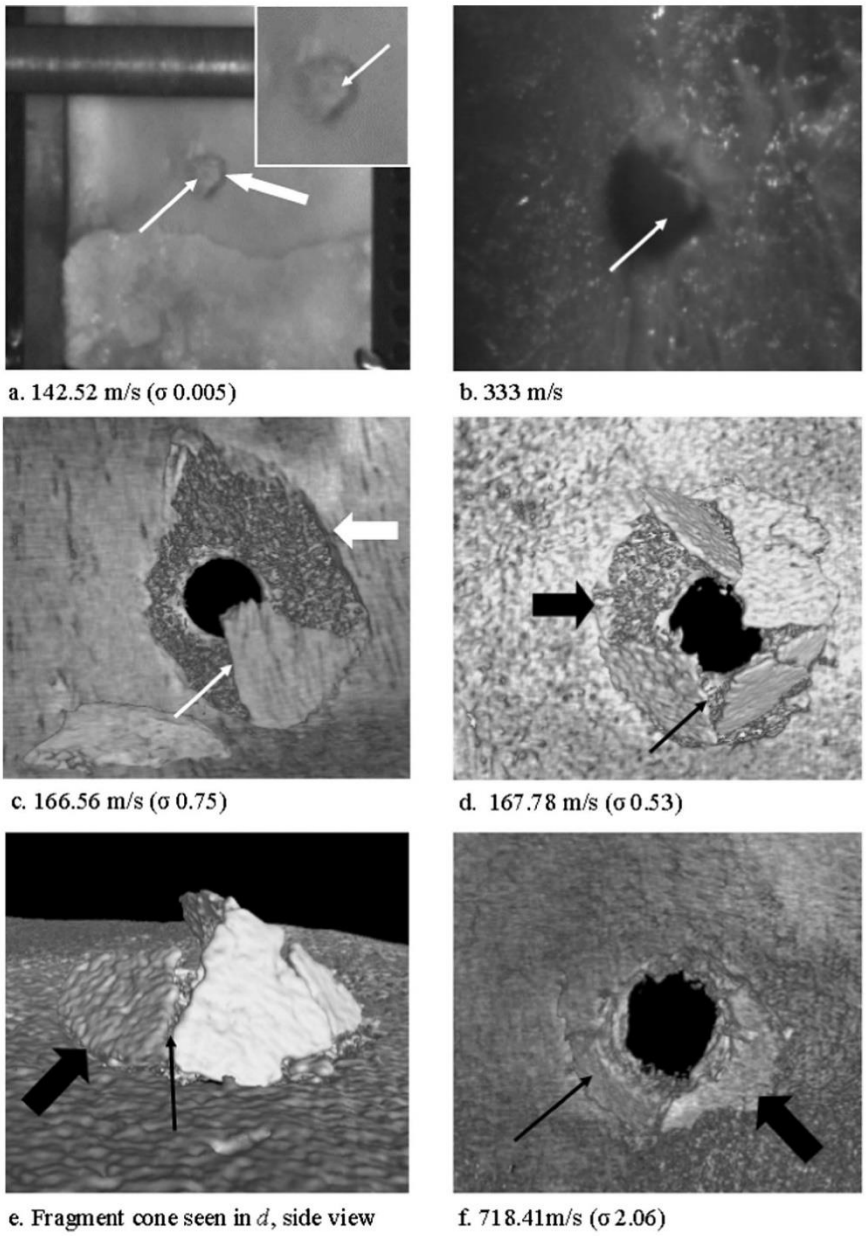

a. 142.52 m/s (σ 0.005)

b. 333 m/s

c. 166.56 m/s (σ 0.75)

d. 167.78 m/s (σ 0.53)

e. Fragment cone seen in *d*, side view

f. 718.41m/s (σ 2.06)

arrow). Morphologically, inner cortical plate fragments with counterpart relationship to the internal bevel thus formed the floor of the conoidal wound volume. A structure corresponding to this feature was observed in high-speed video (Fig. 4a), fully displaced from the wound and moving ahead of the projectile before its subsequent fragmentation.

◀ **Fig. 4** High-speed footage of projectile exit and selected μ-CT views of inner cortical plate damage; in all images, thick arrows denote the exit cortical fracture edge of the internal bevel. **a** Circular fragment of inner cortical plate dislodged from exit cortical fracture edge (thick arrow) bearing stellate fracture (thin arrow) and moving ahead of projectile, enlarged image inset highlights stellate fracture (arrow). **b** Filmed projectile exit at 333 m/s, just prior to emergence of projectile; triangular plate (arrow) indicates stellate fracture has occurred (velocity determined with time gate). **c–e** 3D images of inner cortical plate damage morphology revealed by μ-CT of two V_1 specimens; radial cracks of stellate fracture (thin arrows) arrest at the exit cortical fracture edge (thick arrows). **e** 3D side view of the fragment cone seen in **d**, with radial fracture indicated by thin arrow. **f** Rectangular, elevated cortical fragment (thin arrow) resulting from high velocity impact; note that in all images elevated fragments are circumscribed by the exit cortical fracture edge

In some sections, an accessory fracture (Fig. 7b, thin arrow) was located peripheral to the trans-laminar fracture producing the conoidal wound (Fig. 7b, thick arrow). In such cases, the presence of an angulated exit cortical fracture edge (Fig. 7b, thick arrow) indicated that the accessory fracture must have formed secondarily to the trans-laminar fracture.

Additional evidence supporting formation of a distinct tri-layered conoidal structure was provided when the inner cortical plate fragments were in close proximity to the bevelled edge from which they were derived. Figure 7c-d shows a photograph and three-dimensional view of such a fragment on the inner cortical plate of a V_2 specimen impacted at 333 m/s; the line across the fragment in Fig. 7d corresponds to the y-z view visible in Fig. 7e. In y-z section (Fig. 7e), the bevel appeared as a marked conoidal fracture in the trabecular layer with the fragment forming a partial floor to this edge of the wound. Part-counterpart relationships between exit cortical fracture edge and fragment meant the latter would slot in and out of the internal bevel in the parent bone. Observation of the whole wound from the right demonstrated the internal bevel running *underneath* the fragment (Fig. 7f), which is thus accurately interpreted as a fragment of the cortical floor of the conoidal wound. Part-counterpart association between inner cortical plate fragments and wound were often so clear that the intact floor could be visualised even when the fragments had been significantly displaced (Fig. 7g). The conoidal fracture residing above lower cortical floor fragments and the part-counterpart relationships between them and the internal bevel was often striking (Fig. 7h). When inner cortical plate fragments showed minimal downwards displacement, the bevelled edge from which they derived was shielded from contact with a cortical shear plug or accumulated material (Fig. 7i, arrows).

Discussion

The anatomical complexity of the human head makes detailed analyses of the terminal ballistics of this region challenging. In order to elucidate the fracture processes operative during perforation of the sandwich bone component of the head, the current study perforated pig scapulae with spherical steel projectiles and utilised a combination of μ-CT and high-speed videography for subsequent fracture analysis. Whilst experimental conditions in the current work resulted in simpler projectile-tissue interactions than would be operative during perforation of the living bio-system, analysis of fracture morphology does not support the view that plug and spall is responsible for conoidal wound formation, as previously proposed [9–14]. Displaced inner cortical plate fragments were often in such close approximation to the bevel that a shear plug could not have been involved in bevel formation. Distinct part-counterpart relationships between inner cortical plate fragments and the internal bevel were also inconsistent with bevel formation by shear plugging. Finally, shear plug involvement in bevel formation was ruled out when the bevel was shielded behind inner cortical plate fragments. These previous features are, however, consistent with wound formation

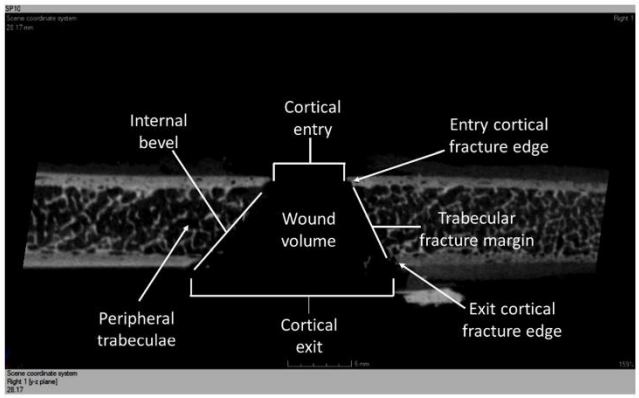

Fig. 5 μ-CT image, y-z section showing cross-sectional anatomy of a perforating gunshot wound through a sandwich bone, incident velocity 335.55 m/s (σ 1.05); see text for explanation. Projectile passed from above downwards

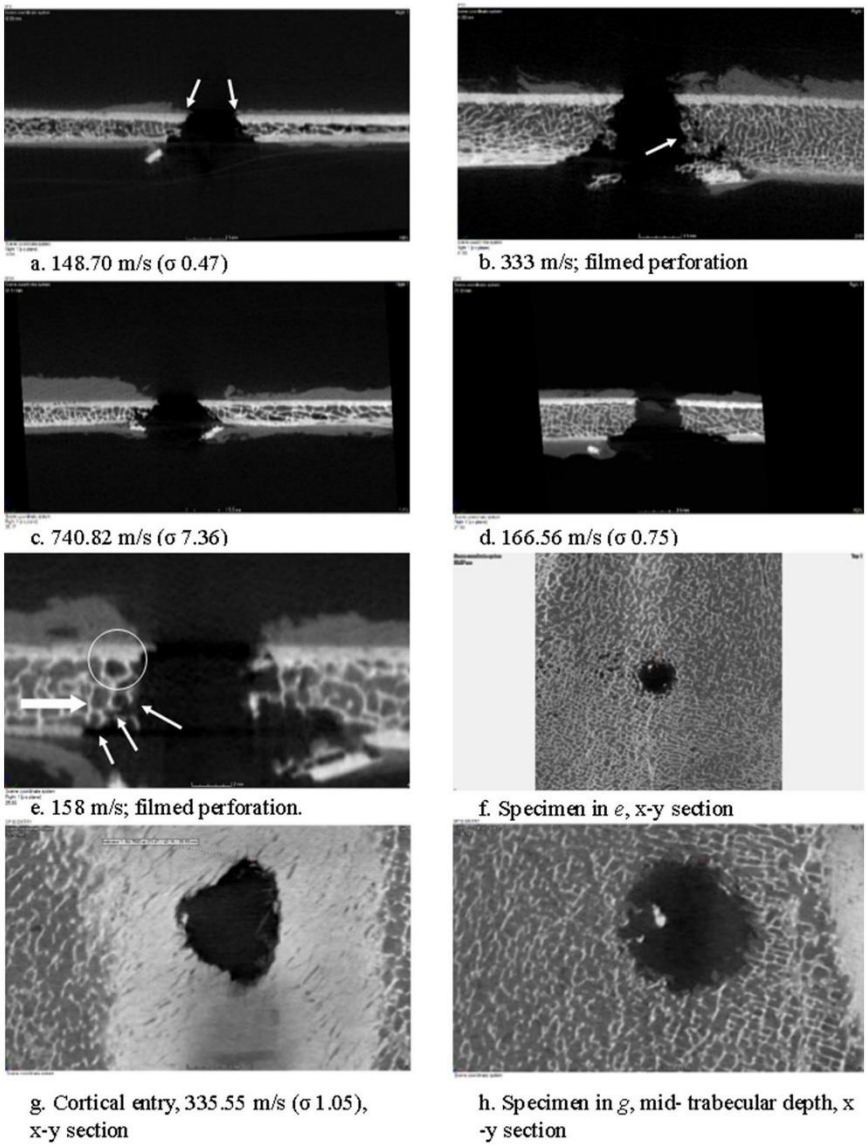

Fig. 6 μ-CT cross-sections of projectile wounds. **a**–**c** y-z views of conoidal morphology with bilateral angulation of entry cortical fracture edges (highlighted with arrows in **a**); trabecular intrusion is shown in **b** (arrow). **d** y-z section showing atypical wound cross-section. **e** Fracture morphology consistent with crack propagation one cell width at a time through trabeculae (thin arrows), y-z section. Note bilateral angulation of entry cortical fracture edges, lack of collapse of trabecular cells (thick arrow) and intact trabecular attachments to cortex (circle). **f** x-y section of specimen seen in **e** showing localisation of wound in trabecular field. **g** x-y section of cortical entry wound in cortex. **h** x-y view of specimen shown in **g** showing loss of cortical irregularity by mid-trabecular depth. **f**–**h** View looking into wound from above. Incident velocities are provided with standard deviations in parentheses; velocities in **b**, **e** and **f** were determined using time gate

Table 4 Mean entry cortical fracture edge angles for wounds exhibiting bilateral angulation of the cortices. All angles obtained from transverse (y-z) plane to eliminate any effects of bone curvature on cortical angles. Standard deviations are in parentheses. Fracture and displacement of cortices meant accurate measurement was not possible in one* and two** specimens in groups 2, 4, and 5

Velocity group	Mean group cortical fracture edge angle, apical half	Mean group cortical fracture edge angle, basal half	Range, apical	Range, basal
1 ($n = 8$)	55.25 (12.19)	49.15 (7.43)	33.02–74.80	38.33–59.42
2 ($n = 5$)*	35.95 (3.30)	43.76 (6.48)	31.15–40.65	31.01–48.34
3 ($n = 3$)	54.97 (9.28)	48.99 (13.27)	41.85–61.89	39.61–58.37
4 ($n = 3$)**	48.13 (5.41)	42.97 (14.81)	41.35–54.60	30.65–63.79
5 ($n = 5$)**	47.06 (6.33)	45.51 (6.66)	36.55–53.40	39.08–54.61

by propagation of a trans-laminar fracture through the sandwich bone.

In addition to morphological features that are inconsistent with plug and spall, fundamental penetration mechanics dictates that shear plugging will not occur in all perforation events within the same material. Shear plugging is sensitive to impact angle and projectile tip shape and is commonly associated with blunt ended projectiles [22]; projectile velocity is also a contributing factor [23]. During plug formation, intense shear occurs in a cylindrical zone under and around the projectile [24]; as a result, shear plugging is associated with cylindrical plugs of approximately the same diameter as the impactor [22, 23], resulting in cylindrical perforating channels through the material. Although data for trabecular bone are lacking, cylindrical shear channels have been reported subsequent to impact in a variety of foam cores in synthetic sandwich panels [25]. Such a morphology is inconsistent with the observed morphology of conoidal wounds in sandwich bones. The contention of Symes et al. [10] that a plug of bone is pushed into the brain ahead of the projectile was not supported by the present study; projectile emergence from the inner cortical plate occurred in the absence of a sheared cortical plug in all filmed perforation events.

At present, the only other study to utilise μ-CT to visualise the internal morphology of perforating projectile wounds to sandwich bones is that of Kieser et al. [14], who reported funnel shaped wound channels consisting of a vertical tunnel through the outer cortical layer and a conoidal bevelled region beneath this. In direct contrast, the present study found few examples where two such regions existed through the wound cross-sections. Rather than exhibiting vertical walls, the entry cortical fracture edges typically exhibited angulation suggestive of cone crack formation under the impacting projectile. Significantly, the crack induced at the cortical surface propagated through the sandwich bone without regard for the change in bone type at the upper or lower cortical-trabecular transitions. The possibility that cone cracks might form in the cortical layers of sandwich bones is supported by existing literature; cone crack formation during indentation or impact is common in brittle materials [26–28] including glass, ceramics and hard polymers [24] and has also been demonstrated in the cortex of long bones subsequent to projectile impact [29]. A principle failure mechanism in ceramics subjected to ballistic impact is the formation of a *ceramic conoid* due to cone crack propagation; a separated conoidal volume of ceramic, flaring in the direction of projectile travel, and typically undergoing fragmentation once formed [30]. Similarity between the bevel and such conoidal fractures in other brittle materials was previously noted by Klepinger [31], although this author ultimately contended that the bevel in entry wounds was formed by shards of bone breaking free from the inner surface.

Compact bone may be classified as a bioceramic composite [32], and conoidal wounds in sandwich bones resemble observed conoidal damage in non-biogenic ceramics to a remarkable degree with the exception that there is an intervening layer of a brittle cellular solid running through the centre of the impacted structure through which the crack must propagate. However, formation of cone cracks in cellular solids is not without precedent; cone cracks have previously been reported in low density polyethylene terephthalate (PET) foams subsequent to impact [25], and morphological evidence revealed by μ-CT suggests the involvement of cone cracks in projectile wound formation through sandwich bones. It has been established that cone cracks propagate into materials along lines of tensile stress initiating at the material surface [26] and that, when subjected to tensile stress, brittle open cell solids fail by propagation of a crack that hops one cell at a time through the material [33]. Observed trabecular fracture morphology in the present series was consistent with such a tensile failure mode; trabecular cells along the wound channel appeared to be bisected by a fracture crossing from one cell edge to another. Once initiated in the trabeculae, tensile fracture of one cell leads to greater load being borne by other cells [34]; provided enough energy is available, the fracture will thus propagate catastrophically through the entire layer [35]. Accordingly, it might reasonably be postulated that conoidal wounds are produced when a cone crack from the outer cortex propagates into and crosses the trabecular and inner cortical layers. Significantly, this process would account for the often straight- edged morphology of the trabecular fracture margin and for the lack of evidence for compression with permanent

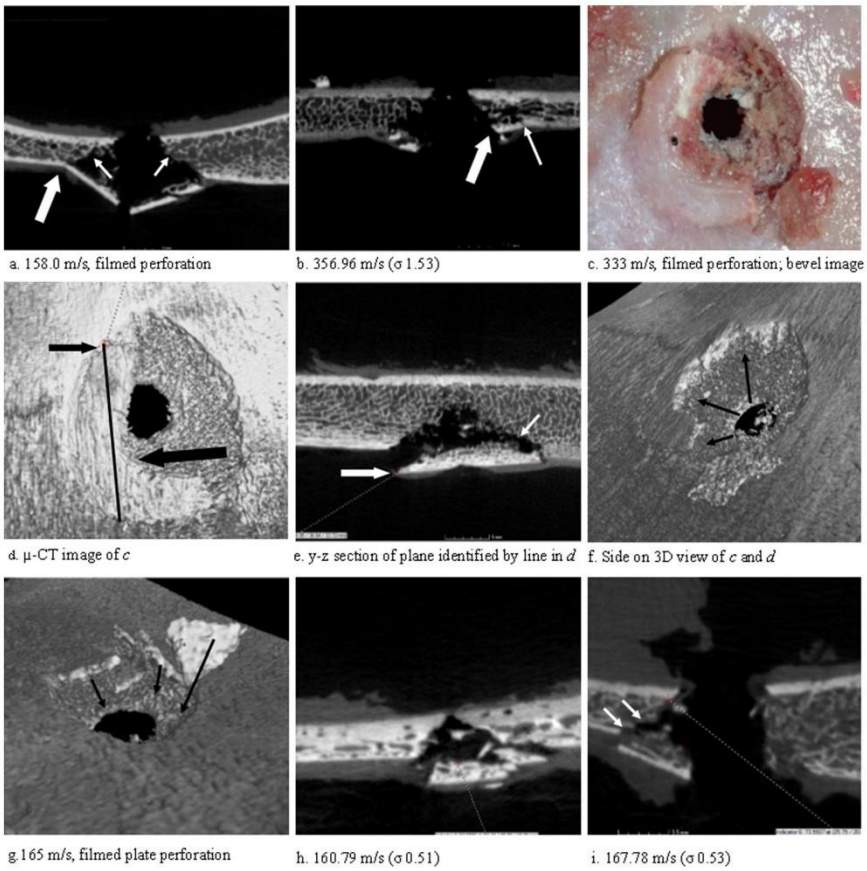

Fig. 7 μ-CT images of inner cortical plate damage. **a** x-z (transverse) cross-section of fragment cone with bevel concealed under fragments (arrows); large arrow marks the exit cortical fracture edge. **b** accessory cortical fracture (thin arrow) outside the exit cortical fracture edge (thick arrow), y-z section. **c** Photograph of C-shaped inner cortical plate fragment partially covering internal bevel after a 333-m/s perforation. **d** μ-CT 3D view of fragment shown in **c**; black line shows plane of slice visible in **e**. **e** y-z view of C-shaped fragment, viewed in direction of large arrow shown in **d**; note the conoidal internal bevel above the fragment and the close approximation between bevel and fragment at right of image, with just over 1 mm separation in the region identified by the small arrow. Left hand arrows in **d** and **e** point to the elevated side of the fragment. **f** 3D view looking under C-shaped fragment in **c**–**e**; viewed from the right side, the internal bevel can be seen running underneath the fragment (arrows). **g** 3D view looking into a conoidal wound from V_1; fragments moved in direction of arrows would partially re-form the floor of the wound. **h** Marked conoidal fracture and counterpart fragments, y-z section. **i** x-z section of bevelled edge (arrows) protected behind inner cortical plate fragment

deformation of trabecular cells lining the wound channel, a feature also noted by Kieser et al. [14].

An issue of central importance to the cone crack hypothesis is the question of how such a fracture crosses the upper and lower interfaces between cortices and trabeculae. Whether a given fracture will arrest, be deflected by or cross a given interface between two materials is determined by the angle of the fracture relative to the interface, the difference in elastic moduli between the two materials and the presence of a third interface material sandwiched between the other two [36, 37]. When considering crack propagation from cortical to trabecular bone, the latter component may be eliminated due to lack of interface material between bone types. The relationship between fracture angle and the probability of a fracture crossing or deflecting an interface is analogous to the process of skimming a stone over water; the more acute the angle, the greater the probability that the fracture will be deflected along the interface, rather than penetrating it [38]. In the present analysis, no crack deflection was observed at the interfaces between cortical and trabecular bone, suggesting that cortical

fracture angles are above the critical limit for crack deflection at the interfaces.

The relative elastic moduli of the two materials is of particular importance to crack behaviour at an interface; when a fracture approaches an interface with a material of lower elastic modulus, crack velocity increases significantly [39] and the crack is thus more likely to propagate into the second material. Although there is a wide range of reported values for the elastic modulus of trabecular bone in the literature, Keaveny et al. [40] summarised data for elastic moduli determined using ultrasound methods and found values approximately 20% lower than that for cortical bone. More recent analyses have suggested that the elastic modulus of trabecular bone is lower than that of cortical bone, but only slightly [40, 41]. In sandwich bones, direct continuity between cortices and trabeculae and abundant cortical-trabecular connections, coupled with elastic modulus mismatch, would enhance the probability of a given fracture propagating into the trabecular layer from the outer cortex. Based upon internal and external fracture morphology and the above theoretical considerations, a novel mechanism for conoidal wound formation through sandwich bones is described below and in diagrammatic form in Fig. 8:

1. Projectile impact initiates the formation of a cone crack within the outer cortical plate.
2. The cortical cone crack propagates across the upper cortical-trabecular transition via trabecular attachments that are in line with the cortical tensile stress. Tensile failure causes propagation of the crack across the trabecular cells one cell width at a time and produces a relatively straight-edged trabecular fracture margin. Local inhomogeneities in trabecular composition and differences in trabecular orientation may cause the crack to deviate and result in trabecular intrusion into the wound channel. High tensile stresses begin formation of stellate fractures on the inner cortical plate before projectile exit.
3. The cone crack propagates from the lower trabeculae through to the inner cortical layer via trabecular attachments in line with the tensile stress trajectory.
4. Propagation of the fracture to the lower cortical table completes formation of the internal bevel and results in formation of a conoidal volume of bone consisting of all three layers of the sandwich bone separated from the parent bone by the bevel. This structure remains intact during low-velocity impacts.
5. Kinetic energy and stress waves associated with high-velocity impacts result in the instantaneous collapse and fragmentation of the formed conoidal volume. The floor of this volume forms *inner cortical plate fragments* which undergo elevation and eversion during projectile exit, leaving fragment cones at low velocity. At higher velocity, these fragments are largely ejected with soft tissue components, although some may remain in situ due to incomplete trans-laminar fracture or retention within soft tissue. Trans-laminar fracture results in part-counterpart relationships between these retained fragments and the internal bevel.

According to this mechanism, the internal bevel is the counterpart to the missing bone volume which, if intact, would slot in and out of the parent bone. The intact conoidal bone volume produced by this mechanism would be identical to the ceramic conoids produced in engineering ceramics subjected to ballistic impact, where a conoid of material is separated from the parent ceramic by the conoidal fracture [30]. In the bone, such a conoidal volume may thus reasonably be termed a *bioceramic conoid*. Once initiated, cone cracks will propagate at the speed of sound for the material in which they are propagating, with conoid formation typically only taking a few microseconds in engineering ceramics [42]. Whilst the plug and spall hypothesis proposes that the bevel is created during projectile exit [9–12], the cone crack hypothesis suggests it is created *at the moment of impact*; the bevel is then revealed by subsequent conoid fragmentation. Additional evidence that bevel formation is due to trans-laminar fracture arises from the observation that bevels are interrupted at pre-existing fractures or sutures; this process, known as crack arrest, occurs when the energy driving fracture dissipates at the discontinuity [43].

Although the cone crack hypothesis suggests that wound formation is driven by tensile stress, this does not preclude the simultaneous operating of other failure modes through the wound volume; indeed, most cracks in bone are formed under a mixture of stresses [44]. Observation of stellate fracture patterns in the inner cortical plate confirms that a compressive stress transfers through the conoid during perforation, resulting in eventual tensile failure there. High-velocity perforation also undoubtedly involves additional mechanisms such as stress wave induced trabecular cell collapse [45], delamination within cortical bone [19] and possibly heating effects [14]. Previous scanning electron microscope analysis of entry cortical fracture edges in bovine (*Bos taurus*) sandwich bones has identified fracture surfaces produced by tensile failure [19]. However, further fracture surface characterisation in both human and non-human bone is required to test the hypothesis that wound formation is driven by tensile stress and also to establish the contribution of additional failure modes to projectile wounding.

In the present experiment, no intact bioceramic conoids were produced and fracture through the sandwich bones was often incomplete, with portions of the conoid floor remaining attached to the exit cortical fracture edge. The rarity of intact bioceramic conoids reported in case work suggests a particular set of circumstances must combine to form them; kinetic

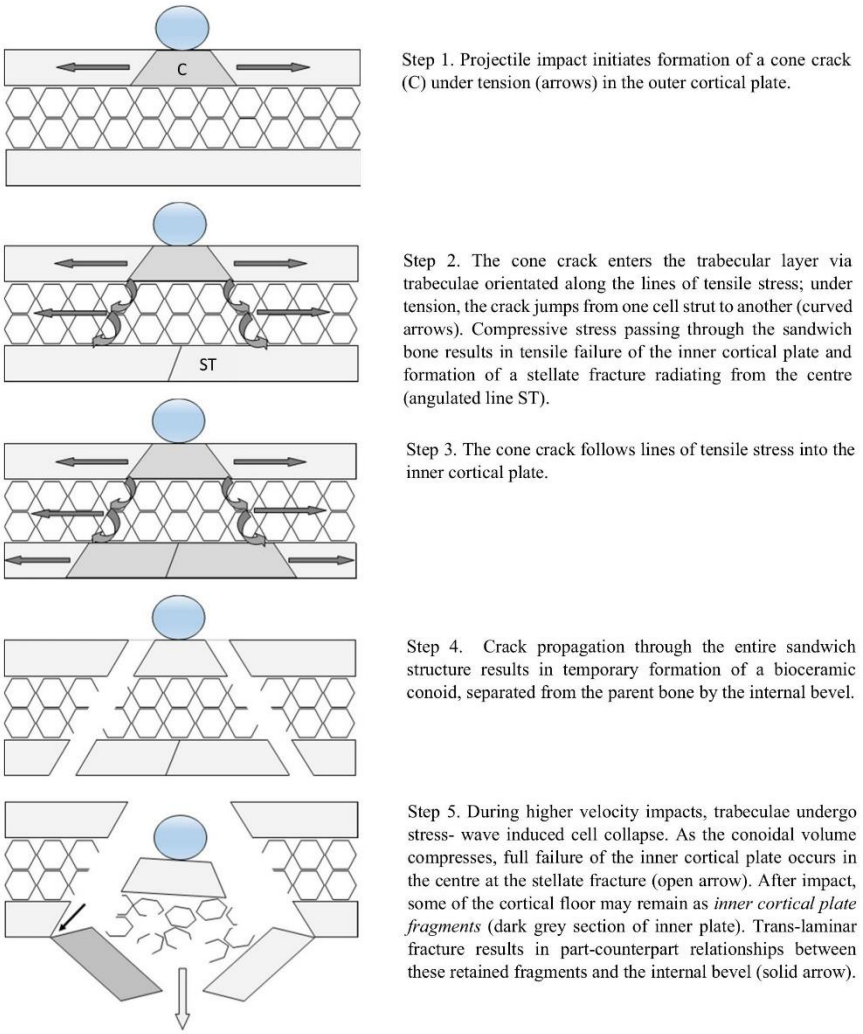

Fig. 8 Novel mechanism for conoidal wound formation through sandwich bones

energy absorption must be low enough to prevent fragmentation and trans-laminar fracture must entirely separate the conoid from the parent bone. In brittle materials, plug fragmentation is likely to occur at velocities 5–10% above the minimum perforation velocity [22]; with higher velocity impacts, it is therefore to be expected that much of the bioceramic conoid would undergo fragmentation. Such behaviour is also consistent with engineering ceramics, where fragmentation is similarly restricted to the separated conoid [24]. Impact data generated in the present study revealed that incident velocity and energy absorption were positively correlated. The law of conservation of energy dictates that both greater fragmentation and greater energy utilisation in fragment ejection must occur as velocity increases, with the latter process becoming particularly significant at higher velocities [46]. A positive correlation between incident velocity and energy absorption has also been found in synthetic sandwich panels, where it is thought to be a characteristic of such structures [47, 48].

It is generally held that perpendicular entry wounds tend to be circular or oval in shape [5] and also that areas of bevel

elongation indicate projectile trajectory [6, 7]. The current study substantiated the high frequency of circular wounds, which accounted for just under half of all cortical entry shapes. Whilst oval and irregular wounds were more common at higher velocities, circular wounds were present in the lowest and highest velocity groups. Variation in cortical entry wound shape subsequent to perpendicular impact with spherical, non-deforming projectiles suggests the importance of intrinsic biological factors, such as bone microarchitecture, in determining wound shape. The frequency of bevel asymmetry was interesting; of 14 circular wounds, 12 (85.71%) exhibited asymmetrical bevelling. Across all cortical entry shapes, asymmetrical bevelling was far more common than symmetrical bevelling, accounting for 82.76% of bevels. These findings are in accordance with previously published data for entry wounds in human crania [21], where only 15% of bevels were classed as symmetrical; an exact correlation between trajectory and bevel asymmetry was found in only five out of 39 entry wounds. In light of these findings, these authors highlighted the importance of intrinsic anatomical features in determination of bevel shape.

Observation of projectile exit in the present analysis suggested that the bevel and its symmetry are determined before projectile exit has occurred, with accessory fractures outside the conoidal wound potentially contributing to apparent bevel asymmetry. The cone crack hypotheses predicts that bevel shape would be determined by the initial angle of the cone crack, which differs around the cortical entry wound, and the subsequent crack path through the trabecular network. In synthetic materials, cone cracks become steeper with a decrease in Poisson's ratio [49] and with an increase in velocity [26]. Although further work is required to investigate relationships between velocity and cone angle in bone, overlap between angles across the velocity groups suggests that material factors might supersede loading rate in determining the angles achieved. Upon establishment of the cone angles in the outer cortex, final bevel shape would be determined by the subsequent path of the cone crack through the trabecular layer and inner cortex. High frequency of bevel asymmetry with perpendicular impacts suggests caution should be applied when using this feature to make trajectory determinations in the absence of an exit wound or other directionality indicators.

A number of authors have noted that irregular cortical entry wounds do not always result in irregular internal bevels [13, 21]. These findings were supported by the present study; irregular or partially irregular entry shape was lost by the internal bevel in 80% of irregular wounds. μ-CT analysis revealed that fine details of cortical irregularity are deleted by approximately mid-depth in the trabecular layer. This phenomenon is consistent with the hypothesis of wound formation by trans-laminar cone crack propagation; minor deviations in crack path through individual trabeculae and differences in trabecular orientation in relation to the advancing crack would have a distorting effect as it propagated downwards, resulting in a deletion of information relating to entry wound shape as depth increased.

Despite lack of production of intact bioceramic conoids, comparison of plug morphology produced by low-velocity impacts [15–17] with residual fracture morphology subsequent to medium and high-velocity impacts reveals similarities that are indicative of a common fracture process. Whilst overlap in external morphology between conoidal wounds produced by blunt and projectile trauma has been reported previously [50–52], this is the first report of wounds inflicted at 150 m/s being identical internally to those produced at 850 m/s. These shared internal and external morphological features suggest that conoidal wounds form a distinct category of trauma characterised by trans-laminar crack propagation and bioceramic conoid production. In cross-section, such conoidal wounds may be diagnosed by angulated entry cortical fracture edges in all or parts of the section and by evidence for crack propagation through all three layers of the sandwich bone. Further work utilising low-velocity impacts is required to confirm their wider role in wound formation. The hypothesis that trans-laminar fracture underlies formation of all conoidal wounds raises interesting research challenges for enhanced differential diagnosis.

In addition to overlap between trauma types, wound diagnosis is complicated by taphonomic agencies including rodent gnawing [53] and carnivore scavenging [54]. Diagnosis may also be complicated by deliberate anthropogenic activities, particularly the use of fire [55, 56]. Traumatic wounds must also be differentiated from pseudotraumatic defects [57] such as missing sutural ossicles, which can combine with other fractures to create defects resembling those produced by traumatic events [58]. Cross-sectional microanatomy revealed by μ-CT provided a number of features that might be of diagnostic value. Sandwich bone response to projectile perforation was found to be extremely localised. Damage localisation is due to the short contact time between impactor and target, resulting in kinetic energy absorption over a small area [59]. Localisation of damage is also a characteristic feature of impacted cellular solids [45], and internal examination of perforated sandwich bones revealed intact peripheral trabeculae even at the highest velocities. Conoidal wounds exhibited angulation of the entry cortical fracture edges, trans-laminar fracture through the trabeculae which crossed from one cell edge to another, lack of sandwich layer delamination and lack of permanent collapse of trabecular cells. Further work with lower velocity impact events is needed to detect when such features appear; comparative work with pseudotraumatic defects is also essential. Elucidation of the taphonomic resistance of any identified diagnostic indicators is also critical if they are to be of use in skeletal remains subjected to deposition in ecosystems.

Acknowledgements We are indebted to Dr. David Wood, Andrew Taylor, David Miller and Alan Peare for their considerable technical input and for operation of the gas guns and projectile housing. We would also like to extend our thanks to Kerrie Smith for the error propagation formula and Dr. Keith Rogers and George Adams for their assistance and advice with micro-computerised tomography.

Compliance with ethical standards

Conflict of interest The authors declare that they have no conflict of interest.

Ethical approval This study was approved by the ethics committee of Cranfield University.

References

1. Maiden N (2009) Ballistics reviews: mechanisms of bullet wound trauma. Forensic Sci Med Pathol 5:204–209. https://doi.org/10.1007/s12024-009-9096-6
2. Aarabi B, Tofighi B, Kufera JA, Hadley J, Ahn ES, Cooper C, Malik JM, Naff NJ, Chang L, Radley M, Kheder A, Uscinski RH (2014) Predictors of outcome in civilian gunshot wounds to the head. J Neurosurg 120:1138–1146
3. Mota A, Klug WS, Ortiz M, Pandolfi A (2003) Finite-element simulation of firearm injury to the human cranium. Comput Mech 31:115–121. https://doi.org/10.1007/s00466-002-0398-8
4. Snell RS (1995) Clinical anatomy. Lipincott Williams and Wilkins, Maryland
5. Berryman HE, Symes SA (1998) Recognising gunshot and cranial trauma through fracture interpretation. In: Reichs KJ (ed) Forensic osteology: advances in the identification of human remains. Charles C Thomas Publishers, Springfield, pp 333–352
6. Rhine and Curran (1990) Multiple gunshot wounds to the head: an anthropological review. J Forensic Sci 35(3):1236–1245
7. Spitz WU (2006) Injuries by gunfire. In: Spitz WU, Spitz DJ, Clark R (eds) Spitz and Fisher's medicolegal investigation of death: guidelines for the application of pathology to crime investigation. Charles C Thomas Publishers, Springfield Available from: Proquest Ebook Central. Accessed 9.11.17
8. Hull D (1999) Fractography: observing, measuring and interpreting fracture surface topography. Cambridge University Press, Cambridge
9. Komar DA, Buikstra JE (2008) Forensic anthropology: contemporary theory and practice. Oxford University Press Inc., New York
10. Symes SA, L'Abbé EN, Chapman EN, Wolff I, Dirkmaat DC (2012) Interpreting traumatic injuries to bone in medicolegal investigations. In: Dirkmaat DC (ed) A companion to forensic anthropology. Wiley-Blackwell Publishing, West Sussex
11. Christensen AM, Passalacqua NV, Bartelink EJ (2014) Forensic anthropology: current methods and practice. Academic Press, Oxford
12. Peterson BL (1991) External beveling of cranial gunshot entrance wounds. J Forensic Sci 36(5):1592–1595
13. Kimmerle EH, Baraybar JP (2008) Skeletal trauma: identification of injuries resulting from human rights abuses and armed conflict. CRC Press, Florida
14. Kieser JA, Tahere J, Agnew C et al (2011) Morphoscopic analysis of experimentally produced bony wounds from low velocity ballistic impact. Forensic Sci Med Pathol 7:322–332. https://doi.org/10.1007/s12024-011-9240-y
15. Murphy MS, Gaither C, Goycochea E, Verano JW, Cock G (2010) Violence and weapon-related trauma at Puruchuko-Huaquerones, Peru. Am J Phys Anthropol 142:636–649
16. Murphy MS, Spatola B, Weathermon R (2014) Allies today, enemies tomorrow: a comparative analysis of perimortem injuries along the biomechanical continuum. In: Martin DL, Anderson CP (eds) Bioarchaeological and forensic perspectives on violence: how violent death is interpreted from skeletal remains. Cambridge University Press, Cambridge, pp 261–288
17. Bird CE, Fleischman JM (2015) A rare case of an intact bone plug associated with a gunshot exit wound. J Forensic Sci 60(4):1074–1077
18. Smith MJ, Brickley MB, Leach SL (2007) Experimental evidence for lithic projectile injuries: improving identification of an underrecognised phenomenon. J Archaeol Sci 34:540–553
19. Rickman JM, Smith MJ (2014) Scanning electron microscope analysis of gunshot defects to bone: an underutilised source of information on ballistic trauma. J Forensic Sci 59(6):1473–1486. https://doi.org/10.1111/1556-4029.12522
20. Currey JD (2002) Bones: structure and mechanics. Princeton University Press, New Jersey
21. Quatrehomme G, İşcan MY (1998) Analysis of bevelling in gunshot entrance wounds. Forensic Sci Int 93:45–60
22. Zukas JA (1982) Penetration and perforation of solids. In: Zukas JA, Nicholas T, Swift HF, Greszczuk LB, Curran DR (eds) Impact dynamics. John Wiley and Sons, Inc., USA, pp 155–214
23. Backman ME, Goldsmith W (1978) The mechanics of penetration of projectiles into targets. Int J Eng Sci 16:1–99
24. Crouch IG (2016) An introduction to armour materials. In Crouch IG, Arthur J (eds) The science of armour materials, available from ProQuest Ebook central
25. Hassan MZ, Cantwell WJ (2012) The influence of core properties on the perforation resistance of sandwich structures: an experimental study. Compos Part B 43:3231–3238
26. Knight CG, Swain MV, Chaudhri (1977) Impact of small steel spheres on glass surfaces. J Mater Sci 12:1573–1586
27. Chen SY, Farris TN, Chandrasekar S (1995) Contact mechanics of Hertzian cone cracking. Int J Solids Struct 2(3/4):329–340
28. Lawn BR (1998) Indentation of ceramics with spheres: a century after Hertz. J Am Ceram Soc 81(8):1977–1994
29. Kieser DC, Riddell R, Kieser JA, Theis J, Swain MV (2013) Bone micro-fracture observations from direct impact of slow velocity projectiles. J Arch Mil Med 2(1):e15614. https://doi.org/10.5812/jamm.15614
30. Zaera R, Sánchez-Gálvez V (1998) Analytical modelling of normal and oblique ballistic impact on ceramic/metal lightweight armours. Int J Impact Eng 21(3):133–148
31. Klepinger LL (2006) Fundamentals of forensic anthropology. John Wiley & Sons, New Jersey
32. Olszta MJ, Cheng X, Jee SS, Kumar R, Kim YY, Kaufman MJ, Douglas EP, Gower LB (2007) Bone structure and formation: a new perspective. Mater Sci Eng R Rep 58:77–116
33. Gibson LJ, Ashby MF (1988) Cellular solids: structure and properties. Pergamon press, Oxford
34. Kaplan SL, Hayes WC, Stone JL (1985) Tensile strength of bovine trabecular bone. J Biomech 18(9):723–727
35. Tomar V (2009) Insights into the effects of tensile and compressive loadings on microstructure dependent fracture of trabecular bone. Eng Fract Mech 76:884–897
36. Imbeni V, Kruzic JJ, Marshall GW, Marshall SJ, Ritchie RO (2005) The dentin-enamel junction and the fracture of human teeth. Nat Mater. https://doi.org/10.1038/nmat1323
37. Zimmermann EA, Gludovatz B, Schaible E, Busse B, Ritchie RO (2014) Fracture resistance of human cortical bone across multiple length scales at physiological strain rates. Biomaterials 35:5472–5481

38. He M-Y, Hutchinson JW (1989) Crack deflection at an interface between dissimilar elastic materials. Int J Solids Struct 25(9):1053–1067
39. Mencík J (2010) Mechanics of components with treated or coated surfaces. Klewer Academic Publishers, Netherlands
40. Keaveny TM, Morgan EF, Yeh OC (2004) Bone biomechanics. In: Kutz M (ed) Standard handbook of biomedical engineering and design. McGraw-Hill Professional, USA, pp 8.1–8.23
41. Bayraktar HH, Morgan EF, Niebur GL, Morris GE, Wong EK, Keaveny TM (2004) Comparison of elastic and yield properties of human femoral trabecular and cortical bone tissue. J Biomech 37:27–35
42. Kaufmann C, Cronin D, Worswick M, Pageau G, Beth A (2003) Influence of material properties on the ballistic performance of ceramics for personal body armour. Shock Vib 10:51–58
43. Madea B, Staak M (1988) Determination of the sequence of gunshot wounds of the skull. J Forensic Sci Soc 28:321–328
44. Zimmermann EA, Launey ME, Barth HD, Ritchie RO (2009) Mixed mode fracture of human cortical bone. Biomaterials 30: 5877–5884
45. Zou Z, Reid SR, Tan PJ, Li S, Harrigan JJ (2009) Dynamic crushing of honeycombs and features of shock fronts. Int J Impact Eng 36: 165–176
46. Abrate S (1998) Impact on composite structures. Cambridge University Press, Cambridge
47. Skvortsov V, Kepler J, Bozhevolnaya E (2003) Energy partition for ballistic penetration of sandwich panels. Int J Impact Eng 28:697–716
48. Hou W, Zhu F, LU G, Fang D-N (2010) Ballistic impact experiments of metallic sandwich panels with aluminium foam core. Int J Impact Eng 37:1045–1055
49. Chaudhri MM (2015) Dynamic fracture of inorganic glasses by hard spherical and conical projectiles. Philos Trans R Soc Lond A 373:20140135. https://doi.org/10.1098/rsta.2014.0135
50. Spatola BF (2015) Atypical gunshot and blunt force injuries: wounds along the biomechanical continuum. In: Passalacqua NV, Rainwater CW (eds) Skeletal trauma analysis: case studies in context. John Wiley & Sons, West Sussex, pp 7–26
51. Quatrehomme G, Piercecchi-Marti M, Buchet L, Alunni V (2015) Bone bevelling caused by blunt trauma: a case report. Int J Legal Med 130(3):771–775. https://doi.org/10.1007/s00414-015-1293-0
52. Vermeij EJ, Zoon PD, Chang SBCG, Keereweer I, Pieterman R, Gerretsen RRR (2012) Analysis of microtraces in invasive traumas using SEM/EDS. Forensic Sci Int 214(1):96–104
53. Nawrocki SP (2009) Forensic taphonomy. In: Blau S, Ubelaker DH (eds) Handbook of forensic anthropology and archaeology. Left Coast Press, California, pp 284–294
54. Moraitis K, Spiliopoulou C (2010) Forensic implications of carnivore scavenging on human remains recovered from outdoor locations in Greece. J Forensic Legal Med 17:298–303
55. Pope EJ, Smith O'BC (2004) Identification of traumatic injury in burned cranial bone: an experimental approach. J Forensic Sci 49(3):1–10
56. Tümer AR, Karacaoğlu E, Keten A, Ünal M (2012) Postmortem burning of the corpses following homicide. J Forensic Legal Med 19:223–228
57. Loe L (2009) Perimortem trauma. In: Blau S, Ubelaker DH (eds) Handbook of forensic anthropology and archaeology. Left Coast Press, California, pp 263–283
58. Machado MPS, Simões MP, Gamba TO, Flores IL et al (2016) A Wormian bone, mimicking a gunshot entrance wound of the skull, in an anthropological specimen. J Forensic Sci 61(3):855–857. https://doi.org/10.1111/1556-4029.13043
59. Cantwell WJ, Morton J (1989) Comparison of low and high velocity impact response of CFRP. Composites 20(6):545–551

APPENDIX 2

Published paper:

Crack propagation through sandwich bones due to low-velocity projectile impact

John M Rickman* (MSc), Dr James Shackel**

Cranfield Forensic Institute

Cranfield University, Defence Academy of the United Kingdom

Shrivenham

SN6 8LA

*Corresponding author email address: j.m.rickman@cranfield.ac.uk

*Phone: 01793785531

*ORCID: 0000-002-1188-8805

International Journal of Legal Medicine
https://doi.org/10.1007/s00414-019-02086-1

ORIGINAL ARTICLE

Crack propagation through sandwich bones due to low-velocity projectile impact

John M. Rickman[1] · James Shackel[1]

Received: 31 January 2019 / Accepted: 22 May 2019

Abstract
Projectile impact in sandwich bones typically results in formation of conoidal wounds exhibiting a larger region of damage on the inner cortical plate termed the bevel. To date, a number of hypotheses have been put forward to explain the formation of this wound type. The plug and spall hypothesis suggests that the conoidal morphology is produced by a two-phase mechanism of shear plug formation followed by internal bevel production during projectile exit. In contrast, the cone crack hypothesis suggests that such wounds are produced by cone crack propagation through the three laminae of the sandwich bone, resulting in the formation of bioceramic conoids consisting of all three bone laminae. In order to test these hypotheses, 28 non-human sandwich bones were impacted with 6-mm carbon steel spheres at velocities ranging from 26 to 96 metres per second (m/s). Impacts were filmed utilizing high-speed videography and fracture morphology analysed using micro-computerized tomography (μ-CT). Sequential increase in velocity successfully captured the genesis of conoidal wounds. Low-velocity impact produced circular depressed fractures in the outer cortex exhibiting angulated cortical fracture edges. An increase in velocity resulted in translaminar fracture and production of one intact and three fragmentary bioceramic conoids. At the highest velocities, conoids were fragmented and lost in the ejecta plume, with attached fragments undergoing dynamic movement during and after perforation. Significantly, projectile exit was not required for bevel production. The implications of these findings in wound interpretation are discussed.

Keywords Skeletal trauma · Projectile trauma · Bevelling · Forensic anthropology · Fracture · Trajectory determination

Introduction

The conoidal fracture expressed in sandwich bones subsequent to projectile impact is an intriguing traumatic feature upon which critical diagnostic and trajectory determinations are based [1–4]. Morphologically, this wound type consists of a conoidal wound volume bordered by a fracture edge through all three layers of the sandwich bone, extending from the entry point in the outer cortex and across the intervening trabeculae to the inner cortical lamina [5]. Such conoidal fracture morphology dictates that the region of missing bone in the inner cortical lamina has a larger surface area than that missing from the opposing cortical entry wound. The bony layers composing this flaring, termed the internal bevel in entry wounds and external bevel in exit wounds [1, 6], are rarely formally defined; however, it is accepted that the conoidal fracture extends in the direction of projectile travel and thus indicates the entry or exit status of the wound [6, 7]. Further diagnostic emphasis has been placed on the symmetry of the bevel, with regions of bevel elongation considered to indicate the trajectory of the projectile through the bone [2, 3, 8], although full correlation between these variables has been disputed [5, 9]. Despite the importance of such determinations in forensic contexts, there is still no consensus in the literature as to the mechanisms underlying formation of this conoidal wound type, and multiple medicolegal cases have now demonstrated that this feature is not unique to projectile impact [10].

In material terms, bone is a bioceramic composite [11] with hierarchical organization [12–14]. At the macroscopic level, the sandwich bones of the neurocranium are constructed of outer and inner layers of cortical bone separated by an intervening trabecular layer of variable thickness, sometimes termed the *diploë* [15]. Fractures through such a sandwich bone may be confined to a single layer (intra-laminar), cross

✉ John M. Rickman
j.m.rickman@cranfield.ac.uk

James Shackel
j.shackel@cranfield.ac.uk

[1] Cranfield Defence and Security, Defence Academy of the United Kingdom, Cranfield University, Shrivenham SN6 8LA, UK

Published online: 08 June 2019

one or more layers (trans-laminar) or pass between layers (inter-laminar, or delamination) [5]. These fractures may be further classified according to mechanism; mode 1 failure indicates a tensile, crack opening mode whilst mode 2 refers to in-plane shear, which occurs in the absence of crack opening [16].

For descriptive purposes, the current paper utilizes nomenclature developed from the micro-computerized tomographic (μ-CT) analysis presented previously by the present authors [5]. In this scheme (Fig. 2), a single conoidal entry wound in a sandwich bone is considered to consist of a cortical entry in the outer cortical layer and a cortical exit in the inner cortical layer, the two encompassing the upper and lower borders of an internal conoidal wound volume. Entry cortical fracture edges form the walls of the cortical entry whilst the cortical exit is bound by the walls of the exit cortical fracture edge. The trabecular fracture margin is formed by the free edges of fractured trabeculae, and peripheral trabeculae are those trabeculae up to 3 mm peripheral to this margin. This entry cortical fracture edge is typically angulated and the crack producing this cortical fracture margin crosses with little to no deviation across the trabeculae and into the inner cortex as a translaminar fracture surface. Such continuous translaminar fracture renders definition of the layers composing the internal bevel an arbitrary process; however, the present paper defines the internal bevel as a conoidal wound volume encompassing the exit cortical fracture edge and trabecular fracture margin.

The plug and spall hypothesis is the most widely cited mechanism for production of this wound type, appearing in multiple standard texts considering the subject of osseous gunshot wounds [e.g. 3, 7, 17]. This hypothesis (see Fig. 1) proposes that conoidal wound formation is a two-phase process involving plug formation in the outer cortex and then bevel production. In the first phase, projectile impact shears a plug or disc of cortical bone from the outer cortical layer [3, 18, 19] (Fig. 1a). This shear plug is then theorized to move ahead of the projectile through the sandwich structure (Fig. 1b), with some interpretations also suggesting that fractured material accumulates ahead of the projectile/plug combination [19]. In the second phase, the internal bevel is believed to be formed by a blow-out process involving fracture or "spall" around the plug during projectile exit (Fig. 1c) [3, 7, 18], with plug-induced shear through the trabeculae posited as a specific mechanism for trabecular failure [4]. Kieser et al. [19] utilized μ-CT to analyse wound cross-sections and proposed that the resultant wound profile due to cortical plug production was funnel shaped, with the neck of the funnel in the external cortex (Fig. 1d). According to the plug and spall hypothesis, the dominant fracture mechanism is considered to be mode 2 (in-plane shear).

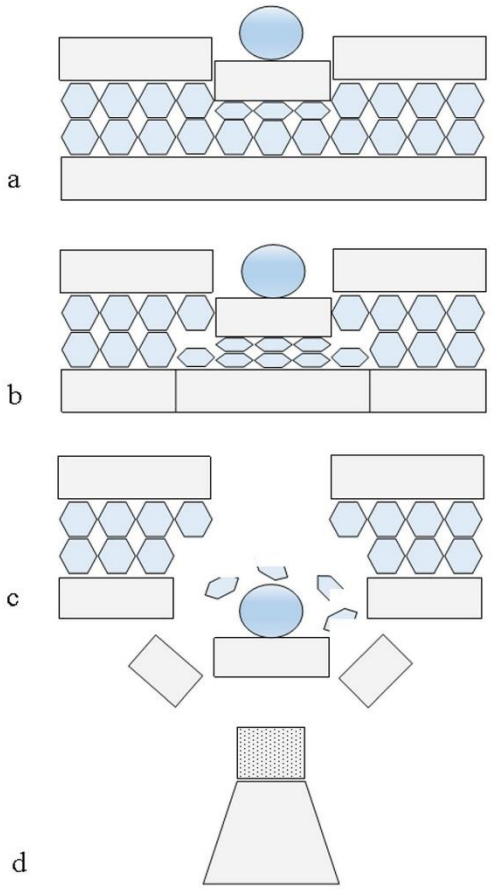

Fig. 1 The plug and spall hypothesis. **a** Projectile impact shears a plug of cortical bone from the outer cortical layer. **b** Projectile and sheared plug move through the trabecular layer, signified by hexagons; note cell collapse and densification due to compressive stresses. **c** Projectile and shear plug blast out the exit to produce the internal bevel. **d** Wound volume profile in section as proposed by Keiser et al (2013); wound is funnel shaped, with vertical neck in the outer cortex (dotted region) and conoidal region through the trabecular layer and internal cortical layer

The plug and spall hypothesis, as described above, involves several key assumptions:

1. Plug production through in-plane shear is independent of projectile tip shape and construction, since conoidal wounds are not restricted to certain projectile designs.
2. The disc of sheared bone does not fragment during transit through the sandwich structure.
3. The projectile must pass through the trabeculae and then exit the bone for the bevel to form

Despite wide usage of this hypothesis, there appears to be no published evidence supporting the role of a cortical plug in wound formation. Shear plugging itself is sensitive to multiple factors including target material characteristics, projectile tip shape, velocity, and angle of impact [20], and thus it will not occur with all impacts in a given material. Recognition of the high-contact stresses developed during impact raises the question as to how a shear plug could participate in perforation without itself being destroyed during the impact event. Analysis of high-speed footage of projectile exit through pig sandwich bones has revealed no evidence for an intact disc of cortical bone exiting ahead of the projectile [5]. Furthermore, cross-sectional analysis has demonstrated that the bevel still forms when it is shielded behind bone fragments retained on the inner cortical plate, effectively ruling out bevel production due to contact with a disc of cortical bone in those regions [5].

In an alternative hypothesis based upon a μ-CT and high-speed video analysis (Fig. 2), Rickman and Shackel [5] proposed that the conoidal wound in sandwich bones is produced by cone crack formation under tension in the outer cortex; this cone crack was then theorized to propagate through the trabecular lamina one cell width at a time before finally entering the inner cortex. According to this scheme, the crack propagates through the tri-laminar sandwich bone as if it were a homogeneous solid, resulting in production of a conoidal structure consisting of all three layers of the sandwich bone, separated from the parent bone by the conoidal fracture, or bevel. This tri-layered plug, or bioceramic conoid, would be identical to the ceramic conoids produced during impact of non-biogenic ceramics [21] but with the addition of a layer of trabecular bone running between cortical plates. Morphological evidence in support of the cone crack hypothesis and bioceramic conoid formation at higher velocities included angulation of the entry cortical fracture edges, apparent trans-laminar fracture through the sandwich structure and part-counterpart relationships between fragments of inner cortical plate and the internal bevel. Unlike the plug and spall theory, the cone crack hypothesis does not assume that projectile exit is required to produce the bevel. Rather, the bevel is theorized to form at the moment of impact by a cone crack propagating at the speed of sound through the material from outer to inner cortical plates. Unlike the plug and spall theory, the cone crack hypothesis suggests that the fracture driving wound formation is primarily a crack opening, mode 1 (tensile) process.

A significant complication when studying plugs during high-velocity impact arises from the fact that plug fragmentation in brittle materials occurs as little as 10 % beyond the minimum perforation velocity [20]; accordingly, their possible formation above this threshold must be inferred from residual fracture morphology. At present, evidence of intact projectile-induced bioceramic conoids in sandwich bones is limited to a few reports in the archaeological and forensic literature of tri-layered plugs that demonstrate part-counterpart relationships with their parent bone [22–24]. However, whilst these valuable finds indicate that conoidal plugs can be produced during at least some projectile impacts, it is not yet clear if their production underlies the formation of all conoidal wounds.

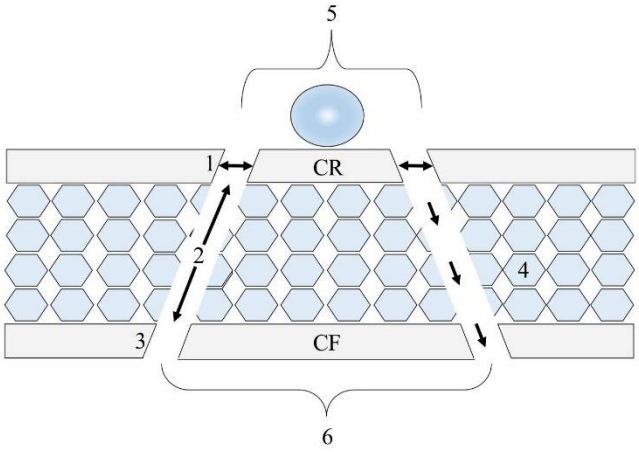

Fig. 2 The cone crack hypothesis and formation of a tri-layered plug or bioceramic conoid; projectile impact elicits cone crack formation under tension in the outer cortical layer (horizontal double headed arrows); crack then propagates under tension through the trabecular cells and through the inner cortical layer (three arrows descending at right); nomenclature for cross-sectional anatomy presented in [5]; 1, entry cortical fracture edge; 2, trabecular fracture margin; 3, exit cortical fracture edge; 4, peripheral trabeculae; 5, cortical entry; 6, cortical exit; the bevel is here defined as the trabecular fracture margin (2) and exit cortical fracture edge (3); intact bioceramic conoid has a cortical roof (CR) and a cortical floor (CF)

To date, no published accounts of their experimental formation could be identified and, accordingly, there is much to be learned about how these structures form and about their possible wider role in conoidal wound formation in sandwich bones.

An alternative approach to the study of crack propagation from post-perforation fracture morphology is to utilize a series of low-velocity increments in an attempt to capture crack propagation through the depth of the structure. Although the assumption that low- and high-velocity impacts elicit identical fracture behaviours may not always be met due to both strain rate and shock wave effects, this technique was successfully utilized by Kieser et al [25] to capture the formation of butterfly fractures in deer femora, a fracture type typical of higher-velocity impacts in long bone shafts. Significantly, these authors also reported cone crack propagation in the compact bone. Although informative footage of long bone projectile perforation has been captured by high-speed videography [26–28], visualization of fracture processes in sandwich bones is currently limited to high-velocity tangential impacts to synthetic analogues [29] and perpendicular impacts to pig scapulae [5]. To further test the plug and spall and cone crack hypotheses, the present study utilizes a combination of μ-CT and high-speed videography to capture crack propagation processes in non-human sandwich bones subjected to a series of incremental low-velocity impacts between 25 m/s (metres per second) and 100 m/s. Fracture processes are described and their significance in relation to wound diagnosis and interpretation is then discussed.

Methods

Adult domestic pig (*Sus scrofa*) scapulae derived from the food chain were selected as proxies for human bones due to the fact they exhibit bevelled wounds when subjected to ballistic impact. Specimens were prepared according to the methods presented in [5]. In brief, only specimens with a layer of soft tissue in the infraspinous fossa, which was selected due to its larger size, were utilized. The glenoid, neck and spine were removed using a band saw, as was a section of cartilage on the anatomically dorsal surface. A target region of the infraspinous fossa no less than 40 mm from any edge was then selected and marked. During impact, specimens were secured in a specially constructed steel clamp that allowed full adjustment for different specimen sizes (Fig. 3). All specimens were impacted with the ventral region forming the apex, the broader dorsal region forming the base and the infraspinous fossa facing outwards.

Surface-hardened 6-mm carbon steel spherical projectiles (Atlas Ball and Bearings, UK) weighing 0.885 g were selected to prevent yaw or deformation from influencing fracture behaviour. These projectiles were fired from a compressed air-powered gas gun capable of achieving a velocity range of approximately 25 to 150 m/s. In order to achieve desired incident velocities for the 6-mm spheres, a calibration curve of pressure versus velocity was created in a series of test shots. During the bone impacts, a muzzle-target distance of 60 cm was chosen to prevent discharged air from influencing fracture processes.

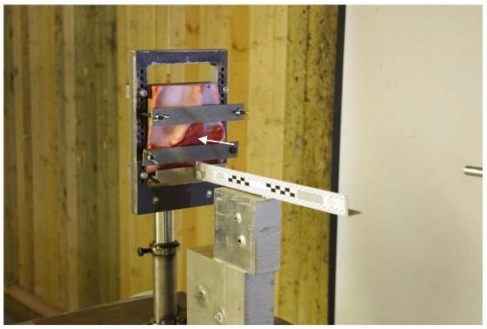

Fig. 3 Machined specimen mounted in adjustable clamping apparatus; target area in the infraspinous fossa indicated by arrow

Incident (pre-impact) velocity, residual (post-impact) velocity and energy absorption values were determined by placing a Phantom V12 camera to the side of the specimens with a scale in the image. Impact data was then calculated using the Phantom Cine Viewer (Vision Research, Inc.); to allow for variation in velocity measurements, projectile velocity was taken as the mean of three velocity determinations for each specimen. Assuming that energy is not utilized in projectile deformation and that energy lost due to frictional heating is minimal, energy absorption (ΔE) by the bone in joules (J) was then determined using the following formula:

$$\frac{m\left(v_1^2-v_2^2\right)}{2}$$

where m is the mass of the projectile in grams, V_1 is the incident velocity and V_2 the residual velocity in metres per second (m/s). In order to derive a standard deviation for the individual energy absorption values, which were calculated from the mean of three velocities, the error propagation formula presented in Rickman and Shackel [5] was utilized. Inner cortical plate behaviour was captured in all impacts using a Phantom V12 12 camera facing the inner plate and recording at 40,000 frames per second.

To determine velocities associated with internal crack formation, initial tests were conducted with six specimens divided into three pairs with selected target velocities of 30 m/s, 40 m/s and 50 m/s. Actual achieved test velocities were 26 m/s and 29 m/s (group 1), 35 m/s and 37 m/s (group 2) and 47 m/s and 49 m/s (group 3). μ-CT examination revealed that internal

cracking was restricted to the specimen impacted at 47 m/s; accordingly, velocities above 50 m/s were selected for subsequent analysis. In the latter experiments, a more refined inter-shot variation of 1–2 m/s was achieved by noting the velocity of the first shot at each selected velocity; all subsequent shots were then discharged with the same air pressure. Utilizing this method, specimens were impacted between 54 and 55 m/s (group 4), 57–58 m/s (group 5), 74–75 m/s (group 6) and 95–97 m/s (group 7). The number of specimens impacted across these velocities is provided in Table 1. Following Goldsmith [30], penetration was considered to occur if the projectile rebounded and induced surface damage to the specimen (including soft tissue) or if it embedded in the target; perforation occurred if the projectile exited the sandwich bone.

In order to remove the concealing effect of soft tissue when observing fracture, soft tissue was dissected away from the outer and inner cortical layers of six additional specimens. Footage of entry and exit was then obtained by placing the Phantom V12 12 camera at the rear of each specimen and the Phantom V12 camera at the front; both cameras were then set to record on the same trigger. Although lack of a camera mounted to the side meant that incident velocities could not be determined from imaging of the projectile, the calibration curve allowed velocity estimation to within approximately 1–2 m/s. Inner cortical plate behaviour during projectile rebound was captured using four specimens impacted at approximately 57 m/s. To view the full perforation process at higher velocity, two final specimens were impacted at approximately 150 m/s. Post-impact analysis revealed that a technical fault in the trigger time of one camera had resulted in a variable delay between front and rear footage, preventing full camera synchronization; however, valuable data on fracture processes was obtained.

Micro-computerized tomography

Specimens were wrapped in cling film, mounted in foam blocks and held securely in place using tape. The impact area of the fleshed specimens was identified and scanned in a Nikon X-Tec XT H 225 scanner at 75 kV, 90 μA and 2.25 magnification, resulting in a voxel size of 89 μm. Scan data was reconstructed using CT Pro 3D; the radius of reconstruction was reduced from 100 to 95–90% in order to remove edge artefacts produced by rotation of the flat plate around the damage area. Reconstructed volumes were analysed in VGStudeo MAX version 2.2 (Volume graphics, Germany). The simple registration function was utilized to orientate specimens across the middle of the screen with the cortical entry facing upwards. Bone surfaces were identified using the surface determination function. Distance and angle-measuring tools were set to recognize and attach to the bone surface using the snap to surface function, allowing precise placement of the tool. The depth of depressed fractures at the impact location was obtained by placing a line across the cortical entry and

Table 1 Summary data for $n = 22$ impact events; n = number of specimens; velocities from 26 to 49 m/s were grouped into three pairs of initial test shots with the velocity indicated; *S*, penetration of soft tissue only; *SB*, penetration of soft tissue and bone; *E*, projectile embedded in bone; *EnCF*, entry cortical fracture edge; absence of cracks or cracks that were too small for accurate measurement in the longitudinal plane resulted in the mean entry cortical fracture edge angle being determined from the sample size indicated in parentheses (groups 4, 5 and 7); angle range indicated in italics

Group	Incident velocity (m/s) (*n*)	Penetration	Perforation	Ring crack/ compressed cortical disc	Angulated entry cortical fracture edge	Tri-layered bioceramic conoid (I, intact; F, fragmentary)	Longitudinal plane; mean apical EnCF angle	Longitudinal plane; mean basal EnCF angle
1	26 (1)	S	–	–	–	–	–	–
	29 (1)	S	–	–	–	–	–	–
2	35 (1)	S	–	–	–	–	–	–
	37 (1)	S	–	–	–	–	–	–
3	47 (1)	SB	–	1	1	0	–	–
	49 (1)	S	–	0	0	0	–	–
4	54–55 (3)	3 SB	–	3	3	0	55.31 (2)	64.82 (2)
							49.24–61.37	*52.57–77.07*
5	56–58 (6)	4 SB; 1 S	1	4	4	1 I	50.33 (3)	47.00
							36.74–62.70	*36.34–53.37*
6	73–75 (3)	–	3	3	3	3 F	45.94	39.42
							44.17–48.97	*27.28–49.34*
7	94–96 (4)	2, E	2	–	4	0	44.44	53.05 (3)
							31.19–57.99	*31.98–70.28*
Total	22	16	6	11	15	4		

then dropping a distance-measuring tool from this to the most compressed region of cortex.

Cortical entry shape and bevel symmetry

Cortical entry shape was classed as circular, oval or irregular; entries were further classed as circular-irregular or oval-irregular if there was irregularity in part of their otherwise symmetrical margin. Bevel symmetry was determined using μ-CT scans in 3D view and by descending through the wound to the exit cortical fracture edge (ExCF). Asymmetrical bevels were defined as those presenting a deviation in the ExCF resulting in a more pronounced bevel margin in one or more areas; in symmetrical bevels, the ExCF showed no such deviation.

Results

A total of 28 specimens were impacted and filmed, with side on camera footage available for 22 of these; summary data for these 22 impacts is provided in Table 1. Energy absorption values could not be calculated in the two group one specimens; in one, projectile re-bound was not captured, whilst in the other the projectile immediately re-bounded off the clamp. Figure 4 shows the relationship between incident velocity, energy absorption and whether impact resulted in re-bound, penetration or perforation for the remaining 20 specimens. Across these impacts, absorbed energy ranged from 0.48 to 4.08 J. An increase in incident velocity resulted in a steep increase in energy absorption. In specimens retaining soft tissue, a total of 16 impacts resulted in penetration, with 14 of these undergoing rebound. Two impacts at the highest velocities in the series (at 94 m/s and 96 m/s) resulted in embedment. In total, perforation was observed in 6 specimens and was found to initiate at 58 m/s. Greater absorbed kinetic energy above this threshold resulted in perforation in five of the seven impacts between 73 and 96 m/s.

Measurement data taken from the four specimens impacted between 94 and 96 m/s suggested factors that might have determined whether projectile penetration or perforation occurred (Table 2). Apical and basal total thicknesses, apical and basal trabecular thicknesses and apical cortical thicknesses were greater in the two embedding impacts. This general trend for a thicker outer cortex in the embedding impacts also existed for the basal side of the wound, although there was overlap between the 96 m/s perforation and 96 m/s embedment. Apical and basal thicknesses of the inner cortical layers were also greater in the two embedding impacts. The thickness of the trabecular lamina in relation to whole bone thickness did not appear to influence projectile behaviour, with one perforating impact actually having a proportionally thicker trabecular layer than the two embedding impacts. Projectile embedment was associated with greater energy absorption in both cases.

Table 3 details external wound morphology in the 6 perforated fleshed specimens. The majority of entries were circular ($n = 3$) or circular-irregular ($n = 2$). The single irregular entry occurred at the lowest incident velocity and in a very thin specimen (0.9 mm at its thinnest point). The majority of bevels ($n = 4$) were asymmetrical. Only one of the three circular entries exhibited symmetrical bevelling.

External and internal fracture morphology

Rebound impacts between 26 and 58 m/s resulted in splitting and retraction of the periosteum at the impact site. In all impacts between 26 and 37 m/s, damage was entirely limited to soft tissue. Rebound impacts induced between 47 and 58 m/s resulted in partial or full penetration of the outer cortical plate. Penetration was associated with formation of a cortical entry bordered by a circular, ring-type crack and a compressed disc of cortex located immediately

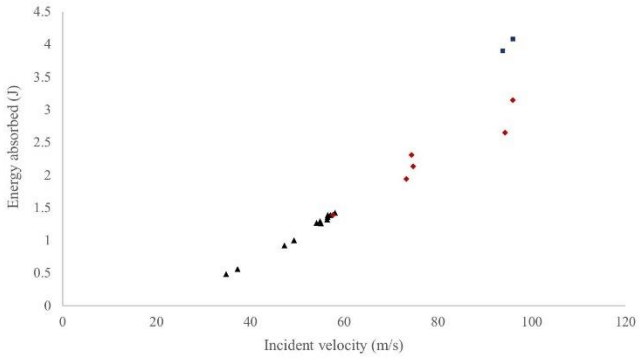

Fig. 4 Relationship between incident velocity (m/s), energy absorption (J) and projectile behaviour during impact; re-bound (triangles); perforation (diamonds) and penetration (squares)

Table 2 Projectile behaviour and energy absorption (J) in relation to total bone thickness, thickness of the outer and inner cortical layers and trabecular thickness; data derived from μ-CT using μ–z (longitudinal) sections; each thickness measured as close to the wound volume as possible; standard deviation for energy absorbed in parentheses was calculated using the error propagation formula in [5]

Incident velocity (m/s)	Projectile behaviour	Total bone thickness (TB), apical (mm)	Total bone thickness (TB), basal (mm)	Outer cortical thickness, apical (mm)	Outer cortical thickness, basal (mm)	Inner cortical thickness, apical (mm)	Inner cortical thickness, basal (mm)	Trabecular thickness (T), apical (mm)	Trabecular thickness (T), basal (mm)	Trabecular proportion (T/TB), apical	Trabecular proportion (T/TB), basal	Energy absorbed (J)
94	Embedment	5.74	6.20	1.34	0.96	0.85	0.92	3.35	4.06	0.58	0.65	3.90 (0.01)
96	Embedment	5.80	6.34	1.04	0.92	0.99	0.72	3.55	4.55	0.61	0.72	4.08 (0.01)
91	Perforation	4.17	4.05	0.71	0.62	0.62	0.47	2.95	2.82	0.71	0.70	2.65 (0.01)
96	Perforation	1.92	3.09	0.99	0.92	0.51	0.68	0.51	1.48	0.27	0.48	3.15 (0.0002)

Table 3 Cortical entry shape and bevel symmetry in relation to incident velocity for perforated specimens

Group	Incident velocity (m/s)	Cortical entry shape	Bevel symmetry
5	58	Irregular	Asymmetrical
6	73	Circular-irregular	Symmetrical
6	74	Circular-irregular	Asymmetrical
6	75	Circular	Asymmetrical
7	91	Circular	Asymmetrical
7	96	Circular	Symmetrical

under the impact location (Fig. 5a). Compressed cortical discs and ring-type cracks were present in the outer cortex of 8 of the 10 rebound impacts between 47 and 58 m/s. The two remaining specimens in this velocity range exhibited no signs of fracture despite one being the highest-velocity impact resulting in rebound at 58 m/s.

The flaws giving rise to the ring-type cracks were below the limit of resolution of the μ-CT in all but one specimen, where a crack emanated from a nutrient foramen in the outer cortical plate before taking a circular course and completing a semi-circular fracture at the impact location (Fig. 5b). In cross-section, specimens exhibited various degrees of compression of the cortical disc, ranging from minimal (Fig. 5c, incident velocity 47 m/s, approximately 0.38-mm compression) to just over a millimetre (Fig. 5d, incident velocity 54 m/s, approximately 1.19-mm compression). Despite being bent from above downwards, plastic deformation occurred without signs of tensile fracture on the inner aspect of the cortical discs (e.g. Fig. 5d). No specimens exhibited any sign of the disc being displaced downwards as an intact shear plug into the trabeculae. Trabecular cells underneath one heavily compressed cortical disc had undergone a degree of cell collapse, resulting in some densification of the cellular solid (Fig. 5d).

Cross-sectional analysis of the compressed cortical discs revealed that fracture of the sandwich bone was restricted to the outer cortical layer in all but one specimen (discussed below). In cross-section, the cortical walls of the circular cracks were angulated with respect to the cortical surface in cone crack fashion, and presented a relatively straight (e.g. Fig. 5e) or gently curving edge (e.g. Fig. 5f). These angulated fracture surfaces were morphologically identical to those seen in fully formed conoidal wounds and may thus be termed entry cortical fracture edges (Fig. 5c–e). Mean apical and basal angles of these fracture edges together with ranges are presented in Table 1. Mean apical and basal angles showed a general decrease with velocity, although the highest velocity impacts in group 7 resulted in higher basal angles than those in group 6. There was great variation in the angles both within and across groups and around the perimeter of a single cortical entry. For example, whilst the apical angle in one specimen impacted at 57 m/s was 62.70°, the angle on the left side of the

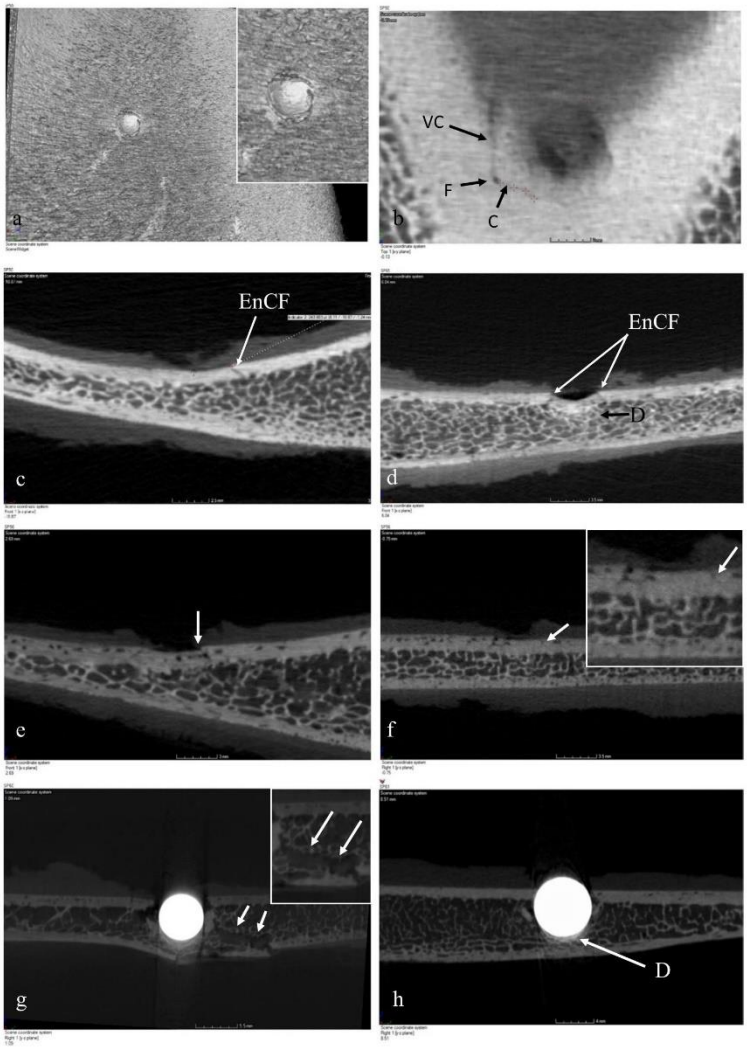

Fig. 5 **a** Example of compressed disc of cortical bone at the impact site. **b** Ring crack (C) originating from nutrient foramen (F) with vascular canal (VC) running vertically. **c** Transverse section of ring crack in **b** showing incipient conoidal wound formation with the presence of an angulated entry cortical fracture edge (EnCF); note minimal compression of the cortex under the impact point. **d** Example of cortical disc showing more extensive compression with some densification (D) of the trabecular cells; note bilateral angulation of the EnCF and crack opening adjacent to the compressed disc. **e** Downward movement of the lateral portion of a compressed cortical disc in relation to the EnCF, indicating a mode 2 (in-plane shear) failure component. **f** Example of mode 1 tensile failure without evidence of in-plane shear. **g** Cross-section of projectile embedment with projectile in situ; wound exhibits bilateral angulation of the EnCF with the cortical disc having fractured in the mid-line and displaced laterally; note formation of a conoidal wound volume despite lack of projectile exit, tensile fracture of inner cortical plate and evidence of crack hopping one cell edge to another (white arrows). **h** Cross-section of second projectile embedment showing bilateral angulation of the EnCF, midline fracture of the cortical disc and densification (D) of the trabecular cells

same entry was 45.59°. Angulation of the entry cortical fracture edge was evident in a perforated specimen where the impact site consisted entirely of cortical bone and was only 0.9 mm thick at its thinnest point.

When internal cracking was restricted to the outer cortex, the angulated cracks were open and their formation must therefore have involved a tensile (mode 1) cracking component (Fig. 5c–f). An additional in-plane shear (mode 2) component to failure of the cortical discs was indicated in some specimens by a slight downward displacement of their lateral fracture surfaces with respect to the entry cortical fracture edge (Fig. 5e, arrow). In one specimen, an angulated crack without associated in-plane shear was observed (Fig. 5f, arrow), suggesting that shear, if it occurs, must follow initial crack opening under tension. Fracture morphology in the outer cortices was thus suggestive of mode 1 or mixed mode 1–2 cracking processes if shear was operative during the impact event.

Two impacts resulted in projectile embedment in the sandwich bone. Although these specimens represented difficult

samples for μ-CT scanning with the projectiles left in situ, scans without removing the spheres to preserve fracture integrity captured details of the penetration process. In section, angulated entry cortical fracture edges were observed in both impacts (Fig. 5g). Neither specimen exhibited an intact cortical shear plug beneath the projectile. Instead, the cortical disc in both cases had been fractured and displaced laterally by the projectile with the fragments so formed remaining in close proximity to the outer cortical layer from which they were derived. Trabecular cell collapse and associated densification of the cellular solid occurred in both impacts but was particularly prominent in the 91 m/s embedment (Fig. 5h, labelled D). Tensile failure of the inner cortical plate was observable in the 96 m/s impact as a vertically orientated crack approximately in-line with the centre of the embedded sphere (Fig. 5g). The latter specimen exhibited a clear internal conoidal morphology despite lack of projectile exit. Bisected trabecular cells consistent with a tensile fracture crossing from one cell edge to another were present on the right of the conoidal volume (Fig. 5g, arrows). The large separation of the lower right portion of the conoidal volume from the parent bone appears to have occurred as the projectile that compressed the densified trabecular bone downwards (Fig. 5g).

Four impacts, at 57 m/s, 73 m/s, 74 m/s and 75 m/s, respectively, resulted in the formation of tri-layered bioceramic conoids (Fig. 6a–h). At 57 m/s, rebound impact left a structurally intact conoidal volume; fragmentation in the three higher velocity perforating impacts resulted in the retention of fragmentary components only. In all cases, the cortical disc derived from the outer cortex was still present in either intact or partially intact form and clearly formed the roof of the conoid. In the rebound impact, this conoidal roof had been compressed downwards without tilting into the trabecular layer, where it contrasted starkly with the spongy bone around it (Fig. 6a). The conoid remained partially attached at one edge to the inner cortical layer, but translaminar fracture had otherwise separated it from the parent bone. Angulated cone fracture propagation without deviation through the sandwich layers was apparent and resulted in a distinct part-counterpart relationship between conoid and conoidal wound (Fig. 6a–c). In section, the outer cortical layer of this conoid was compressed by approximately 1.05 mm and in one part, a delamination in the outer cortical layer was visible (Fig. 6c). In this region, the upper border of the entry cortical fracture edge exhibited little to no angulation and the conoidal crack flared approximately mid-depth in the trabecular layer (Fig. 6c, arrow). The relationships between the fracture morphology of this specimen and a typical conoidal perforating wound are illustrated in more detail in Fig. 6b. Despite formation due to rebound impact, this specimen had a cortical entry (CE) and cortical exit (CEx) and a fully formed internal bevel (IB). The inner cortical plate in this specimen had failed in tension, resulting in the production of radial fractures emanating from a central point in a stellate pattern (Fig. 6d, thin arrows). These radial fractures arrested at the exit cortical fracture edge, which must therefore have formed first (Fig. 6d, thick arrow). Stellate fracture was detectable in cross-section as an angulated crack in the inner cortical plate (Fig. 6b, labelled S).

In both the 73 m/s and 75 m/s impacts, the fragmentary conoidal volume was tilted and compressed below the inner cortical layer (Fig. 6e–h). The conoidal structure exhibited better preservation in the 75 m/s impact (Fig. 6e–g). Viewed from above, the cortical roof of the conoid was visible through the cortical entry wound (Fig. 6e). The conoid fragments remained attached to the inner cortex on one side (Fig. 6f) and exhibited a tensile fracture that bisected it into two halves. Adjustment of the cross-sectional plane so that it was perpendicular to the displaced three-layered structure confirmed its status as a partial conoid with stellate fracture (Fig. 6g). In the 73 m/s and 74 m/s impacts, the cortical disc forming the roof of the fragmentary conoid was again visible through the cortical entry wound, with the most intact morphology resulting from the 73 m/s impact (Fig. 6h, CR). The presence of a fragmentary conoid in the latter is demonstrated well in cross-section, where both upper and lower cortical components of the structure are readily apparent (Fig. 6h). A single trabecular connection between cortical layers in both the 73 m/s and 74 m/s specimens confirmed that the structures consisted of an entire tri-layered segment of sandwich bone (see Fig. 6h, Tr).

Two higher velocity impacts at 91 m/s and 96 m/s resulted in perforation without retention of any tri-layered fragments. In these specimens, inner cortical plate fragments exhibited part-counterpart relationships with the exit cortical fracture edge and retained some attached trabeculae (Fig. 6i, j). These fragments were therefore identical to the lower portion of the intact bioceramic conoid illustrated in Fig. 6a–c, with their upper parts having been fragmented and ejected. In the 91 m/s impact, some parts of the section through the conoidal wound presented a cleanly fractured edge on one side but exhibited protrusion of the trabeculae into the conoidal wound volume on the other due to alteration in the path of translaminar fracture (Fig. 6i).

High-speed footage of the outer cortical plate

Front on footage of impact at approximately 57 m/s was obtained for four dissected specimens. In this series, rebound occurred in three cases and embedment in the fourth. In all four specimens, impact resulted in a deformation pulse causing vibration at the free specimen edges. In two of the rebound impacts and the embedment, projectile impact resulted in a pulse of elastic deformation in the cortex immediately around the impact point, with rebound occurring during the recoil phase of cortical

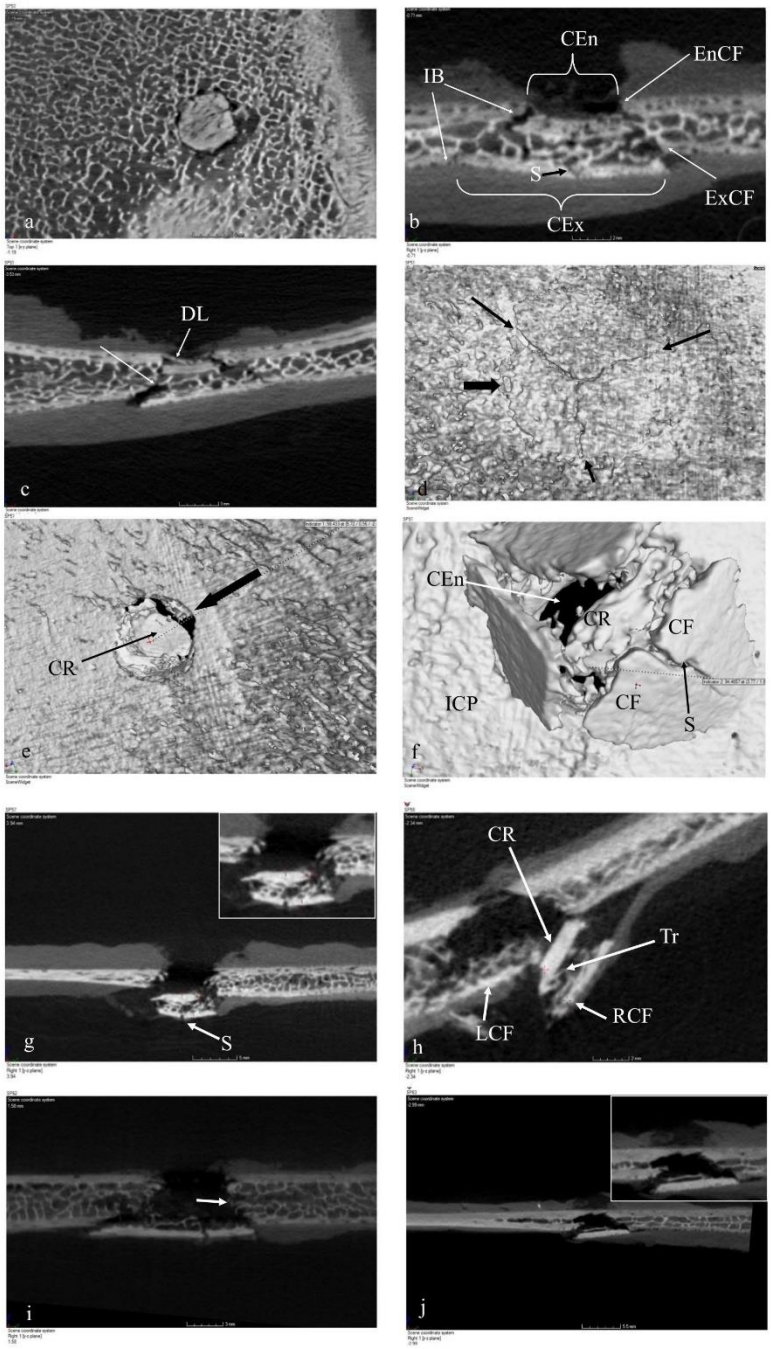

◀ **Fig. 6** Bioceramic conoid morphology. **a–d** Intact conoid produced by a 57 m/s impact. **a** Cortical roof of conoid compressed into the trabecular layer. **b** Longitudinal section of conoid showing relationships with typical perforating conoidal projectile wound; CEn, cortical entry; CEx, cortical exit; EnCF, entry cortical fracture edge; ExCF, exit cortical fracture edge; IB, internal bevel; S, stellate fracture. **c** Transverse section showing delamination (DL) of upper cortical layer and flaring of the conoidal crack within the trabeculae (arrow). **d** Inner cortical plate showing exit cortical fracture edge (large black arrow) and radial fractures of stellate fracture pattern (small black arrows). **e–g** Fragmented conoid produced by a 75 m/s impact. **e** View through cortical entry showing depressed cortical roof of conoid and entry cortical fracture edge (arrow). **f** Conoid fragment viewed from inner cortical plate; CR, cortical roof; CF, cortical floor; S, stellate fracture; CEn, cortical entry; ICP, inner cortical plate. **g** Cross-section perpendicular to the conoid fragment visible in **f**. **h** Fragmented conoid produced by 73 m/simpact; CR, cortical roof; Tr, trabecular connection between cortical roof and cortical floor of fragmentary conoid; LCF, left cortical floor and RCF, right cortical floor corresponding to fragments visible in Fig. 8j–l; recoil resulted in the cortical roof (CR) being in line with the left cortical floor (LCF). **i**, **j**, structures consistent with being the inner cortical vestiges of bioceramic conoids formed by 91 m/s (**i**) and 96 m/s impacts (**j**)

deformation. Estimated rebound times at approximately 58 m/s, taken as the time difference between the frames capturing initial contact and retrograde movement, were 227.23 μs, 227.24 μs and 136.34 μs, respectively. During rebound impacts, projectiles partially penetrated the outer cortex (Fig. 7b), with the compressed cortical discs so formed visible as a whitened region of cortex (Fig. 7c). μ-CT analysis of the specimen illustrated in Fig. 7a–c revealed a vertically orientated fracture in the cortical disc just adjacent to the mid-line (Fig. 7d). Cross-sectional fracture morphology revealed bilateral angulation of the entry cortical fracture edges (Fig. 7e, f), identical in form to that observed in impacted fleshed specimens; densification of the trabeculae was also apparent (Fig. 7f, labelled D**)**. In the penetrated specimen, the projectile fractured the outer cortical layer before moving in a retrograde direction and embedding at a depth of approximately half its diameter in the sandwich bone.

Impact at approximately 150 m/s in two defleshed specimens resulted in full perforation, with a deformation pulse visible at the specimen edges in only one of these. Unlike the 58 m/s impacts, the cortex around the impact site showed no visible signs of elastic deformation. Cortical behaviour under the projectile was captured in one specimen, where a semi-circular section of fractured cortex was visible to the right of the projectile (Fig. 7g). Rather than descending with the projectile through the sandwich structure as a shear plug, this fragment folded downwards as the projectile completed perforation (Fig. 7h). Such behaviour was consistent with this fragment being part of the originally circular cortical roof of a bioceramic conoid, identical in morphology to the fractured discs resulting from both embedding (Fig. 5g, h) and rebound impact (Fig. 7d–f). Fracture and ejection of the cortical roof left an approximately circular cortical entry (Fig. 7i).

High-speed footage of the inner cortical plate

There was no evidence of an intact shear plug arising from the outer cortical layer in any of the impact events. In contrast, observation of the inner cortical plate revealed a common fracture process between impacts that resulted in intact or fragmentary conoid production and higher velocity impacts that did not. During formation of an intact bioceramic conoid (illustrated in Fig. 8a–c), the tri-layered structure elevated with respect to the inner cortical plate, and the conoid floor simultaneously underwent stellate fracture due to high tensile stresses there (Fig. 8b). As impact proceeded, the conoid then underwent recoil in relation to the exit cortical fracture edge (Fig. 8c). The time taken to reach maximal elevation, measured from the frame prior to damage initiation, was 175 μs; the total time taken to reach maximum recoil was 600 μs.

Perforating impact resulting in partial fragmentation of a bioceramic conoid is illustrated in Fig. 8d–f. Impact again resulted in elevation of the conoid floor and stellate fracture (Fig. 8e, arrow). Subsequently, the inner cortical plate fragments formed by stellate fracture then went through a process of elevation and eversion, resulting in their trabecular surfaces facing outwards (Fig. 8f), with some then being ejected. Projectile exit occurred through the aperture created by the inner cortical plate fragments before full eversion. The sequence of elevation, stellate fracture, fragment eversion and ejection occurred in the absence of residual tri-layered fragment morphology at 91 m/s and 96 m/s (Fig. 6i, j), and was also seen in dissected specimens impacted at approximately 150 m/s where fragments were ejected. A sequence of images of capturing the exit process is provided for a defleshed specimen impacted at approximately 150 m/s in Fig. 8g–i.

Retained inner cortical plate fragments underwent considerable dynamic movement which in one case resulted in unusual fragment positions after impact (Fig. 8j–l). In this specimen, also illustrated in cross-section in Fig. 6h, two large conoid fragments were produced to the left and right of the cortical exit, with the right fragment retaining the tri-layered morphology. During impact, the conoid elevated and underwent stellate fracture (Fig. 8j, arrow). Although soft tissue partially obscures the bone in the high-speed footage (Fig. 8k**)**, a feature consistent with the left fragment (black arrow) could be seen elevating adjacent to the right tri-layered fragment (white arrow). Subsequent to projectile exit, fragment recoil resulted in the right fragment covering the left (Fig. 8l). In cross-section, this process resulted in the outer cortex of the tri-layered fragment being level with the inner cortex of the left fragment (Fig. 6h).

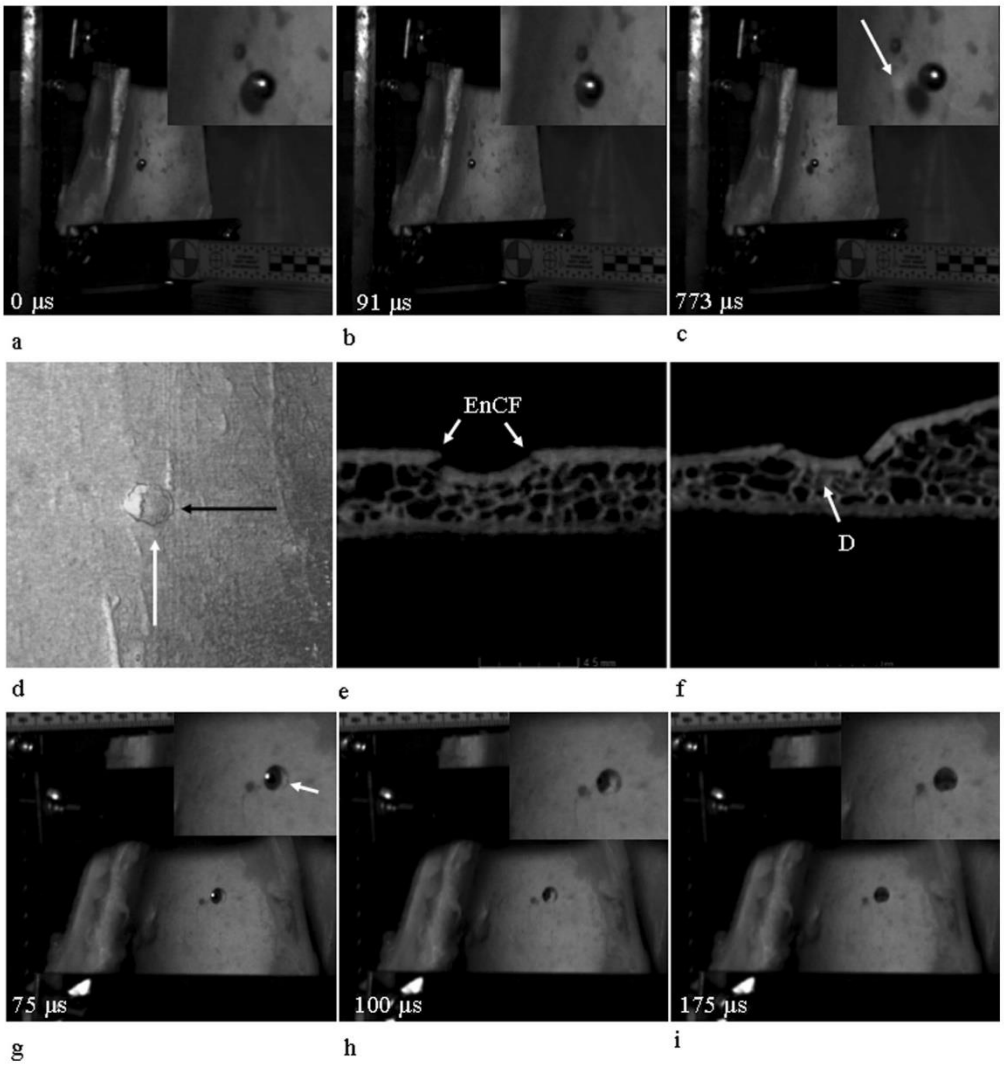

Fig. 7 Rebound and perforating impacts to defleshed outer cortical plates. **a**–**c** Rebound impact resulting from impact at approximately 57 m/s. **a** Pre-impact. **b** Maximum projectile penetration. **c** Rebound revealing compressed cortical disc (arrow). **d**–**e** µCT images of specimen in **a**–**c**. **d** Three-dimensional view of compressed cortical disc revealing vertical fracture. **e** Section of impact area at approximately mid-cortical entry (direction of section indicated by black arrow in **d**); note angulated entry cortical fractures edges (EnCF) and compression of cortical disc. **f** Section through region of vertical fracture within the cortical disc (direction of section indicated by white arrow in **d**); note densification of trabeculae (D). **g**–**i** Perforating impact at approximately 150 m/s, indicated times are from the pre-impact frame (not shown). **g** Projectile has perforated the outer cortical plate, which has fractured and displaced downwards (arrow in enlargement). **h** Projectile has completed exit of the outer cortical plate, revealing fractured and displaced cortical disc still in the process of fragmentation and ejection. **i** Final morphology of cortical entry

Discussion

Projectile perforation is a complex event and the exact mechanisms involved depend upon multiple factors such as target material properties, projectile design and incident velocity [20]. Failure modes can also compete during penetration, with the ultimate mechanism determined by material and projectile characteristics [31]. The complex hierarchical organization of bone also dictates that failure can occur at multiple length scales, introducing a complexity to failure processes that is not typical of synthetic composites [32]. In order to test the plug and spall and cone crack hypotheses, the present study therefore utilized a simplified experimental model consisting of non-human sandwich bones impacted with spherical projectiles. Low-velocity impacts induced using this system successfully captured the genesis of conoidal wounds, at least with the projectile-target combination utilized. Impacts between 26 and 96 m/s resulted in rebound, penetration and perforation, with projectile embedment apparently associated with greater bone thicknesses. Multiple aspects of fracture morphology induced by this range of projectile behaviours did not substantiate the contention that a cortical shear plug participates in perforation and instead were consistent with a tensile, cone cracking process resulting in production of tri-layered bioceramic conoids.

The initial phase of wound formation in rebound impacts below 58 m/s was the production of permanently compressed discs of cortical bone in the outer cortex identical in form to those described in the compact bone of deer femora subjected to sub-100 m/s impact [25]. Although seemingly consistent with shear plug formation when present in sandwich bones, cross-sectional fracture morphology revealed no evidence of these discs being driven through the remaining two sandwich layers, as predicted by the plug and spall hypothesis [4, 7, 18, 19]. In two embedding impacts and high-speed footage of one perforation, the cortical disc underwent fracture in the approximate mid-line and then underwent downward displacement during projectile passage. In four specimens, the cortical disc clearly formed the roof of a bioceramic conoid that displaced downwards as a unit consisting of all three sandwich layers. Significantly, the intact bioceramic conoid induced at 57 m/s shared multiple features with the plugs described in human material by Murphy et al. [22], Murphy et al. [23] and Bird and Fleishman 2015 [24]. Shared structural features included stellate fracture of the inner cortical plate, compression of the outer cortical plate, minimal to no trabecular compression and part-counterpart relationship with the internal bevel in the parent bone. Such morphological correspondence is highly indicative of common fracture processes in human and pig sandwich bones subjected to projectile impact.

A central component of the plug and spall hypothesis is that perforation of the outer cortical layer and bevel formation are separate events, with bevel formation suggested to occur during projectile exit [e.g. 3, 7, 18, 33, 34]. However, the present study confirms that bevel formation occurs in the absence of projectile exit; indeed, a fully formed conoidal wound was produced by a rebound impact. Numerous lines of evidence now converge to support the hypothesis that production of tri-layered bioceramic conoids is central to conoidal wound formation regardless of incident velocity. In addition to morphological correspondence between experimentally and non-experimentally produced bioceramic conoids, cross-sectional fracture morphology induced by impacts below 100 m/s is identical to that described for impacts between 150 and 897 m/s [5].

The fragmentary nature of three of the conoids formed in the current experiment, coupled with identical deformation and fracture behaviour in perforated specimens lacking conoids, strongly suggests that their absence subsequent to higher velocity impacts is not due to lack of formation but to their complete comminution and ejection, as predicted by the cone crack hypothesis [5]. Incident velocity apparently need not be great to fragment the conoidal volume, with comminution occurring between 73 and 75 m/s. Comminution appears to initiate with midline fracture and downward displacement of the conoidal roof. Subsequently, trabecular cells undergo the process of cell collapse resulting in densification of the trabecular layer. Finally, projectile exit elevates the inner cortical plate fragments and the majority of the conoidal volume is then ejected. Interestingly, the formation of intact conoids highlights a notable difference between biological and synthetic sandwich structures; whilst outer and inner laminae are perforated separately in the latter [35], intact conoid formation does not involve perforation of either layer.

Previous case reports have described conoidal wounds induced by low-velocity impact that are macroscopically identical to those induced at high velocity [36–38], raising a significant diagnostic challenge. The current study indicates that increasing velocity imparts a sequence to conoid behaviour that may assist in such diagnoses. Production of intact conoids was rare, with total fragmentation of the conoidal structure being the norm above 90 m/s. Conoid vestiges produced by impacts in the 73–75 m/s range consisted of variably comminuted outer and inner cortical layers with retained trabecular connections. As velocity increased, conoid collapse from above downwards resulted in loss of the tri-layered morphology, leaving retained inner cortical plate fragments with attached trabeculae as the only vestige of their formation. This morphological data supports the contention of Bird and Fleishman [24] that the retention of intact conoids (termed "plugs" in their article) is consistent with a relatively low-velocity impact event; however, it extends the diagnostic value of these features down to the fragment level. Accordingly, in cases where attached fragments or bony ejecta are retained, it may prove beneficial to search for the vestiges of a tri-layered morphology.

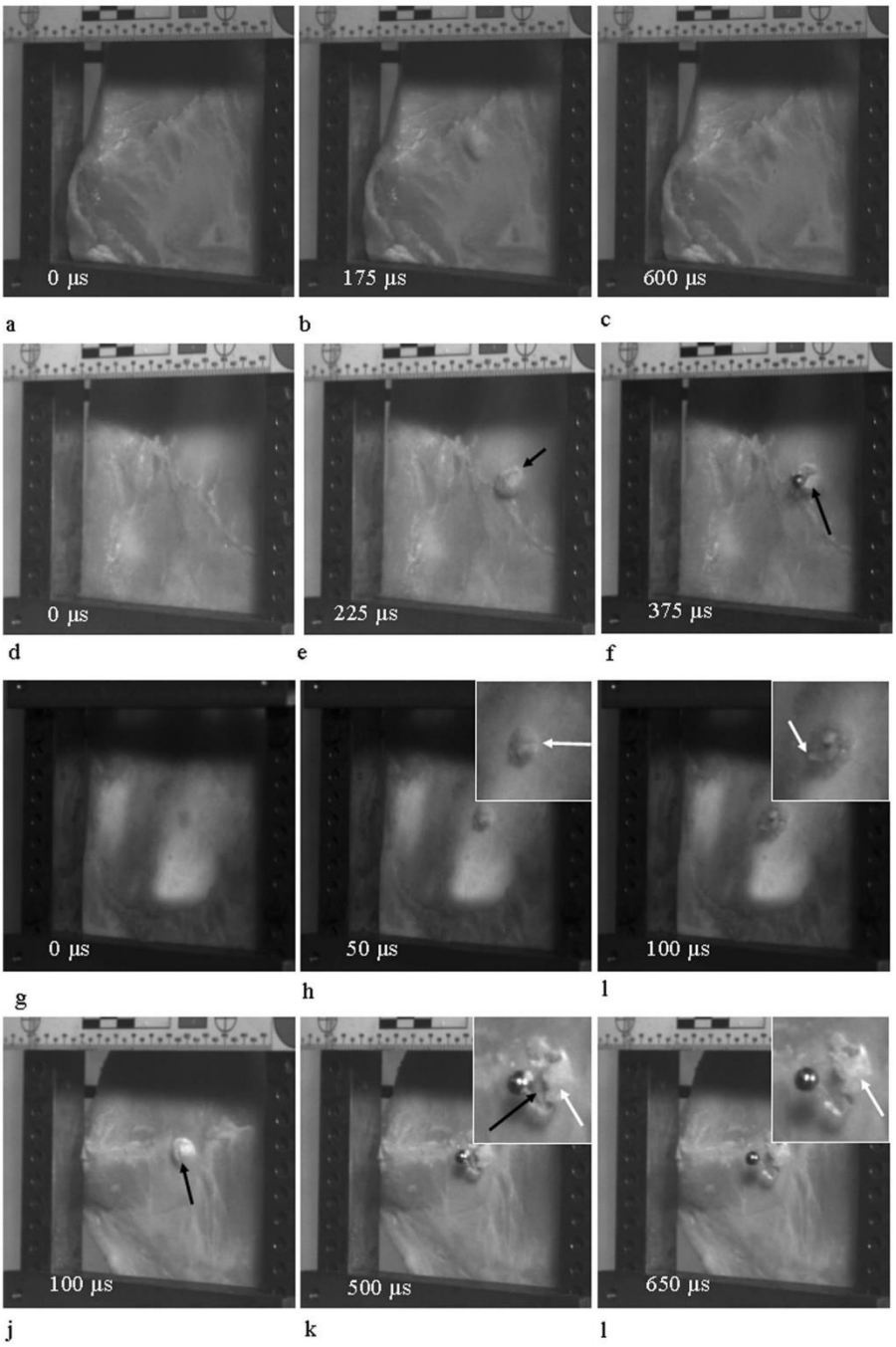

◀ **Fig. 8** High-speed footage of conoid behaviour viewed from inner cortical plate; all times from frame prior to visible damage. **a**–**c** Damage sequence capturing intact bioceramic conoid behaviour during 57 m/s re-bound impact. **a** Pre-impact. **b** Maximum conoid elevation. **c** Final damage pattern resulting from recoil of conoid. **d**–**f** 75 m/s perforation that resulted in partial conoid fragmentation. **d** Pre-impact. **e** Early elevation of conoid floor with stellate fracture (arrow) forming inner cortical plate fragments. **f** Eversion of inner cortical plate fragments (arrow). **g**–**i** Perforation sequence in dissected specimen, approximately 150 m/s. **g** Pre-impact. **h** Elevation and stellate fracture (arrow). **i** Inner cortical plate fragment elevation and eversion (arrow). **j**–**l** Dynamic movement of conoid fragments during a 73 m/s impact. **j** Stellate fracture of conoid floor (arrow) with central aperture between inner cortical plate fragments. **k** Enlargement shows left cortical floor fragment (black arrow) adjacent to right cortical floor fragment (white arrow).**l** Enlargement shows right fragment has recoiled over left fragment resulting in sectional view visible in Fig. 6h.

Numerous features of fracture morphology were consistent with a cone cracking failure mode. The first stage in cone crack formation during indentation or impact of brittle materials is the initiation of a surface crack from flaws at or slightly outside the contact radius of the projectile in the region of highest tensile stress; this crack then curves around in a circle to produce a ring crack [39–41]. Whilst the origin of the circular crack in the outer cortex was not captured in all specimens, in one, a fracture appeared to originate from a nutrient foramen located in the outer cortex before following a circular path delineating the indented cortical disc. Although a larger sample capturing the origin of such cracks is required to draw definitive conclusions, fracture morphology in this case was inconsistent with a shear failure mode and instead suggested the cortical disc was formed as a result of ring cracking. During cone crack formation, increasing contact pressure from the projectile results in the ring crack flaring to form a cone within the tensile stress field [41]. Similarly, in the present series, all fractured specimens exhibited crack angulation, initiating either in the outer cortical layer, the trabecular layer or both through different parts of the cross-section. Significantly, these angulated cracks were open and in close approximation suggesting the predominance of a tensile, crack opening failure mode. An additional tensile contribution to wound formation appears to arise when the projectile compresses the conoidal volume downwards relative to the trabecular fracture margin, a process that enhances separation of the conoid from the parent bone.

The establishment of projectile trajectory is often a critical aspect of medicolegal investigations [42], with the results of such analyses potentially influencing the outcome of criminal trials [2]. In this regard, the findings presented herein have considerable significance for our understanding of the factors underlying bevel morphology and thus the information that can be gathered from it. At present, prevailing theory indicates that regions of asymmetrical bevelling reflect the trajectory of the projectile [2, 8]. However, work addressing this proposed relationship with human skeletal material reported a poor correlation between these variables [9]. Bevel asymmetry was also found to be more common than bevel symmetry in experimentally induced perpendicular projectile wounds in pig sandwich bones [5]. The current analysis suggests this trend extends below 100 m/s, with 4/6 perforating wounds between 58 and 96 m/s classified as having an asymmetrical bevel despite resulting from perpendicular impact.

Whilst projectile trajectory in all likelihood does play a part in determining bevel symmetry, the finding that bevel formation occurs in the absence of perforation indicates it is but one of a number interacting factors underlying bevel shape. The production of bioceramic conoids in the present study confirms that a principle determinant of bevel symmetry must be the path of the translaminar fracture through the sandwich bone subsequent to its origin in the outer cortex. This path will be influenced by material factors such as Poisson's ratio, which is a key determinant of cone crack angle [43], the orientation of the trabecular struts in relation to the advancing crack tip [5] and the presence and distribution of cortical features altering crack direction, such as the cement sheaths of secondary osteons [32]. Loading rate may also play a part in fracture path, with cracks at lower loading rates tending to follow tortuous routes through regions of least resistance and cracks at high loading rates showing no such preference [44–46]. Further quantitative analyses of bevel symmetry and the potential influence of impact angle on this variable are required to quantify the accuracy of bevel shape in trajectory determinations.

The position of retained bone fragments is another indicator that has been utilized to establish trajectory, based on the assumption that their orientation results from direct interaction with the projectile [47]. However, unusual fragment positions can also enhance the challenge of trajectory determination and how the wound is interpreted in general. For example, Kieser [48] reported a keyhole entry with the outer cortical layer adjacent to the cortical entry compressed inwards rather than outwards as expected for a keyhole entry wound [49]. The results of high-speed videography may help explain such unusual fragment placements. Observation of impact revealed that kinetic energy imparted to attached fragments results in their dynamic motion and oscillation after the projectile has exited the specimen. Such fragment behaviour in one impact event resulted in the outer cortical layer of one conoid fragment residing below the inner cortical layer of another. When considering fragment position in trajectory determination, it must therefore be kept in mind that their final placement is not necessarily due to a direct interaction with the projectile; rather, it might represent their resting position after dynamic movement has ceased.

The presence and location of bevelling is fundamental to the determination of the entry or exit status of projectile wounds [1, 7], and in this regard, it is significant that some authors have noted its absence in thin areas of bone that lack a

trabecular layer [6, 9, 34]. Whilst the trabecular fracture margin and exit cortical fracture edge will be absent in such bones, the translaminar fracture resulting in bevel formation typically begins as an angulated crack in the outer cortical layer. This angulated crack was restricted to the outer cortical layer in 7 specimens and was also present in a perforated specimen consisting entirely of cortical bone, indicating it forms independently of the trabecular lamina. The possibility therefore arises that cross-sectional analysis may be able to identify the entry or exit status of wounds in thin cortical bone that lacks bevelling. Interestingly, images of angulated entry cortical fracture edges have been captured using multidetector computed tomography (MDCT) [50], suggesting they can be detected in situ during post-mortem analysis.

Whilst the present work focused specifically on sandwich bones, it is important to consider conoidal fracture in a wider skeletal context; at present, it is not clear if this mechanism is responsible for conoidal wound formation during impact in all bone types. For example, Huelke et al. [51, 52] attributed conoidal wound formation in the femoral epiphyses to temporary cavitation of fluid located in the interstices of the trabeculae. Although the formation and dynamic behaviour of bioceramic conoids was captured by the current experimental model, further research is required to confirm that incident kinetic energy drives a process of translaminar fracture and bioceramic conoid formation in human material. Finally, whilst spherical projectiles are ideal for eliminating confounding variables such as deformation on the impact process, future analyses should seek to address the influence of projectile design on perforation mechanisms.

Acknowledgements We are indebted to Alan Peare for running the compressed airgun and high-speed cameras and also for his technical input. We would also like to extend our sincere thanks to Gary Cooper for the design and manufacture of the clamping apparatus.

Compliance with ethical standards

Ethical approval This study was fully approved by the ethics committee of Cranfield University.

Conflict of interest The authors declare that they have no conflict of interest.

References

1. Berryman HE, Symes SA (1998) Recognising gunshot and cranial trauma through fracture interpretation. In: Reichs KJ (ed) Forensic osteology: advances in the identification of human remains. Charles C Thomas Publishers, Springfield, pp 333–352
2. Rhine, Curran (1990) Multiple gunshot wounds to the head: an anthropological review. J Forensic Sci 35(3):1236–1245
3. Komar DA, Buikstra JE (2008) Forensic anthropology: contemporary theory and practice. Oxford University Press Inc., New York
4. Kimmerle EH, Baraybar J (2008) Skeletal trauma: identification of injuries resulting from human rights abuses and armed conflict. CRC Press, Florida
5. Rickman JM, Shackel J (2018) A novel hypothesis for the formation of conoidal wounds in sandwich bones. Int J Legal Med 133: 501–519. https://doi.org/10.1007/s00414-018-1946-x
6. DiMaio VJM (1999) Gunshot wounds: practical aspects of firearms, ballistics and forensic techniques. CRC Press, Florida
7. Symes SA, L'Abbé EN, Chapman EN, Wolff I, Dirkmaat DC (2012) Interpreting traumatic injuries to bone in medicolegal investigations. In: Dirkmaat DC (ed) A companion to forensic anthropology. Wiley- Blackwell Publishing, West Sussex
8. Spitz WU (2006) Injuries by gunfire. In: Spitz WU, Spitz DJ, Clark R (eds) Spitz and Fisher's medicolegal investigation of death: guidelines for the application of pathology to crime investigation. Charles C Thomas Publishers, Springfield **Available from: Proquest Ebook Central (accessed 8.8.17)**
9. Quatrehomme G, İşcan MY (1998) Analysis of bevelling in gunshot entrance wounds. Forensic Sci Int 93:45–60
10. Rickman JM, Smith MJ (2014) Scanning electron microscope analysis of gunshot defects to bone: an underutilised source of information on ballistic trauma. J Forensic Sci 59(6):1473–1486. https://doi.org/10.1111/1556-4029.12522
11. Olszta MJ, Cheng X, Jee SS, Kumar R, Kim YY, Kaufman MJ, Douglas EP, Gower LB (2007) Bone structure and formation: a new perspective. Mater Sci Eng R Rep 58:77–116
12. Rho JY, Kuhn-Spearing L, Zioupos P (1997) Mechanical properties and the hierarchical structure of bone. Med Eng Phys 20:92–102
13. Fratzl P, Weinkamer R (1998) Nature's hierarchical materials. Prog Mater Sci 52:1263–1334
14. Weiner S, Wagner HD (1998) The material bone: structure-mechanical function relations. Annu Rev Mater Sci 28:271–298
15. Gray H (1997) Gray's anatomy. The promotional reprint company, London
16. Hull D (1999) Fractography: observing, measuring and interpreting fracture surface topography. Cambridge University Press, Cambridge
17. Christensen AM, Passalacqua NV, Bartelink EJ (2014) Forensic anthropology: current methods and practice. Academic Press, Oxford
18. Peterson BL (1991) External beveling of cranial gunshot entrance wounds. J Forensic Sci 36(5):1592–1595
19. Kieser JA, Tahere J, Agnew C, Kieser DC, Duncan W, Swain MV, Reeves MT (2011) Morphoscopic analysis of experimentally produced bony wounds from low velocity ballistic impact. Forensic Sci Med Pathol 7:322–332. https://doi.org/10.1007/s12024-011-9240-y
20. Zukas JA (1982) Penetration and perforation of solids. In: Zukas JA, Nicholas T, Swift HF, Greszczuk LB, Curran DR (eds) Impact dynamics. John Wiley and Sons, Inc, USA, pp 155–214
21. Zaera R, Sánchez-Gálvez V (1998) Analytical modelling of normal and oblique ballistic impact on ceramic/metal lightweight armours. Int J Impact Engng 21(3):133–148
22. Murphy MS, Gaither C, Goycochea E, Verano JW, Cock G (2010) Violence and weapon-related trauma at Puruchuko-Huaquerones, Peru. Am J Phys Anthropol 142:636–649
23. Murphy MS, Spatola B, Weathermon R (2014) Allies today, enemies tomorrow: a comparative analysis of perimortem injuries along the biomechanical continuum. In: Martin DL, Anderson CP (eds) Bioarchaeological and forensic perspectives on violence: how violent death is interpreted from skeletal remains. Cambridge University Press, Cambridge, pp 261–288
24. Bird CE, Fleischman JM (2015) A rare case of an intact bone plug associated with a gunshot exit wound. J Forensic Sci 60(4):1074–1077

25. Kieser DC, Riddell R, Kieser JA, Theis J, Swain MV (2013) Bone micro-fracture observations from direct impact of slow velocity projectiles. J Arch Mil Med 2(1):e15614. https://doi.org/10.5812/jamm.15614
26. Amato JJ, Lawrence BJ, Lawson NS, Norman R (1974) High velocity missile injury. Am J Surg 127:454–459
27. Amato JJ, Syracuse D, Seaver PR, Rich N (1989) Bone as a secondary missile: an experimental study in the fragmenting of bone by high velocity missiles. J Trauma 29(5):609–612
28. Ragsdale BD, Josselson A (1988) Experimental gunshot fractures. J Trauma 28 (No.1 suppl): S109-S115
29. Thali MJ, Kneubuehl BP, Zollinger U, Dirnhoffer R (2002) A study of the morphology of gunshot entrance wounds, in connection with their dynamic creation, utilising the "skin-skull-brain" model. Forensic Sci Int 125:190–194
30. Goldsmith W (1960) Impact: the theory and physical behaviour of colliding solids. Edward Arnold Publishers, London
31. Wilkins ML (1978) Mechanics of penetration and perforation. Int J Eng Sci 16:793–807
32. Currey JD (2002) Bones: structure and mechanics. Princeton University Press, New Jersey
33. Dodd MJ (2006) Terminal ballistics: a text and atlas of gunshot wounds. CRC Press, Taylor and Francis Group, Florida
34. Loe L (2009) Perimortem trauma. In: Blau S, Ubelaker DH (eds) Handbook of forensic anthropology and archaeology. Left Coast Press, California, pp 263–283
35. Abrate S (1998) Impact on composite structures. Cambridge University Press, Cambridge
36. Vermeij EJ, Zoon PD, Chang SBCG, Keereweer I, Pieterman R, Gerretsen RRR (2012) Analysis of microtraces in invasive traumas using SEM/EDS. Forensic Sci Int 214(1):96–104
37. Spatola BF (2015) Atypical gunshot and blunt force injuries: wounds along the biomechanical continuum. In: Passalacqua NV, Rainwater CW (eds) Skeletal trauma analysis: case studies in context pp, pp 7–26
38. Quatrehomme G, Piercecchi-Marti M, Buchet L, Alunni V (2015) Bone bevelling caused by blunt trauma: a case report. Int J Legal Med 130(3):771–775. https://doi.org/10.1007/s00414-015-1293-0
39. Zeng K, Breder K, Dowcliffe DJ (1992) The Hertzian stress field and formation of cone cracks-I. Theoretical approach. Acta Metall Mater 40(10):2595–2600
40. Chen SY, Farris TN, Chandrasekar S (1995) Contact mechanics of Hertzian cone cracking. Int J Solids Struct 2(3/4):329–340
41. Lawn BR (1998) Indentation of ceramics with spheres: a century after Hertz. J Am Ceram Soc 81(8):1977–1994
42. Berryman HE, Gunther WM (2000) Keyhole defect production in tubular bone. J Forensic Sci 45(2):483–487
43. Chaudhri MM (2015) Dynamic fracture of inorganic glasses by hard spherical and conical projectiles. Philos Trans R Soc Lond A 373:20140135. https://doi.org/10.1098/rsta.2014.0135
44. Piekarski K (1970) Fracture of bone. J Appl Phys 41(1):215–223
45. Pope MH, Outwater JO (1972) The fracture characteristics of bone substance. J Biomech 5:457–465
46. Pechníková M, Mazzerelli D, Poppa P, Gibelli D, Baggi ES, Cattaneo C (2015) Microscopic pattern of bone fractures as an indicator of blast trauma: a pilot study. J Forensic Sci 60(5):1140–1145
47. Ubelaker DH (1996) The remains of Dr Carl Austin Weiss: anthropological analysis. J Forensic Sci 41(1):60–79
48. Kieser J (2012) Biomechanics of bone and bony trauma. In: Kieser J, Taylor T, Karr D (eds) Forensic Biomechanics. John Wiley & Sons, United Kingdom
49. Dixon DS (1982) Keyhole lesions of the skull and direction of fire. J Forensic Sci 23(3):555–566
50. Harcke HT, Levy AD, Getz JM, Robinson SR (2008) MDCT analysis of projectile injury in forensic investigation. AJR Am J Roentgenol 190(2):W106–W111
51. Huelke DF, Buege LJ, Harger JH (1967) Bone fractures produced by high velocity impacts. Am J Anat 120:123–132
52. Huelke DF, Harger JH, Buege LJ, Dingman HG, Harger DR (1967) Bone fractures produced by high velocity impacts. J Biomech 1:97–103

APPENDIX 3

Paper in press with the journal *Forensic Anthropology*

Entitled:

Forensic fractography of bone: fracture origins from impacts, and an improved understanding of the failure mechanism involved in beveling

Authors:

Angi M. Christensen, PhD, D-ABFA[a]

John M. Rickman, MSc[b]

Hugh E. Berryman, PhD, D-ABFA[c]

[a] Federal Bureau of Investigation Laboratory; Quantico, VA 22135 USA

[b] Cranfield Forensic Institute
Cranfield University
Defence Academy of the United Kingdom
Shrivenham
SN6 8LA

[c] Middle Tennessee State University; Murfreesboro, TN 37132 USA

Contributions to paper

As co-author I wrote a section covering cone cracking, the hypotheses for bevel formation and a review of the cone crack hypothesis presented in Chapters 3 and 4. I also wrote a section on failure modes and contributed to a section detailing the utility of fractographic analysis in the examination of bone failure surfaces, including its potential forensic significance. I prepared a figure that included µ-CT images and a macro photograph of a cleaned and dried tri-layered plug located *in situ* that formed part of the results of Chapter 2. Co-authorship also included regular editing, comments on other author's contributions, sharing of ideas on content and topic order and making pertinent changes considering reviewer feedback.